A thesis submitted in fulfilment of the requirements for the degree of
Doctor of Philosophy (Medicine and Health)

Investigating Novel Treatments to Improve Radiation Response in Diffuse Intrinsic Pontine Glioma

Faiqa Mudassar

Bachelor of Medical Science (Honours Class I)
SID: [Redaction]

The research reported in this thesis was supported by the Research Training Program Fee Offset

Supervisors: A/Prof Eric Hau, Dr Han Shen &
Prof Geraldine O'Neill

Translational Radiation Biology and Oncology Group
Centre for Cancer Research
The Westmead Institute for Medical Research

Faculty of Medicine and Health
The University of Sydney

2025

Statement of Originality

This is to certify that, to the best of my knowledge; the content of this thesis is my own work. This thesis has not been submitted for any degree or other purpose.

I certify that the intellectual content of this thesis is the product of my own work and that all the assistance received in preparing this thesis and sources have been acknowledged.

In cases where I am not the first author or corresponding author of a publication, permission has been obtained to include the published material in my thesis by the first and corresponding authors. This includes the immunohistochemistry staining in Figure 2E in the publication. Those experiments were performed by myself during my PhD and have been included as part of **Chapter 6**.

Faiqa Mudassar

Date: _____

Author's Contributions

Chapter 1: Introduction chapter includes parts of my review publication, where I am the first author:

> **Mudassar F**, Shen H, Cook KM, Hau E. Improving the synergistic combination of programmed death-1/programmed death ligand-1 blockade and radiotherapy by targeting the hypoxic tumour microenvironment. J Med Imaging Radiat Oncol. 2022;66(4):560–574.

Chapter 6: Animal studies chapter includes immunohistochemistry staining results some of which are presented in the following publication (Figure 2E), where I am the second author. I have contributed towards obtaining this data for the manuscript.

> Shen H, **Mudassar F**, Ma S, Wang X, Nguyen S, Bal N, Huynh QS, Wang D, Chang C, Ing P, Varikatt W, Lai J, Gloss B, Holst J, O'Neill GM, Gee H, Cook KM, Hau E. Inhibition of Mitochondrial Bioenergetics and Hypoxia to Radiosensitize Diffuse Intrinsic Pontine Glioma. Neuro-oncology (Charlottesville, Va). 2024.

Author Attribution Statement:

I certify that in cases where I am not the first or corresponding author of an item under review, permission to include the data has been granted by the first and corresponding author.

Faiqa Mudassar

Date: _____

As primary supervisor for the candidature upon which this thesis is based, I can confirm that the authorship attribution statements above are correct.

A/Prof Eric Hau
Date: _____

As auxiliary supervisor for the candidature upon which this thesis is based, I can confirm that the authorship attribution statements above are correct.

Dr Han Shen
Date: _____

As auxiliary supervisor for the candidature upon which this thesis is based, I can confirm that the authorship attribution statements above are correct.

Prof Geraldine M O'Neill
Date: _____

Ethical Clearance

This thesis includes animal research and animal ethics approval was obtained for all experiments conducted on mice. Ethics approval was granted by *Western Sydney Local Health District Animal Ethics Committee (WSLHD-AEC) (Approval number - 4370).*

Conferences, Publications and Awards

Conferences: Oral Presentations

- **Mudassar F**, Chang C, Ing P, Cook KM, O'Neill G, Shen H, Hau E. Investigating Novel Treatments to Improve Radiation Response in Diffuse Intrinsic Pontine Glioma; Student Oral Presentation (10 mins); Sydney Cancer Conference 2021, 9-10 September 2021 (virtual).
- **Mudassar F**, Chang C, Ing P, Cook KM, O'Neill G, Shen H, Hau E. Investigating Novel Treatments to Improve Radiation Response in Diffuse Midline Glioma; HDR "Funding for Impact" Pitch Session (5 mins) at The Drug Discovery Initiative Symposium 2022, 5th May 2022 at The University of Sydney, Sydney.
- **Mudassar F**, Chang C, Ing P, Cook KM, O'Neill G, Shen H, Hau E. Investigating Novel Treatments to Improve Radiation Response in Diffuse Midline Glioma; Student 3-minute Thesis Talk at The Westmead Research and Innovation Conference, 18th-19th August 2022 at The Westmead Innovation Centre, Sydney.
- **Mudassar F**, Chang C, Ing P, Cook KM, O'Neill G, Shen H, Hau E. Targeting Mitochondrial Metabolism and Tumour Hypoxia as an Approach to Improve Radiation Response in Diffuse Midline Gliomas; Student Oral Presentation (10 mins); EMBL Australia Postgraduate Symposium (EAPS2022), 9th-11th November 2022 at The Bio21 Institute, Melbourne.
- **Mudassar F**, Chang C, Ing P, Cook KM, O'Neill G, Shen H, Hau E. Targeting Mitochondrial Metabolism and Tumour Hypoxia as an Approach to Improve Radiation Response in Diffuse Midline Gliomas; Student Oral Presentation (10 mins); HDR Cancer Conference 2022, 17th November 2022 at The University of Sydney, Sydney.
- **Mudassar F**, Chang C, Ing P, Cook KM, O'Neill G, Shen H, Hau E. Targeting Mitochondrial Metabolism and Tumour Hypoxia as an Approach to Improve Radiation Response in Diffuse Midline Gliomas; Rapid Fire Talk (5 mins); 6th National Particle Therapy Symposium 2022, 24th and 25th November 2022 at The Westmead Innovation Centre, Sydney.
- **Mudassar F**, Ing P, Chang C, Nguyen S, Warnken ZN, Cook KM, O'Neill G, Shen H, Hau E. Atovaquone Radiosensitises Diffuse Midline Glioma by Targeting Mitochondrial Metabolism and Tumour Hypoxia; Student Oral Presentation (12 mins);

Cancer Research Network HDR Student Cancer Research Symposium, 16th November 2023 at The University of Sydney, Sydney.

- **Mudassar F**, Ing P, Nguyen S, Chang C, Cook KM, Warnken ZN, O'Neill G, Shen H, Hau E. Inhibiting Oxidative Phosphorylation and Hypoxia with Atovaquone – a Strategy to Radiosensitize Diffuse Midline Gliomas; Rapid Report Oral Presentation (4 mins); Society for Neuro-Oncology 2024 Annual Meeting, 21-24 November 2024 at Houston, Texas.

Conferences: Poster Presentations

- **Mudassar F**, Chang C, Ing P, Cook KM, O'Neill G, Shen H, Hau E. Targeting Tumour Hypoxia and Mitochondrial Metabolism with Anti-Parasitic Drugs as an Approach to Improve the Radiosensitivity of Diffuse Intrinsic Pontine Glioma; Society for Neuro-Oncology 2021 Annual Meeting, 18th-21st November 2021 at Boston, Massachusetts (virtual).
- **Mudassar F,** Chang C, Ing P, Cook KM, O'Neill G, Shen H, Hau E. Investigating Novel Treatments to Improve Radiation Response in Diffuse Intrinsic Pontine Glioma; The Westmead Association Hospital Week Research Symposium, 8th March 2022 at The Westmead Hospital, Sydney.
- **Mudassar F**, Chang C, Ing P, Cook KM, O'Neill G, Shen H, Hau E. Targeting Mitochondrial Metabolism and Tumour Hypoxia – A Promising Strategy to Improve the Radiosensitivity of Diffuse Midline Glioma; Children's Brain Cancer Conference, 23rd and 24th March 2023 at Sofitel Brisbane Central, Brisbane.
- **Mudassar F**, Ing P, Chang C, Nguyen S, Cook KM, Warnken ZN, O'Neill G, Shen H, Hau E. Atovaquone Radiosensitises Diffuse Midline Glioma by Inhibiting Mitochondrial Metabolism and Hypoxia; The Westmead Association Hospital Week Research Symposium, 16-18th August 2023 at The Westmead Hospital, Sydney.
- **Mudassar F**, Ing P, Chang C, Nguyen S, Warnken ZN, Cook KM, O'Neill G, Shen H, Hau E. Atovaquone Radiosensitises Diffuse Midline Glioma by Targeting Mitochondrial Metabolism and Tumour Hypoxia; NSW Cancer Conference 2023, 18-19th September 2023 at International Convention & Exhibition Centre, Sydney.

- **Mudassar F**, Ing P, Nguyen S, Chang C, Cook KM, Warnken ZN, O'Neill G, Shen H, Hau E. Inhibiting Oxidative Phosphorylation and Hypoxia with Atovaquone – a Strategy to Radiosensitize Diffuse Midline Gliomas; Society for Neuro-Oncology 2024 Annual Meeting, 21-24 November 2024 at Houston, Texas.

Additional Presentations

- *Translational Radiation Biology and Oncology Group, The Westmead Institute for Medical Research, (presented several times throughout the year).*
- *Westmead Hospital Radiation Oncology Department, (presented once every year during my PhD).*
- *Centre for Cancer Research (CCR), The Westmead Institute for Medical Research, (presented once every year during my PhD).*

Publications arising from this candidature

- **Mudassar F**, Shen H, Cook KM, Hau E. Improving the synergistic combination of programmed death-1/programmed death ligand-1 blockade and radiotherapy by targeting the hypoxic tumour microenvironment. J Med Imaging Radiat Oncol. 2022;66(4):560–574.
- Shen H, **Mudassar F**, Ma S, Wang X, Nguyen S, Bal N, Huynh QS, Wang D, Chang C, Ing P, Varikatt W, Lai J, Gloss B, Holst J, O'Neill GM, Gee H, Cook KM, Hau E. Inhibition of Mitochondrial Bioenergetics and Hypoxia to Radiosensitize Diffuse Intrinsic Pontine Glioma. Neuro-oncology (Charlottesville, Va). 2024.

Publications prior this candidature

- **Mudassar F,** Shen H, O'Neill G, Hau E. Targeting tumor hypoxia and mitochondrial metabolism with anti-parasitic drugs to improve radiation response in high-grade gliomas. J Exp Clin Cancer Res. 2020;39(1):1-17.

Awards

- Best Student Oral Presentation (by Cancers Journal) at The Sydney Cancer Conference in September 2021.
- Best Student Oral Presentation (People's choice award) at The Sydney Cancer Conference in September 2021.
- Best Poster Presentation at the Westmead Association Research Symposium in March 2022.
- Best Student Oral Presentation at the EMBL Australia Postgraduate Symposium (EAPS2022) in November 2022 at The Bio21 Institute, Melbourne.
- Best Student Oral Presentation at Cancer Research Network HDR Student Cancer Research Symposium in November 2023 at The University of Sydney.
- Sydney Cancer Partner Travel Grants for attending Children's Brain Cancer Conference 2023 and NSW Cancer Conference 2023.

Abstract

Diffuse intrinsic pontine glioma (DIPG), now categorised under Diffuse Midline Glioma (DMG) is a uniformly fatal paediatric brainstem tumour with median survival of less than 1 year. Radiotherapy (RT) has been the only effective treatment for decades, but most DIPGs recur within several months due to radioresistance. The hypoxic tumour microenvironment is a major contributor to clinical radioresistance. Therefore, alleviating tumour hypoxia could enhance the effectiveness of RT and improve the survival outcomes of DIPG patients.

We found evidence suggesting increased mitochondrial oxidative phosphorylation (OXPHOS) in DIPG/DMG patient samples suggesting that these tumour cells are utilizing more oxygen and that could lead to the development of localised hypoxia. Hence, we aimed to target OXPHOS by decreasing the oxygen consumption rate (OCR) of DIPG cells. This will alleviate hypoxia by sparing more oxygen and subsequently improve the radiosensitivity of DIPG cells. First, we performed an anti-parasitic drug screening using FDA-approved drugs to identify potent OCR inhibitors. The best OCR inhibitor identified from the screening was atovaquone. Using several *in vitro* experiments, we found that atovaquone inhibited the OCR of several DIPG cell lines. It specifically targeted the mitochondrial complex III resulting in a shutdown of overall mitochondrial bioenergetics, enhancing oxidative stress, decreasing hypoxia in DIPG neurospheres and sensitising DIPG cell lines to RT. The efficacy of commercial atovaquone was tested against the higher blood-brain barrier (BBB) penetrant version, the amorphous solid dispersion (ASD) atovaquone formulation. We found no differences in the OCR inhibition and hypoxia modification of both formulations paving way for investigating ASD atovaquone using orthotopic DIPG models. The next best OCR inhibitor with excellent BBB penetration was mefloquine. We found that it significantly decreased both mitochondrial and glycolytic metabolism of DIPG cells, increased oxidative stress, decreased hypoxia in DIPG neurospheres and also sensitised these cells to RT.

Furthermore, we validated the presence of hypoxia in DIPG tumour-bearing mice brain sections and found positive HIF-1α, VEGFA, and EF5 staining, colocalised in the tumour region, thus providing support towards the presence of hypoxia in DIPG. Finally, we assessed the radiosensitising efficacy of ASD atovaquone using *in vivo* orthotopic DIPG models. ASD atovaquone also appears to be promising radiosensitiser *in vivo* as the combination of ASD

atovaquone+RT significantly enhanced the survival of HSJD-DIPG-007 xenograft model compared to single treatments.

In summary, this thesis provides valuable evidence to support upregulated OXPHOS and the presence of hypoxia in DIPG tumour. It shows that targeting OXPHOS can decrease hypoxia and improve the radiosensitivity of DIPG cells. It identifies atovaquone and mefloquine as hypoxia modifiers and radiosensitisers of DIPG *in vitro*, with the ASD atovaquone showing promising efficacy *in vivo* orthotopic DIPG models. Validating atovaquone's efficacy using additional DIPG xenograft models will further strengthen these findings and pave way for clinical studies. These findings are promising and could be translated to other brain tumours as well as extracranial tumours with hypoxic profile. Overall, this study makes important contribution towards identifying novel treatments for the incurable DIPG tumour.

Acknowledgements

First, I would like to express my deepest appreciation and gratitude to my primary supervisor A/Prof Eric Hau for his valuable guidance and mentorship throughout my PhD candidature. Thank you Eric for being very encouraging throughout all my achievements and being very supportive of me gaining domestic and international conferences experience. I am very grateful to get the opportunity to do my PhD in the Translational Radiation Biology and Oncology group. I would like to extend special thanks to my co-supervisor Dr Han Shen for being an amazing support in the lab, for his regular guidance with experiments and troubleshooting throughout my candidature. I would also like to extend my gratitude to my co-supervisor Geraldine O'Neill for providing me with support towards learning the organoid culture technique and lentiviral transductions. I would like to thank Dr Kristina Cook for her advices and guidance on several experiments. I would also like to extend special thanks to my lab members Cecilia Chang, Prunella Ing and Sandy Nguyen for being a great research support in the lab and always assisting me with experiments where needed. Thanks to Poonam, Neha, Susan and Lucy for being very supportive and helpful at various stages of my PhD. I have made beautiful memories with all of you!

Further, I would extend special thanks to Dr Zachary N Warnken for providing the ASD atovaquone formulation for my PhD project, Samuel Bax for teaching me the organoid culturing technique, Dr Yuyan Chen for teaching me lentiviral transductions, A/Prof Winny Varikatt for helping validate our H&E and IHC staining, Dr Ryan Duchatel for performing brain and plasma concentration analysis of ASD atovaquone, Dr Hui Zhang for technical support with microscopy and IVIS imaging, Dr Li Ma and Urvashi Varsani for helping with tissue processing and sectioning and guidance on IHC staining, Dr Joey Lai for processing RNA sequencing data, and Dr Brian Gloss and Dr Shiyong Ma for analysing and generating figures for RNA sequencing work.

I would also acknowledge all my fellow students and members of the centre for cancer research – Twingle, Dee, Parul, Sarah, Mel, Carl, Lauren, Eunice, Atharva for creating a fun and inspiring environment at WIMR.

Additionally, I would like to thank my family for being my biggest support in this long journey. I strongly believe that their constant support and motivation has made my PhD candidature possible.

Finally, I would like to thank my dearest husband, Hassan for his emotional and moral support through the challenging final year of my PhD. You are a lovely partner.

Table of Contents

List of Tables

List of Figures

List of Abbreviations

DIPG	Diffuse intrinsic pontine gliomas
HGG	High-grade gliomas
MRI	Magnetic resonance imaging
FLAIR	Fluid-attenuated inversion recovery
DMG	Diffuse midline glioma
WHO	World Health Organisation
RT	Radiotherapy/Radiation
BBB	Blood-brain-barrier
HDAC	Histone deacetylase
IDO	Indoleamine 2,3-dioxygenase
ICI	Immune checkpoint inhibitors
DNX-2401	Delta-24-RGD
HSV1716	Herpes simplex virus 1716
ADCVs	Autologous dendritic cell vaccines
TME	Tumour microenvironment
EMT	Epithelial-mesenchymal transition
HIF	Hypoxia-inducible factor
VHL	von Hippel-Lindau
PHD	Prolyl hydroxylases
HRE	Hypoxia-responsive elements
lncRNAs	Long noncoding RNAs
OER	Oxygen enhancement ratio
ROS	Reactive oxygen species
GBM	Glioblastoma multiforme

TCA	Tricarboxylic acid cycle
HAPs	Hypoxia-activated prodrugs
ATP	Adenosine triphosphate
OXPHOS	Oxidative phosphorylation
ETC	Electron transport chain
NADH	Nicotinamide adenine dinucleotide
$FADH_2$	Flavin adenine dinucleotide
ADP	Adenosine diphosphate
OCR	Oxygen consumption rate
NSCLC	Non-small cell lung cancer
PCP	*Pneumocystis carinii* pneumonia
MMP	Mitochondrial membrane potential
DHODH	Dihydroorotate dehydrogenase
ASD	Amorphous solid dispersion
DHFR	Dihydrofolate reductase
CRC	Colorectal cancer
DMEM/F-12	Dulbecco's Modified Eagle Medium/Nutrient Mixture F-12
FGF	Human Fibroblast Growth Factor
EGF	Human Epidermal Growth Factor
PDGF-AA	Human Platelet Derived Growth Factor-AA
PDGF-BB	Human Platelet Derived Growth Factor-BB
DPBS	Dulbecco’s Phosphate Buffered Saline
DMSO	Dimethyl Sulfoxide
FBS	Fetal bovine serum

MTT	Thiazolyl Blue Tetrazolium Bromide
KH_2PO_4	Potassium phosphate monobasic
$MgCl_2$	Magnesium chloride solution
EGTA	Ethylene glycol-bis(2-aminoethylether)-N,N,N',N'-tetra acetic acid
TMPD	N,N,N',N'-Tetramethyl-p-phenylenediamine dihydrochloride
ADP	Adenosine 5'-diphosphate monopotassium salt dihydrate
PMP	Plasma Membrane Permeabilizer
PI	Pierce Protease and Phosphatase Inhibitor
BSA	Bovine Serum Albumin
HBSS	Hanks' Balanced Salt Solution
DHE	Dihydroethidium
TSM-B	Tumor Stem Medium Base
TSM-W	TSM Working
MAS	Mitochondrial Assay Solution
TBST	Tris Buffered Saline with Tween-20
PBST	Phosphate Buffered Saline with Triton-X
IHA-hTERT	Immortalized human astrocytes
ECAR	Extracellular acidification rate
CFA	Colony formation assay
DHE	*Dihydroethidium*
WSLHD-AEC	*Western Sydney Local Health District Animal Ethics Committee*
ARC	*Animal Resources Centre*
BSF	*Biological Services Facility*
MS	Mass Spectrometry

MRM	Multiple reaction monitoring
H&E	Haematoxylin and eosin
SD	Standard deviation
EPEN	Ependymoma
HGG-IDH-WT/H3-WT	High-grade gliomas (IDH-wildtype and H3-wildtype)
CAUD	Caudate
CERB	Cerebellum
HYPO	Hypothalamus
FAD	Flavin adenine nucleotide
NSCLC	Non-small cell lung cancer
KEGG	Kyoto Encyclopedia of Genes and Genomes
GSVA	Gene Set Variation Analysis
DEGs	Differentially expressed genes
ESCC	Esophageal squamous cell carcinoma
VEGFA	Vascular endothelial growth factor A
CA-IX	Carbonic anhydrase IX
GFP	Green fluorescent protein
IVIS	In vivo imaging system
MOI	Multiplicity of infections
FBS	Fetal bovine serum

Chapter 1

Introduction

Publications incorporated into this chapter:
Mudassar F, Shen H, Cook KM, Hau E. Improving the synergistic combination of programmed death-1/programmed death ligand-1 blockade and radiotherapy by targeting the hypoxic tumour microenvironment. J Med Imaging Radiat Oncol. 2022;66(4):560–574.

The above citation has been incorporated at some parts in this introductory chapter, indicated with "quotation marks", with some modifications, all of which was written by the author of this thesis.

Chapter 1. Introduction

1.1. Diffuse intrinsic pontine glioma

1.1.1 Epidemiology

Diffuse intrinsic pontine gliomas (DIPGs) are highly aggressive and incurable tumours of the brainstem, and are the major cause of brain tumour-related deaths in children. These tumours comprise nearly 50% of all the high-grade gliomas (HGGs) primarily affecting children (1). DIPGs represent about 10-20% of all paediatric brain tumours and about 80% of all paediatric brainstem tumours (2-4). Approximately 20-30 children are diagnosed with DIPG annually in Australia and about 300 children in the United States (4). The median age of diagnosis of patients with DIPG is about 6-8 years (5). The prognosis of this devasting disease is dismal as the median survival is less than 1 year, and about 90% of children succumb to the disease within 2 years from initial diagnosis (3).

Each of the four terms in DIPG (diffuse, intrinsic, pontine, glioma) refer to the four characteristics of this tumour. “Diffuse” refers to the growth pattern of the tumour as it infiltrates diffusely across the brainstem region. This diffuse pattern also means that surgical resection of this tumour is challenging (6). “Intrinsic” refers to the growth of the tumour in the deep brain parenchyma, the pons. “Pontine” explains to the location of the tumour, originating in the pons in the brainstem. Finally, “glioma” defines the origin of the tumour, the glial cells (7).

1.1.2 Clinical presentation and diagnosis

At initial stages of diagnosis, DIPG patients may demonstrate several classic neurological symptoms including long tract signs (Babinski reflex and hyperreflexia), cranial neuropathy

(diplopia and facial asymmetry), ataxia and dysmetria (8, 9). As DIPG tumour grows, the cranial nerves VI and VII are predominantly affected and patients present signs of dysfunction specific to these nerves (9). At later stages, patients could develop hydrocephalus and present symptoms of elevated intracranial pressure (10).

Diagnosis of DIPG can be made by clinical presentation and magnetic resonance imaging (MRI) scans, both with and without contrast. **Figure 1.1** shows that these tumours demonstrate hypointensity on T1-weighted imaging and hyperintensity on T2-weighted/fluid-attenuated inversion recovery (FLAIR) imaging (11). In most instances, MRI scans show enlargement of pons with a mass covering more than 50% of the diameter of pons (10). The growing tumour also typically envelops the basilar artery. In some cases, areas of necrosis with serpiginous contrast enhancement is evident (10).

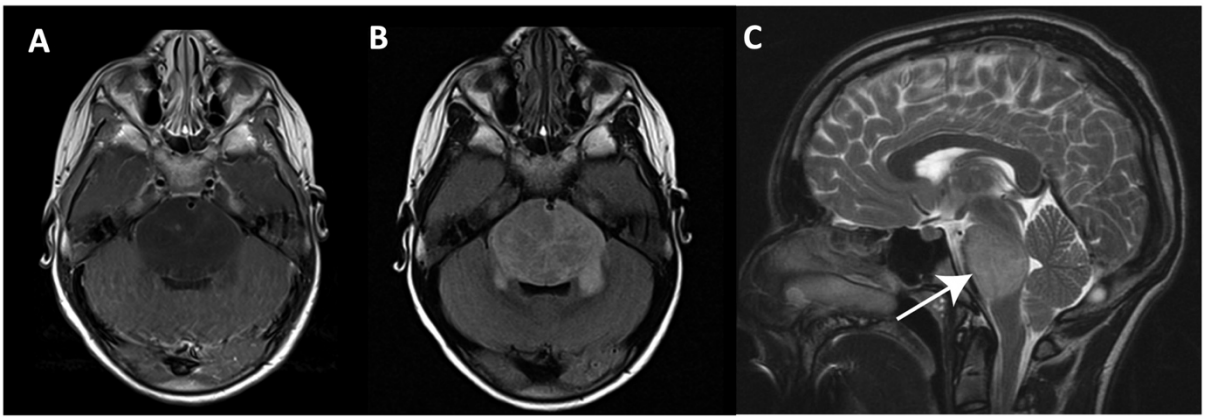

Figure 1.1 MRI Scans showing typical presentation of DIPG at diagnosis.
(A) T1-weighted image post-contrast showing enlarged pons. The enhancement is not clear and the tumour appears poorly marginated (10). (B) FLAIR image showing hyperintense tumour region in the pons with clear tumour margins and enveloped basilar artery (10). (C) Sagittal T2-weighted image showing hyperintense tumour mass in the pons with well circumscribed border (3).

1.1.3 Molecular subtypes

DIPGs can be classified into three molecularly distinct subgroups – H3K27M, MYCN and silent (3). More than 80% of DIPG patients present with the histone mutation – H3K27M. The post-translational modifications of histone (H3) at lysine 27 (K27) plays significant role in the regulating the expression of genes and maintaining a balance between cell differentiation and proliferation. Dysfunction of the methylation of this histone (H3K27me3) appears to be an emerging target present in several cancer types (12). The presence of histone mutation H3K27M means a substitution of lysine-to-methionine at the amino acid position 27. H3K27M

is present on the histone variants H3.1 and H3.3 encoded by *HISTIH3B* and *H3F3A* genes respectively (3). This mutation is a hallmark of DIPG, leading to a loss of histone trimethylation and causing a global hypomethylation of H3K27 and subsequent increase in acetylation. H3K27 hypomethylation results in the loss of gene silencing, decreasing cell differentiation ability and increasing pro-oncogenic transcriptional activities, all of which induces the growth and formation of gliomas (**Figure 1.2)** (13). Moreover, other genomic and proteomic alterations identified in DIPG tumour include *TP53* mutation, *MYCN* amplification, *ATRX* depletion, *ACVR1* mutation, alterations in receptor tyrosine kinase (RTK), and amplification of cell cycle related genes (**Figure 1.2)** (14).

The molecular classification of DIPG has transformed over the past decade leading to the new entity "diffuse midline glioma (DMG) – H3K27-mutant (H3K27M)" (15). This terminology included paediatric tumours with K27M mutation including H3.1 and H3.3 growing along the midline brain structures. DIPG is now included as a subset of DMG with tumour diagnosed in the pons, whereas DMG is the comprehensive terminology encompassing brain tumours of the midline brain structures, the brainstem, thalamus, cerebellum, or the spinal cord (7). In 2021, the World Health Organisation (WHO) further updated the terminology of DMG from "H3K27-mutant" to "H3K27-altered" to encompass additional identified pathophysiological mechanism in these tumours (16).

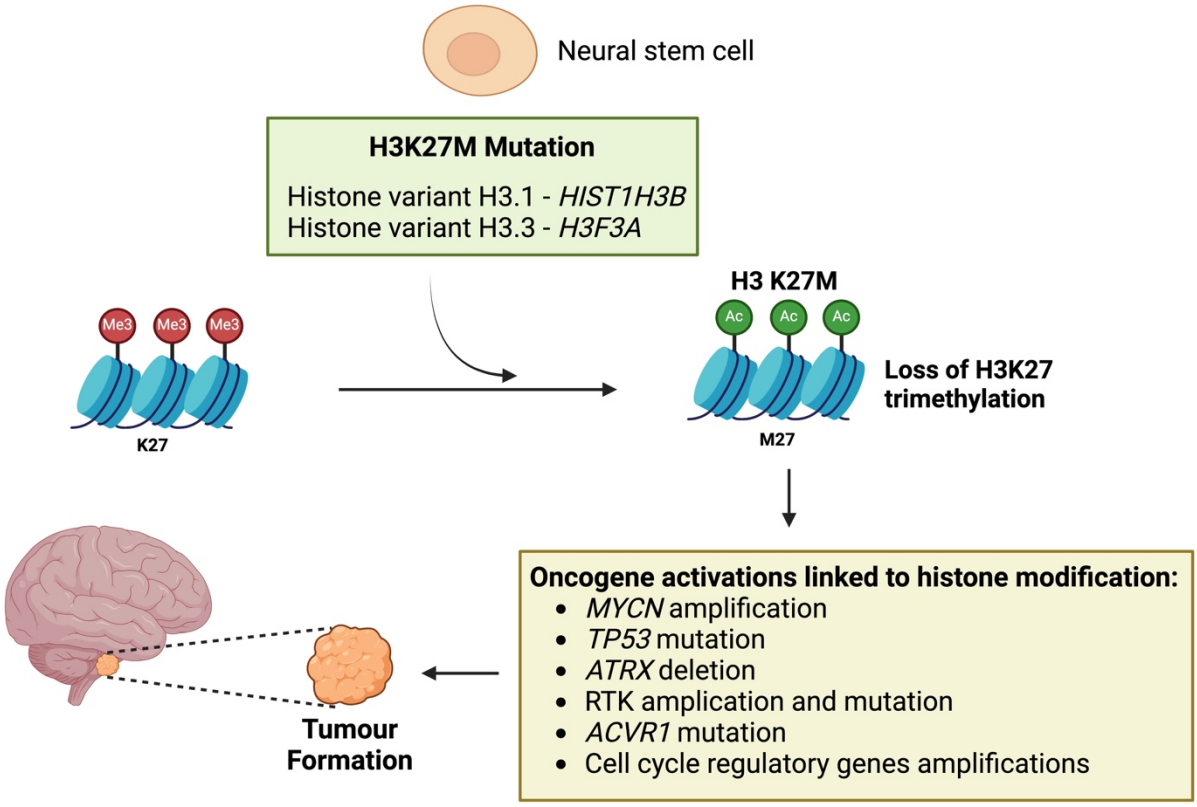

Figure 1.2. H3K27M mutation and pathogenesis of DIPG.
The presence of lysine-to-methionine substitution at amino acid 27 (K27 mutation) on histone 3 (H3) variant results in a global loss of trimethylation (Me3) of the histones and gain of acetylation (Ac). The histone modification is linked to additional oncogene activations which subsequently lead to tumour formation. (Figure created using Biorender and adopted with modifications from (17))

1.1.4 Current treatments and management

Despite decades of clinical research, DIPG remains incurable with no available effective therapies. To date, more than 250 clinical trials assessing a range of targets have been performed, however no significant outcomes were achieved. Therefore, there is an urgent need for more research and to develop novel therapies for DIPG patients.

1.1.4.1 Surgery

The infiltrative growth pattern of DIPG into the pons of the brainstem poses a significant challenge to maximal safe surgical resection (4). The pons is critical to various life supporting functions including facial sensations, coordinating face and eye movements, and hearing and balance. The cranial nerves V, VI, VII and VIII also originate from the pons (18). The growing DIPG tumour could damage these key nerves with patients demonstrating symptoms relevant

to the nerves damaged. Therefore, the diffuse nature of DIPG means that surgery is not a feasible option in this tumour type.

1.1.4.2 Radiotherapy

Radiotherapy (RT) has been the cornerstone of treatment for the management of DIPG patients for over two decades. External beam RT is delivered at a standard dose of 54-60 Gy, in 1.8-2.0 Gy fractions daily for 5 days/week over a period of 6 weeks (2). RT treatment can be associated with neurocognitive dysfunction in children aged under 3 years (19). It is still considered but is less likely used as a management option in that age group. Nonetheless, RT only provides symptomatic relief and extends survival of DIPG patients by approximately 3 months (4, 20). Within 3-8 months after the completion of RT, most DIPG patients begin to display recurrent symptoms of disease progression (21).

Although fractionated RT is the standard treatment for children with DIPG, studies have also evaluated hypofractionated RT. In hypofractionated RT treatment, the total RT dose is divided into larger doses and the treatment course is shortened compared to conventional RT schedule. It was found that hypofractionated RT is feasible and well-tolerated by DIPG patients, yielding similar results in comparison to conventional fractionated RT. This suggested that hypofractionated RT could be useful in terms of reducing the ongoing treatment burden on DIPG patients (22). The effectiveness and feasibility of hypofractionated RT is still being evaluated in other studies (NCT03841435, (23)).

Following tumour recurrence, re-irradiation has also been considered as a palliative intervention for DIPG patients (24). Studies have demonstrated that re-irradiation can be useful in providing symptomatic relief and extending survival when compared to patients not undergoing re-irradiation (25, 26). Some ongoing clinical trials (NCT01777633, NCT03126266) are still assessing the potential benefits and outcomes of re-irradiation in DIPG patients.

Additionally, a recent study also investigated the efficacy of proton therapy on DIPG patients compared to conventional photon RT (27). Proton therapy delivers proton particles to the tumour location and offers therapeutic benefit by localising the dose to the tumour area and reducing irradiation to the normal surrounding brain tissue. This study recruited 12 DIPG

patients and delivered proton therapy at 50 Gy in 30 fractions. Although proton therapy was well-tolerated by DIPG patients, it did not yield superior results to conventional photon therapy and further research is needed (27).

1.1.4.3 Chemotherapy

Ongoing research to understand the biology and pathophysiology of DIPG has led to the identification of novel therapeutic targets. Various chemotherapeutics have been evaluated showing promising efficacy in DIPG preclinical studies. However, the intact blood-brain-barrier (BBB) poses a significant challenge for new chemotherapeutics against DIPG treatment. This is because several drugs that show promising efficacy *in vitro*, fail to reach clinical trials due to poor penetrability across the BBB (28). Nonetheless, many promising candidates are currently under investigation in clinical trials including the CDK 4/6 inhibitor - Ribociclib (NCT05843253), histone deacetylase (HDAC) inhibitor – Vorinostat (NCT02420613), CIpP activator – ONC201 (NCT05476939, NCT05580562), IDO (indoleamine 2,3-dioxygenase) inhibitor - Indoximod (NCT04049669), and others. Others studies are also investigating PARP inhibitors, hedgehog pathway inhibitors, and traditional chemotherapy agents (temozolomide, doxorubicin) for DIPG treatment (29).

1.1.4.4 Immunotherapy

There has also been an emerging interest in understanding the immune microenvironment of DIPG to develop immunotherapies against this tumour. Due to limited availability of tumour samples and appropriate animal models, there still exist gaps in the clear understanding of the immune microenvironment of DIPG. DIPG appear to possess a "cold tumour microenvironment" characterised by poor infiltration of immune cells, lack of antigen presenting cells, lower levels of inflammatory secretions, and defective immune death mechanisms, all of which point towards a non-inflammatory immune microenvironment (14). There is also lack of expression of the immune checkpoint proteins PD-1 and PD-L1, limited detection of several immune-inhibitory molecules such as soluble NKG2D and few immunosuppressive factors, suggesting poor activation of immune escape mechanisms in DIPG (14).

Currently, the potential immunotherapies against DIPG includes immune checkpoint inhibitors (ICIs), CAR-T Cells, oncolytic viruses and vaccine therapy. ICIs have been trialled in DIPG, however no survival benefit was observed (30-32). CAR-T cell therapy holds promise especially after identification of a novel disialoganglioside target, GD2, that is highly expressed in DIPG tumour cells (33). The exciting preclinical findings led to a recent clinical trial assessing the efficacy of GD2-CAR-T cells for H3K27M DMG which has also shown encouraging results (34). Furthermore, two oncolytic viruses, the adenovirus DNX-2401 (delta-24-RGD) and the herpes simplex virus 1716 (HSV1716), have been developed against paediatric gliomas. Oncolytic viruses aim to specifically target cancer cells while sparing normal cells (35). Both of these oncolytic viruses have demonstrated promising efficacy in preclinical DIPG studies (36-38), and a clinical trial has also validated the efficacy of delta-24-RGD (NCT03178032). Finally, vaccine therapy works by reactivating the immune system to induce an immune response and has also gained attention in DIPG research. Peptide vaccines targeting H3K27M specific proteins and autologous dendritic cell vaccines (ADCVs) have been studied against DIPG (39-41). An ongoing trial is investigating ADCVs against DIPG (NCT03396575).

1.1.5 Proposing radiosensitisers for DIPG management

To date, the management of DIPG remains complex and more research involving new treatment combinations are subjects of ongoing research. Although palliative in intent, RT still remains the mainstay of treatment for the management of DIPG patients. Efforts to understand the biological mechanisms responsible for tumour recurrence and resistance to RT, and targeting those pathways could help improve the efficacy of RT in this deadly disease. Combination of radiosensitisers with RT could therefore prolong survival outcomes of children with DIPG.

Radioresistance can be classified as inherent or acquired radioresistance. Inherent radioresistance is an important aspect of RT failure and it relates to the presence of a hypoxic tumour microenvironment (TME), cancer stem cells and oncogenic mutations (42). Acquired radioresistance is primarily associated with modifications in TME by inflammation, epithelial-mesenchymal transition (EMT), tumour metabolic reprogramming, immune response, and tumour microbiota and senescence cells (42). It is also important to note that there can be differences in inherent or acquired radioresistance across tumour types and both may not

coexist in certain tumour types (43). In this thesis, we will primarily focus on discussing how the hypoxic TME is a major obstacle to RT and could be a significant contributing factor to radioresistance in DIPG. We will further address how targeting hypoxia using radiosensitisers can be a potential therapeutic strategy to improve the efficacy of RT in DIPG.

1.2. Tumour hypoxia – a barrier to radiotherapy

1.2.1 Hypoxia and the tumour microenvironment

Hypoxia is a characteristic feature of most solid tumours. "Hypoxia occurs when the oxygen pressure in the TME drops below normal for the surrounding tissue. It arises due to the high oxygen consumption and rapid proliferation of tumour cells, leading to a mismatch between oxygen supply and demand (44)." The growing tumour and poor vasculature develop regions with decreasing oxygenation gradient, with areas containing hypoxic and necrotic cells furthest away from the blood supply (**Figure 1.3A**) (45). The poorly oxygenated tumours have aggressive phenotypes, are highly metastatic, and are shown to be resistant to radiotherapy, chemotherapy and immunotherapy (46-48). There are also close links between hypoxic tumours and poor patient prognosis (49).

Hypoxia-regulated changes and homeostasis is maintained by the heterodimeric transcription factors, hypoxia-inducible factors (HIFs). HIFs consist of the oxygen-sensitive isoforms, HIF-1α, HIF-2α and HIF-3α and a constitutively expressed HIF-1β subunit (50). Of these, HIF-1α and HIF-2α are the most studied isoforms. Although appearing to be differentially expressed, both HIF-1α and HIF-2α share several target genes with positive responses to hypoxia (51). There is little understanding on HIF-3α mechanisms but it appears to act as both a positive and a negative regulator of hypoxia (51). Under hypoxic conditions, the presence of oxygen causes hydroxylation of the proline residues on the HIF-1α, HIF-2α, or HIF-3α. The hydroxylation is mediated by either of the three HIF prolyl hydroxylases (PHD1, PHD2, PHD3). This hydroxylation results in the binding of von Hippel-Lindau (VHL) protein to the hydroxylated HIF-α subunits, leading to ubiquitination and proteasomal degradation of HIF-αs (50). Under hypoxic conditions, lack of oxygenation prevents hydroxylation of the HIF-as. The accumulated HIF-a dimerises with HIF-β and binds to the hypoxia-responsive elements (HRE) sequences on the DNA. The coactivator proteins p300 and CBP bind to the HIF-a and this activates the transcription of target genes (50).

Hypoxia modifies the TME, creating a favourable microenvironment for the growth of tumour cells. It can modify the extracellular matrix composition of the TME enhancing the invasive potential of tumour cells (52). Hypoxia can promote angiogenesis in attempts to restore oxygen levels and replenish nutrients in the TME. Angiogenesis also allows tumour cells to disseminate and migrate to distant locations, resulting in tumour metastasis (45). Moreover, hypoxia can modulate long noncoding RNAs (lncRNAs) which regulate genes at protein, transcriptional, post-transcriptional regulation and epigenetic levels (53, 54). These lncRNAs appear to regulate tumorigenesis and progression by maintaining a cross-talk between the tumour cells and the other cells in the TME (55, 56). Hypoxia also promotes metabolic reprogramming, changing the composition of key metabolites present in the TME, all of which could contribute to tumour growth (57). Furthermore, presence of hypoxia can play significant role in dampening the immune response by regulating the function of immune cells and inhibitory molecules in the TME, which in turn allows tumour progression and immune evasion (58).

1.2.2 How does hypoxia contribute to RT resistance?

In 1909, Gottwald Schwarz work demonstrated the first clinical observation of linking hypoxia and resistance to RT. It was found that irradiating areas of the skin with compressed blood flow appeared to have decreased response to RT, highlighting the importance of oxygen for effective cell killing by RT (59). In 1950s, Gray and his colleagues investigated the relationship between oxygen concentration and RT (60). They found greater tumour regression in mice irradiated in presence of oxygen alone compared to when irradiated in presence of various mixtures of oxygen, nitrogen, and air at 1 atmosphere pressure (61). In the following years, several studies have been performed concluding that hypoxia induces radioresistance.

The correlation between oxygen concentration and cellular response to RT is referred to as oxygen enhancement ratio (OER). OER is a ratio of the radiation dose required to achieve the same biological effect when irradiating cells under normoxic vs hypoxic conditions (62). The OER of normoxic vs hypoxic cells is around 2.5-3. This means that hypoxic tumours are radioresistant, requiring triple the amount of RT dose to achieve same cell killing effect compared to normoxic tumours (63).

Ionizing radiation induces DNA damage by producing free radicals. This process involves radiolysis of water in the cells to produce reactive oxygen species (ROS), such as hydroxyl (OH•) and hydrogen radicals (H•) (62). Under normoxic conditions, these radicals can react with molecular oxygen to produce more toxic peroxides which "fix" the radiation-induced DNA damage, thus causing permanent damage to DNA and cell death (**Figure 1.3B**) (62). Whereas under hypoxic conditions, low levels of oxygen prevents formation of toxic peroxides and the radicals produced by ROS can be deactivated by antioxidants and restored back to their original form (**Figure 1.3B**). This reduces the amount of chromosomal aberrations and irreversible DNA damage, thus compromising the efficacy of RT in hypoxic tumour cells (62).

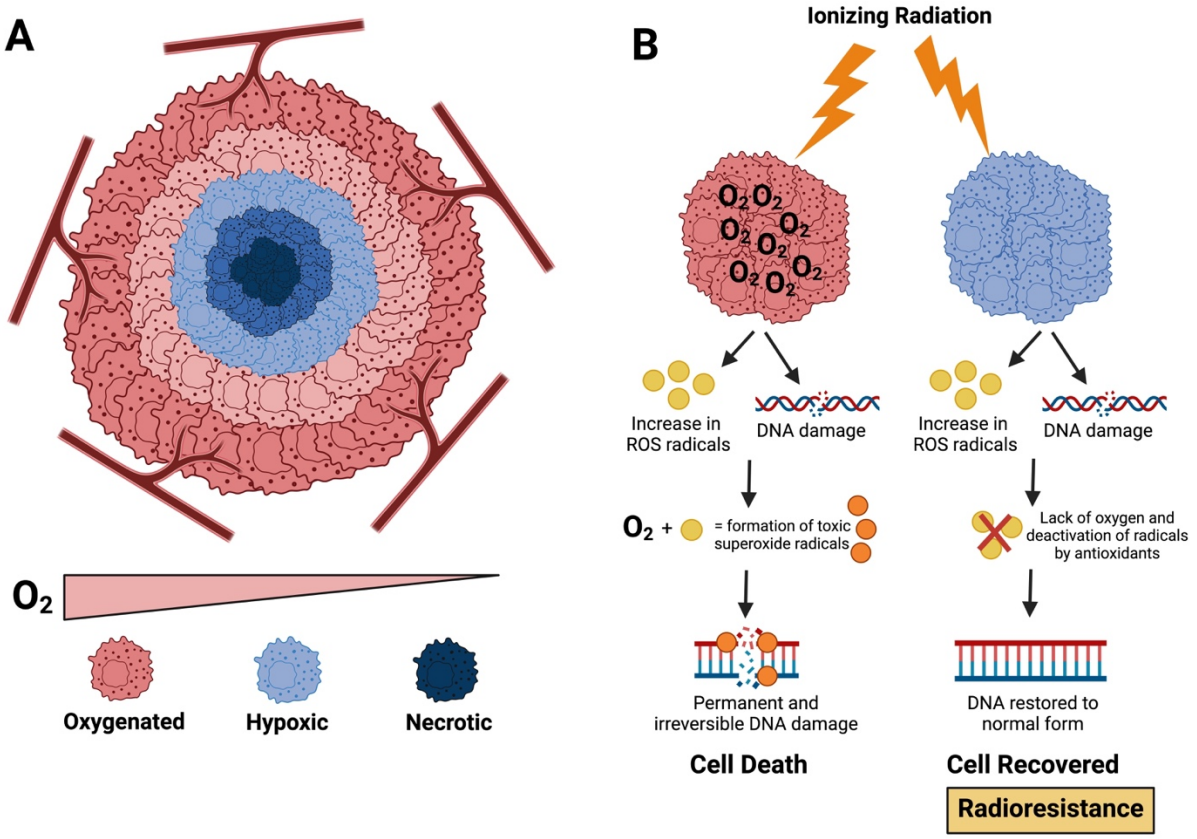

Figure 1.3. Hypoxia and radiation resistance.
(A) Presence of oxygenation gradients in the solid tumours leading to development of hypoxic and necrotic regions. (B) Efficacy of ionizing radiation under normoxic vs hypoxic conditions. Ionizing radiation induces permanent DNA damage and cell death under normoxic conditions (well oxygenated tumour regions). This is mediated by the toxic superoxide radicals formed under the presence of oxygen and these "fix" the DNA damage, inducing irreversible damage. Hypoxic tumour regions are resistant to radiation due to lack of oxygen preventing the formation of toxic superoxide radicals. The ROS radicals are deactivated and DNA is restored back to its original state. Thus, hypoxic tumour regions are radioresistant. (Figure created using Biorender)

1.2.3 Hypoxia in brain tumours and DIPG

Studies have reported close association between hypoxia and poor clinical prognosis in a range of cancer types including brain, head and neck, bowel, pancreas, lung, and prostate (64). Our brain requires the most amount of oxygen compared to other organs of the body. Although weighing only 2% of the total body weight, the brain still consumes approximately 20% of the body's oxygen (65). Oxygen levels are not consistent across the different regions of the brain, for example pia mater has around 8.0 kPa (60mmHg) which is equivalent to 8% oxygen level, whereas the midbrain has around 0.5-1.0 kPa (4.1-8.0 mmHg) which is equivalent to 0.5% oxygen level (66). Moreover, the oxygen levels in the brain tumour areas are comparatively lower at 1.25% compared to the peritumoral areas which are around 2.5%, thus suggesting that brain tumours are more hypoxic compared to the surrounding normal brain tissue (67). Hypoxia appears to be a hallmark of brain tumours and the most aggressive adult HGG, glioblastoma multiforme (GBM) are also characterised by areas of extensive tissue hypoxia (67, 68). There is also accumulating evidence highlighting an association between hypoxia and radioresistance in gliomas (69, 70).

The development and progression of paediatric HGG also appear to have a frequent involvement of HIF-hypoxia signalling (71). To date, there is no direct evidence showing presence of hypoxia in DIPG, however the study by Yeom et al. (2015) provides some evidence towards support this hypothesis. They found low tissue perfusion in DIPG patients pointing towards the presence of a hypoxic TME in DIPG. The hypoperfusion in DIPG patients correlated with increased accumulation of citrate, an intermediate product of tricarboxylic acid cycle (TCA cycle) (72). The mechanism of increased citrate concentrations is not fully understood however, there is evidence suggesting a rise in cytosolic citrate levels under hypoxic conditions (73). This indicates that hypoxia could be an important factor driving DIPG oncogenesis and contributing to RT resistance in DIPG patients. Thus, efforts to decrease tumour hypoxia in DIPG could improve radiosensitivity of the tumour and induce more tumour cell death. In this thesis, we also intend to support the presence of hypoxia in DIPG with some experimentation. We will now discuss the past and present strategies to target tumour hypoxia.

1.3. Strategies to target tumour hypoxia to improve the efficacy of radiotherapy in DIPG

1.3.1 Increasing oxygen supply to the tumour

"Since hypoxia develops due to lack of oxygen supply, the most relevant approach to resolve hypoxia and improve radiotherapy outcomes is to increase the oxygen supply to the tumour region. Initial attempts involved the use of blood transfusions to increase haemoglobin levels and therefore improve responses to radiotherapy. However, clinical studies reported that these transfusions did not improve treatment outcomes significantly (74, 75). Other approaches that attempted to increase oxygen supply included hyperbaric oxygen breathing or the use of carbogen (95% oxygen and 5% carbon dioxide). Despite promising preclinical and early-phase data, both approaches failed to show significant radiosensitization outcomes in patients (76-78). Interestingly, the combination of carbogen with nicotinamide targets hypoxia and is reported to improve radiation responses in clinical trials (79, 80). However, the increase in oxygenation is short and temporary suggesting that there is need for other approaches that result in sustained oxygenation to improve the responses to radiotherapy (81)."

1.3.2 Hypoxia-activated prodrugs

"Hypoxia-activated prodrugs (HAPs) have also been explored to selectivity target hypoxic tumour cells. HAPs are inactive compounds that convert to active drugs in hypoxic regions (82). Despite preclinical data showing cytotoxicity from various HAPs, the clinical studies of HAPs as single agent or combined with chemoradiotherapy were generally disappointing (82). Recently, a second-generation HAP evofosfamide (TH-302) been assessed in combination with radiation, showing increased tumour growth delay in various preclinical tumour models (83-85). Research on TH-302 is still ongoing and because previous clinical studies suggest that TH-302 may only provide benefit to patients with high tumour hypoxic fractions, determining the hypoxia status of the patient's tumour will be beneficial before the clinical application of TH-302 (86). Future preclinical studies could use tumour models with high hypoxic burden to assess whether TH- 302 could improve tumour control."

1.3.3 Inhibiting HIF activity

Targeting HIFs is a another prospective strategy to decrease tumour hypoxia and improve oncotherapy. Several small molecule inhibitors or drugs have been developed that target various HIF processes, however, only limited of those have been assessed in clinical studies

(87). Some HIF-2α specific antagonists have been developed include PT2385 and Belzutifan (PT2977) (88, 89). Of these, Belzutifan obtained FDA-approved in 2021 for the treatment of von Hippel-Lindau disease including advanced-stage clear cell renal cell carcinoma. There are also several HIF-1 inhibitors under development, with some novel agents undergoing clinical evaluation (90). Other approaches that are actively considered include the indirect inhibition of HIF by targeting HIF-related hypoxia signalling pathway (45). Inhibition of HIF pathway is an attractive area of ongoing research and more work is needed to advance our understanding on inhibition of HIF-1's carcinogenic pathway to advance cancer management.

1.3.4 Decreasing oxygen consumption of the tumour by targeting mitochondrial metabolism

1.3.4.1 Structure and function of the mitochondria

Mitochondria (singular: mitochondrion) are the powerhouse of the cell, responsible for the generation of adenosine triphosphate (ATP) through oxidative phosphorylation (OXPHOS). "OXPHOS is a metabolic pathway comprising of an electron transport chain (ETC) with complexes I, II, III and IV where a series of redox reactions occur, eventually resulting in the generation of ATP at complex V (91)." Mitochondria also essential for other cellular processes including the maintenance of calcium homeostasis, redox signalling, apoptosis, steroid synthesis, and lipid metabolism (92). **Figure 1.4** shows a basic structure of the human mitochondria and the ETC. The mitochondria comprise of an outer membrane, intermembrane space, inner membrane with folds known as cristae, and the matrix. The inner mitochondrial membrane contains the five multi-subunit complexes which regulate the ETC and two electron carriers, cytochrome c and ubiquinone (also known as coenzyme Q_{10}). The mitochondrial matrix is enriched with mitochondrial DNA, RNA, ribosomes, various organic and inorganic molecules, and the enzymes of TCA cycle (also called the citric acid cycle or Krebs cycle) and the fatty acid cycle (93).

The TCA cycle generates electron donors' nicotinamide adenine dinucleotide (NADH) and flavin adenine dinucleotide ($FADH_2$) which provide electrons for the functioning of the ETC. The first protein complex – complex I (NADH-ubiquinone oxidoreductase) uses electrons from NADH and transfers it to the electron carrier molecule ubiquinone in the membrane. Ubiquinone is reduced to ubiquinol which carriers the electrons to complex III (cytochrome bc_1) (94). The energy released in the electron transfer results in pumping of four hydrogen ions

(H^+) across the inner membrane into the intermembrane space. The complex II (succinate dehydrogenase) uses electrons from $FADH_2$ and passes them to ubiquinone. Ubiquinone is reduced to ubiquinol which then carries the electrons to the complex III. No H^+ are transported to the intermembrane space at complex II. The passage of electrons at the complex III drives the pumping of four more H^+ ions into the intermembrane space. Here, ubiquinol is oxidised back to ubiquinone and the electrons are passed to the second electron carrier molecule cytochrome c (94). Cytochrome c passes electrons to complex IV (cytochrome c oxidase) and two H+ ions are pumped into the intermembrane space. Complex IV is the final protein complex in the ETC and transfers the electrons to molecular oxygen (O_2) which splits and uses H^+ to form water molecules. Thus, at the complex IV, oxygen is being consumed and acts as the final electron acceptor. The fifth protein complex, complex V (ATP synthase) moves H^+ ions from the intermembrane space into the mitochondrial matrix, releasing energy which is used to phosphorylate adenosine diphosphate (ADP) to generate ATP (**Figure 1.3**) (94).

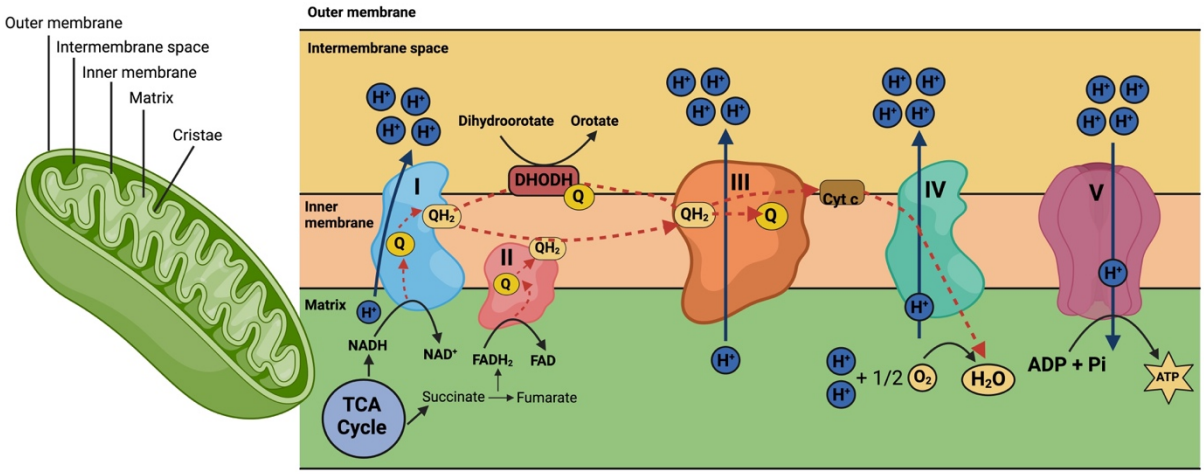

Figure 1.4. Basic structure of the human mitochondria and the electron transport chain.
The mitochondrial electron transport chain comprises of complexes I, II, III, IV and V. This involves transport of electrons across these complexes results in pumping of protons into the intermembrane space, generating a proton gradient. Protons are then passed through the complex V (ATP synthase), leading to generation of ATP. This metabolic pathway generates cellular energy and is referred to as oxidative phosphorylation. (Figure created using Biorender)

1.3.4.2 Targeting mitochondrial oxidative phosphorylation to reduce tumour hypoxia

"In contrast to the aforementioned strategies, the current attractive alternative to overcome hypoxia is to reduce tumour cells demand for oxygen by inhibiting the mitochondrial OXPHOS (95). Increasing evidence suggests that along with active glycolysis, cancer cells also have

increased mitochondrial OXPHOS, which results in increased oxygen consumption and ATP production in the tumour (91, 96-99). Oxygen is critical for OXPHOS as it is the terminal electron acceptor in this process. The hypothesis is that OXPHOS inhibition will decrease the oxygen consumption rate (OCR) of tumour cells, allowing for the diffusion of unmetabolized oxygen into hypoxic regions, reserving more available oxygen, and thus reducing tumour hypoxia. Mathematical modelling also indicates that decreasing cellular oxygen consumption appears to be a more efficient method to alleviate tumour hypoxia than increasing oxygen supply (95)."

"The assumptions underlying the use of OXPHOS inhibitors are that elevated oxidative metabolism in cancers is associated with increased tumour hypoxia, which impedes the success of RT. Indeed, several studies have now demonstrated that OXPHOS inhibitors could decrease OCR and tumour hypoxia. Metformin, an antidiabetic drug and a mitochondrial complex I inhibitor, is the first compound tested in this context. It decreased tumour hypoxia and improved tumour radiation response in colorectal and brain tumour preclinical models (100, 101). As a result, metformin has been evaluated in clinical trials as a potential radiosensitizer (102). Another compound, atovaquone, an anti-malarial drug and a mitochondrial complex III inhibitor, was found to reduce the OCR in numerous cancer cell lines (103). It alleviated tumour hypoxia in colorectal and hypopharyngeal carcinoma xenograft models and caused a significant tumour growth delay in combination with radiation (103). Additionally, the hypoxia modification efficacy of atovaquone was corroborated in a recent clinical trial (NCT02628080) showing increased tumour oxygenation and inhibition of hypoxic gene expression in non-small cell lung cancer (NSCLC) patients. These promising findings led to the initiation of another trial testing the efficacy of atovaquone in combination with chemoradiotherapy on NSCLC (NCT04648033). Furthermore, papaverine, an antispasmodic drug and a mitochondrial complex I inhibitor, has provided further support towards hypoxia inhibition by OXPHOS inhibitors. This drug also reduced OCR in vitro, decreased tumour hypoxia and enhanced radiation response in *in vivo* breast and lung cancer models (104). Collectively, these findings provide a strong rationale to investigate OXPHOS inhibitors to eliminate the hypoxic TME and improve the efficacy of RT." A close assessment of all hypoxia modifying strategies suggests that investigating OXPHOS inhibitors against DIPG would be promising approach to reduce tumour hypoxia in DIPG and sensitise this tumour to RT.

1.4. OXPHOS Inhibitors for DIPG management

The limited treatment options of DIPG directs towards the urgency and need for new approaches to manage children with this devastating disease. In this thesis, our approach involves targeting the tumour metabolism of DIPG cells using OXPHOS inhibitors to decrease hypoxia. This would make the hypoxic radioresistant tumour areas sensitive to RT, improving the efficacy of RT and subsequently resulting in improving survival outcomes of DIPG patients (**Figure 1.5**).

In this project, we aim to investigate the hypoxia modification and radiosensitisation of DIPG using drugs that have already undergone FDA-approval. Repurposing of drugs that are FDA-approved for other treatments provides a faster approach for clinical translation of compounds from bench to bedside. This is beneficial as the safety and side effects of those compounds are already establishment from prior clinical studies. In our previous review (105), we proposed some potential OXPHOS inhibitors (atovaquone, mefloquine, proguanil, quinacrine and ivermectin). In this PhD project, these compounds were screened against DIPG cultures to identify the most potent OCR inhibitors. Here, we review atovaquone, proguanil and mefloquine because our preliminary findings (**in Chapter 3**) led us to investigating the efficacy of atovaquone, the combination of atovaquone+proguanil and mefloquine against DIPG in this thesis.

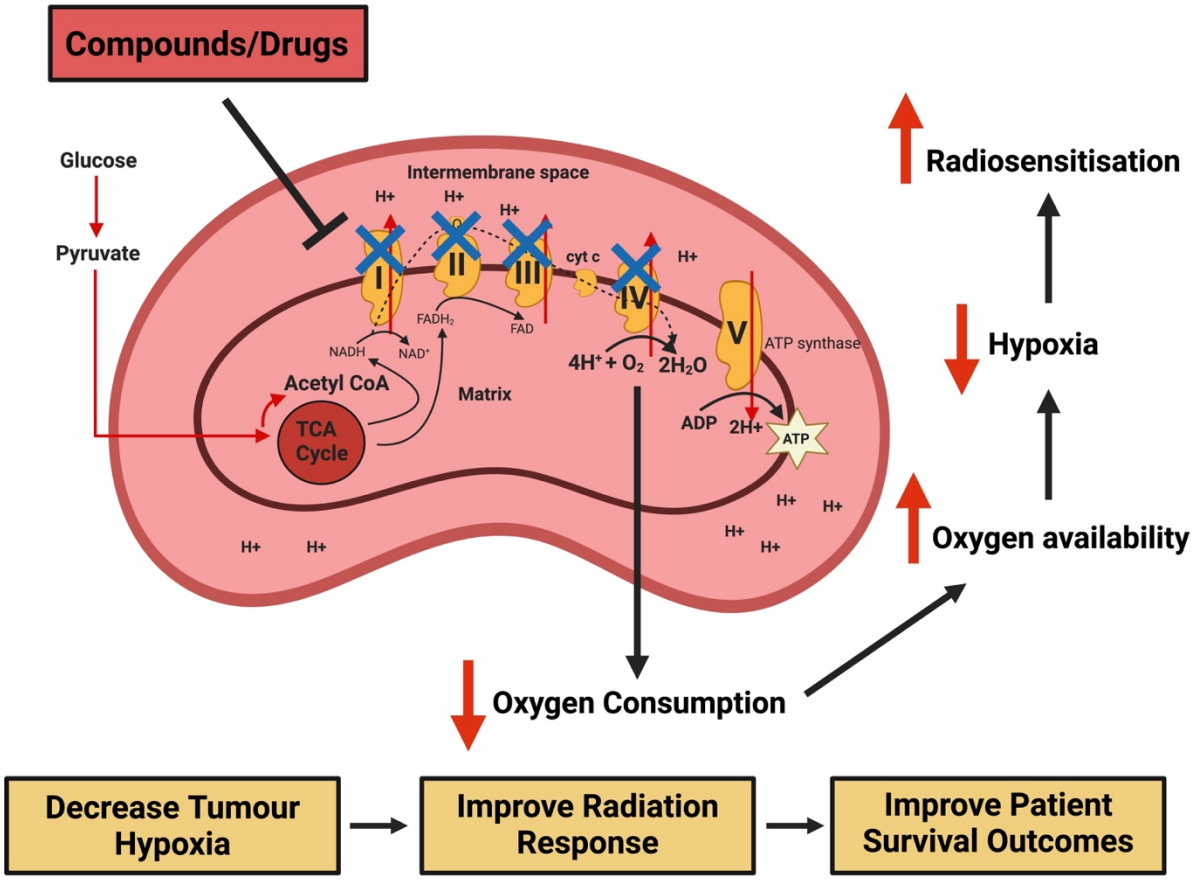

Figure 1.5. Our strategy to reduce tumour hypoxia and improve radiosensitization of DIPG cells.
We aim to target mitochondrial oxidative phosphorylation of DIPG cells using compounds that target mitochondrial electron transport chain (ETC). Inhibition of any of the ETC complex would reduce the oxygen consumption rate of DIPG tumour cells. This means that there will be sufficient oxygen available. As a result, there will be an increase in oxygen availability, leading to reduction in tumour hypoxia. This would result in improved radiosensitisation of DIPG tumour cells and thus lead to improved survival outcomes of DIPG patients. (Figure created using Biorender)

1.4.1 Atovaquone

1.4.1.1 Background and development of atovaquone

Atovaquone belongs to the class of naphthoquinones and possesses a broad-spectrum antiprotozoal activity. It was initially developed as an antimalarial monotherapy for the treatment and prevention of the lung infection *Pneumocystis carinii* pneumonia (PCP, caused by the fungus *Pneumocystis jiroveci)* (106). It is also found to be effective in prevention of the HIV infection – Toxoplasma encephalitis and can prevent babesiosis in conjunction with the antibiotic azithromycin (106). Currently, atovaquone in combination with the biguanide, proguanil, at a fixed-dose, is approved for the prophylaxis and treatment of uncomplicated *Plasmodium Falciparum* (*P. falciparum*) malaria in adults and children (107, 108).

It was first investigated during the World War II when the shortage of antimalarial drug quinine prompted research into thousands of structurally diverse compounds, some of which included hydroxynaphthoquinones (109). The antimalarial activity of these compounds was identified by administering them to ducks infected with *plasmodium lophurae*. This led to identification of several quinones which had greater activity than quinines (109). Despite promising results observed in the duck assay, the efficacy of the quinones in malarial patients was limited due to poor absorption and limited metabolism (110, 111). With continued research on quinones in 1960s, the compound lapinone was developed and found to be effective on patients infected with *Plasmodium vivax*, however due to limitations in parenteral administration, this compound was not pursued as therapy (112). In 1980s, investigation on quinones was revisited and various lapinone analogs were synthesised in experiments using *P. falciparum in vitro* and in *Aotus* monkeys (109). Of these analogues, several showed potency against *P. falciparum in vitro*, however only atovaquone was found to be metabolically stable (113, 114).

In 1992, atovaquone was released as a tablet, however due to the poor bioavailability, this formulation was discontinued (115). Later in the same year, it was reformulated as a micronized suspension formulation with micro-fine particles of atovaquone, to improve the drug absorption compared to the tablet formulation. The micronized formulation is currently available as Mepron (GlaxoSmithKline), which is a bright yellow citrus-flavoured liquid suspension. For the treatment of PCP, mepron is recommended at 750mg atovaquone/5mL suspension, twice a day (total dose = 1500mg), for 21 days with food (106).

1.4.1.2 Mechanism of action of atovaquone

Atovaquone, a hydroxy-1,4-napthoquinone, is a ubiquinone analogue and a competitive inhibitor of ubiquinol, specifically inhibiting the mitochondrial ETC at ubiquinol oxidation (Q_o) site in the complex III (116). This results in inhibition of mitochondrial function and sustained depolarisation of mitochondrial membrane potential (MMP), maintenance of which is critical to parasites survival. This process will also inhibit several mitochondrial enzymes linked to the ETC (117, 118). During the intraerythrocytic stages, the parasite mitochondrion is the main organelle that provides metabolites (orotate) for pyrimidine synthesis through the action of the mitochondrial enzyme Dihydroorotate dehydrogenase (DHODH). In support of this, the inhibition of complex III by atovaquone decreases the turnover of ubiquinone, thus also inhibiting DHODH and *de novo* pyrimidine synthesis (119, 120). Since *Plasmodium spp.*

are dependent on *de novo* pyrimidine synthesis and are unable to salvage preformed pyrimidines, inhibition of DHODH by atovaquone blocks nucleic acid synthesis and replication cycle, thus inducing parasite cell death (120). The ubiquinone-dependent DHODH activity of atovaquone is further supported by a study which found that transgenic *P. falciparum* parasites expressing ubiquinone-independent DHODH are resistant to atovaquone's effect (121). In addition, it has been suggested that the inhibition of mitochondrial function by atovaquone can also lead to inhibition of purine biosynthesis (122).

Furthermore, the efficacy of atovaquone has also been investigated against a range of cancer types (summarised in **Table 1.1**). It has not been explored on brain tumours. There is only one study showing atovaquone inhibits proliferation of GBM cells *in vitro* (123). It would therefore be interesting to assess the efficacy of atovaquone against DIPG.

1.4.1.3 Absorption, plasma concentration and elimination of atovaquone

Atovaquone is a lipophilic compound with poor aqueous solubility (106). It binds to plasma proteins extensively (>99%), however, the plasma concentrations of atovaquone are not found to increase proportionally with increase in drug dose (109). The oral absorption of atovaquone is increased when taken with food. Studies have shown that when administered with high-fat meal, the blood concentrations of atovaquone can rise by approximately 2 to 3 fold, reaching steady-state concentrations of 15 to 30µg/ml with doses of 750 to 1500mg. Thus, it is recommended to take atovaquone with a high-fat meal (115, 124, 125). Atovaquone can reach a steady-state mean plasma concentration of 65 µM in patients following 1-2 week of treatment (125, 126). Also, a mean plasma concentration of 68.5 µM was achieved in mice treated with atovaquone for 5 days (103). Furthermore, the elimination half-life of atovaquone is approximately 50-84 hours and more than 90% of atovaquone is eliminated in its parent form by the liver (115, 125, 127).

1.4.1.4 Safety and toxicology of atovaquone

Hydroxynaphthoquinones exhibit different sensitivities to plasmodial and mammalian electron transport system and that explains the selective toxicity of atovaquone to *Plasmodium spp* (128). Atovaquone is found to significantly inhibit the parasite mitochondria at nanomolar range however, similar effect is seen in mammalian cells at micromolar range (103, 113). Additionally, unlike *Plasmodium spp*, which only depend upon the *de novo* pyrimidine

synthesis for nucleic acid synthesis and replication, the mammalian cells are also able to use the salvage pathway to form pyrimidines. Thus, when *de novo* pyrimidine synthesis is inhibited, the mammalian cells are still able to survive under atovaquone's effect (128).

Atovaquone is found to be well-tolerated with only few reported side effects. The associated adverse events include abdominal pain, rash, diarrhoea, sweating, fever, vomiting, and headache and these are generally mild. The favourable safe profile of atovaquone is further supported by the evidence showing little or no symptomatology at overdoses up to 31500 mg (129).

1.4.1.5 Blood-brain barrier penetration profile of atovaquone

Atovaquone penetrates the BBB as it was found to significantly reduce the number of *Toxoplasma gondii* cysts in the brains of mice infected with *Toxoplasma gondii* (130). Atovaquone has been also been found be effective for the treatment of patients with cerebral toxoplasmosis. However, the atovaquone concentration achieved in the cerebrospinal fluid appears to be less than 1% of the plasma concentration, representing levels below 1μM (106). Since then, several strategies to improve the oral bioavailability and brain concentrations of atovaquone have been investigated. These include atovaquone being formulated as a nanosuspension formulation, however the brain levels achieved from this formulation still appear to be insufficient for the treatment of brain tumours (131). Moreover, another study prepared atovaquone as a nanoemulsion formulation. The issue with this formulation is that the preparation required more than 20% of dimethyl sulfoxide to dissolve sufficient quantity of atovaquone, and this level exceeds the values used in any previous FDA-approved compound (132). In order to overcome the issues of previous atovaquone formulations, another study formulated atovaquone as amorphous solid dispersion (ASD) formulation. ASD formulations are a promising strategy to improve the solubility of drugs that are poorly soluble (133). This study used excipients that are safe for humans and aimed to improve the bioavailability of atovaquone to achieve high brain concentrations required for the treatment of brain tumours. Interestingly, they achieved a significantly higher brain concentration (~ 37μM) in mice treated with atovaquone compared to what is previously obtained by the commercially available atovaquone formulation (less than 1μM) (123). Therefore, in this thesis, we will also be investigating the efficacy of the higher BBB penetrant version ASD atovaquone against DIPG.

Table 1.1 The efficacy of atovaquone in cancers and its potential anti-cancer mechanisms.

Cancer type	Mechanisms of action	Efficacy assessed - *In vitro* or *In vivo*?	Source
Retinoblastoma	• Mitochondrial dysfunction • Oxidative damage • Akt/AMPK/mTOR inhibition	In vitro	(134)
Ovarian and endometrial cancer	• Mitochondrial dysfunction • Oxidative damage	In vitro & In vivo	(135)
Breast cancer	• Mitochondrial dysfunction	In vitro	(136)
Cervical cancer	• Mitochondrial dysfunction	In vitro & In vivo	(137)
Renal cell carcinoma	• Mitochondrial dysfunction	In vitro & In vivo	(138)
B-cell Acute lymphoblastic leukemia	• Mitochondrial dysfunction	In vitro	(139)
Hypopharyngeal carcinoma	• Mitochondrial dysfunction • Hypoxia inhibition • Tumour radiosensitisation	In vitro & In vivo	(103)
Colorectal carcinoma	• Mitochondrial dysfunction • Hypoxia inhibition	In vitro & In vivo	(103)
Non-small cell lung carcinoma	• Mitochondrial dysfunction • Hypoxia inhibition • AMPK activation and mTOR inhibition	In vitro	(103, 140)
Thyroid cancer	• Mitochondrial dysfunction • STAT3 inhibitor	In vitro	(141)
Acute myeloid leukemia	• STAT3 inhibitor	In vitro & In vivo	(142)
Ovarian cancer	• STAT3 inhibitor	In vivo	(143)
Glioblastoma	• No mechanism seen, however, proliferation inhibition was observed	In vitro	(123)

1.4.2 Proguanil

1.4.2.1 Background and development of proguanil

Proguanil belongs to the class of biguanides and was introduced as an antimalarial agent in 1940s (144). It was initially investigated for the treatment of acute *Plasmodium vivax* malaria and was found to be highly effective (145). It then began to be used for the prophylaxis of *Plasmodium vivax* malaria, initially as a single agent and later in combination with chloroquine (145). It was also investigated against acute *P. falciparum* malaria in Thailand, and the overall cure rate was only 1 in 17 (6%) patients (128). Although, ineffective as single therapy, proguanil was found to be synergistic with atovaquone against *P. falciparum*. Malarone (the combination of atovaquone and proguanil), was then developed and is available in many countries for management of malaria prophylaxis, alleviating the concerns of resistance to atovaquone as monotherapy (128). Malarone is currently available as an adult formulation (250 mg atovaquone and 100 mg proguanil) and a paediatric formulation (62.5 mg atovaquone and 25 mg proguanil) (106).

1.4.2.2 Mechanism of action of proguanil

Proguanil, a prodrug, is relatively inactive and needs to be metabolised to its active cyclic metabolite, cycloguanil. Cycloguanil inhibits dihydrofolate reductase (DHFR), a key enzyme essential for folate metabolism (146). This will result in depletion of tetrahydrofolate cofactors required for DNA synthesis and thus, will prevent parasite growth and survival (146). The conversion of proguanil to cycloguanil is mediated in the liver by certain isoforms of hepatic cytochrome P450 enzymes (146). However, studies have reported large inter-subject variability in plasma concentrations of cycloguanil following oral administration of proguanil (147). The variability in metabolism was observed in some Asian and African population and was attributed to genetic polymorphisms in their metabolic isoenzymes (144, 148). Additionally, more than half of the population in the endemic areas appear to be poor metabolisers of proguanil. Interestingly, proguanil was shown to be effective in poor proguanil metabolisers, thus suggesting that proguanil could have another target separate from DHFR (149). Furthermore, similar to other known biguanides phenformin and metformin, proguanil might also function via the inhibition of mitochondrial complex I. However, studies report poor mitochondrial penetrability of proguanil and this mechanism needs to further assessed (150). Another hypothesis underlining proguanil's mechanism suggests that it could be inhibiting

ATP hydrolysis and thus affecting mitochondrial function (151). The exact mechanism of the proguanil's intrinsic activity against parasites is not fully understood, however, evidence suggests that parasites with impaired mitochondrial ETC are hypersensitive to proguanil (152). Proguanil also lowers the effective concentration of atovaquone required to collapse MMP (148).

Proguanil as a single drug has also been explored as an anti-cancer agent in some studies (**Table 1.2**). However, we are primarily interested in assessing the efficacy of the combination of atovaquone/proguanil against DIPG as the proguanil appears to enhance the efficacy of atovaquone. The combination has not been widely studied against cancer types. However, a clinical study on colorectal cancer (CRC) suggest that atovaquone/proguanil can be effective against the development of CRC (153). Therefore, it would be interesting to investigate whether the combination is efficacious in DIPG compared to single treatments.

1.4.2.3 Absorption, plasma concentration and elimination of proguanil

Proguanil is rapidly absorbed in humans and concentrations peak within 2 to 5 hours (154). It is about 75% protein-bound molecule and has an elimination half-life of ranging from 12 to 21 hours (106, 155). The major route of elimination of proguanil is via hepatic metabolism and about 40% of the drug is cleared through the kidneys (106). The mean atovaquone plasma concentration from Malarone appears to peak to approximately 10 µM from a single dose due to lower atovaquone concentration used (109). There still remains a considerable knowledge gap on the pharmacology of Malarone and more studies are required to understand the pharmacokinetics/pharmacodynamics profile.

1.4.2.4 Safety and toxicology of proguanil

There are no documented adverse reactions from proguanil and it is a well-tolerated and safe drug (154). The addition of proguanil to atovaquone (as Malarone) does not significantly alter the side effect profile of the single drugs. However, some combination studies have reported gastrointestinal side effects and headaches (106).

1.4.2.5 Blood-brain barrier penetration profile of proguanil

Proguanil can penetrate the BBB (155). There is no information in literature about BBB penetration profile of atovaquone/proguanil combination.

Table 1.2 The efficacy of proguanil in cancers and its potential anti-cancer mechanisms.

Cancer type	**Mechanisms of action**	**Efficacy assessed - *In vitro* or *In vivo*?**	**Source**
Breast cancer	• Mitochondrial dysfunction • Oxidative damage	In vitro & In vivo	(156)
Bladder cancer	• EGFR inhibitor	In vitro & In vivo	(157)
Ovarian cancer	• Increases Olaparib-induced DNA damage and apoptosis	In vitro	(158)

1.4.3 Mefloquine

1.4.3.1 Background and development of mefloquine

Mefloquine, a fluorinated 4-quinoline methanol compound, was first developed in late 1960s as an anti-malarial drug. It became FDA-approved for malarial prophylaxis in 1972 (159). As the guidelines for mefloquine's dosing regimen involve taking one tablet per week, this makes mefloquine's use convenient and preferred by long-term travellers and military personnel compared to other prophylactic medications which require daily dosing (e.g., primaquine, atovaquone/proguanil and doxycycline) (159, 160). After a few years of use, there were several reports of adverse neuropsychiatric reactions from mefloquine's use resulting in several changes in the FDA-label of the drug. There has been several assessments of mefloquine's side effects, however the drug continues to be recommended for the prophylaxis of chloroquine-resistant malaria as due to its strong efficacy against all *Plasmodium* species (160).

1.4.3.2 Mechanism of action of mefloquine

The exact mechanism of action of mefloquine is unclear. A study reported that mefloquine targets the cytoplasmic ribosome 80S of *P. falciparum*, thus inhibiting protein synthesis and resulting in parasite cell death (161). Mefloquine has been widely explored as an anti-cancer agent with a range of therapeutic targets (Table 1.3). It has been shown to inhibit proliferation of GBM cells, however, the exact mechanism of action against GBM is unknown (162). Its efficacy has not been assessed against DIPG and this thesis will be investigating the efficacy mefloquine against DIPG.

1.4.3.3 Absorption, plasma concentration and elimination of mefloquine

Mefloquine is available as a tablet formulation. It is moderately well absorbed and has a high affinity for liver, lung and lymphoid tissues (163). It is highly protein bound (>98%). Mefloquine is recommended to be taken with food as it causes a significant increase in bioavailability by 40% (155). The peak plasma concentrations of mefloquine following prophylaxis and treatment are 3.8 μM and 2.1 to 23 μM, respectively (164, 165). Mefloquine is principally cleared by the liver and the elimination half-life of mefloquine could range between 0.9 - 13.8 days, whereas some studies report it to be around 2-4 weeks (155, 163).

1.4.3.4 Safety and toxicology of mefloquine

Some unwanted effects from high dose of mefloquine include headache, dizziness, sleep disturbance although these symptoms might be resulting from both the effects of the drug and the disease (163). Other less common symptoms relate to neuropsychiatric disturbances including depression, anxiety, nightmares (163). Mefloquine's use is contraindicated in people with a history of psychiatric disorders (166). The serious risk of neurotoxicity toxicity of mefloquine is around 1:10,000 people (167). It appears that children tolerate mefloquine well compared to adults (168). Following mefloquine treatment, it recommended to monitor cardiac rhythm with electrocardiogram, and assess neuropsychiatric status for up to 24 hour and provide medication as necessary (169).

1.4.3.5 Blood-brain barrier penetration profile of mefloquine

Mefloquine is highly BBB penetrant compound. It readily accumulates in the brain and studies have reported high mefloquine brain concentrations of about 50 μM in human postmortem cases (170, 171). Another study reported mefloquine brain concentration reaching 90 μM in rats receiving the drug at therapy-equivalent dose rate (172). The high BBB penetration of mefloquine makes it an ideal drug candidate to be explored against DIPG.

Table 1.3 The efficacy of mefloquine in cancers and its potential anti-cancer mechanisms.

Cancer type	Mechanisms of action	Efficacy assessed - *In vitro* or *In vivo*?	Source
Cervical cancer	• Mitochondrial dysfunction • mTOR inhibition	In vitro & In vivo	(173)
Chronic myeloid leukemia	• Oxidative stress • Lysosomal disruption	In vitro	(174)
Acute myeloid leukemia	• Lysosomal disruption	In vitro & In vivo	(175)
Breast cancer	• Autophagy inhibition • Increasing endoplasmic reticulum stress	In vitro	(176)
Chronic lymphocytic leukemia	• Lysosomal disruption	In vitro	(177)
Colorectal cancer	• NF-κB signalling inhibitor	In vitro & In vivo	(178)
Esophageal squamous cell carcinoma	• Inducing mitochondrial autophagy	In vitro & In vivo	(179)
Gastric cancer	• PI3K/Akt/mTOR signalling pathway inhibitor	In vitro & In vivo	(180)
Liver cancer	• Suppression of β-catenin pathway	In vitro & In vivo	(181)
Prostate cancer	• Oxidative stress • Decreased Akt phosphorylation and increased ERK, JNK and AMPK signalling	In vitro & In vivo	(182, 183)
Glioblastoma	• Lysosomotropic compound, but exact mechanism not shown	In vitro	(162)

1.5. Aims and hypothesis

1.5.1 Aims

The overall goal of this thesis is to investigate novel therapies to improve RT response in DIPG and thus improve survival outcomes of DIPG patients. As DIPGs inevitably recur secondary to RT resistance, and tumour hypoxia is a significant barrier to effective RT, we aim to target hypoxia using mitochondrial OXPHOS inhibitors. Here, we intend to investigate the efficacy of OXPHOS inhibitors against DIPG cultures by assessing their mechanism of action, hypoxia inhibition and radiosensitisation efficacy. The promising *in vitro* findings will then be validated using *in vivo* orthotopic DIPG models.

The first aim of this thesis is to investigate whether DIPG tumour has upregulated oxidative metabolism. An increase in OXPHOS would mean that there is increased oxygen utilisation and would provide some support towards the presence of hypoxia in DIPGs. In **Chapter 3**, we used publicly available datasets and assessed the mRNA expression of ETC complex genes in DIPG/DMG patient samples and compare it to normal brain tissue. An increased mRNA expression of the ETC genes would suggest an upregulated OXPHOS activity in DIPG/DMG. Next, we perform an OXPHOS inhibition screening using DIPG cultures (in **Chapter 3**). The drugs with the most potent OCR inhibition and a positive BBB penetration will be selected for further evaluation against DIPG models. Here, atovaquone and mefloquine were picked as the most potent OCR inhibitors.

The second aim of this thesis is to assess the efficacy of atovaquone against DIPG *in vitro* (**Chapter 4**). We assessed its specific target of action, overall mitochondrial inhibition, hypoxia inhibition and radiosensitisation using several DIPG cell lines. Because commercially available atovaquone has limited BBB penetration, we also assessed it's *in vitro* efficacy against the higher BBB penetrant version, the ASD atovaquone formulation. Furthermore, as the combination of atovaquone/proguanil (Malarone) appears to be more effective in malaria treatment compared to atovaquone alone, we also aimed to investigate whether the combination has a better efficacy than atovaquone alone against DIPG.

The third aim of this thesis is to assess the efficacy of mefloquine against DIPG *in vitro* (**Chapter 5**). We assessed its effect on cell viability on a panel of DIPG cell lines. We further

looked at its anti-proliferative efficacy, specific target of action, overall mitochondrial inhibition, hypoxia inhibition and radiosensitisation using several DIPG cell lines.

The fourth aim of this thesis is to validate the promising *in vitro* findings of atovaquone and mefloquine using orthotopic DIPG models (**Chapter 6**). In **Chapter 6**, we first aimed to performed lentiviral transduction to generate a GFP/luciferase-expressing HSJD-DIPG-007 DIPG model that will enable us to track tumour progression over time and guide with treatment responses. Next, we aimed to use the DIPG tumour-bearing mice brain sections to perform a range of immunohistochemistry (IHC) staining to validate the presence of DIPG tumour cells (using H3K27M and ki67 antibodies) and support presence of hypoxia in DIPG (using HIF-1α, VEGFA, CA-IX, EF5 and pimonidazole antibodies). Finally, we aimed to perform drug+RT studies. Due to time constraints, we could only conduct animal studies using atovaquone and the work on mefloquine is yet to be performed. We used the higher BBB penetrant version, ASD atovaquone and assessed its radiosensitisation efficacy using two orthotopic DIPG models – SU-DIPG-13P* and HSJD-DIPG-007. Prior to ASD atovaquone + RT study, we also performed other studies including determining optimal RT dose to combine with ASD atovaquone and determining brain/plasma concentration achieved by ASD atovaquone.

1.5.2 Hypotheses

- We hypothesise that there should be higher mRNA expression of ETC complex genes in DIPG patient samples compared to normal tissue samples suggesting upregulated OXPHOS in DIPG (**Chapter 3**). Moreover, DIPG tumour-bearing mice brains should have should higher expression of hypoxia markers colocalising in the tumour regions (**Chapter 6**). This is hypothesised based on previous evidence in literature where DIPG patients tissue appeared hypoperfused suggesting hypoxia might be a feature in DIPG oncogenesis (72).

- If atovaquone significantly reduces the OCR of DIPG cultures, it should reduce hypoxia in 3D DIPG neurosphere models. The combination of atovaquone+RT should kill more DIPG cells and reduce colony formation, thus showing radiosensitisation of DIPG cells. Moreover, commercial atovaquone and ASD atovaquone should exhibit similar OCR

and hypoxia inhibition profiles as both formulations possess similar quantity of atovaquone. Furthermore, the combination of atovaquone+proguanil might exhibit better efficacy compared to atovaquone alone (**Chapter 4**).

- If mefloquine significantly reduces the OCR of DIPG cultures, it should reduce hypoxia in 3D DIPG neurosphere models. The combination of mefloquine+RT should kill more DIPG cells and reduce colony formation, thus showing radiosensitisation of DIPG cells (**Chapter 5**).

- If lentiviral transduction is successful, we will be able to generate a stable GFP/luciferase-expressing HSJD-DIPG-007 model (**Chapter 6**).

- As ASD atovaquone has higher BBB penetration, the promising *in vitro* findings should be translated *in vivo*. We hypothesise that the combination of ASD atovaquone+RT should extend survival of orthotopic DIPG models compared to single treatments (**Chapter 6**).

Chapter 2

Materials and Methods

Chapter 2. Materials and Methods

2.1. Materials

Table 2.1 Cell Lines

DIPG Cell Lines	Source
SU-DIPG-XVII	Monje Lab, Stanford University, California, USA
SU-DIPG-VI	Monje Lab, Stanford University, California, USA
HSJD-DIPG-007	Sant Joan de Déu Research Foundation, Barcelona, Spain
HSJD-DIPG-012	Sant Joan de Déu Research Foundation, Barcelona, Spain
HSJD-DIPG-013	Sant Joan de Déu Research Foundation, Barcelona, Spain
SU-DIPG-13P*	Professor Matt Dun's Lab, University of Newcastle, Australia
GFP/luciferase-expressing HSJD-DIPG-007	Generated by myself under the guidance of Dr Yuyan Chen at Kids Research, Australia
GFP/luciferase-expressing SU-DIPG-24	Generated by Dr Yuyan Chen, Kids Research, Australia

Other Cell Lines	Source
Immortalized human astrocytes, fetal – hTERT	Resolving Images, Australia

Table 2.2 Reagents

Reagents	Source/Identifier
Neurobasal-A Medium (1X)	Life Technologies (10888022)
Dulbecco's Modified Eagle Medium/Nutrient Mixture F-12 (DMEM/F-12) 1:1	Life Technologies (11320082)
MEM Non-Essential Amino Acids Solution	Life Technologies (11140050)
HEPES Buffer Solution	Life Technologies (15630080)
MEM Sodium Pyruvate Solution	Life Technologies (11360070)
GlutaMAX™ Supplement	Life Technologies (35050061)
Antibiotic-Antimycotic	Life Technologies (15240096)
Human Fibroblast Growth Factor-basic 154 (FGF)	Jomar Life Research (100-146-100UG)

Human Epidermal Growth Factor (EGF)	Jomar Life Research (100-26-100UG)
Human Platelet Derived Growth Factor-AA (PDGF-AA)	Jomar Life Research (100-16-100UG)
Human Platelet Derived Growth Factor-BB (PDGF-BB)	Jomar Life Research (100-18-100UG)
Heparin	Stem cell Technologies (7980)
B-27 Supplement, minus vitamin A (50X)	Life Technologies (12587001)
Dulbecco's Phosphate Buffered Saline (DPBS)	Lonza (17-512F)
Dimethyl Sulfoxide (DMSO)	Sigma (D2650-100ML)
Prigrow IV Medium	Applied Biological Materials Inc. (TM004)
Applied Cell Extracellular Matrix	Applied Biological Materials Inc. (G422)
Penicillin/Streptomycin Solution	Thermo Fisher Scientific (15140122)
Fetal bovine serum (FBS)	Applied Biological Materials Inc (TM999-100)
L-glutamine	Thermo Fisher Scientific (25030081)
Tryple Express (1X)	Thermo Fisher Scientific (12604013)
CellTiter 96 AQ_{ueous} One Solution Cell Proliferation Assay (MTS)	Promega (G3581)
SeaPlaque™ Agarose	Lonza (50100)
Thiazolyl Blue Tetrazolium Bromide (MTT)	Sigma (M2128)
Crystal Violet	Sigma (C0775-100G)
Laminin	Sigma (L2020-1MG)
ECM Matrigel	Corning (354234)
Poly-D-Lysine	Thermo Fisher Scientific (A3890401)
SeaPlaque™ Agarose	Lonza (50100)
XF DMEM Medium, pH 7.4	Agilent Technologies (103575-100)
XF Pyruvate solution (100 mM)	Agilent Technologies (103578-100)
XF Glutamine solution (200 mM)	Agilent Technologies (103579-100)
XF Glucose solution (1M)	Agilent Technologies (103577-100)
XF Calibrant, pH 7.4	Agilent Technologies (100840-000)
D-Mannitol	Sigma (M9546-250G)
Sucrose	Sigma (S9378-10MG)

Potassium phosphate monobasic (KH_2PO_4)	Sigma (P0662-25G)
Magnesium chloride solution ($MgCl_2$)	Sigma (M1028-100ML)
Ethylene glycol-bis(2-aminoethylether)-N,N,N',N'-tetra acetic acid (EGTA)	Sigma (E3889-10G)
Rotenone	Sigma (R8875-1G)
L-(-)-Malic acid/malate	Sigma (02288-10G)
Succinic acid/succinate	Sigma (S3674-100G)
Antimycin A	Sigma (A8674-25MG)
L-Ascorbic acid/ascorbate	Sigma (A5960-10MG)
N,N,N',N'-Tetramethyl-p-phenylenediamine dihydrochloride (TMPD)	Sigma (87890-5G)
Distilled Water DNase/Rnase-free	Thermo Fisher Scientific (10977015)
Myxothiazol	Sigma (T5580-1MG)
Adenosine 5'-diphosphate monopotassium salt dihydrate (ADP)	Sigma (A5285-100MG)
Seahorse XF Plasma Membrane Permeabilizer (XF PMP)	Agilent Technologies (102504-100)
Tetramethyl hydroquinone >95.0%, Duroquinol	Tokyo Chemical Industry (TCI) (T0822-1G)
Ethyl Potassium Malonate	Sigma (360899-25G)
Potassium Hydroxide	Sigma (221473)
Trypan Blue (0.4%)	Life Technologies (15250061)
Pierce Protease and Phosphatase Inhibitor (PI)	Thermo Fisher Scientific (A32959)
Ponceau S Solution	Sigma (P7170-1L)
DNAse I Solution	Thermo Fisher Scientific (90083)
RIPA Lysis and Extraction Buffer	Thermo Fisher Scientific (89901)
Bolt™ LDS Sample Buffer (4X)	Life Technologies (B0007)
Instant Skim Milk Powder	Coles Supermarkets (7910660P)
Spectra™ Multicolor Broad Range Protein Ladder	Thermo Fisher Scientific (26634)
Bolt™ MES SDS Running Buffer (20X)	Thermo Fisher Scientific (B0002)
Bovine Serum Albumin (BSA)	Sigma (A7906-50G)

Antibody Diluent	Agilent Technologies (S080983-2)
Harris Haematoxylin	POCD Scientific (HHX5)
Eosin	POCD Scientific (EOSVJ/5)
Scotts Blue Solution	POCD Scientific (SCOTB5)
Ethanol	Sigma (1009831011)
Xylene	Sigma (247642-1L-CB)
Hydrogen peroxide solution	Sigma (H1009-100ML)
Normal Goat serum	Sigma (G9023-10ML)
Solid pimonidazole HCl (Hypoxyprobe™-1)	Hypoxyprobe (HPI-XXX)
Hoechst Solution (20 mM)	Thermo Fisher Scientific (62249)
Image-iT™ Green Hypoxia Reagent (5 mM)	Thermo Fisher Scientific (I14833)
CyQUANT™ Cell Proliferation Assay	Thermo Fisher Scientific (C7026)
Hanks' Balanced Salt Solution (HBSS), calcium, magnesium, no phenol red	Thermo Fisher Scientific (14025092)
Staurosporine (1 mM)	Sigma (S5921-1MG)
SYTOX™ Blue Dead Cell Stain – (1 mM)	Thermo Fisher Scientific (S34857)
Dihydroethidium (DHE) – (5 mM)	Thermo Fisher Scientific (D11347)
MitoSOX™ Red Mitochondrial Superoxide Indicator – (5 mM)	Thermo Fisher Scientific (M36008)
D-Luciferin, Sodium Salt monohydrate	Gold Biotechnology (LUCNA-10G)
Polybrene (hexadimethrine bromide)	Sigma (H9268)
pLentipuro3/TO/V5-GW/EGFP-Firefly Luciferase	Addgene (Cat no. 119816)
Accutase solution	Sigma (A6964-500ML)
10% Neutral Buffered Formalin	Livingstone (IPOS 558)
Antibody Diluent	Agilent Technologies Australia (S080983-2)
Bright-Glo™ Luciferase Assay System	Promega Corporation (E2610)
EF5 Hypoxia Detection Kit, Alexa Fluor® 488	Merck (EF5-30A4)
Vita Pos Eye Ointment	Pet Care Pharmacy
3M Vetbond Tissue Adhesive	Pet Care Pharmacy
Bone Wax, 2.5 Grams Sachets	Livingstone (JJ83750)

Table 2.3 Drugs

Drugs	Source/Identifier
Atovaquone	Sigma (A7986-10MG)
Proguanil	Sigma (G7048-10MG)
Mefloquine	Sigma (M2319-100MG)
Ivermectin	Sigma (I8898-250MG)
Quinacrine	Sigma (Q3251-25G)
Amorphous solid dispersion atovaquone formulation	Formulated by Zachary N. Warnken (Via Therapeutics LLC, Austin)
Phenformin	Sigma (P7045-10G)
Metformin	Sigma (D150959-5G)

Table 2.4 Antibodies

Antibodies	Source/Identifier
HIF-1α	Abcam (ab51608)
β-Actin	Cell Signaling Technology (4967S)
SDHC	Abcam (ab155999)
SDHD	Abcam (ab189945)
Ki67	Abcam (ab16667)
H3K27M	Abcam (ab190631)
HIF-1α	Abcam (ab51608)
CA-IX	Abcam (ab15086)
VEGFA	Santa Cruz Biotechnology – (sc-7269)
Anti-pimonidazole rat IgG1 monoclonal antibody (MAb1)	Hypoxyprobe (HPI-XXX)
Goat anti-Mouse IgG (H+L) Secondary Antibody, HRP	Cell Signaling Technology (7076S)
Goat anti-Rabbit IgG (H+L) Secondary Antibody, HRP	Cell Signaling Technology (7074S)
Goat anti-Rat IgG (H+L) Secondary Antibody, HRP	Thermo Fisher Scientific (31470)

Table 2.5 Commercial Kits

Commercial Kits	Source/Identifier
Seahorse XF Cell Mito Stress Test Kit	Agilent Technologies (103015-100)
DAB Substrate Kit	Abcam (ab64238)
Pierce™ BCA Protein Assay Kit	Thermo Fisher Scientific (23225)
SuperSignal™ West Pico PLUS Chemiluminescent Substrate	Thermo Fisher Scientific (34580)
SuperSignal™ West Femto Maximum Sensitivity Substrate	Thermo Fisher Scientific (34096)
BOLT™ Welcome Pack + iBlot™ 2 System	Thermo Fisher Scientific (NW0412AIB2)
RNeasy Mini Kit	QIAGEN (74104)

Table 2.6 Solutions

Solutions	Notes
Tumor Stem Medium Base (TSM-B)	1:1 DMEM/F-12, 1x Neurobasal-A Medium, 100mM MEM Non-Essential Amino Acids solution, 100mM MEM Sodium Pyruvate solution, 200mM GlutaMAX™ supplement, Antibiotic-Antimycotic, 1M HEPES solution.
TSM Working (TSM-W)	TSM Base, 20ng/mL FGF, 20ng/mL EGF, 10ng/mL PDGF-BB, 10ng/mL PDGF-AA, 0.2% 2µg/mL Heparin, B-27 Supplement minus vitamin A.
Prigrow Complete Medium for Astrocytes	Prigrow IV Base Medium, 10% Fetal-bovine serum, 10ng/mL EGF, 1% L-glutamine, 1% Penicillin/Streptomycin Solution.
XF Seahorse Assay Medium	XF DMEM Medium, XF Glutamine (2mM), XF Pyruvate (1mM), XF Glucose (10mM).
3x Mitochondrial Assay Solution (MAS)	70 mM sucrose, 220 mM mannitol, 10 mM KH_2PO_4, 5 mM $MgCl_2$, 2 mM HEPES, and 1 mM EGTA; pH 7.2.
1x MAS	3x MAS in Distilled Water DNase/Rnase-free
Citrate Buffer pH6	0.01M Citrate Buffer in 1x PBS
Tris-EDTA Buffer pH9	10 mM Tris Base, 1mM EDTA, 0.05% Tween 20 in Milli-Q water
Running Buffer (1X)	Bolt™ MES SDS Running Buffer (20X) and Milli-Q water (1:20)
BSA Solution	5% BSA in TBST

Skim Milk (5%)	5% Skim Milk powder in TBST
Tris Buffered Saline with Tween-20 (TBST) (1X)	10X TBS per 1L, 0.5% Tween-20 in Milli-Q water
Phosphate Buffered Saline with Triton-X (PBST) (1X)	10X PBS per 1L, 0.5% Triton-X in Milli-Q water
Agarose (3%)	3% agarose in Milli-Q water
MTT Solution	5 mg/mL in PBS
Hoechst solution	1 µg/ml in PBS

Table 2.7 Equipment

Equipment	Source/Identifier
ChemiDoc™ Touch Imaging System	Bio-Rad
Seahorse XFe24 Analyzer	Agilent Technologies
SpectraMax iD5 Plate Reader	Molecular Devices
X-Rad 320	Precision X-Ray
Cell-Rad	Precision X-Ray
Rotary Microtome	Leica Biosystems
Decloaking Chamber NxGen	BioCare Medical
Nanozoomer Slide Scanner	Hamamatsu
KOPF Stereotactic Frame	SDR Scientific
Hamilton syringe	Sigma (20751)
Premium scalpel handles	Able Scientific (AS500236)
Size 70 drill bit (0.028”)	SDR Scientific (8170)
Animal feeding needle, sterile, disposable, PTFE	Merk (CAD9931)
Livingstone Surgical Scalpel Blade, Size 11	Livingstone (SBLDCL11)
Everyday ONYX dumont#7 S/S tweezers 12cm curved	Able Scientific (ASE11407-07)
Graefe iris anatomic forceps premium ONYX 10cm curved	Able Scientific (AS11151-10)
Iris fine premium ONYX operating scissors s/s German 10cm straight	Able Scientific (AS09340-10)

BD FACSCanto II	BD Biosciences
Flow Cytometry Sorter Aria III	BD Biosciences
FV1000 Laser Scanning Confocal Microscope	Olympus
FastPrep-24^{TM} 5G Lysis System	MP Biomedicals
High Performance Liquid Chromatography System	Shimadzu
SCIEX 6500 Qtrap Mass Spectrometer	SCIEX
Nanodrop 2000	Thermofisher Scientific
Illumina Novaseq 6000 platform	Illumina
IVIS Lumina X5 Optical Imager	PerkinElmer
Zeiss Live Cell Imaging Microscope	ZEISS

2.2. Methods

2.2.1 Cell culture

The primary and GFP/luciferase-expressing DIPG cell lines were maintained in DMEM/F12 and Neurobasal-A media (50:50) supplemented with sodium pyruvate, non-essential amino acids, glutamax, hepes buffer, antibiotic-antimycotic, heparin, B-27, and growth factors (EGF, FGF, PDGF-AA and PDGF-BB). The immortalized human astrocytes (IHA) – hTERT were grown in culture flasks coated with applied cell extracellular matrix and maintained in Prigrow IV medium supplemented with 10% FBS, 10ng/ml EGF, 1% L-glutamine and 1% penicillin/streptomycin. Cells were grown in humidified incubator at 37°C with 5% CO2. All cell lines were routinely tested for mycoplasma contamination and the cumulative length of culturing did not exceed 10 passages.

Once 80-90% confluency was reached, the adherent cell cultures were washed with PBS and harvested using trypLE. TrypLE was neutralised by adding culture media and removed by centrifugation at 1300 rpm for 5 minutes. For neurosphere cultures, trypLE was not needed and cells resuspended in the media were collected and centrifuged at the same conditions as above. The cell pellets were resuspended in culture media, stained with 0.4% trypan blue, and counted using haemocytometer. Only cells with >85-90% viability were used in all the experiments described in this thesis.

2.2.2 Cell viability assays

For cell viability assays, DIPG and IHA-hTERT cells were seeded in 96-well plates for 24 hour at the following seeding densities - SU-DIPG-XVII (3000 cells/well), SU-DIPG-VI (5000cells/well), HSJD-DIPG-007 (3000cells/well), HSJD-DIPG-012 (5000 cells/well), HSJD-DIPG-013 (5000 cells/well), SU-DIPG-13P* (5000 cells/well) and IHA-hTERT (4000 cells/well). Cells were treated with DMSO or drugs at the indicated doses for 24-72 hour. 20 µL of MTS reagent was added per well post-treatment and incubated at 37°C with 5% CO2. Absorbance was measured using SpectraMax iD5 Plate Reader at 490 nm. Data was normalised to DMSO-treated controls (set as 100%).

2.2.3 Extracellular flux assays

The effects of drugs on changes in oxygen consumption rate (OCR) and extracellular acidification rate (ECAR) was measured using extracellular flux assays. Briefly, SU-DIPG-XVII (40,000 cells/well), HSJD-DIPG-007 (65,000 cells/well), SU-DIPG-VI (100,000 cells/well) and IHA-hTERT (60,000 cells/well) were seeded overnight in DIPG media on laminin coated plates (1:100 laminin in PBS). The probes in XF24 sensor cartridge plate were hydrated in XF24 calibrant (pH 7.4) overnight in non-CO2 incubator. After 24 hour incubation, media of cells was replaced by XF DMEM medium (supplemented with 10 mM glucose, 1 mM sodium pyruvate and 2 mM glutamine) and incubated for 1 hour in non-CO2 incubator. DMSO control or drugs were prepared in XF DMEM medium and added to the cartridge ports at indicated doses. The plate was calibrated in XFe24 Analyzer (~ 30 minutes), then replaced by cell culture plate and the assay was run for 30 cycles with 5 measurement cycles for basal readings and 25 measurement cycles after drug injection (~ 4 hour). All the experiments were normalised to cell number using hoechst. Results were analysed using XFe Wave Software (Seahorse Biosciences).

2.2.4 Extracellular flux assays using XF Cell Mito Stress Test Kit

Seahorse XF Cell Mito Stress Test was used to measure the effect of drugs on various mitochondrial parameters of DIPG cultures based on real-time changes in OCR/ECAR. Here, the XF Cell Mito Stress Test kit was used and experimental layout was similar as in section 2.2.3. The kit components were prepared as per manufacturer's instructions. The assay was processed following sequential addition of drug, followed by 1 µM oligomycin, 1 µM FCCP and 0.5 µM rotenone/antimycin A in ports A-D. Pre-treatment assays were also performed where DIPG cells were pre-treated with drugs for 24 hour. Similar experimental setup was then followed as in section 2.2.3 and assay processed by addition 1 µM oligomycin, 1 µM FCCP and 0.5 µM rotenone/antimycin A in ports A-C. All the experiments were normalised to cell number using hoechst. Results were analysed using XFe Wave Software (Seahorse Biosciences).

2.2.5 Extracellular flux assays – mitochondrial complexes assay

For mitochondrial complex specific targeting assay, HSJD-DIPG-007 (65,000 cells/well) were seeded overnight in DIPG media on laminin coated plates (1:100 laminin in PBS). For these assays permeabilization of plasma membrane is essential as it enables the permeability of non-membrane permeable substrates present in the assay medium to enter the mitochondria. This approach enables measurements of the activities of mitochondrial complexes using substrates specific to each complex. The changes in OCR in response to the different injections used to determine complex specific activity. To determine optimal concentration for XF PMP, cells were permeabilised using 0-5 nM XF PMP according to the manufacturer's instructions. The OCR rate was measured in 1× Mitochondrial Assay Solution (MAS) [70 mM sucrose, 220 mM mannitol, 10 mM KH2PO4, 5 mM MgCl2, 2 mM Hepes, and 1 mM EGTA; pH 7.2] using XFe24 Analyzer (Seahorse Biosciences). Complex II dependent OCR was calculated as follows – (OCR after succinate/rotenone injection – OCR at rotenone injection). Seahorse media containing 10 mM pyruvate, 1 mM malate, and 2 mM ADP (substrates for complex I) was used and injections were as follows - 2 µM rotenone (injection 1, complex I inhibitor), 10 mM succinate and 2 µM rotenone (injection 2, substrate for complex II and inhibitor for complex I) and 2 µM Antimycin A (injection 3, complex III inhibitor). Complex II dependent OCR was calculated as follows – (OCR after succinate/rotenone injection – OCR at rotenone injection).

To measure complexes inhibition by drugs, HSJD-DIPG-007 (65,000 cells/well) were seeded overnight and treated with 30 µM Atovaquone, 5-10 µM Mefloquine overnight and 2 µM Antimycin A and 2 µM Myxothiazol for 2 hour. Following treatment, cells were permeabilized using 3 nM XFPMP according to the manufacturer's instructions. The OCR rate was measured in 1× MAS using XFe24 Analyzer (Seahorse Biosciences). Two different experiments were performed to validate the specific target of these drugs. In experiment 1, seahorse media containing 10 mM pyruvate, 1 mM malate, and 2 mM ADP (substrates for complex I) was used and injections were as follows - 2 µM rotenone (injection 1, complex I inhibitor), 10 mM succinate and 2 µM rotenone (injection 2, substrate for complex II and inhibitor for complex I), 2 µM Antimycin A (injection 3, complex III inhibitor) and 10 mM ascorbate plus 100 µM TMPD (injection 4, substrate for complex IV). Complex specific OCR was calculated as follows – Complex I: Baseline OCR – OCR at rotenone injection; Complex II: OCR after succinate injection – OCR at rotenone injection; Complex III: OCR after succinate injection –

OCR at antimycin A injection; Complex IV: OCR after ascorbate/TMPD injection – OCR at antimycin A injection. In experiment 2, seahorse media containing 10 mM pyruvate, 1 mM malate, and 2 mM ADP (substrates for complex I) was used and injections were as follows – 10 mM succinate and 2 µM rotenone (injection 1, substrate for complex II and inhibitor for complex I), 20 mM malonate (injection 2, complex II inhibitor) and 0.5 mM duroquinol (injection 3, complex III substrate) and 10 mM ascorbate plus 100 µM TMPD (injection 4, substrate for complex IV). Complex specific OCR was calculated as follows – Complex II: OCR after succinate injection – Baseline OCR; Complex III: OCR after duroquinol injection – OCR at malonate injection. All the experiments were normalised to cell number using hoechst.

2.2.6 Colony formation assays

Colony formation assays (CFAs) were used to assess the colony forming ability DIPG cells post drug/RT treatments. For adherent cells, colony formation assay with crystal violet staining was followed. SU-DIPG-XVII (400 cells/well) were seeded overnight using 6-well plates. Cells were treated with atovaquone or mefloquine for 6 hour followed by RT administered at 2, 4, 6 Gy using Cell-Rad. After 24 hours of drug treatment, the drug was removed and replaced with fresh DIPG medium. Cells were kept in culture undisturbed for 10-12 days during which colonies were formed. Colonies (defined by ~ 50 or more cells) were fixed and stained with 0.5% crystal violet in 25% methanol (v/v). Plates were washed with water, air-dried and scanned using ChemiDocTM Touch Imaging System. For suspension cells, soft agar colony formation assay with MTT staining was followed. Briefly, HSJD-DIPG-007 ($3x10^5$ cells/well) and SU-DIPG-VI ($3x10^5$ cells/well) were seeded overnight or for 72 hour using 6-well plates. Cells were treated with atovaquone or mefloquine for 6 hour followed by RT administered at 2, 4, 6 Gy using Cell-Rad. Agarose coated 24-well plates were prepared with a bottom layer of 0.6% agarose. After 24 hour of drug treatment, HSJD-DIPG-007 (2500 cells) and SU-DIPG-VI (3000 cells) were mixed with 0.3% agarose and seeded onto the 24-well plate to form the top layer. Colonies were allowed to grow undisturbed for 2 weeks and then stained with MTT dye for 30 minutes. Plates were scanned using ChemiDocTM Touch Imaging System. Colonies were manually counted using ImageJ and plating efficiency and surviving fractions were calculated.

2.2.7 Western Blot

DIPG cells were collected and protein extraction was performed by resuspending the pellet in RIPA lysis buffer containing protease and phosphatase inhibitors and DNAse I as per manufacturer's instructions. Protein quantification was performed using Pierce BCA Protein Assay Kit as per manufacturer's instructions. Protein samples (30 µg) were loaded onto Bolt 4-12% Bis-Tris Plus Gels with SDS-PAGE at 200 V for 32 mins, followed by transfer to nitrocellulose membrane using iBolt 2 Dry Blotting System. Membrane was then stained with Ponceau S (~3 minutes) to confirm efficient transfer, followed by washing in PBS. The blot was blocked in 5% skim milk for 1 hour. Membranes were incubated at 4°C overnight with primary antibodies rabbit anti-HIF-1α (ab51608 Abcam, 1:1000), rabbit anti-beta-actin (4967S Cell Signalling Technology, 1:1000), rabbit anti-SDHC (ab155999 Abcam, 1:10,000) and rabbit anti-SDHD (ab189945 Abcam, 1:500). Membranes were washed with TBST, three times for 5 minutes each. Membranes were incubated with secondary anti-rabbit IgG, HRP-linked antibody (7074S Cell Signalling Technology, 1:2000) at room temperature for 1 hour. Membranes were washed again with TBST, three times for 5 minutes each. Labelled protein bands were detected by chemiluminescence SuperSignal West Femto and SuperSignal West Pico and were imaged using ChemiDocTM Touch Imaging System.

2.2.8 3D Neurosphere Assay

HSJD-DIPG-007 (4000 cells/well) and SU-DIPG-VI (8000 cells/well) were seeded using 96-well Corning™ spheroid plate. Once single neurospheres of the observable sizes were visualized (~ 500 µm at 72 hour culture), these were then treated with atovaquone, ASD atovaquone and mefloquine. After 24 hour treatment, the entire drug + medium was removed and neurospheres were stained with Image-iT™ Green Hypoxia Reagent (5 µM) and Hoechst 33342 (1 µg/mL) and incubated for 1 hour. Dyes were then removed and replaced with fresh DIPG medium and incubated for 3 hour. Fluorescent images of the neurospheres were acquired using Olympus FV1000 Confocal Microscope and analysed using FV10-ASW Viewer Software 4.2 (Olympus).

2.2.9 Measurement of Mitochondrial and Cytosolic Reactive Oxygen Species

Mitochondrial and cytosolic ROS levels were measured by Mito-SOX™ Red and Dihydroethidium superoxide indicators respectively. SU-DIPG-XVII ($3x10^5$ cells/well) and HSJD-DIPG-007 ($3x10^5$ cells/well) were seeded overnight using 6-well plates. Cells were treated with atovaquone, mefloquine or RT at the desired dose. At the end of the treatment, Mito-SOX™ Red (50 µM, 30 minutes) or DHE (2.5 µM, 30 minutes) were added. Cells were then washed with Hanks Balanced Salt Solution (HBSS) or PBS and Sytox Blue was added (1 µM, 5 minutes). Cell suspension was analysed using BD FACSCanto II flow cytometer with filters PE (Excitation 488, Emission 585/42) for MitoSOX Red/DHE and Pacific Blue (Excitation 405, Emission 450/50) for Sytox Blue. Mean Mito-SOX Red/DHE fluorescence for the entire population was calculated.

2.2.10 Patient cohorts

Patient mRNA expression of mitochondrial ETC genes in specific paediatric brain tumour types was obtained from Pediatric cBioportal tool using the Open Pediatric Cancer (OpenPedCan) Project v15 dataset (downloaded on 29/05/24) (184, 185). The mRNA levels of these genes in normal brain tissue samples was obtained from GTEx.

2.2.11 RNA Sequencing

HSJD-DIPG007 cells (3×10^5 cells/well) seeded overnight using 6-well plates. After 24 hours, cells were treated with atovaquone for 6 hours, followed by 6 Gy RT. Cells were collected 24 hours post drug treatment and RNA extraction was performed using RNeasy Mini Kit (Qiagen). High quality total RNA (RIN > 8) was used for library preparation using the Illumina Truseq stranded mRNA library preparation kit. Sequencing was performed on the Illumina Novaseq 6000 platform using the SP flow cell with single-end 100bp reads. FastQC (Babraham Bioinformatics) was used to determine the library sequencing quality. Trim Galore (Babraham Bioinformatics: www.bioinformatics.babraham.ac.uk/) was used to perform Illumina adaptor sequence and low quality read trimming (read pair removed if < 20 base pairs). Next, the reads were aligned to human genome hg38 by STAR using ENSEMBL gene annotations as a guide. HTSeq was used to generate read counts data corresponding to ENSEMBL gene annotations. All the data was analysed in R Statistical Environment with tidyverse. EdgeR was used for

background correction and normalising the counts data for the library size. Pheatmap package (v1.0.12) was used to generate the heatmap to visualise the expression pattern of differentially expressed genes (DEGs), with hierarchical clustering and row scaling applied to both columns and rows. The colour in the heatmap shows fold change (log2). KEGG analysis was performed using the clusterProfiler package(v4.6.2) with enrichKEGG function. The parameters used here include p-value adjustment method set to Benjamini-Hochberg (BH), keyType as "kegg", organism set to "hsa", and p-value and q-value cutoffs set to 0.05. KEGG enrichment pathways are presented as dot plots (Figures 4.11 D, F, H). Bar plots are used to present significant KEGG pathways with their associated gene changes and corresponding fold changes (log2) (Figures 4.11 E, G, I). The length of the bars represent gene count, colours of the bar represent adjusted p values, and the bars are coloured as per the direction of regulation (downregulated/upregulated). Hallmark gene signatures were accessed using msigdbr (Dolgalev I (2022). _msigdbr: MSigDB Gene Sets for Multiple Organisms in a Tidy Data Format_. R package version 7.5.1) and scored for each sample using GSVA (http://www.biomedcentral.com/1471-2105/14/7).

2.2.12 Lentiviral Transductions

Virus production for the transductions was performed by Dr Yuyan Chen, our collaborator at Kids Research. HSJD-DIPG-007 cells were plated on matrigel coated 12-well plates. Virus titre was calculated and 3.6 MOI of lentivirus with polybrene was added to the cells. Polybrene, a cationic polymer, increases virus transfer efficiency by enhancing virus absorption into mammalian cells. The virus containing media was replaced with fresh media at day 2 following transduction. After few days, the cells were then transferred to 6-well plates. GFP expression was assessed at several steps in the protocol. Cells were then serially expanded by transferring to T25 flask and later to T75 flasks to obtain enough cells for sorting. Cells were sorted to separate out the GFP-positive HSJD-DIPG-007 population. Following transduction, cells were sorted by flow-assisted cell sorting to isolate the GFP-positive HSJD-DIPG-007 population. Following sorting, quantification revealed that only 15% of transduced cell population was GFP positive. The isolated positive cells were serially expanded from 6-well plates to T25 flask and to T75 flasks before freezing down.

2.2.13 Measuring luminescence using plate reader and assessing GFP expression with microscopy

Luciferase expression of GFP/luciferase-expressing HSJD-DIPG-007 and SU-DIPG-24 cells was detected using SpectraMax iD5 plate reader. Cells were seeded in 100 µL at a range of densities ranging up to 5 x 10^4 cells in 96-well flat bottom black polystrene plates. Bright-Glo dye was added to the cells 1:1, incubated for 3 minutes and luminescence was measured. GFP expression was assessed with Zeiss Live Cell Imaging Microscope.

2.2.14 Animal Studies

All the animal studies were performed following approval from the Western Sydney Local Health District Animal Ethics Committee (WSLHD-AEC) (Approval number - 4370). Female balb/c nude mice aged 6-8 weeks were purchased from Animal Resources Centre (ARC). Mice were housed in WIMR Biological Services Facility (BSF) in ventilated cages with air flow at cage level and provided with environmental enrichment, nesting material and houses as per WIMR BSF procedures and protocols. All the animals were acclimatised for 1 week prior to any procedures.

2.2.14.1 Orthotopic Injections

Orthotopic injections were performed with the following DIPG cell lines - SU-DIPG-13P*, parental HSJD-DIPG-007 and GFP/luciferase-expressing HSJD-DIPG-007. SU-DIPG-13P* ($4x10^5$ cells in 2 µL HBSS), parental HSJD-DIPG-007 ($2x10^5$ cells in 2 µL Matrigel) and GFP/luciferase-expressing HSJD-DIPG-007 (2x105 cells in 2 µL Matrigel) were injected intracranially into the brainstem of balb/c nude mice using the KOPF Stereotactic Frame at coordinates 6.0 mm posterior to bregma, 0.5 mm lateral to midline and at a depth of 3.5 mm. Mice were routinely monitored and treatments were started as described below.

Mice were monitored for clinical signs of tumour growth and any signs of distress post-treatments. Mice were humanely euthanised if they exhibited signs of severe head tilting, severe ataxia or circling lethargy, and/or if they reached 20% weight loss. Brains were excised and fixed in 10% neutral buffered formalin solution for 24 hours. The solution was replaced with 70% ethanol for 24 hours, following which the brains were sectioned in sagittal plane and embedded in paraffin wax.

2.2.14.2 Radiation Treatment using XRAD320

Whole-brain RT was delivered using X-RAD 320. Mice were restrained using individual fixtures and head exposed shields were used to ensure that RT is only delivered to the brain. RT treatment was started at 2 weeks post-intracranial injection for SU-DIPG-13P* model and at 4 weeks post-intracranial injection for HSJD-DIPG-007 model. RT was administered at a range of doses based on experiment design i.e., 10, 20 and 30 Gy as multiple fractionated doses of 2 Gy per day. Mice were monitored post-RT for any signs of distress or adverse effects.

2.2.14.3 Oral Gavage

ASD atovaquone formulation was given in PBS via oral gavage. As this formulation contains only 20% pure of atovaquone, we delivered 1000 mg/kg to achieve dose equivalent to 200 mg/kg pure atovaquone. To measure brain concentration of ASD atovaquone, the drug was given daily for 6 days. To assess the efficacy of ASD atovaquone in combination with RT, the drug treatment was started at 9 days post-intracranial injection for SU-DIPG-13P* and treatment given for 10 consecutive days. For the HSJD-DIPG-007 model, ASD atovaquone treatment was started at 21 days post-intracranial injection and treatment given for 12 consecutive days. For both the models, ASD atovaquone was given 1 hour before RT administration and the last 5 days of ASD atovaquone coincided with RT treatment.

2.2.14.4 Pimonidazole and EF5 injections

For pimonidazole staining experiments, end-point mice were intraperitoneally injected with 100 mg/kg pimonidazole 1 hour post-euthanisation. For EF5 staining experiments, end-point mice were intraperitoneally injected with 10 mg/kg EF5 3 hour post-euthanisation. FFPE sections were prepared and immunohistochemistry staining was performed to detect pimonidazole and EF5.

2.2.14.5 ASD atovaquone brain and plasma concentration determination

Brain and plasma concentration measurements of ASD atovaquone was performed by Dr Ryan J. Duchatel at The University of Newcastle. Snap frozen brain sections were weighed then homogenised in 1 mL of ice-cold methanol (LC/MS grade, Merck) using a FastPrep-24 5G lysis system (MP Biomedicals). 10 mg equivalent of each brain sample was taken and diluted to 400 µL with ice-cold methanol containing a spike of internal standard (Ponatinib to final

concentration of 1000 fmol/µL). For plasma samples, 20 µL was taken and diluted to 400 µL with ice-cold methanol containing a spike of internal standard (Ponatinib to final concentration of 1000 fmol/µL). Two sets of matrix-matched calibration standards ranging from 10 fmol/µL to 5000 fmol/µL atovaquone was prepared using untreated mouse brain and plasma, and containing 1000 fmol/µL of internal standard. All samples were shaken for 30 minutes at 1500 rpm at room temperature using an Eppendorf Thermoblock, then centrifuged at 18000 g for 7 minutes. 200 µL of supernatant was transferred to a Mass Spectrometry (MS) vial for analysis. Reverse phase LC-MS/MS was performed using a Shimadzu analytical flow high-performance liquid chromatography system coupled to a SCIEX 6500 Qtrap mass spectrometer with an electrospray ion source. 1 µL of each sample was separated on a Phenomenex Luna Omega 1.6 µm Polar C18 100 x 2.1mm column, employing a gradient of 2-99% solvent B (solvent A = 0.1% formic acid, solvent B = acetonitrile, 0.1% formic acid) at a flow rate of 300 µL/min over 6 minutes. Multiple reaction monitoring (MRM) was performed in negative mode using optimised source parameters. Briefly, these were source gas: 40; ion spray voltage: −3500; source temperature: 450°C. Entrance potential and delustering potential were optimised for atovaquone and equalled -8 and -165 respectively. The ion transition m/z 365.0 -> 337.0 (CE: -41) was used for quantification of atovaquone, and the additional transitions m/z 365.0 -> 227.1 (CE: -45) and 365.0-> 171.1 (CE: -60) were monitored for qualitative peak validation. Peak integration was performed in Skyline, using internal standard abundance to normalise between samples. Atovaquone concentration was quantified by interpolation using the matrix-matched calibration curves.

2.2.15 Measuring luminescence using IVIS Lumina X5 Imaging

Luciferase expression of GFP/luciferase-expressing HSJD-DIPG-007 and SU-DIPG-24 cells was detected using In Vivo Imaging System (IVIS) Lumina X5 imaging. For assessing luciferase activity in vitro, GFP/luciferase-expressing HSJD-DIPG-007 and GFP/luciferase-expressing SU-DIPG-24 cells were seeded in 100 µL at a range of densities ranging up to 60,000 cells in 96-well flat bottom black polystrene plates. Bright-Glo dye was added to the cells 1:1. Following that, images were taken every 1 minute for 10 minutes with optimal signal achieved at 3 minutes. For assessing luciferase activity of in vivo, mice were injected with 150 mg/kg D-luciferin via intraperitoneal injection. After 5 minutes, mice were anesthetised with 2-3% isoflurane, 1L/min oxygen and were positioned into IVIS Lumina chamber and continuous sedation was ensured throughout the imaging procedure. Bioluminescence images

were taken every 5 minutes for 30 minutes. Animals were placed in a heating pad for 20 minutes to recover from anaesthesia and then returned back to respective cages.

2.2.16 Immunohistochemistry

Paraffin sections were cut at 4 µm using standard Leica microtome. Tumour cells were visualised using hematoxylin and eosin (H&E) staining as per manufacturer's instructions (Harris). H&E sections were also reviewed by pathologist A/Prof Winny Varikatt to cross-check the tumour areas. A generalised IHC protocol is mentioned below with antibody specific details in **Table 2.9**. Sections were deparaffinized and hydrated manually using xylene and graded-ethanols to distilled water. Antigen retrieval was performed using Decloaking Chamber NxGen (Biocare Medical) at 95°C for 30 mins, with either 0.01 M citrate buffer (pH 6) or Tris-EDTA buffer (pH 9). Sections were allowed to cool down for 30 mins in PBS. Sections were blocked in 5% hydrogen peroxide for 5 minutes and then washed twice with 1x PBS, 5 minutes each. Sections were then blocked in normal goat serum for 30 minutes, followed by staining with desired primary antibody in Dako antibody diluent overnight at 4℃. Sections were washed with 1x PBST (1 wash, 5 minutes) followed by 1x PBS (2 washes, 5 minutes each). Sections were then incubated in HRP-conjugated secondary antibodies for 30 mins. Sections were washed again with 1x PBST (1 wash, 5 minutes) followed by 1x PBS (2 washes, 5 minutes each). DAB substrate kit was used to visualise antibody staining as per manufacturers' instructions. Sections were then counterstained with hematoxylin. Slides were allowed to dry and were cover slipped. Slides were scanned using Cell Imaging Nanozoomer Slide Scanner.

Table 2.8 Antibodies for immunohistochemistry

Primary Antibody	Dilution	Antigen Retrieval Buffer	Secondary Antibody	Dilution
H3K27M - ab190631	1:1000	Tris-EDTA Buffer (pH9)	Goat anti-Rabbit IgG (H+L) Secondary Antibody, HRP – 7074S	1:100
Ki67 - ab16667	1:400	Citrate Buffer (pH6)	Goat anti-Rabbit IgG (H+L) Secondary Antibody, HRP – 7074S	1:100
HIF-1α - #ab51608	1:200	Tris-EDTA Buffer (pH9)	Goat anti-Rabbit IgG (H+L) Secondary Antibody, HRP – 7074S	1:100
VEGF – sc-7269	1:50	Citrate Buffer (pH6)	Goat anti-Mouse IgG (H+L) Secondary Antibody, HRP – 7076S	1:100

CA-IX - ab15086	1:50	Tris-EDTA Buffer (pH9)	Goat anti-Rabbit IgG (H+L) Secondary Antibody, HRP – 7074S	1:100
EF5 – Part no. CS222729	1:120	Citrate Buffer (pH6)	Goat anti-Mouse IgG (H+L) Secondary Antibody, HRP – 7076S	1:100
Pimonidazole Hypoxyprobe – HPI - #HPI-XXX – clone 11.23.22.R	1:25	Citrate Buffer (pH6) Tris-EDTA Buffer (pH9)	Goat anti-Rat IgG (H+L) Secondary Antibody, HRP – 31470	1:100

2.2.17 Statistical analysis

Statistical analysis was performed using GraphPad Prism. All of the in vitro experiments were performed at least thrice unless otherwise indicated. All results are expressed as means ± standard deviation (SD) unless otherwise indicated. The IC50 values of the drug dose response curves was calculated using non-linear regression. The data consisted of three independent experiments, with mean ± SD. Depending upon the experiment and groups, statistical significance was either calculated using t-tests or using one-way ANOVA with Tukey's multiple comparisons test. Statistics was not performed on CFA results as it is not standard to run statistics on these results. For animal studies, Kaplan-Meier survival curves are presented and statistical significance was calculated using log-rank (Mantel-Cox) test. A p-value < 0.05 was considered significant.

Chapter 3

Targeting Oxidative Phosphorylation – a Therapeutic Strategy to Radiosensitize Diffuse Intrinsic Pontine Glioma

Chapter 3. Targeting Oxidative Phosphorylation – a Therapeutic Strategy to Radiosensitize Diffuse Intrinsic Pontine Glioma

3.1. Introduction

Deregulated cellular energetics is a hallmark of cancer progression (186). An understanding of the metabolic requirements and upregulated pathways of specific cancers can enable the development of therapeutic targeting approaches. Over the past decade, a lot of focus has been directed towards targeting tumour metabolism as an emerging anti-cancer cancer strategy. Previously, the primary focus of targeting the metabolic reprogramming of cancer cells was on inhibition of glycolysis. However, recent studies have shown that several cancers, including gliomas, are also reliant on mitochondrial OXPHOS for cancer progression suggesting that cancers are metabolically heterogenous (91, 187-189). This has shifted attention towards the research on and the development of OXPHOS inhibitors.

An increase in OXPHOS dependency means increase in oxygen utilisation and this can give rise to diffusion limited hypoxia (190). The presence of hypoxia in solid tumours has a negative impact on the outcomes of cancer therapies including chemotherapy, radiotherapy and immunotherapy (191-193). To date, there has been no direct evidence of hypoxia in DIPG, however, the study by Yeom et al. (2015) found increased citrate concentrations in DIPG patients in areas of tissue hypoperfusion (72). As an increase in citrate accumulation is observed under hypoxic conditions (73), this suggests that DIPGs are potentially hypoxic group of tumours and hypoxia could also be a main factor driving DIPG oncogenesis (72). As DIPG is a radioresistant tumour type, and hypoxia is an important factor compromising the efficacy of radiotherapy (194), alleviating hypoxia could render DIPG sensitive to radiotherapy. Evidence that DIPGs are also reliant on OXPHOS could provide further support to the hypothesis that DIPGs have a hypoxic tumour microenvironment. This would mean that developing strategies to target OXPHOS could decrease hypoxia, improving the efficacy of radiotherapy in DIPGs, and thus leading to improved patient survival outcomes.

In this chapter, we intend to directly investigate whether DIPG are reliant on mitochondrial OXPHOS by assessing changes in gene expression of OXPHOS related genes. Under the guidance of Dr Kristina Cook, we used publicly available dataset the paediatric cbioportal tool

to specifically look at changes in the expression of the structural genes of mitochondrial ETC complexes I, II, III, IV and V as majority of the OXPHOS inhibitors under development are targeting these complexes. **Table 3.1** lists the structural genes of all of the mitochondrial complexes, both the nuclear DNA encoded genes and the mitochondrial DNA encoded genes. The mRNA expression data of the genes was downloaded from Open Pediatric Cancer (OpenPedCan) Project v15 comparing the mRNA abundance of brainstem glioma (BS) DIPG and DMG H3K27M. We also looked at other brain cancer categories - ependymoma (EPEN), glioblastoma (GBM) and high-grade gliomas (IDH-wildtype and H3-wildtype – HGG-IDH-WT/H3-WT) as hypoxia appears to be a significant feature in these tumours (195-197). The mRNA levels of genes in all of these brain tumours were compared against the mRNA levels from normal brain tissue samples including caudate (CAUD), cerebellum (CERB), and hypothalamus (HYPO) taken from GTEx.

Changes in OXPHOS is reflective of mitochondrial dysfunction. This can be inferred by measuring the OCR using seahorse analyser, a widely used instrument to investigate OXPHOS inhibitors. After studying the OXPHOS expression in DIPG/DMGs samples, we performed an OXPHOS inhibition screening against DIPG cultures using five FDA-approved anti-parasitic drugs (atovaquone, proguanil, ivermectin, mefloquine and quinacrine). Repurposing of drugs provides an opportunity for faster clinical translation of compounds from bench to bedside as the side effects of these compounds are already widely studied. These drugs were amongst the many others identified in a past DIPG screening by my supervisor and have been investigated in a range of cancer types for several distinct anti-cancer targets (reviewed in (105)). Here, we measure the changes in OCR of DIPG cultures following the injection of anti-parasitic drugs. Our aim is to identify the best OXPHOS inhibitors by looking at the OCR inhibition profile of DIPG cultures. We then perform further investigations on the best candidates and assess their hypoxia modification and radiosensitising efficacy against DIPG using both *in vitro* cultures and *in vivo* orthotopic DIPG models.

Table 3.1. Structural genes of each of the mitochondrial electron transport chain complexes.

	Structural Genes	
Mitochondrial Complex	**Nuclear DNA encoded subunit genes**	**Mitochondrial DNA encoded subunit genes**
I	1. *NADH:Ubiquinone Oxidoreductase Core Subunit S1 (ndufs1),* 2. *ndufs2,* 3. *ndufs3,* 4. *ndufs7,* 5. *ndufs8,* 6. *ndufv1,* 7. *ndufv2,* 8. *ndufab1,* 9. *ndufa1,* 10. *ndufa2,* 11. *ndufa3,* 12. *ndufa4,* 13. *ndufa5,* 14. *ndufa6,* 15. *ndufa7,* 16. *ndufa8,* 17. *ndufa9,* 18. *ndufa10,* 19. *ndufa11,* 20. *ndufa12,* 21. *ndufa13,* 22. *ndufb1,* 23. *ndufb2,* 24. *ndufb3,*	1. *Mitochondrially Encoded NADH:Ubiquinone Oxidoreductase Core Subunit 1 (mt-nd1),* 2. *mt-nd2,* 3. *mt-nd3* 4. *mt-nd4,* 5. *mt-nd4l,* 6. *mt-nd5,* 7. *mt-nd6.*

	25. *ndufb4,* 26. *ndufb5,* 27. *ndufb6,* 28. *ndufb7,* 29. *ndufb8,* 30. *ndufb9,* 31. *ndufb10,* 32. *ndufb11,* 33. *ndufc1,* 34. *ndufc2,* 35. *ndufs4,* 36. *ndufs5,* 37. *ndufs6,* 38. *ndufv3.*	
II	1. *Succinate Dehydrogenase Complex Flavoprotein Subunit A (sdha),* 2. *sdhb,* 3. *sdhc,* 4. *sdhd.*	
III	1. *Cytochrome C1 (cyc1),* 2. *Ubiquinol-Cytochrome c Reductase Core Protein 1 (uqcrc1),* 3. *uqcrc2,* 4. *Ubiquinol-Cytochrome c Reductase, Rieske Iron-Sulfur Polypeptide 1 (uqcrfs1),* 5. *Ubiquinol-Cytochrome c Reductase Hinge Protein (uqcrh),* 6. *Ubiquinol-Cytochrome c Reductase Complex III Subunit VII (uqcrq),* 7. *Tetratricopeptide Repeat Domain 19 (ttc19),* 8. *Ubiquinol-Cytochrome c Reductase Binding Protein (uqcrb),* 9. *Ubiquinol-Cytochrome c Reductase, Complex III Subunit X (uqcr10),*	1. *Mitochondrially encoded cytochrome b (mt-cyb)*

	10. *Ubiquinol-Cytochrome c Reductase, Complex III Subunit XI (uqcr11).*	
IV	1. *Cytochrome C Oxidase Subunit 4I1 (cox4i1),* 2. *cox4i2,* 3. *cox5a,* 4. *cox5b,* 5. *cox6a1,* 6. *cox6a2,* 7. *cox6b1,* 8. *cox6b2,* 9. *cox6c,* 10. *cox7a1,* 11. *cox7a2,* 12. *cox7b,* 13. *cox7b2,* 14. *cox7c,* 15. *cox8a,* 16. *cox8c.*	1. *Mitochondrially Encoded Cytochrome c Oxidase I (mt-co1),* 2. *mt-co2,* 3. *mt-co3.*
V	1. *ATP Synthase F1 Subunit Alpha (atp5f1a),* 2. *atp5f1b,* 3. *atp5f1c,* 4. *atp5f1d,* 5. *atp5f1e,* 6. *ATP Synthase Membrane Subunit c Locus 1 (atp5mc1),* 7. *atp5mc2,* 8. *atp5mc3,* 9. *ATP Synthase Membrane Subunit k (atp5md),* 10. *ATP Synthase Membrane Subunit e (atp5me),* 11. *atp5mf,*	1. *Mitochondrially Encoded ATP Synthase Membrane Subunit 6 (mt-atp6),* 2. *mt-atp8.*

	12. *atp5mg,* 13. *ATP Synthase Membrane Subunit 6.8PL (atp5mpl),* 14. *ATP Synthase Peripheral Stalk-Membrane Subunit b (atp5pb),* 15. *atp5pd,* 16. *atp5pf,* 17. *ATP Synthase Peripheral Stalk Subunit OSCP (atp5po),* 18. *ATP synthase inhibitory factor subunit 1 (atp5if1)*	

3.2. Results

3.2.1 DIPG/DMG clinical samples have increased expression of OXPHOS-related genes

3.2.1.1 Increase in the expression of mitochondrial complex I nuclear DNA encoded structural genes

The mitochondrial complex I, also referred to as NADH-ubiquinone oxidoreductase, is the first and largest component of the mitochondrial respiratory chain (198). It oxidises NADH, produced in the TCA cycle, generating two electrons and reducing ubiquinone to ubiquinol (198). It comprises of a total of 45 subunits, 38 of which are nuclear DNA encoded subunits and 7 are mitochondrial DNA encoded subunits (**Table 3.1**). We used publicly available datasets and analysed the mRNA expression of all the complex I subunit genes in normal brain tissue clinical samples and compared it to the clinical samples from DIPG/DMG and other brain tumour categories. Interestingly, the mRNA expression was found to be significantly upregulated in 13 of the mitochondrial complex I nuclear DNA encoded subunits in tissues of DIPG/DMG patients compared to healthy tissues (**Figure 3.1**). These genes are *ndufs3, ndufv2, ndufa3, ndufa9, nudfa11, ndufa12, ndufa13, ndufb1, ndufb2, ndufb4, ndufb5, ndufc2* and *ndufs6*. The mRNA expression of most of these 13 mitochondrial complex I genes was also significantly upregulated in tissues of EPEN and HGG-IDH-WT/H3-WT compared to healthy tissues (**Figure 3.1**). As for the GBM patients samples, the mRNA expression appeared to be varied across all of these complex I genes compared to healthy tissues (**Figure 3.1**). The expression patterns of these genes are also summarised as a heatmap in **Figure 3.7**, illustrating differences between tumour and normal tissues.

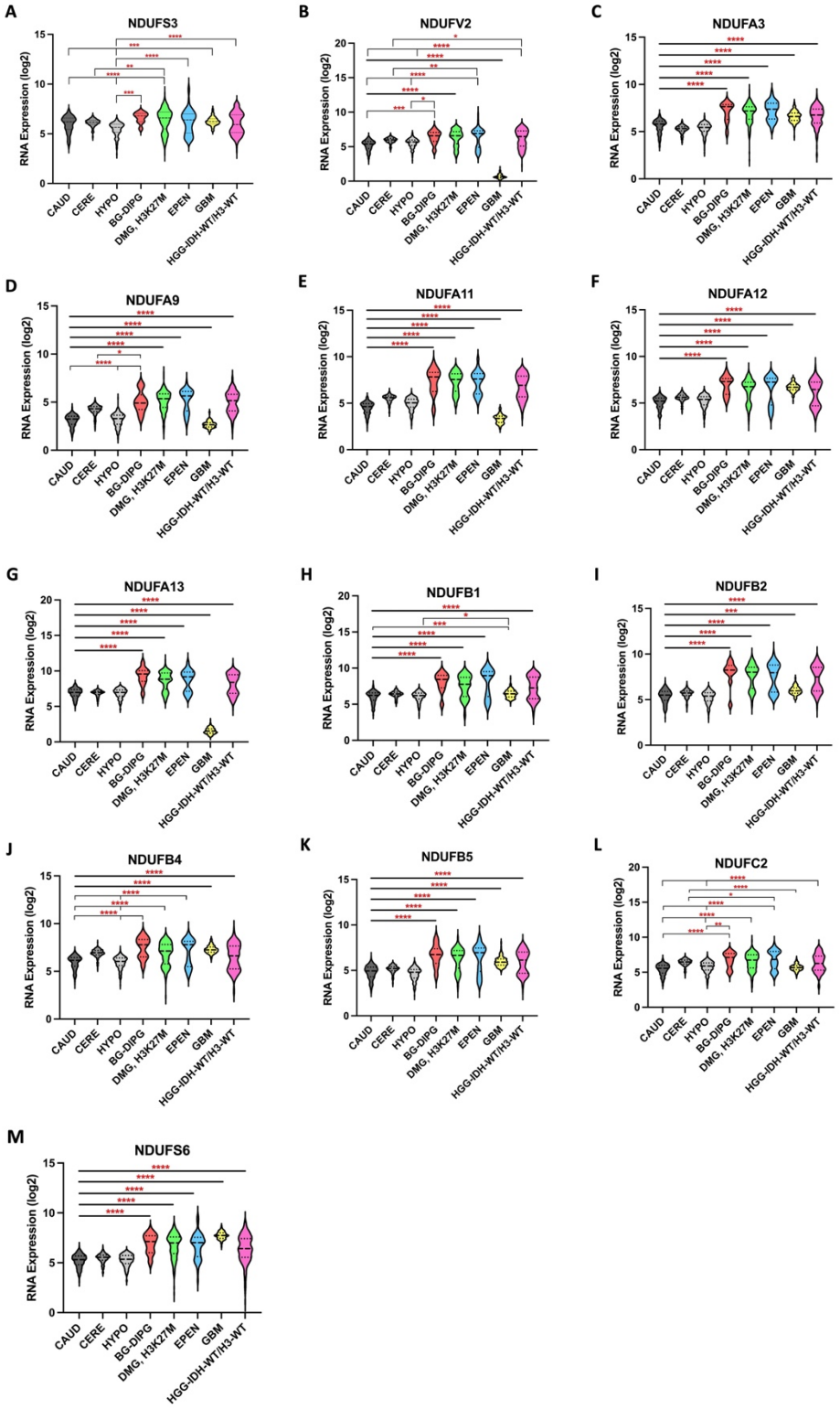

Figure 3.1. mRNA levels of 13 nuclear DNA encoded structural genes of mitochondrial complex I upregulated in DIPG/DMG clinical samples.

There are three categories of normal brain tissue samples - caudate (CAUD, n=246), cerebellum (CERE, n=456), hypothalamus (HYPO, n=202) and five categories of brain tumour clinical samples - brainstem glioma (BS) DIPG (n=10), DMG H3K27M (n=220), ependymoma (EPEN, n=60), glioblastoma (GBM, n=167), and high-grade gliomas IDH-wildtype and H3-wildtype (HGG-IDH-WT/H3-WT, n=196). Statistical analysis was performed using one-way ANOVA with Tukey's multiple comparisons test (*P < 0.05, **P < 0.01, ***P < 0.001, ****P < 0.0001).

3.2.1.2 Increase in the expression of mitochondrial complex II nuclear DNA encoded structural genes

The mitochondrial complex II, also referred to as succinate dehydrogenase or succinate-ubiquinone oxidoreductase, is the second and relatively smaller component of the mitochondrial respiratory chain (199). It comprises of a total of 4 nuclear DNA encoded subunits only (**Table 3.1**). The complex II plays essential role in oxidising succinate to fumarate in the TCA cycle. The electrons generated here reduce the flavin adenine nucleotide (FAD) to $FADH_2$, and finally reduce ubiquinone to ubiquinol (199). Our analysis of the mRNA expression of all the complex II subunit genes revealed a significant upregulation of *sdhc* in tissues of DIPG/DMG patients compared to healthy tissues, whereas *sdhd* was only found to be upregulated in DMG patients compared to healthy tissues (**Figure 3.2**). The mRNA expression of *sdhc* was also significantly upregulated in other the brain tumour categories – EPEN, GBM and HGG-IDH-WT/H3-WT whereas the *sdhd* expression was only significantly upregulated in GBM compared to healthy tissues (**Figure 3.2**). The expression patterns of these genes are also summarised as a heatmap in **Figure 3.7**, illustrating differences between tumour and normal tissues.

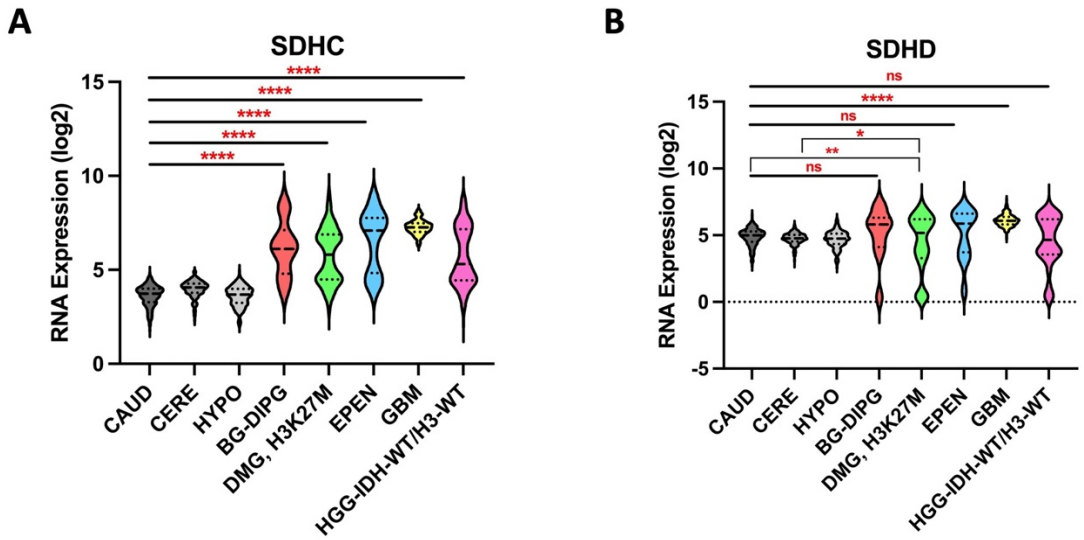

Figure 3.2. mRNA levels of 2 nuclear DNA encoded structural genes of mitochondrial complex II upregulated in DIPG/DMG clinical samples.
There are three categories of normal brain tissue samples - caudate (CAUD, n=246), cerebellum (CERE, n=456), hypothalamus (HYPO, n=202) and five categories of brain tumour clinical samples - brainstem glioma (BS) DIPG (n=10), DMG H3K27M (n=220), ependymoma (EPEN, n=60), glioblastoma (GBM, n=167), and high-grade gliomas IDH-wildtype and H3-wildtype (HGG-IDH-WT/H3-WT, n=196). Statistical analysis was performed using one-way ANOVA with Tukey's multiple comparisons test (**P < 0.01, ****P < 0.0001).

3.2.1.3 Increase in the expression of mitochondrial complex III nuclear DNA encoded structural genes

The mitochondrial complex III, also referred to as cytochrome bc_1 complex or ubiquinol-cytochrome c oxidoreductase, is the third and the central component of the mitochondrial respiratory chain. It functions to transfer electrons from ubiquinone to the cytochrome c in the complex IV, establishing a proton gradient and resulting in pumping of protons into the intermembrane space (200). It comprises of a total of 11 subunits, 10 of which are nuclear DNA encoded subunits and 1 is mitochondrial DNA encoded subunit (**Table 3.1**). We found a significant increase in the mRNA expression of two nuclear DNA encoded subunit genes of the complex III (*uqcrh* and *uqcrb*) in tissues of both DIPG/DMG patients compared to healthy tissues, suggesting an upregulation of these genes (**Figure 3.3**). Another gene *uqcrq* was only upregulated in DMG patients (**Figure 3.3**). The mRNA expression of *uqcrh* was also significantly upregulated in all other brain tumour categories, *uqcrq* only appeared to be upregulated in EPEN and GBM, and *uqcrb* was upregulated in EPEN and HGG-IDH-WT/H3-WT compared to healthy tissues (**Figure 3.3**). The expression patterns of these genes are also summarised as a heatmap in **Figure 3.7**, illustrating differences between tumour and normal tissues.

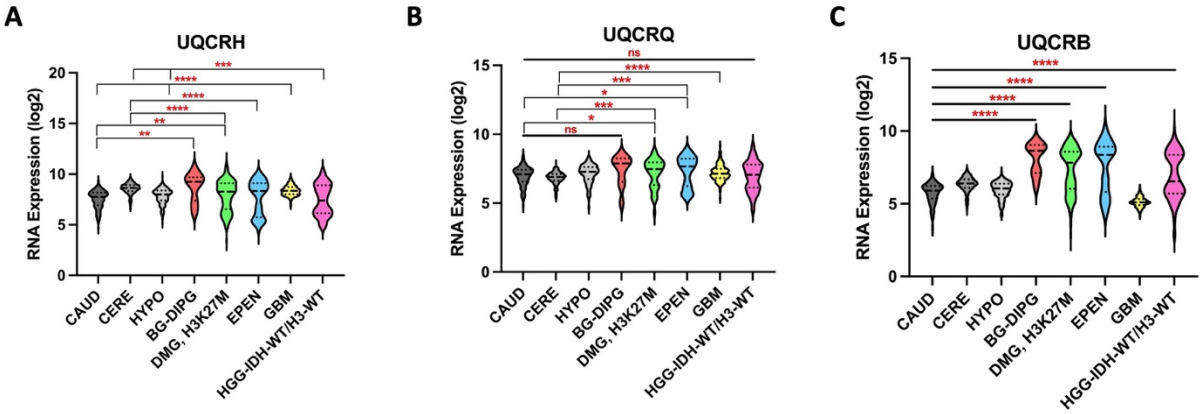

Figure 3.3. mRNA levels of 3 nuclear DNA encoded structural genes of mitochondrial complex III upregulated in DIPG/DMG clinical samples.
There are three categories of normal brain tissue samples - caudate (CAUD, n=246), cerebellum (CERE, n=456), hypothalamus (HYPO, n=202) and five categories of brain tumour clinical samples - brainstem glioma (BS) DIPG (n=10), DMG H3K27M (n=220), ependymoma (EPEN, n=60), glioblastoma (GBM, n=167), and high-grade gliomas IDH-wildtype and H3-wildtype (HGG-IDH-WT/H3-WT, n=196). Statistical analysis was performed using one-way ANOVA with Tukey's multiple comparisons test (*P < 0.05, **P < 0.01, ***P < 0.001, ****P < 0.0001).

3.2.1.4 Increase in the expression of mitochondrial complex IV nuclear DNA encoded structural genes

The mitochondrial complex IV, also referred to as cytochrome c oxidase, is the fourth and the terminal enzyme in the mitochondrial respiratory chain. Electrons from cytochrome c are transferred to the complex IV which then functions to reduce oxygen to water (201). This results in pumping of two protons into the intermembrane space, thus establishing a proton gradient (201). The complex IV comprises of a total of 19 subunits, 16 of which are nuclear DNA encoded subunits and 3 are mitochondrial DNA encoded subunits (**Table 3.1**). The mRNA expression of all the complex IV subunit genes suggest a significant upregulation of 7 of the nuclear DNA encoded subunit genes in tissues of DIPG/DMG patients compared to healthy tissues (**Figure 3.4**). These genes are *cox4i1, cox6a1, cox6b1, cox6c, cox7a2, cox7b* and *cox7c*. Most of these genes were also significantly upregulated in other brain tumour categories – EPEN, GBM and HGG-IDH-WT/H3-WT compared to healthy tissues (**Figure 3.4**). The expression patterns of these genes are also summarised as a heatmap in **Figure 3.7**, illustrating differences between tumour and normal tissues.

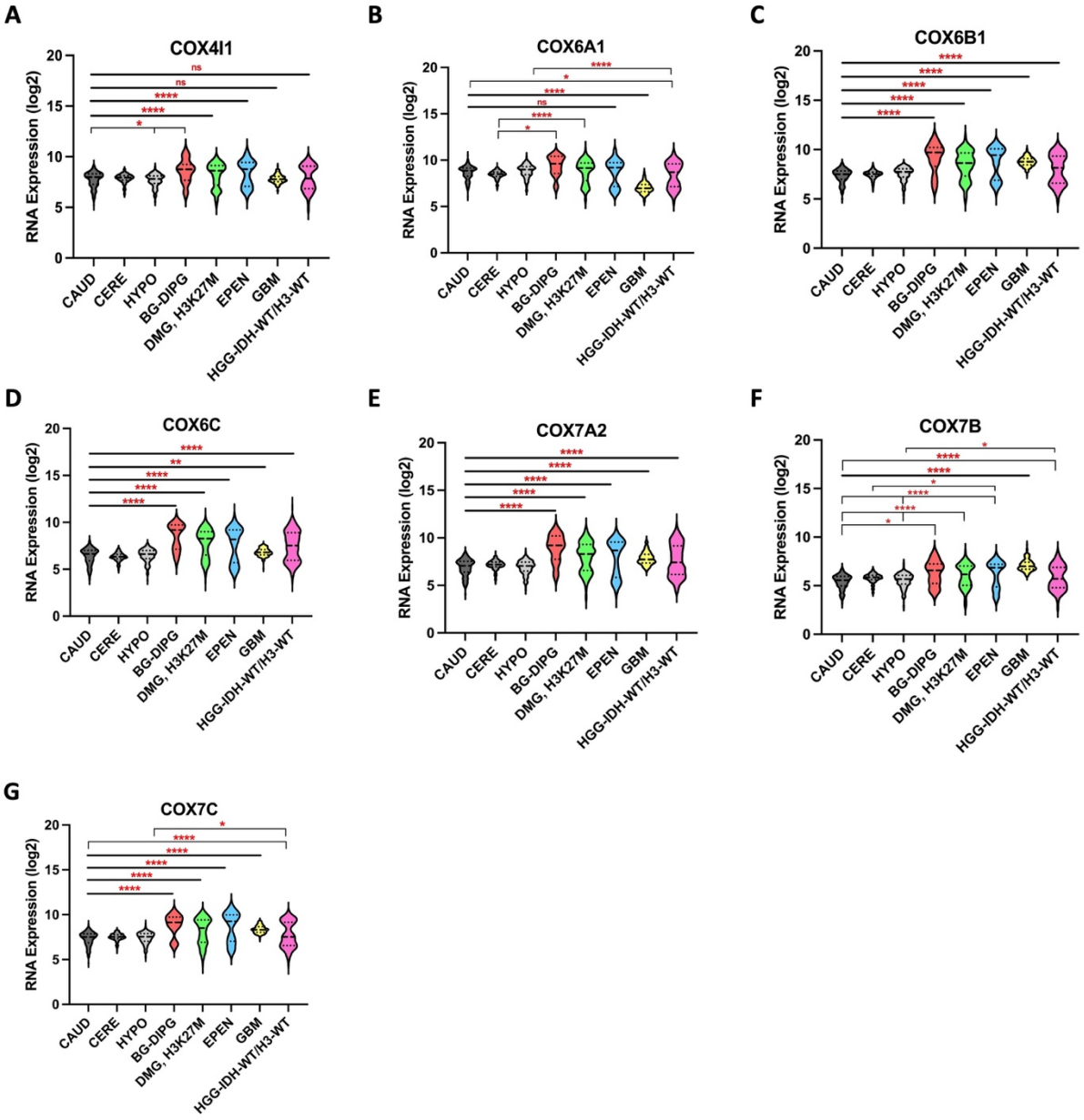

Figure 3.4. mRNA levels of 7 nuclear DNA encoded structural genes of mitochondrial complex IV upregulated in DIPG/DMG clinical samples.

There are three categories of normal brain tissue samples - caudate (CAUD, n=246), cerebellum (CERE, n=456), hypothalamus (HYPO, n=202) and five categories of brain tumour clinical samples - brainstem glioma (BS) DIPG (n=10), DMG H3K27M (n=220), ependymoma (EPEN, n=60), glioblastoma (GBM, n=167), and high-grade gliomas IDH-wildtype and H3-wildtype (HGG-IDH-WT/H3-WT, n=196). Statistical analysis was performed using one-way ANOVA with Tukey's multiple comparisons test (*P < 0.05, **P < 0.01, ***P < 0.001, ****P < 0.0001).

3.2.1.5 Increase in the expression of mitochondrial complex V nuclear DNA encoded structural genes

The mitochondrial complex V, also referred to as the F_1/F_0 ATP synthase is the last multi-subunit complex in the mitochondrial respiratory chain. This complex phosphorylates ADP to synthesize ATP using the energy generated by the electrochemical proton gradient (202). The complex V comprises of a total of 20 subunits, 18 of which are nuclear DNA encoded subunits and 2 are mitochondrial DNA encoded subunits (**Table 3.1**). We found a significant upregulation of 7 nuclear DNA encoded subunit genes of the complex V in tissues of DIPG/DMG patients compared to healthy tissues (**Figure 3.5**). These genes are *atp5f1a, atp5mc2, atp5mc3, atp5me, atp5mf, atpfmg* and *atp5pb*. The mRNA expression of all these genes was also significantly upregulated in other brain tumour categories – EPEN and HGG-IDH-WT/H3-WT compared to healthy tissues (**Figure 3.5**). Five of these genes *atp5f1a, atp5mc2, atp5mc3, atp5mf* and *atp5pb* were also significantly upregulated in GBM patient samples compared to healthy tissues (**Figure 3.5**). The expression patterns of these genes are also summarised as a heatmap in **Figure 3.7**, illustrating differences between tumour and normal tissues.

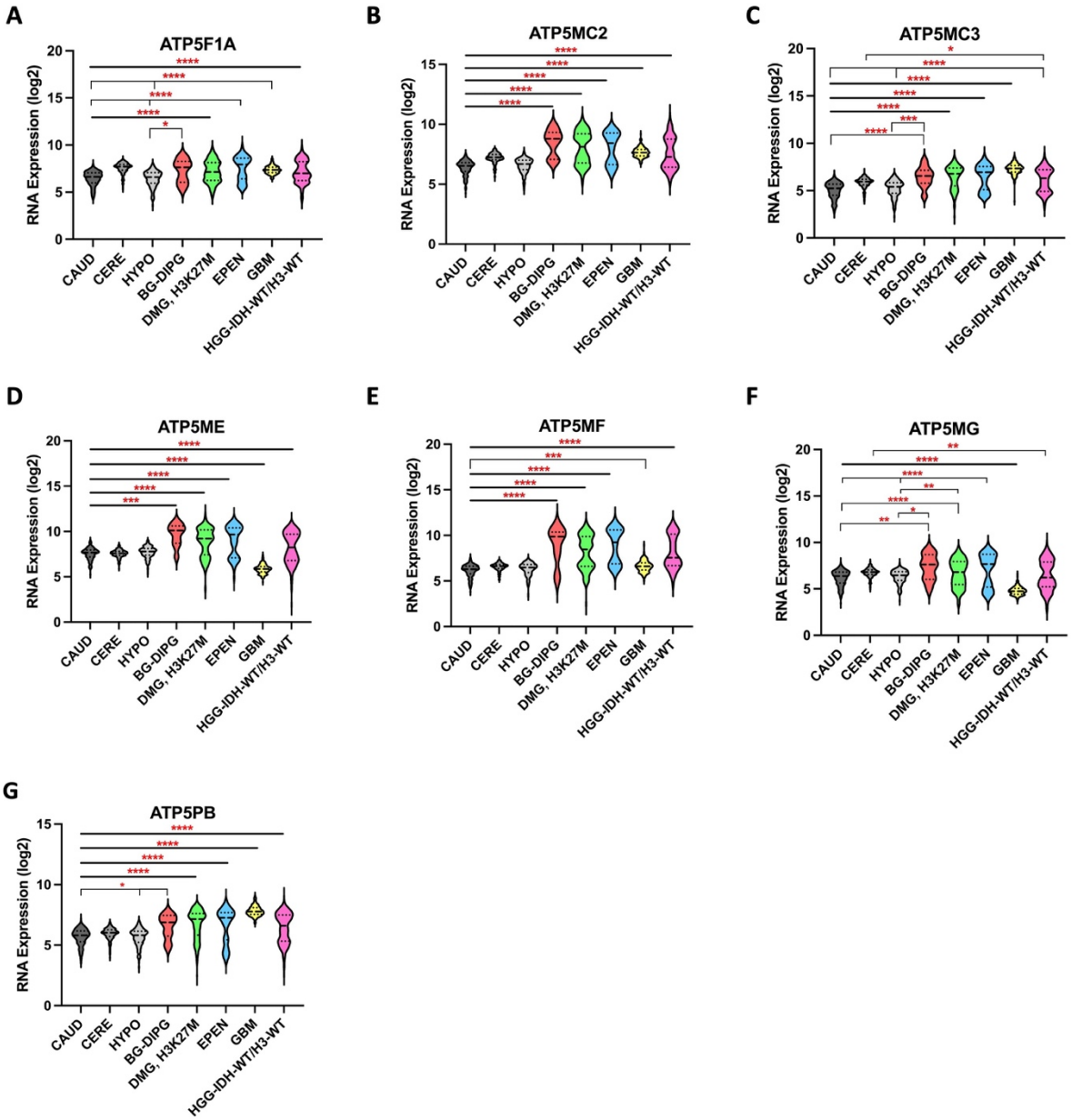

Figure 3.5. mRNA levels of 7 nuclear DNA encoded structural genes of mitochondrial complex V upregulated in DIPG/DMG clinical samples.

There are three categories of normal brain tissue samples - caudate (CAUD, n=246), cerebellum (CERE, n=456), hypothalamus (HYPO, n=202) and five categories of brain tumour clinical samples - brainstem glioma (BS) DIPG (n=10), DMG H3K27M (n=220), ependymoma (EPEN, n=60), glioblastoma (GBM, n=167), and high-grade gliomas IDH-wildtype and H3-wildtype (HGG-IDH-WT/H3-WT, n=196). Statistical analysis was performed using one-way ANOVA with Tukey's multiple comparisons test (*P < 0.05, **P < 0.01, ***P < 0.001, ****P < 0.0001).

3.2.1.6 Changes in the expression of mitochondrial DNA encoded structural genes of all the complexes

Table 3.1 shows that there are a total of 13 mitochondrial DNA encoded subunit genes of the ETC complexes. We also assessed the mRNA expression of all these genes in healthy tissues, DIPG/DMG patient samples and other brain tumour categories. We were unable to locate the overall mRNA expression of the complex III subunit gene (*mtcyb*) and complexes V subunit genes (*mtatp6* and *mtatp8*) in the public dataset. However, we found that the mRNA expression of all these mitochondrial DNA encoded subunit genes were significantly lower in DIPG/DMG patient samples compared to healthy tissues (**Figure 3.6**). Similarly, the mRNA expression of these mitochondrial DNA encoded subunit genes was also significantly lower in EPEN, GBM and HGG-IDH-WT/H3-WT patient samples compared to healthy tissues (**Figure 3.6**). The expression patterns of these genes are also summarised as a heatmap in **Figure 3.7**, illustrating differences between tumour and normal tissues.

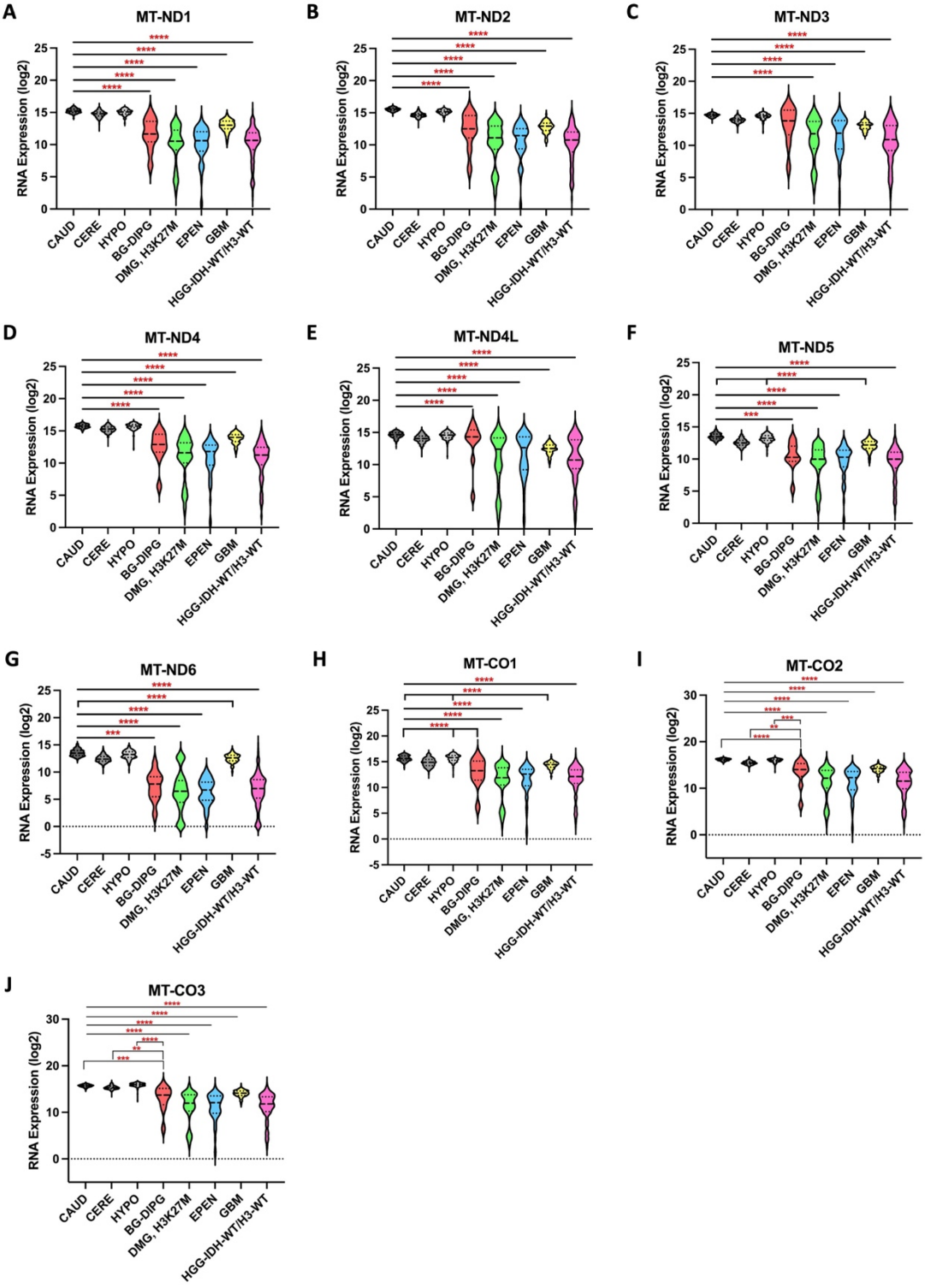

Figure 3.6. mRNA levels of 10 mitochondrial DNA encoded structural genes of complexes I and IV in clinical samples.

There are three categories of normal brain tissue samples - caudate (CAUD, n=246), cerebellum (CERE, n=456), hypothalamus (HYPO, n=202) and five categories of brain tumour clinical samples - brainstem glioma (BS) DIPG (n=10), DMG H3K27M (n=220), ependymoma (EPEN, n=60), glioblastoma (GBM, n=167), and high-grade gliomas IDH-wildtype and H3-wildtype (HGG-IDH-WT/H3-WT, n=196). Statistical analysis was performed using one-way ANOVA with Tukey's multiple comparisons test (**P < 0.01, ***P < 0.001, ****P < 0.0001).

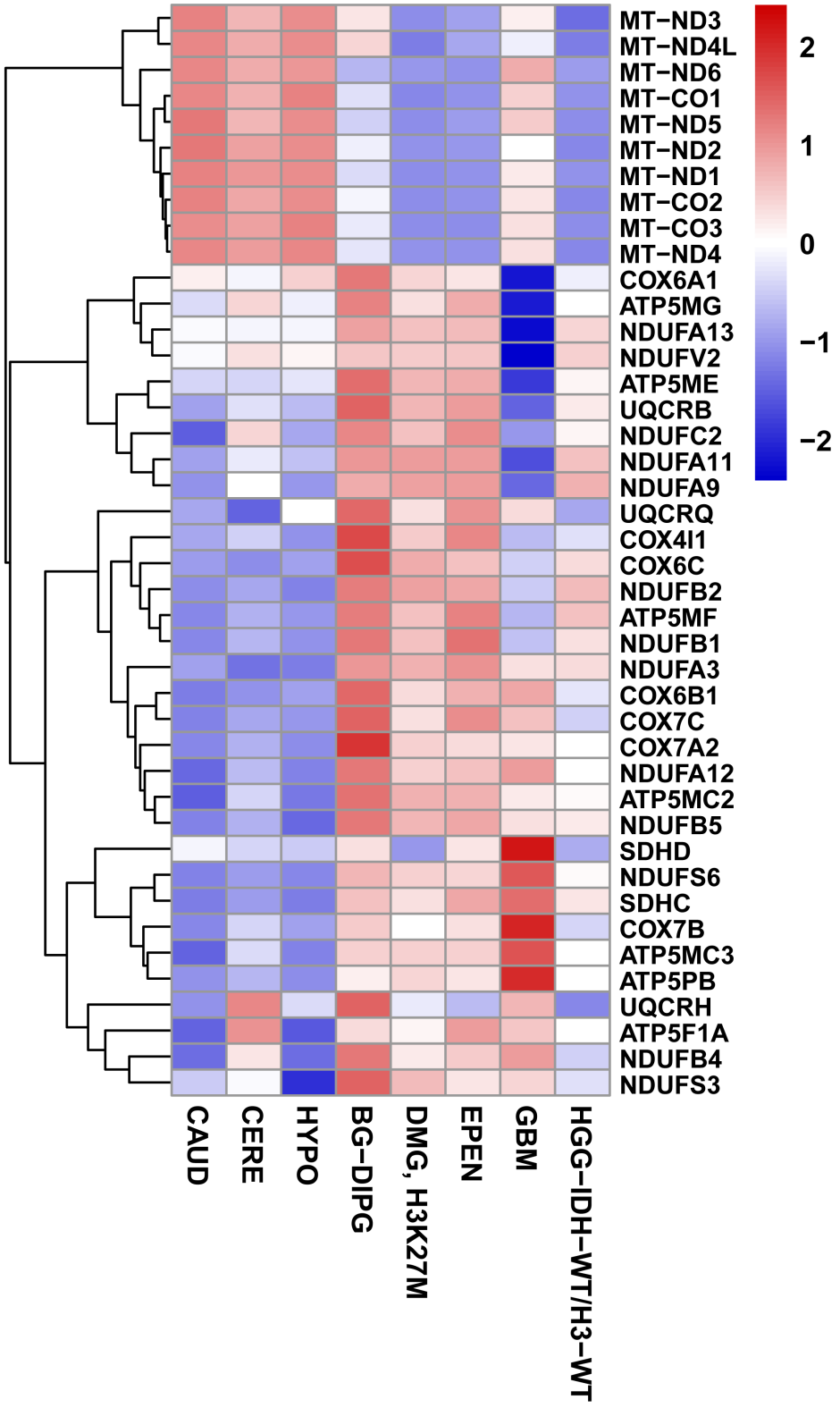

Figure 3.7. Heatmap of mitochondrial gene expression in brain tumours and control samples.
Mean logCPM values of mitochondrial genes across tumour subtypes (BS-DIPG, DMG-H3K27M, GBM, EPEN, HGG-IDH-WT/H3-WT) and control tissues (caudate, cerebellum and hypothalamus). Expression values were normalised and are represented on a colour scale ranging from −2 (low expression, blue) to +2 (high expression, red).

3.2.2 Oxidative phosphorylation inhibition screening with anti-parasitic drugs against DIPG cell lines

With the increased expression of several mitochondrial complexes structural genes suggesting increased OXPHOS in DIPG/DMGs, we now performed an OXPHOS inhibition screening using ivermectin, mefloquine, atovaquone, proguanil and quinacrine. All the drugs were assayed at 10 µM and OCR inhibition was assessed using two DIPG cell lines – HSJD-DIPG-007 and SU-DIPG-XVII (**Figure 3.8**). Ivermectin, mefloquine, atovaquone and quinacrine significantly reduced the OCR of HSJD-DIPG-007 cells relative to DMSO control reaching 37.9%, 56%, 2.5%, and 66.9% respectively (*P < 0.05, **P < 0.01, ***P < 0.001, ****P < 0.0001; **Figure 3.8A**). Similarly, all of the four drugs ivermectin, mefloquine, atovaquone and quinacrine also significantly reduced the OCR of SU-DIPG-XVII cells relative to DMSO control reaching 14.7%, 66.5%, 7.5%, and 64.8% respectively (***P < 0.001, ****P < 0.0001; **Figure 3.8B**). Proguanil at 10 µM did not have a significant effect on the OCR of both the DIPG cell lines (**Figure 3.8A-B**).

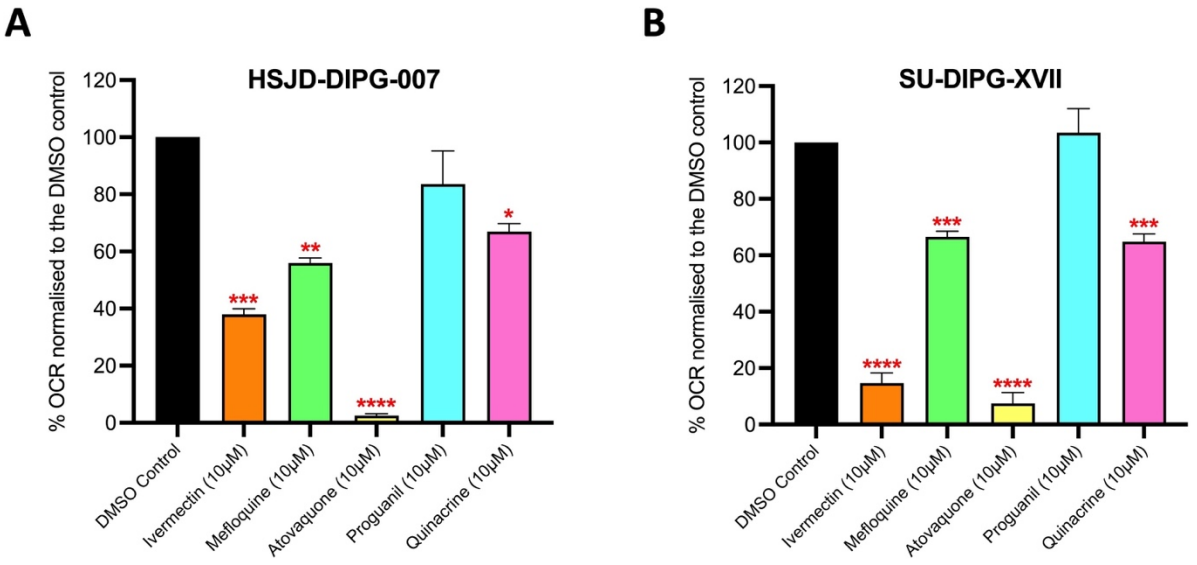

Figure 3.8. OXPHOS inhibition screening using five anti-parasitic drugs (ivermectin, mefloquine, atovaquone, proguanil and quinacrine).
(A-B) HSJD-DIPG-007 and SU-DIPG-XVII were treated with the five drugs at 10 µM or DMSO control and OCR was measured in real-time using Seahorse XFe24 Analyser over a period of 4 hours. Data is normalised to DMSO control. Statistical analysis was performed using one-way ANOVA with Tukey's multiple comparisons test, data is presented relative to DMSO control (*P < 0.05, **P < 0.01, ***P < 0.001, ****P < 0.0001). Data are presented as means ± SD of two independent experiments with three replicates in each.

3.3. Discussion

The expression of mitochondrial ETC complex genes have not been extensively studied in DIPG previously. Here, we have demonstrated increased expression of several mitochondrial ETC complex structural genes in DIPG/DMG clinical samples compared to normal brain tissue samples. This suggests that there could be increased OXPHOS dependency in DIPG/DMG which could also be contributing to tumorigenesis in this tumour.

The mitochondrial OXPHOS is controlled by two distinct genomes, the nuclear genome and the mitochondrial genome (203). Interestingly, our results suggest that only the genes encoded by nuclear genome appeared to be upregulated in DIPG/DMG and other brain tumours with increased expression seen in these only. Whereas, all the genes encoded by mitochondrial genome of all complexes appeared to have lower expression in DIPG/DMG samples and most of the brain tumour categories compared to healthy tissues. It is reported in the literature that in some conditions there exists a positive interaction between both nuclear and mitochondrial genes whereas in other instances mutations or decrease in mitochondrial genes are linked to high induction of nuclear genes (203, 204). This increase is to compensate for the OXPHOS defects and to stimulate mitochondrial biogenesis (204). Therefore, the above mentioned suggests that there could be real differences in the nuclear and mitochondrial DNA encoded genes in patient samples.

Mutations in the complex I subunit genes have been associated with a range of mitochondrial hereditary disorders (reviewed in (205)). These mutations compromise the functionality of the complex I and negatively impact OXPHOS (205). This suggests that an increase in the expression of the complex I genes would therefore increase the activity of the complex and stimulate the pumping of protons across the membrane. Mutations or loss of function of complex II-related genes increase the risks towards certain tumour types and cause poor OXPHOS (206). Increased expression of some of the complex II genes would therefore increase the activity and functionality of the complex. Furthermore, mutations in complexes III and IV result in defects in OXPHOS and have also been associated with several human pathologies (207). Finally, complex V deficiency or mutations can have severe developmental impact and impair respiratory function (202). This indicates that increased expression of the genes encoding complexes III-V would also increase the activity of these complexes and

upregulate OXPHOS. Our overall findings highlight that there is significant upregulation of a total of 32 nuclear DNA encoded subunit genes in DIPG/DMG providing promising evidence and support towards the hypothesis of upregulated OXPHOS in DIPG. Additionally, the violin plots presented in **Figures 3.1-3.7** depict an interesting pattern as there is a spread in the distribution of data points. This suggests that there is a diversity in patients with varied expression, with majority having higher expression of these genes and some also exhibiting lower expression of these genes. This means that careful patient selection will be needed when targeting OXPHOS in these patients to maximise benefit and prevent unnecessary toxicities. Moreover, developing sensitive biomarkers will be useful in selecting patients for OXPHOS inhibition (208).

With the observed upregulated OXPHOS in cancers, there has been an increasing interest in the development of OXPHOS inhibitors. Several past studies have investigated the theory of the inhibition of mitochondrial OXPHOS as a strategy reduce tumour hypoxia in cancers (100, 103, 104). However, this has not been explored in the area of DIPG. Various OXPHOS inhibitors have also been trialled for this purpose however, none has advanced to end stage clinical practice (208). Our drug screening against DIPG involved investigating the FDA-approved anti-parasitic drugs, all of which have been clinically used on adults and children for years. We found atovaquone, a drug used for the treatment of pneumocystis pneumonia and malaria, as the most potent OCR inhibitor across both the DIPG cultures. Atovaquone was then picked for further investigations against DIPG. We investigated the efficacy of atovaquone against DIPG and this is further discussed in **Chapter 4**. The second best OCR inhibitor from our screening was ivermectin however its limited BBB penetration prevented us from further investigations on this drug. Mefloquine was the third best candidate with excellent BBB penetration and we also investigated its efficacy against DIPG and is further addressed in **Chapter 5**. Quinacrine appeared to decrease OCR at comparable levels to mefloquine and is another candidate for future studies to explore.

Overall, the findings in this chapter strengthen our study hypothesis that targeting OXPHOS is a therapeutic strategy to radiosensitize DIPG. The observed upregulated mitochondrial ETC complexes genes in DIPG/DMG support upregulated OXPHOS in DIPG. Evidence to support the presence of hypoxia in DIPG is demonstrated in **Chapter 6**. Finally, our OXPHOS inhibition screening identified atovaquone and mefloquine as potent OCR inhibitors of DIPG

cells and their hypoxia modification and radiosensitisation will be further investigated in the next chapters.

Chapter 4

Atovaquone – A Potential Radiosensitiser for Diffuse Intrinsic Pontine Glioma

Chapter 4. Atovaquone – A Potential Radiosensitiser for Diffuse Intrinsic Pontine Glioma

4.1. Introduction

The previous chapter demonstrated increased expression of mitochondrial complexes genes in DIPG/DMG tumour samples compared to non-tumour brain tissue samples. An increase in mitochondrial complexes gene expression correlates with increased OXPHOS activity *in vivo* (208), thus suggesting that DIPGs may also be reliant on OXPHOS as a metabolic pathway for tumour progression. Inhibiting OXPHOS has been shown to reduce tumour hypoxia and improve the radiosensitivity of some tumour models (100, 103, 104). We therefore aimed to target OXPHOS and performed an anti-parasitic drug screening that identified atovaquone as the most potent OCR inhibitor of all tested DIPG cultures. This chapter will investigate atovaquone as a hypoxia modifier and radiosensitiser of DIPG *in vitro*.

Atovaquone, an FDA-approved anti-parasitic drug, is used for the treatment and prevention of PCP, caused by the fungus *Pneumocystis Jiroveci)*, the HIV infection – Toxoplasma encephalitis, and can prevent babesiosis in conjunction with the antibiotic azithromycin (106). Atovaquone is a ubiquinone analogue and a competitive inhibitor of ubiquinol, specifically inhibiting the mitochondrial ETC at ubiquinol oxidation (Q_o) site in the complex III in parasites (106). This prevents transport of electrons across the ETC, leading to sustained depolarisation of MMP and disruption of key mitochondrial ETC enzymes, thus compromising the parasites mitochondrial function and survival (106).

Atovaquone has been shown to reduce OCR and induce mitochondrial dysfunction in a range of cancer types including breast cancer (136), cervical cancer (137), renal cell carcinoma (138), retinoblastoma (134), hypopharyngeal carcinoma (103), colorectal carcinoma (103), thyroid cancer (141), lung cancer (103), ovarian cancer (135), and B-cell acute lymphoblastic leukaemia (139). It was found to decrease hypoxia in hypopharyngeal carcinoma, colorectal carcinoma and lung carcinoma spheroids (103). It also reduced hypoxia in hypopharyngeal carcinoma xenograft model and significantly improved the survival of these mice in combination with radiation, thus suggesting its promising radiosensitising efficacy (103). A recent clinical study has also validated the hypoxia modification efficacy of atovaquone

(NCT02628080), resulting in another ongoing trial assessing atovaquone and chemoradiotherapy combination in NSCLC patients (NCT04648033).

The radiosensitising efficacy of atovaquone has not been investigated in brain tumours including DIPG possibly due to limited BBB penetration. To overcome this issue, an ASD formulation of atovaquone has been developed (123). ASD atovaquone formulation has not be tested against brain tumours, however it has been shown to improve the oral bioavailability of atovaquone to help achieve therapeutically effective brain levels of atovaquone (123). Further investigation of ASD atovaquone formulation is required to assess its efficacy against DIPG.

Currently, atovaquone in combination with the biguanide (complex I inhibitors) proguanil is approved for the prophylaxis and treatment of uncomplicated *P. falciparum* malaria in adults and children (109). Clinical studies have validated the synergism between atovaquone and proguanil. However, the exact molecular basis behind the synergistic effects are not completely understood (209). Literature suggests that atovaquone impairs the mitochondrial complex III and proguanil appears to enhance this destabilisation effect, thus collapsing mitochondrial integrity and parasite survival (148). Therefore, it will be interesting to explore the synergistic combination of atovaquone/proguanil compared to atovaquone alone against the DIPG cultures.

In this chapter, mitochondrial inhibition, hypoxia inhibition and radiosensitising efficacy of atovaquone are assessed in a range of DIPG cell lines. The efficacy of commercially available atovaquone is then compared against the ASD atovaquone formulation. The efficacy of atovaquone alone is also compared against the combination of atovaquone/proguanil and also with other biguanides (phenformin and metformin). A range of experimental techniques including MTS cell proliferation assays, extracellular flux assays, western blots, 3D neurosphere assays for hypoxia, flow cytometry and clonogenic assays were used to test our findings.

4.2. Results

4.2.1 Atovaquone treatment inhibits mitochondrial metabolism of DIPG cells by targeting the mitochondrial complex III

As atovaquone is reported to reduce the OCR of a range of cancer types, we assessed its OCR inhibition efficacy against 3 representative DIPG cell lines. HSJD-DIPG-007, SU-DIPG-VI and SU-DIPG-XVII were treated with 2.5-30 μM atovaquone for 1 hour and the OCR and ECAR were analysed using a XFe24 Seahorse Analyser. Atovaquone significantly inhibited the OCR of all the DIPG cells lines at 5-30 μM (*P < 0.05, ***P < 0.001, ****P < 0.0001; **Figure 4.1A-C**), whereas the ECAR was not significantly varied compared to DMSO control (**Figure 4.1D-F**).

We then examined the effect of atovaquone on the overall mitochondrial profile of DIPG cells. As a potent OCR inhibitor, atovaquone (10-30 μM) treatment for 4 hours was found to completely shut down the mitochondrial bioenergetics of HSJD-DIPG-007, SU-DIPG-VI and SU-DIPG-XVII cell lines, evidenced by a significant decrease in key mitochondrial parameters - maximal respiration, ATP production, spare respiratory capacity and proton leak compared to control (**P < 0.01, ***P < 0.001, ****P < 0.0001; **Figure 4.2A-L**).

As a ubiquinone analogue and a competitive inhibitor of ubiquinol, atovaquone induces parasite cell death by inhibiting the ubiquinol oxidation (Q_o) site in the mitochondrial complex III of the parasite mitochondrion (116). Atovaquone has also been shown to specifically inhibit the complex III in several cancer cell lines (103, 135, 137, 138). To validate the complex III specific inhibition of atovaquone in DIPG cultures, we assessed its effect on the activity of the electron transport chain complexes I-IV. The mitochondrial complexes inhibition assay requires permeabilization of mitochondrial plasma membrane. This is required to enable the permeability of non-membrane permeable substrates present in the assay medium to enter the mitochondria, allowing for the measurement of the activity of specific mitochondrial complex. First, we aimed to determine the optimal concentration of XF PMP sufficient to permeabilise the mitochondria of DIPG cells. We tested 0-5 nM XF PMP using HSJD-DIPG-007 cells and assessed the penetration of succinate (substrate for complex II) demonstrated by a rise in OCR at succinate/rotenone injection (injection 2, **Figure 4.3A**). All the tested XF PMP concentrations significantly increased succinate penetration with 2.5 nM and 5 nM providing the maximum penetration evidenced by the highest OCR achieved at these concentrations

(***P < 0.001, ****P < 0.0001; **Figure 4.3B**). Based on this finding, 3 nM XF PMP was picked as an optimal concentration for the subsequent experiments.

HSJD-DIPG-007 cells were then pre-treated with 30 μM atovaquone for 24 hours and cells permeabilised with 3 nM XF PMP. Atovaquone 30 μM was found to significantly inhibit the complex specific OCR for complex I, complex II and complex III, whereas the activity of complex IV was not impaired as seen by a significant decrease in OCR at complexes I-III compared to DMSO control (****P < 0.0001; **Figure 4.3C**). As the ETC is arranged in an order from complexes I, II, III and IV, inhibition of complex III also decreased the activity of the complexes below it i.e., complexes I and II. The complex IV is after the complex III and no change in the complex IV OCR indicates that atovaquone specifically inhibits the complex III of the DIPG cells.

The results above were confirmed by comparing atovaquone's activity against known complex III inhibitors myxothiazol and antimycin A. HSJD-DIPG-007 cells were pre-treated with 30 μM atovaquone for 24 hour and 2 μM myxothiazol and 2 μM Antimycin A for 1 hour. There was a similar significant decrease in the OCR of complex I, complex II and complex III from atovaquone, myxothiazol and Antimycin A whereas complex IV dependent OCR was not varied (****P < 0.0001; **Figure 4.3D**). These findings confirm that atovaquone inhibits the mitochondrial metabolism of DIPG cells by specifically targeting the mitochondrial complex III.

The metabolic changes from atovaquone were also investigated on normal human astrocytes – hTERT (hTERT IHA) as a control cell line to understand atovaquone's effects on the normal brain cells. Atovaquone 10 μM significantly reduced the OCR of hTERT IHA within 1 hour of treatment (****P < 0.0001; **Figure 4.4A-B**). A significant increase in the ECAR of hTERT IHA was also observed from 10 μM atovaquone treatment (**P < 0.01; **Figure 4.4C-D**).

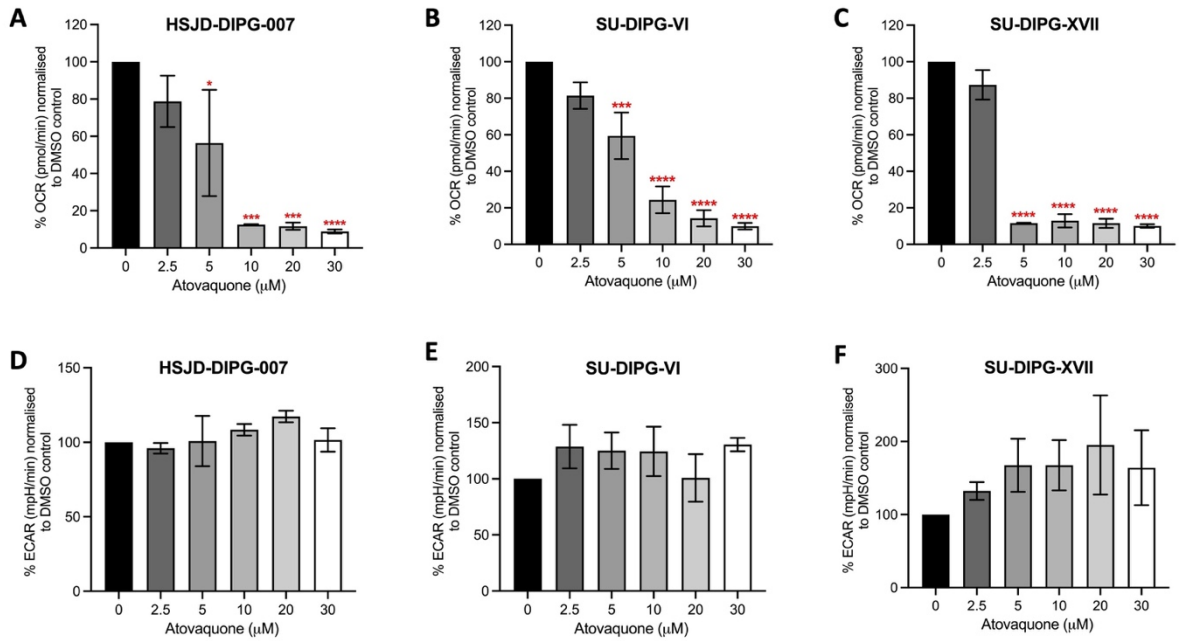

Figure 4.1. Metabolic changes in oxygen consumption rate (OCR) and extracellular acidification rate (ECAR) of DIPG cell lines following treatment with atovaquone.
HSJD-DIPG-007, SU-DIPG-VI and SU-DIPG-XVII were treated with atovaquone (2.5-30 μM) or DMSO control and OCR and ECAR were measured in real-time using Seahorse XFe24 Analyser over a period of 1 hour. Data is normalised to DMSO control (0 μM Atovaquone). Statistical analysis was performed using one-way ANOVA with Tukey's multiple comparisons test, data is presented relative to control (0 μM Atovaquone) (*P < 0.05, ***P < 0.001, ****P < 0.0001). Data are presented as means ± SD of two independent experiments with three replicates in each.

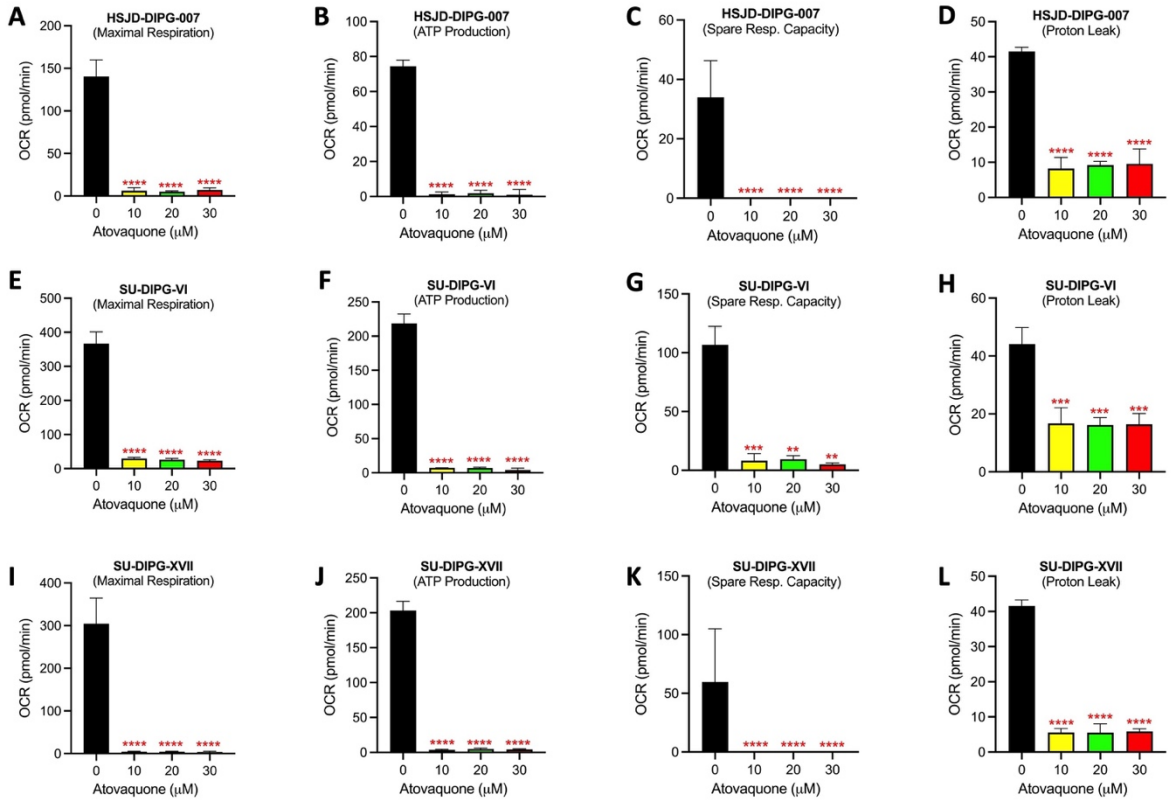

Figure 4.2. Quantification of mitochondrial function following atovaquone treatment.
HSJD-DIPG-007, SU-DIPG-VI and SU-DIPG-XVII were treated with atovaquone (10-30 μM) or DMSO control and several mitochondrial parameters - maximal respiration, ATP production, spare resp. capacity and proton leak were measured using Seahorse XF Cell Mito Stress Test Assay. Statistical analysis was performed using one-way ANOVA with Tukey's multiple comparisons test, data is presented relative to control (0 μM Atovaquone) (**P < 0.01, ***P < 0.001, ****P < 0.0001). Data are presented as means ± SD of two independent experiments with three replicates in each.

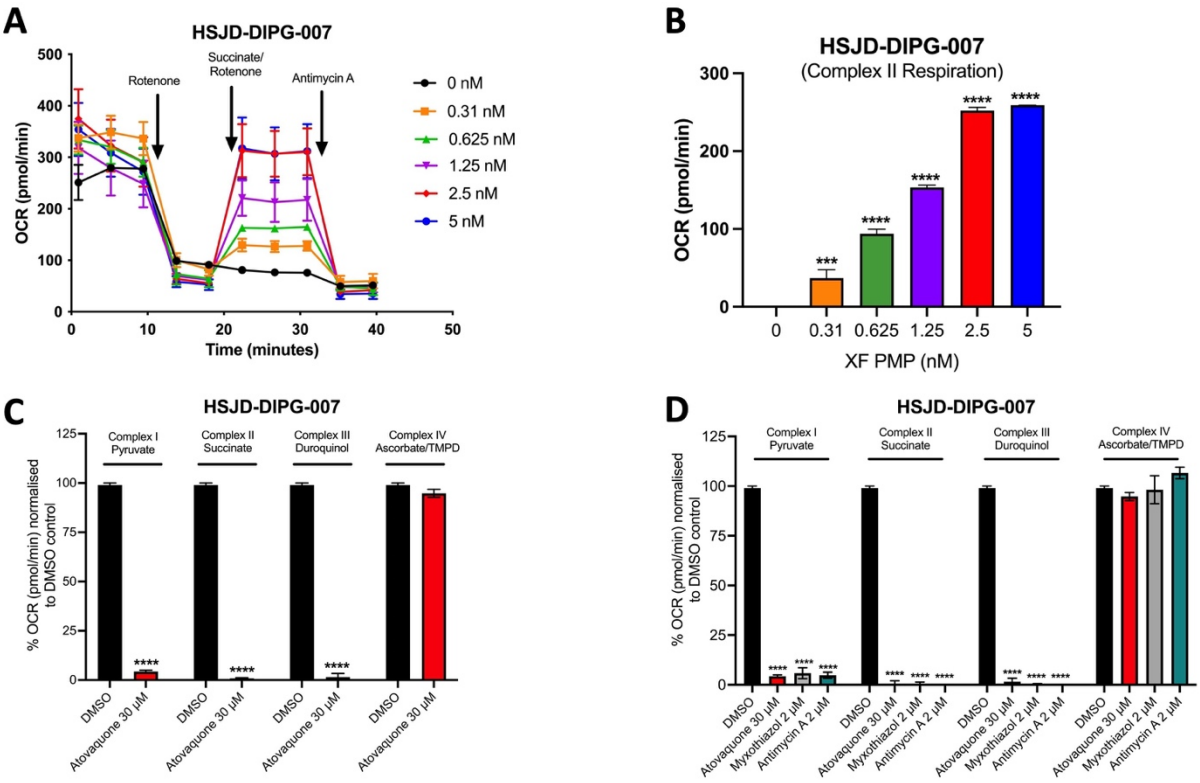

Figure 4.3. Real-time XF assay measuring mitochondrial complexes specific activity.
(A) XF PMP concentration optimisation (0-5 nM) using HSJD-DIPG-007 cells. (B) Oxygen consumption rate measuring complex II activity of HSJD-DIPG-007 cells at the range of XF PMP concentrations (0-5 nM). Complex II dependent OCR was calculated as follows – (OCR after succinate/rotenone injection – OCR at rotenone injection). (C-D) HSJD-DIPG-007 cells were pretreated with 30 µM atovaquone, 2 µM myxothiazol, 2 µM Antimycin A. Cells were permeabilised with 3 nM XF PMP and OCR was measured using XFe24 analyser. The changes in OCR in response to the different injections was used to determine complex specific activity. Details for calculating complex specific OCR are outlined in the methods chapter. Statistical analysis was performed using one-way ANOVA with Tukey's multiple comparisons test, data is presented relative to control (***P < 0.001, ****P < 0.0001). Data are presented as means ± SD of two independent experiments with three replicates in each.

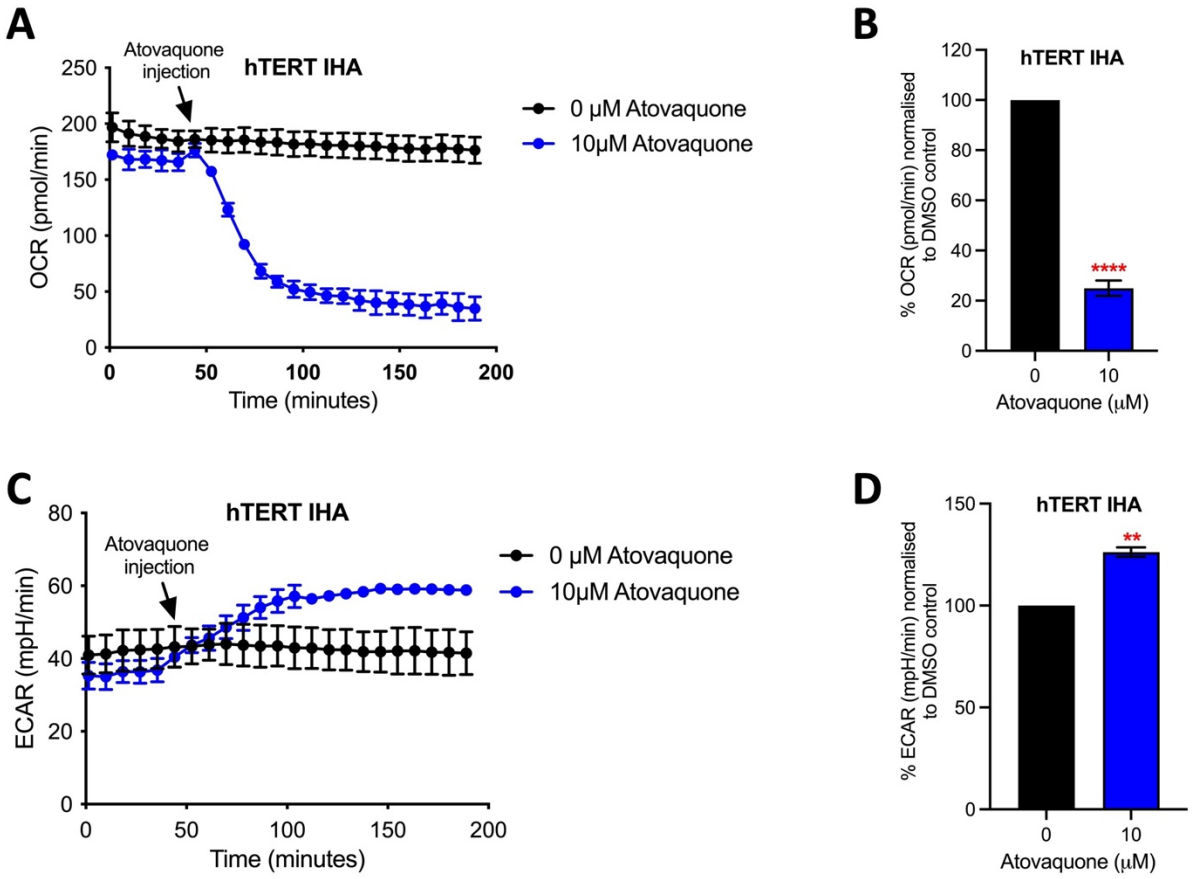

Figure 4.4. Metabolic changes in oxygen consumption rate (OCR) and extracellular acidification rate (ECAR) of hTERT IHA following treatment with atovaquone.
Cells were treated with atovaquone 10 µM or DMSO control and OCR and ECAR were measured in real-time using Seahorse XFe24 Analyser over a period of 4 hour. Data is normalised to DMSO control (0 µM Atovaquone). Statistical analysis was performed using t-tests for treated samples compared to untreated samples, data is presented relative to control (0 µM Atovaquone) (**P < 0.01, ****P < 0.0001). Data are presented as means ± SD of two independent experiments with three replicates in each.

4.2.2 Effect of atovaquone treatment on the viability of DIPG cells

The effect of atovaquone on the viability of DIPG cells (HSJD-DIPG-007, SU-DIPG-XVII, SU-DIPG-13P*, SU-DIPG-VI) and hTERT IHA was assessed using MTS assays. We used the highest dose of atovaquone investigated in this study (30 μM) and treated the cells for 24 and 72 hours. Treatment with 30 μM atovaquone for 24 hours did not significantly affect the viability of either DIPG cells or hTERT IHA (**Fig 4.5A**). However, treatment with 30 μM atovaquone for 72 hours significantly decreased the viability of DIPG cell lines HSJD-DIPG-007 (48.5%), SU-DIPG-XVII (35.3%), SU-DIPG-13P* (35.0%) compared to hTERT IHA (81.1%) (****P < 0.0001; **Figure 4.5B**). Interestingly, 72 hour treatment with atovaquone only decreased the viability of SU-DIPG-VI by 20% compared to control (**Figure 4.5B**).

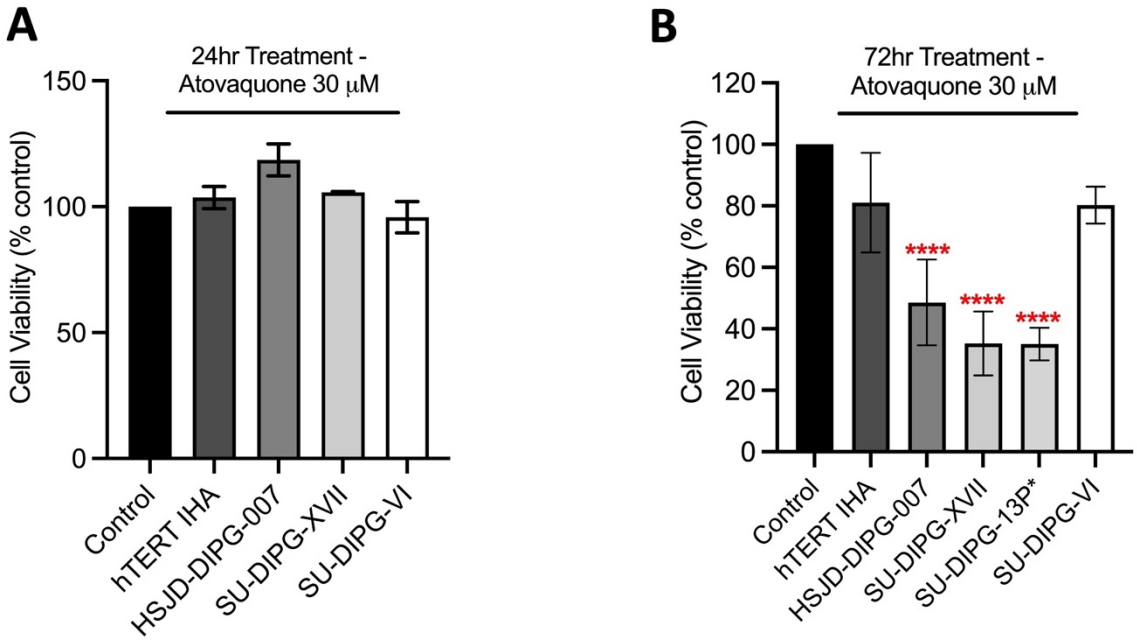

Figure 4.5. In vitro effect of atovaquone on the cell viability of DIPG cells and hTERT IHA.
Cells were treated with 30 μM atovaquone for 24 and 72 hr and cell viability assessed using MTS cell proliferation assay. Data represents mean cell viability following atovaquone treatment of three independent experiments with three replicates in each. Error bars indicate SD; n=3. Statistical analysis was performed using one-way ANOVA with Tukey's multiple comparisons test, data is presented relative to control (****P < 0.0001).

4.2.3 Atovaquone treatment increases reactive oxygen species mediated oxidative stress in DIPG cells

Inhibition of mitochondrial activity is a major source of mitochondrial and cellular reactive oxygen species (ROS) production (210). Specifically, mutations in the complex III (cytochrome bc_1 complex) have resulted in increased ROS production in cancer cells (211). To assess atovaquone's effect on ROS generation, HSJD-DIPG-007 and SU-DIPG-XVII were treated with 10-30 μM atovaquone for 1 hr and MitoSOX Red and DHE dyes were used as specific indicators for mitochondrial and cellular ROS. As expected, there was a significant dose dependent increase in MitoSOX Red and DHE fluorescence in both HSJD-DIPG-007 and SU-DIPG-XVII cell lines (**Figure 4.6A-D**). The mean MitoSOX Red fluorescence was 2.34- and 3.34-fold higher with 20 μM and 30 μM atovaquone compared to control in HSJD-DIPG-007 (**P < 0.01, ***P<0.001; **Figure 4.6A**). The mean MitoSOX Red fluorescence was 2.00- and 3.70-fold higher with 20 μM and 30 μM atovaquone compared to control in SU-DIPG-XVII (**P < 0.01, ****P<0.0001; **Figure 4.6B**). The mean DHE fluorescence was 1.71- and 2.41-fold higher with 20 μM and 30 μM atovaquone compared to control in HSJD-DIPG-007 (***P<0.001; **Figure 4.6C**). The mean DHE fluorescence was 3.61- and 3.69-fold higher with 20 μM and 30 μM atovaquone compared to control in SU-DIPG-XVII (***P<0.001; **Figure 4.6D**).

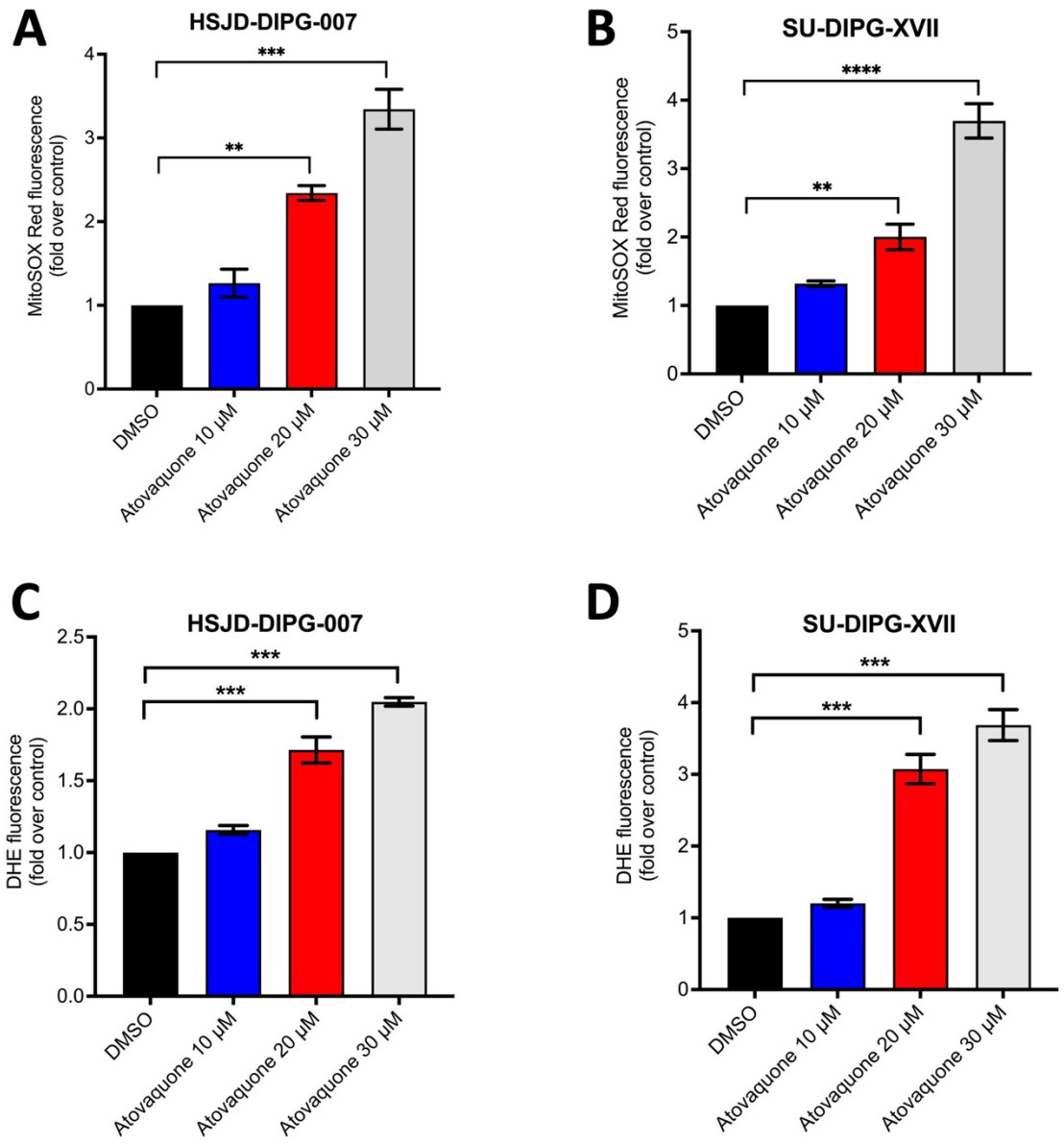

Figure 4.6. Reactive oxygen species production in DIPG cells in response to atovaquone treatment.
HSJD-DIPG-007 and SU-DIPG-XVII were treated with 10-30 µM atovaquone for 1 hour. Cells were then stained with MitoSOX Red and dihydroethidium (DHE) dyes for 30 mins, washed and analysed with flow cytometry. (A-B) Mean MitoSOX Red fluorescence. (C-D) Mean DHE fluorescence. Statistical analysis was performed using one-way ANOVA with Tukey's multiple comparisons test, data is presented as mean fluorescence normalised to DMSO control within each experiment (**P<0.01, ***P<0.001, ****P < 0.0001). Data are presented as means ± SD of two independent experiments with three replicates in each.

4.2.4 Atovaquone reduces hypoxia and inhibits HIF-1α expression in DIPG cells

Inhibiting mitochondrial metabolism and OCR of the DIPG cells would spare more available oxygen and thus reduce hypoxia. This hypothesis has previously shown to reduce hypoxia in some cancer models. As atovaquone was shown to shut down the mitochondrial metabolism of DIPG cells (**Figure 4.1** and **4.2**), we now assessed the hypoxia inhibition efficacy of this drug using HSJD-DIPG-007 cells. Hypoxic regions have been shown to develop in 3D spheroids reaching a size of 500-600 µm (212). As HSJD-DIPG-007 is a 3D neurosphere model, we aimed to model hypoxia by culturing these cells for 3 days to obtain neurospheres of ~500 µm in diameter. The DMSO-treated control neurosphere shows a strong green staining with image iT hypoxia dye representing hypoxia. There was a significant dose dependent decrease in hypoxia at 2.5-30 µM atovaquone treatment, with a complete loss of hypoxia seen at 30 µM atovaquone (**Figure 4.7**).

To corroborate hypoxia inhibition, the effect of atovaquone on HIF-1α was also evaluated. HIF-1α is a subunit of the heterodimeric transcription factor HIF-1 which plays critical role in oxygen homeostasis in the cells (213). HIF-1α is stabilised under hypoxic conditions whereas it is degraded under normoxic conditions (213). Previously, we assessed atovaquone's effect on HIF-1α by culturing HSJD-DIPG-007 cells for 24 and 48 hours (at 20% O_2) before treatment with 10-30 µM atovaquone. There was no increase in HIF-1α expression under these culture conditions i.e., 24 and 48 hours, thus showing that HIF-1α was not stabilised under control condition (0 µM atovaquone) (**Figure 4.8A**). Hence, a comparison of change in HIF-1α expression before and after atovaquone treatment could not be easily made under these conditions. Therefore, HSJD-DIPG-007 and SU-DIPG-VI cells were then cultured for 3 days (at 20% O_2) to form neurospheres with hypoxic cores before treatment with atovaquone. Strong HIF-1α protein expression under control condition (0 µM atovaquone) was observed indicating that HIF-1α is stabilised (**Figure 4.8B-C**), aligning with hypoxia staining visualised in **Figure 4.7**. Treatment with atovaquone at 6 and 24 hours caused a significant dose-dependent decrease in HIF-1α expression with a complete loss of HIF-1α expression seen at 20-30 µM in both the DIPG models (**Figure 4.8B-C**).

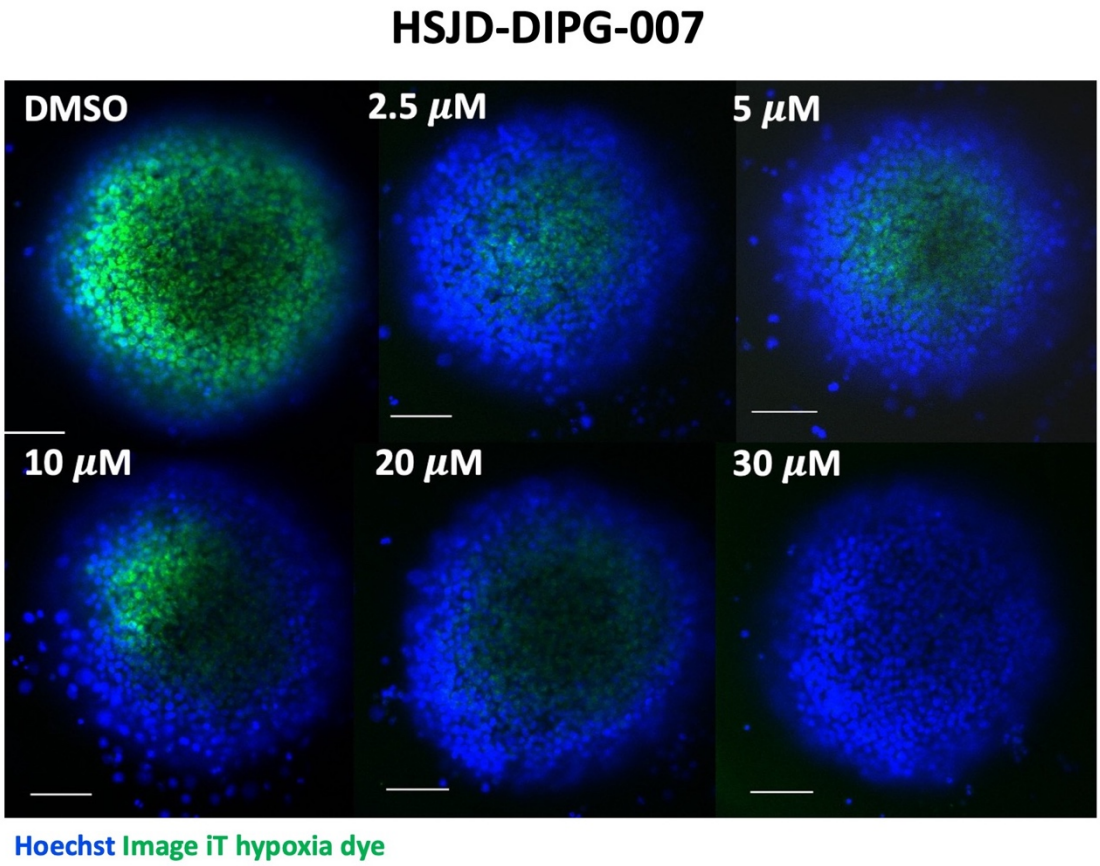

Figure 4.7. Effect of atovaquone treatment on hypoxia within DIPG neurospheres.
HSJD-DIPG-007 neurospheres were cultured for 3 days to obtain neurospheres ~500 μm in diameter. These were treated with a range of atovaquone doses 2.5-30 μM for 24 hours. Image iT hypoxia dye (green staining for hypoxia) and Hoechst (blue staining for nuclei) were used to stain the neurospheres. Representative images are shown from five replicates per condition and the experiment was performed twice. Scale bar = 100 μm.

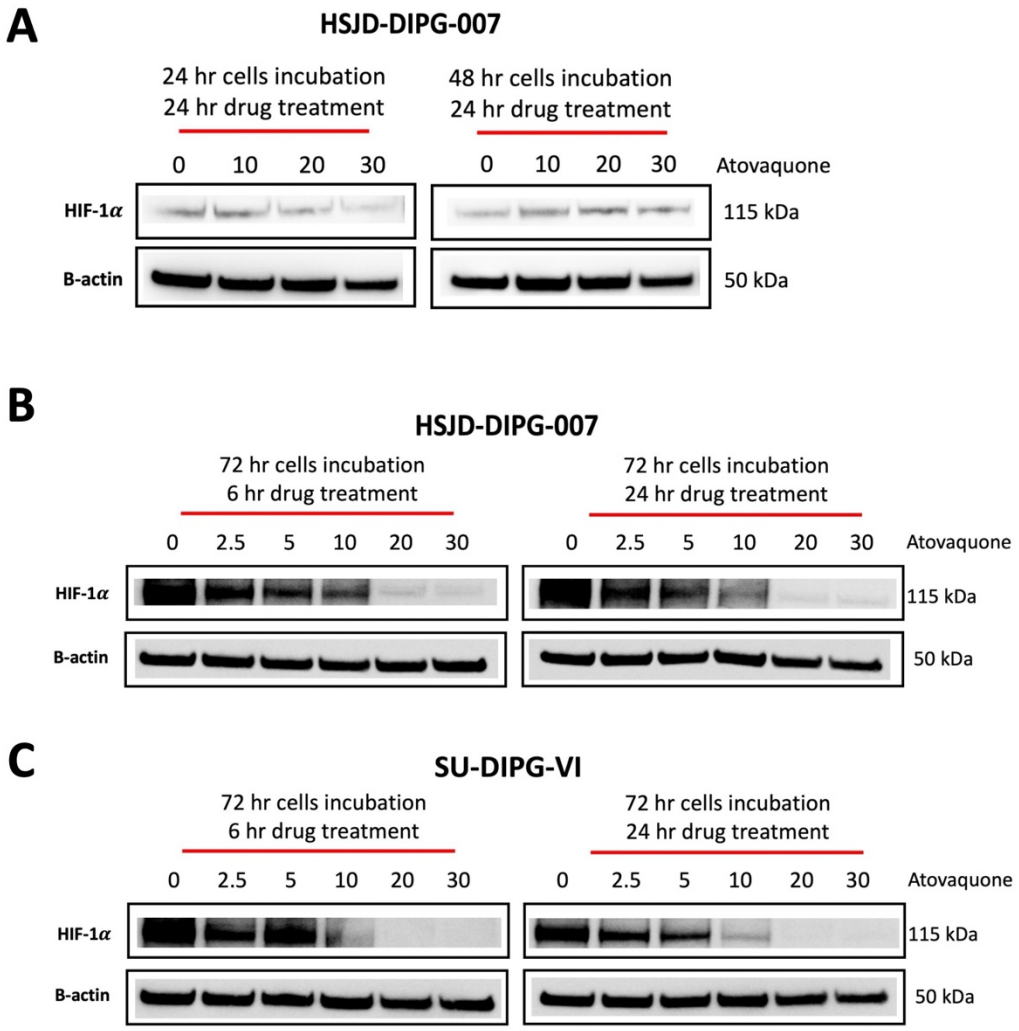

Figure 4.8. Effect of atovaquone treatment on HIF-1α expression in DIPG neurospheres.
(A) HSJD-DIPG-007 neurospheres were cultured for 24 and 48 hours and treated with 10-30 μM atovaquone for 24 hours. (B-C) HSJD-DIPG-007 and SU-DIPG-VI neurospheres were cultured for 72 hours and treated with 2.5-30 μM atovaquone for 6 and 24 hours. Staining was performed using primary antibodies rabbit anti-HIF-1α (1:1000) and rabbit anti-β-actin (1:1000) for HIF-1α and β-actin respectively. Each experiment was performed twice.

4.2.5 Atovaquone improves the radiosensitivity of DIPG cells

Once the OCR and hypoxia inhibition was confirmed, we then examined the radiosensitising efficacy of atovaquone on DIPG cultures using clonogenic assays. The 3D suspension cultures, HSJD-DIPG-007 and SU-DIPG-VI cells were cultured for 3 days (at 20% O_2) and then treated with 10-30 µM atovaquone and 2-4 Gy RT. Atovaquone sensitised both suspension DIPG cultures to RT and there was a significant increase in sensitivity with increasing doses of atovaquone and RT, with the best response seen at 30 µM atovaquone and 4 Gy RT (**Figure 4.9A-D**).

Following the observed radiosensitising effects seen in 3D suspension cultures, we also assessed whether atovaquone radiosensitises 2D monolayer cultures. As hypoxia cannot be easily modelled in the monolayer cultures, we suspected that if hypoxia modification is a major factor contributing to radiosensitivity by atovaquone, there should be minimal radiosensitising effect on the 2D monolayer cultures. To assess this, the monolayer SU-DIPG-XVII were cultured for 24 hours followed by 20-30 µM atovaquone and 2-4 Gy RT treatment. There was a significant decrease in surviving fraction following 30 µM atovaquone+RT and no change in surviving fraction at 20 µM atovaquone+RT in SU-DIPG-XVII (**Figure 4.9E-F**). We also cultured the suspension HSJD-DIPG-007 as attached cells on laminin coated plates followed by treatment with atovaquone and RT. Similar to SU-DIPG-XVII, only 30 µM atovaquone improved the radiosensitivity of HSJD-DIPG-007 (as monolayer culture) shown by lower surviving fraction at 30 µM atovaquone+RT compared to 20 µM atovaquone+ RT and RT only (**Figure 4.9G-H**). This indicates that atovaquone alters the intrinsic radiosensitivity of DIPG cells at higher doses and there must be additional mechanisms contributing to radiosensitising effect by atovaquone in monolayers cultures.

ROS-mediated oxidative stress has been linked to improved tumour cell radiosensitivity (214). As atovaquone increased ROS in monolayer cultures (**Figure 4.6B and 4.6D**), we investigated whether the combination of atovaquone+RT induces higher ROS levels in the monolayer cultures. SU-DIPG-XVII cells were treated with atovaquone for 6 hours, followed by RT (total drug treatment was 24 hours) and ROS was measured using MitoSOX Red and DHE dyes. There was a significantly higher fold change of mean MitoSOX Red fluorescence in all the treatment groups – 2.75-fold at 30 µM atovaquone, 1.95-fold at 4 Gy RT and the highest at 4.5-fold at 30 µM atovaquone+RT compared to control (**P<0.01, ***P<0.001; **Figure**

4.10A). Similarly, there was also a significantly higher fold change of mean DHE fluorescence in all the treatment groups – 1.65-fold at 30 μM atovaquone, 1.45-fold at 4 Gy RT and the highest at 2.07-fold at 30 μM atovaquone+RT compared to control (**P<0.01, ***P<0.001; **Figure 4.10B**). Overall, the combination of 30 μM atovaquone+RT had the greatest MitoSOX red and DHE fluorescence compared to single treatments and control.

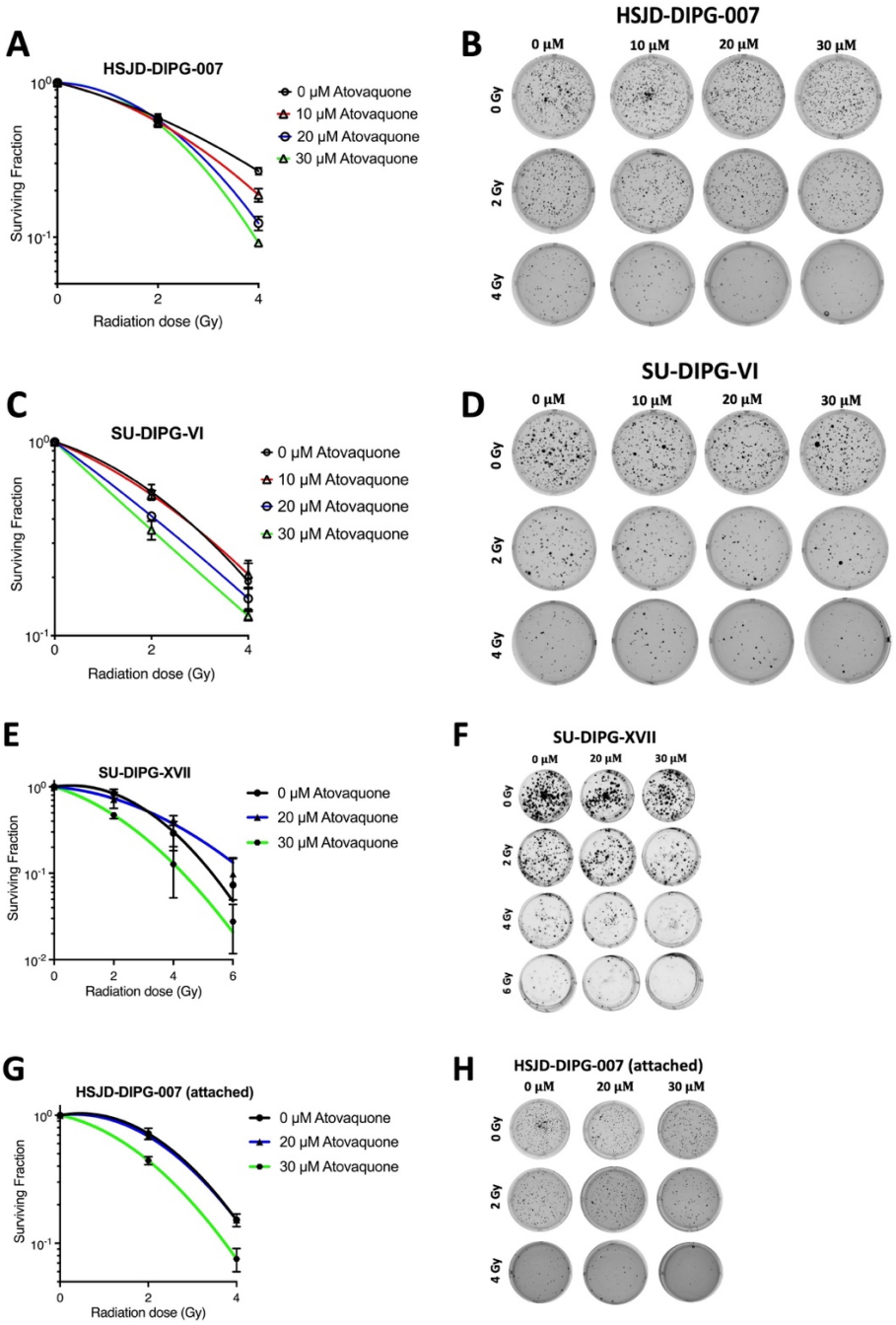

Figure 4.9. Effect of atovaquone on the radiosensitivity of DIPG cultures.
(A-D) HSJD-DIPG-007 and SU-DIPG-VI neurospheres were cultured for 72 hours and treated with 10-30 µM atovaquone for 6 hours followed by 2-4 Gy RT. After 24 hour treatment, drug was removed and cells were seeded on agarose and grown for 14 days. Colonies were stained with MTT. (E-F) SU-DIPG-XVII cells were cultured for 24 hours and treated with 10-30 µM atovaquone for 6 hours followed by 2-4 Gy RT. After 24 hour treatment, drug was removed and cells allowed to grow for 14 days. Colonies were stained with crystal violet dye. (G-H) HSJD-DIPG-007 were cultured as attached cells on laminin coated plated for 24 hours and treated with 10-30 µM atovaquone for 6 hours followed by 2-4 Gy RT. After 24 hour treatment, drug was removed and cells were seeded on agarose and grown for 14 days. Colonies were stained with MTT. Data are presented as means ± SD of two independent experiments with three replicates in each.

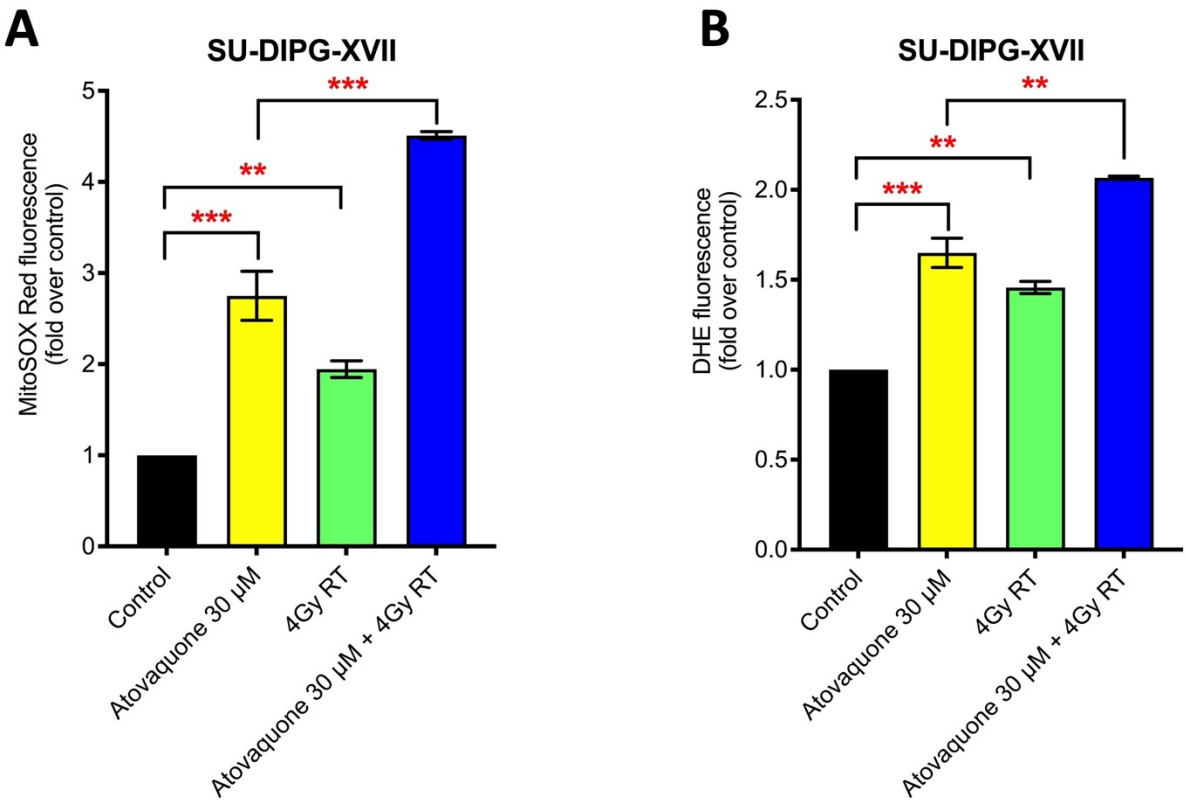

Figure 4.10. Reactive oxygen species production in DIPG cells in response to atovaquone and RT treatment. SU-DIPG-XVII were treated with 30 µM atovaquone for 6 hours followed by 4 Gy RT. After 24 hour drug treatment, cells were then stained with MitoSOX Red and dihydroethidium (DHE) dyes for 30 mins, washed and analysed with flow cytometry. (A) Mean MitoSOX Red fluorescence. (B) Mean DHE fluorescence. Statistical analysis was performed using one-way ANOVA with Tukey's multiple comparisons test, data is presented as mean fluorescence normalised to DMSO control within each experiment (**P<0.01, ***P<0.001, ****P < 0.0001). Data are presented as means ± SD of two independent experiments with three replicates in each.

4.2.6 Transcriptomic changes in DIPG cells following treatment with atovaquone, RT and the combination of atovaquone+RT

Once the mitochondrial inhibition, hypoxia inhibition, and radiosensitising efficacy of atovaquone was shown, we also performed RNA sequencing to gain insight into the transcriptomic alterations in DIPG cells following atovaquone, RT and the combination of atovaquone+RT treatments. Here, the aim was to support our previous *in vitro* findings and discover additional genes and pathways upregulated and downregulated following single and combination treatments. HSJD-DIPG-007 neurospheres were cultured for 3 days (at 20% O_2) and treated with 30 μM atovaquone for 6 hours followed by 6 Gy RT. Cells were collected at 24 hour post-drug treatment for RNA extraction and analysis. Data analysis and figure generation for RNA sequencing was performed by Dr Brian Gloss and Dr Shiyong Ma. All the treatments caused several genes to be differentially expressed in DIPG cells as shown in the hierarchical clustering heatmaps (with cut-offs of adjusted p-value of <0.05 and a foldchange of >2-fold) (**Figure 4.11A-C**). Atovaquone treatment resulted in a total of 1063 genes to be differentially expressed, with 433 downregulated and 630 upregulated genes (**Figure 4.11A**). RT treatment resulted in a total of 109 genes to be differentially expressed, with 20 downregulated and 89 upregulated genes (**Figure 4.11B**). Atovaquone+RT treatment resulted in a total of 1461 genes to be differentially expressed, with 741 downregulated and 720 upregulated genes (**Figure 4.11C**). **Tables 4.1-4.3** list the top upregulated and downregulated genes following each of these three treatments.

We then used the Kyoto Encyclopedia of Genes and Genomes (KEGG) tool to look for the top pathways impacted by the single and combination treatments. **Figure 4.11D-E** shows that glycolysis/gluconeogenesis and HIF-1 signalling were the top pathways downregulated following atovaquone treatment and other metabolic pathways including steroid biosynthesis and glycine, serine and threonine metabolism were found to be upregulated. The specific genes in each of these pathways are shown in **Figure 4.12A**. In support of this, **Table 4.1** also identifies that atovaquone treatment downregulated several genes involved in the HIF-1 signalling pathway (*egln3, pgk1, slc2a1, pdk1, eno2* and *ca9*) and glycolysis/gluconeogenesis pathway (*pgk1* and *eno2*).

Moreover, the results in **Figures 4.11F4-G** shows that differentially expressed genes (DEGs) from RT treatment were enriched in p53 signalling and cytokine-cytokine receptor interaction pathways. The specific genes altered in the p53 pathway are shown in **Figure 4.12B**. Some of

these upregulated (*cdkn1a, ddb2* and *bax*) and downregulated (*ccne2, tp73* and *rrm2*) genes of p53 pathway are also identified in **Table 4.2**.

Finally, the combination of atovaquone+RT resulted in significant downregulation of several pathways including cell cycle, DNA replication, glycolysis/gluconeogenesis, HIF-1 signalling, and p53 signalling pathways (**Figures 4.11H-I**). A significant number of genes in the p53 pathway were also upregulated following atovaquone+RT treatment (**Figures 4.11H-I**). The specific genes in each of these pathways are shown in **Figure 4.12C**. Several of these genes are also identified in **Table 4.3** listing the top upregulated and downregulated genes following the combination treatment including genes in the cell cycle pathway (*plk1, ccnb1, ccna2, bub1, cdc20* downregulated genes and *cdkn1a* upregulated), in p53 pathway (*igfbp3, ccnb1, gtse1* downregulated and *cdkn1a* upregulated) and in the HIF-1 signalling pathway (*egln3* downregulated and *cdkn1a* upregulated).

Furthermore, Gene Set Variation Analysis (GSVA) was also performed looking at variations in several hallmark pathways in DIPG cells following the treatments. **Figure 4.13** demonstrates that atovaquone treatment led to upregulation of several pathways in DIPG cells including cholesterol homeostasis, p53 pathway, reactive oxygen species, and various immune system related pathways (interferon gamma response, interferon alpha response, IL-6/JAK/STAT3 signalling, TNFA signalling via NFKB, and IL2/STAT5 signalling). The GSVA results also demonstrate that atovaquone treatment downregulates pathways related to cell cycle control (E2F, G2M checkpoint MYC targets V1 and V2) and also hypoxia pathways in DIPG cells (**Figure 4.13**). Moreover, the GSVA score for p53 pathway was highest following atovaquone+RT treatment demonstrating significant activation of p53 pathway with combination treatment (**Figure 4.13**). Additionally, the GSVA score for E2F and G2M checkpoint pathways is lower following atovaquone+RT treatment compared to atovaquone alone suggesting further downregulation of these pathways following combination treatment (**Figure 4.13**).

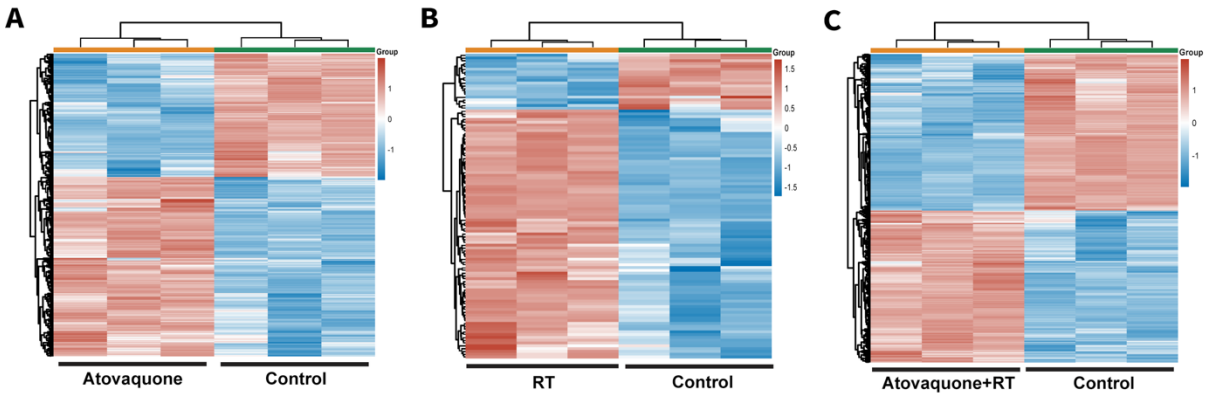
A
Group
Atovaquone
Control
B
Group
RT
Control
C
Group
Atovaquone+RT
Control

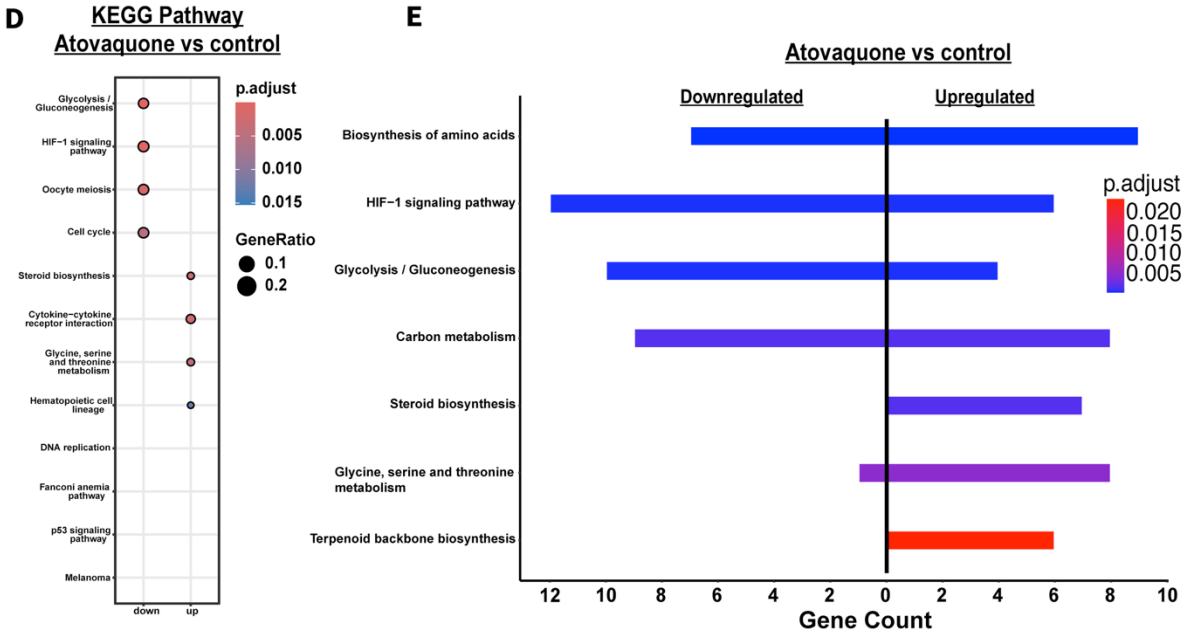
D
KEGG Pathway
Atovaquone vs control
p.adjust
0.005
0.010
0.015
GeneRatio
0.1
0.2
Glycolysis / Gluconeogenesis
HIF−1 signaling pathway
Oocyte meiosis
Cell cycle
Steroid biosynthesis
Cytokine−cytokine receptor interaction
Glycine, serine and threonine metabolism
Hematopoietic cell lineage
DNA replication
Fanconi anemia pathway
p53 signaling pathway
Melanoma
down
up
E
Atovaquone vs control
Downregulated
Upregulated
Biosynthesis of amino acids
HIF−1 signaling pathway
Glycolysis / Gluconeogenesis
Carbon metabolism
Steroid biosynthesis
Glycine, serine and threonine metabolism
Terpenoid backbone biosynthesis
p.adjust
0.020
0.015
0.010
0.005
12 10 8 6 4 2 0 2 4 6 8 10
Gene Count

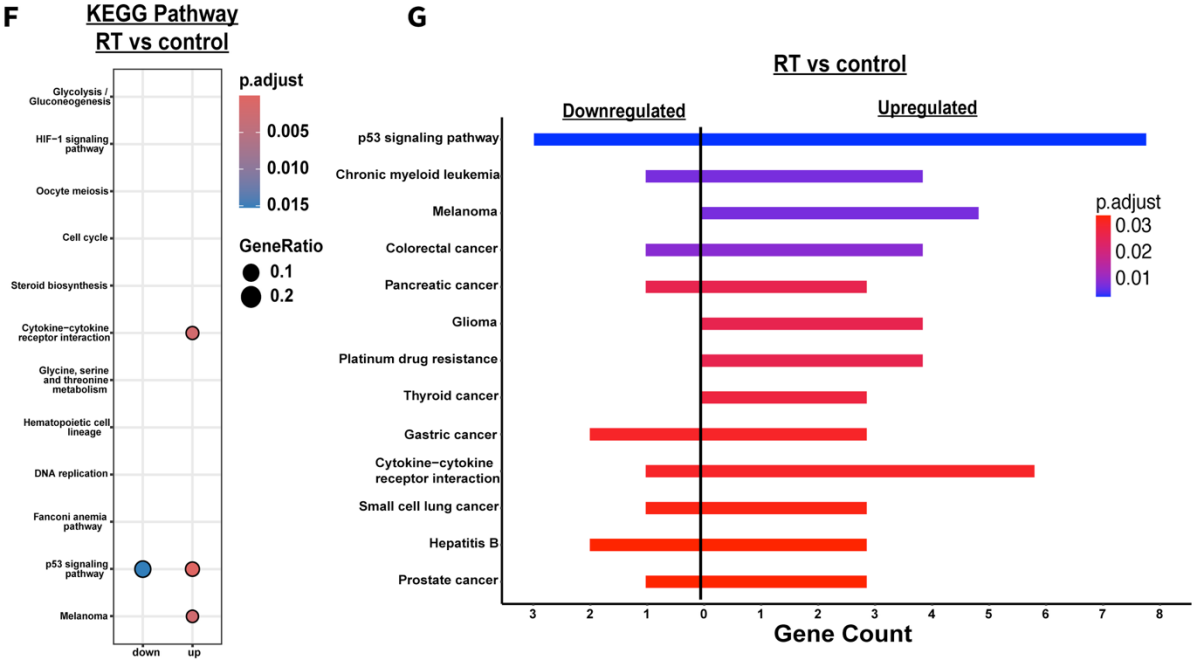
F
KEGG Pathway
RT vs control
p.adjust
0.005
0.010
0.015
GeneRatio
0.1
0.2
Glycolysis / Gluconeogenesis
HIF−1 signaling pathway
Oocyte meiosis
Cell cycle
Steroid biosynthesis
Cytokine−cytokine receptor interaction
Glycine, serine and threonine metabolism
Hematopoietic cell lineage
DNA replication
Fanconi anemia pathway
p53 signaling pathway
Melanoma
down
up
G
RT vs control
Downregulated
Upregulated
p53 signaling pathway
Chronic myeloid leukemia
Melanoma
Colorectal cancer
Pancreatic cancer
Glioma
Platinum drug resistance
Thyroid cancer
Gastric cancer
Cytokine−cytokine receptor interaction
Small cell lung cancer
Hepatitis B
Prostate cancer
p.adjust
0.03
0.02
0.01
3 2 1 0 1 2 3 4 5 6 7 8
Gene Count

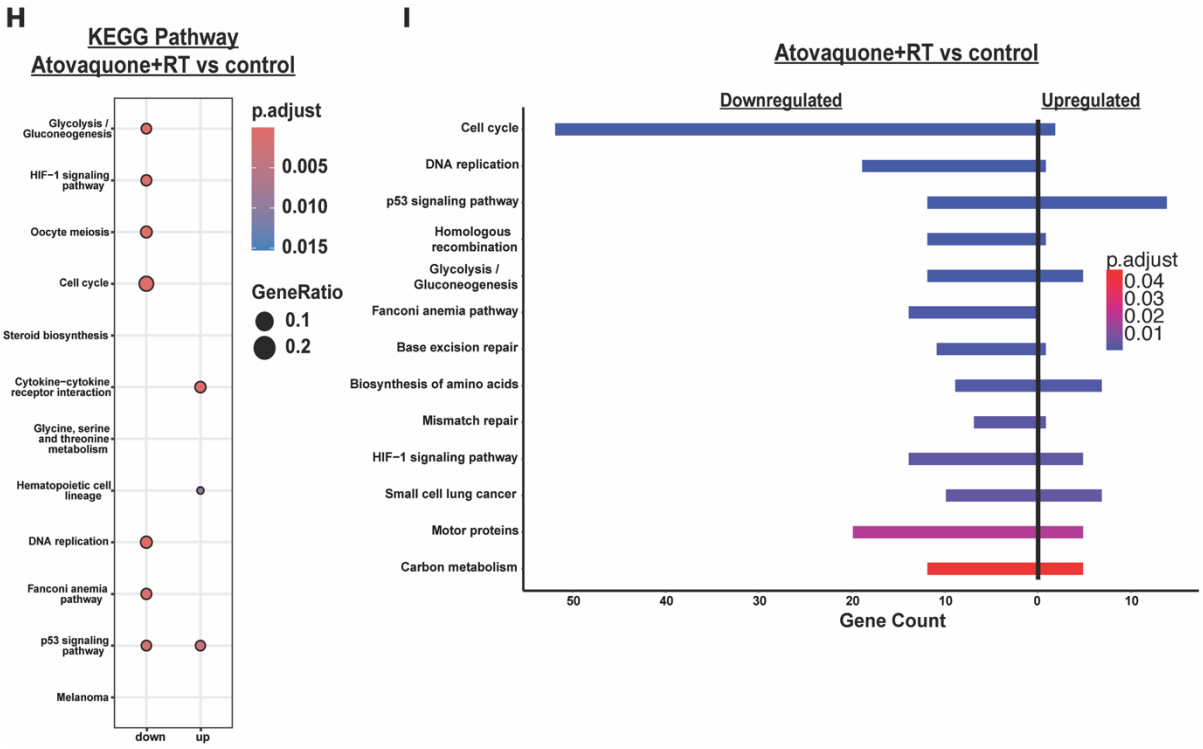

Figure 4.11. Transcriptomic changes from RNA sequencing in HSJD-DIPG-007 cells treated with atovaquone, RT, and atovaquone+RT.
(A-C) Heatmap representation of all the DEGs between atovaquone vs control, RT vs control and atovaquone+RT vs control. The colour key represents fold change (log2). (D) Dotplot analysis of KEGG enrichment showing the top altered pathways from atovaquone vs control. (E) Visualisation of the number upregulated and downregulated genes in KEGG terms for atovaquone vs control. (F) Dotplot analysis of KEGG enrichment showing the top altered pathways from RT vs control. (G) Visualisation of the number upregulated and downregulated genes in KEGG terms for RT vs control. (H) Dotplot analysis of KEGG enrichment showing the top altered pathways from atovaquone+RT vs control. (I) Visualisation of the number upregulated and downregulated genes in KEGG terms for atovaquone+RT vs control.

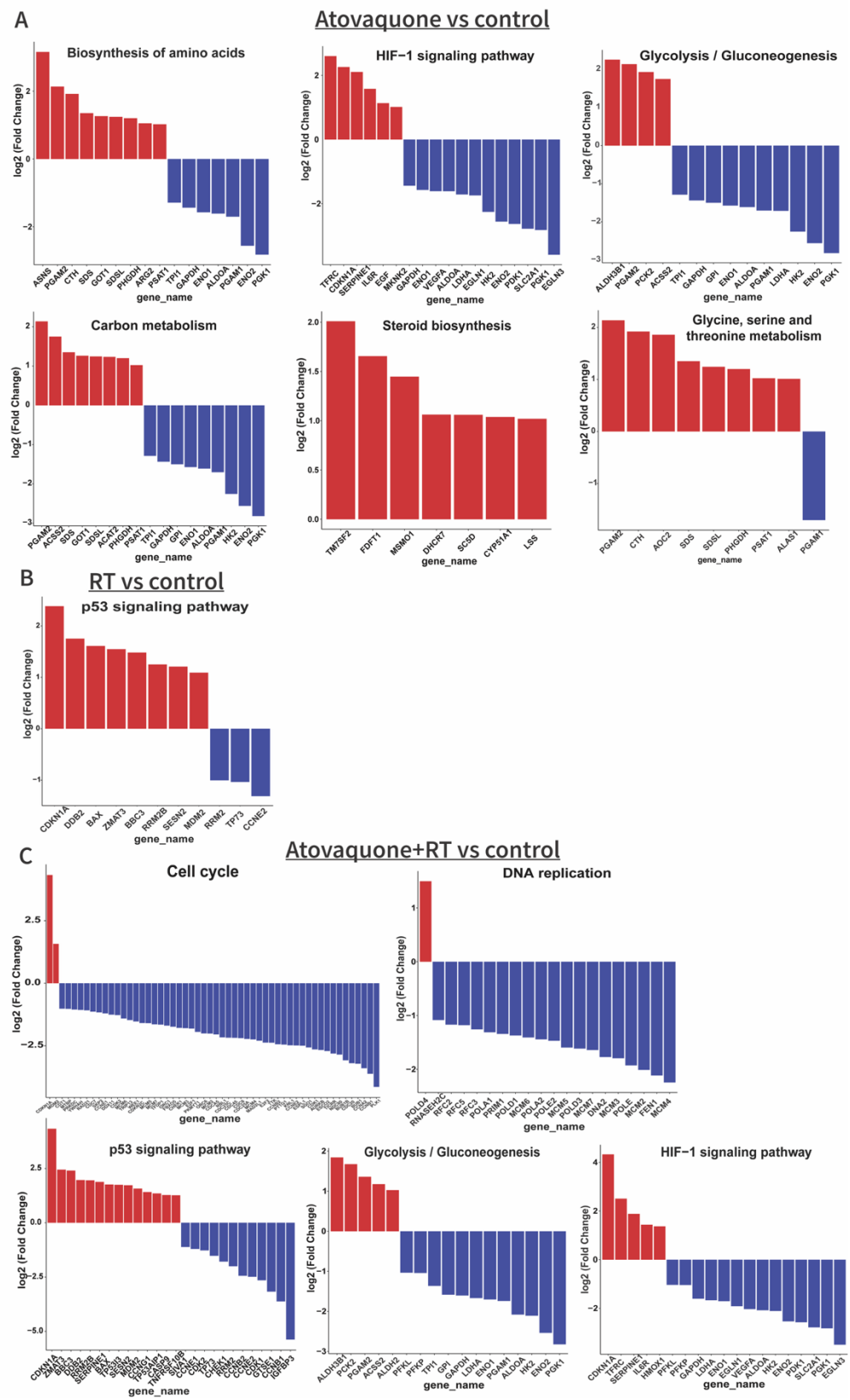

Figure 4.12. Individual genes altered in some statistically significant KEGG pathways from figures 4.11E, G and I.

(A) Genes altered following atovaquone alone treatment. (B) Genes altered following RT alone treatment. (C) Genes altered following atovaquone+RT treatment.

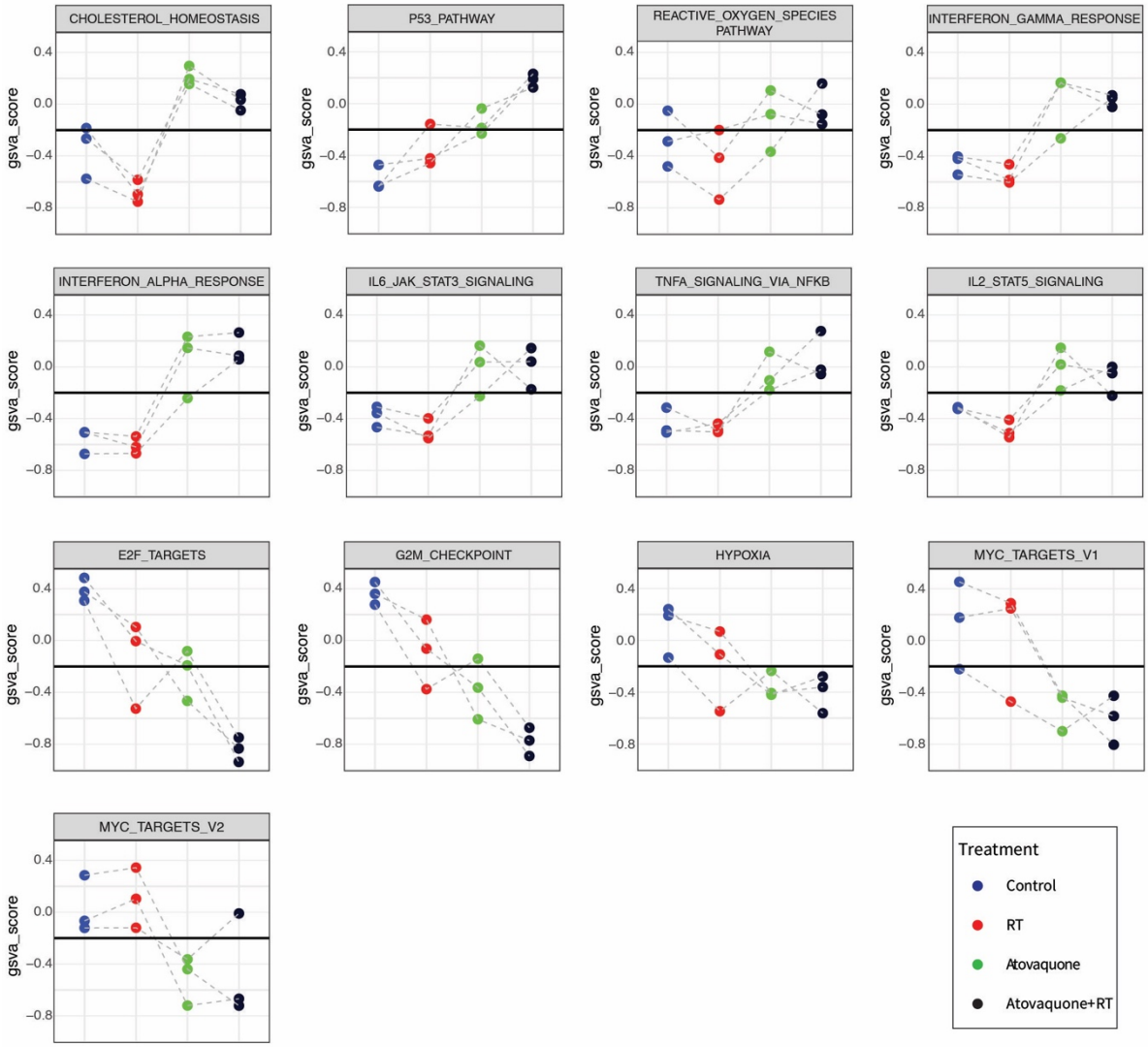

Figure 4.13. GSVA scores of specific pathways altered in HSJD-DIPG-007 cells treated with atovaquone, RT and atovaquone+RT treatments.

Table 4.1. Top 50 upregulated and 50 downregulated genes in HSJD-DIPG-007 cells following atovaquone treatment.

Upregulated Genes				Downregulated Genes			
	Gene	Log2FC	P-value		Gene	Log2FC	P-value
1	FUT1	6.59	5.06E-11	1	ANGPTL4	-8.65	1.46E-18
2	PRODH	4.14	4.02E-05	2	PPDPFL	-8.48	2.72E-07
3	INHBE	3.93	3.54E-11	3	CA9	-5.62	3.33E-10
4	CHRNA9	3.89	1.14E-06	4	HNF1A	-5.39	1.28E-06
5	LINC00475	3.82	1.17E-05	5	STC1	-5.32	8.76E-15
6	FLRT1	3.76	9.08E-08	6	IGFBP3	-5.30	1.72E-17
7	GDF15	3.67	1.25E-16	7	PTGS2	-5.15	3.96E-15
8	MAP1LC3C	3.65	6.34E-11	8	ADM	-5.13	1.28E-16
9	CYBA	3.63	4.51E-08	9	MIR210HG	-5.03	2.83E-14
10	MYOM2	3.51	3.03E-11	10	AL109615.2	-4.87	1.62E-07
11	MIR7-3HG	3.48	7.86E-10	11	AC114803.1	-4.59	1.74E-10
12	TH	3.38	3.79E-07	12	NDRG1	-4.09	4.88E-13
13	GLS2	3.19	3.51E-04	13	AP002852.1	-3.92	1.51E-11
14	SLC6A9	3.18	2.07E-13	14	PTPRN	-3.91	9.53E-07
15	ASNS	3.16	7.32E-14	15	IGFBP5	-3.81	3.81E-14
16	AL139246.5	3.08	6.12E-09	16	TMEM45A	-3.77	6.87E-14
17	HHATL	3.07	1.17E-04	17	C4orf47	-3.68	8.36E-12
18	PLA2G4C	3.06	2.23E-11	18	DOK3	-3.64	7.67E-12
19	HES5	3.02	4.69E-07	19	SLAMF9	-3.60	6.07E-06
20	HAP1	2.96	4.09E-08	20	EGLN3	-3.59	3.70E-12
21	OSCAR	2.96	9.98E-07	21	APLN	-3.48	7.61E-07
22	DDIT3	2.78	7.22E-12	22	AK4	-3.33	1.40E-11
23	CACNG6	2.78	7.10E-08	23	AC093503.3	-3.32	6.36E-09
24	PPP1R14A	2.73	3.24E-04	24	HILPDA	-3.26	2.07E-14
25	IP6K3	2.72	5.52E-09	25	TCAF2	-3.23	4.11E-06
26	FABP3	2.64	6.76E-10	26	DDIT4L	-3.04	1.65E-07
27	FMNL1	2.62	5.12E-08	27	BNIP3	-3.04	2.54E-15
28	ITGA11	2.62	3.57E-08	28	LINC02783	-3.03	1.27E-06
29	TFRC	2.60	4.47E-13	29	FKBP9P1	-2.97	4.48E-11
30	SYTL1	2.54	1.19E-06	30	VWA1	-2.93	9.44E-11
31	ATF3	2.54	3.03E-10	31	GPR22	-2.93	7.19E-08
32	NUPR1	2.50	1.56E-13	32	ID2	-2.91	8.52E-12
33	AC004264.1	2.49	4.36E-07	33	LINC00683	-2.89	1.04E-06
34	TNXB	2.48	2.19E-08	34	PRTN3	-2.83	2.99E-07
35	IL11	2.47	6.81E-04	35	PGK1	-2.82	1.27E-14
36	GPAT3	2.45	2.66E-08	36	AC097534.2	-2.78	1.04E-10
37	PLIN4	2.44	1.37E-08	37	SLC2A1	-2.78	5.35E-13
38	NECTIN4	2.43	4.13E-07	38	ESPN	-2.77	4.17E-10
39	AC008897.3	2.43	1.09E-04	39	AMPD3	-2.73	2.12E-07
40	FAM114A1	2.43	1.08E-12	40	MYEOV	-2.69	7.83E-06
41	TRIB3	2.42	1.78E-12	41	LNP1	-2.68	1.62E-09
42	SCG2	2.40	1.13E-11	42	AL109615.3	-2.65	7.13E-08
43	CLDN4	2.39	6.77E-07	43	PFKFB4	-2.64	2.17E-11
44	IL3RA	2.37	3.18E-08	44	PDK1	-2.63	2.72E-15

45	IL21R	2.37	2.62E-07	45	AC078883.1	-2.62	1.59E-05
46	CSDC2	2.35	5.93E-11	46	HIC1	-2.60	5.90E-11
47	AC021739.3	2.34	2.79E-06	47	ENO2	-2.56	1.43E-11
48	PDIA2	2.34	1.46E-06	48	AC107021.2	-2.49	4.50E-05
49	CD70	2.34	1.09E-06	49	DARS-AS1	-2.48	1.25E-06
50	KCNN3	2.32	6.85E-10	50	AC022400.7	-2.46	4.02E-06

Table 4.2. Top 50 upregulated and 20 downregulated genes in HSJD-DIPG-007 cells following RT treatment.

Upregulated Genes				Downregulated Genes			
	Gene	Log2FC	P-value		Gene	Log2FC	P-value
1	MUC19	6.59	5.06E-11	1	PIM1	-1.70	1.88E-08
2	LINC00475	4.14	4.02E-05	2	E2F8	-1.56	1.16E-08
3	PURPL	3.93	3.54E-11	3	SPIB	-1.53	2.05E-05
4	PINCR	3.89	1.14E-06	4	HRH3	-1.41	4.96E-05
5	ABCA12	3.82	1.17E-05	5	CCNE2	-1.31	2.39E-08
6	GAS6-AS1	3.76	9.08E-08	6	MYB	-1.12	6.91E-07
7	TRIM22	3.67	1.25E-16	7	ATP1B1	-1.10	2.22E-05
8	PTCHD4	3.65	6.34E-11	8	SLC7A11	-1.06	2.67E-05
9	PHLDA3	3.63	4.51E-08	9	FAM111B	-1.06	6.71E-10
10	AC068057.1	3.51	3.03E-11	10	TP73	-1.04	1.01E-05
11	EDA2R	3.48	7.86E-10	11	TCF19	-1.01	7.81E-08
12	FXYD2	3.38	3.79E-07	12	RRM2	-1.00	1.42E-10
13	WDR63	3.19	3.51E-04	13	DBP	-0.98	2.02E-06
14	GAS6	3.18	2.07E-13	14	MXD3	-0.97	6.35E-06
15	HHATL	3.16	7.32E-14	15	MNS1	-0.95	4.94E-06
16	TSPAN11	3.08	6.12E-09	16	PASK	-0.95	1.38E-07
17	PLK2	3.07	1.17E-04	17	INSIG1	-0.94	7.35E-06
18	ZNF423	3.06	2.23E-11	18	EEPD1	-0.93	8.96E-05
19	LNCTAM34A	3.02	4.69E-07	19	GRM8	-0.93	4.08E-05
20	ENC1	2.96	4.09E-08	20	CENPE	-0.92	4.72E-07
21	CD70	2.96	9.98E-07				
22	TFEC	2.78	7.22E-12				
23	PLIN4	2.78	7.10E-08				
24	AC119751.3	2.73	3.24E-04				
25	CR381653.2	2.72	5.52E-09				
26	CDKN1A	2.64	6.76E-10				
27	FDXR	2.62	5.12E-08				
28	PRODH	2.62	3.57E-08				
29	AL353138.1	2.60	4.47E-13				
30	IP6K3	2.54	1.19E-06				
31	MIR34AHG	2.54	3.03E-10				
32	AC138776.1	2.50	1.56E-13				
33	KLLN	2.49	4.36E-07				
34	GDF15	2.48	2.19E-08				
35	NECTIN4	2.47	6.81E-04				
36	TMEM229B	2.45	2.66E-08				
37	GLS2	2.44	1.37E-08				
38	GRIN2C	2.43	4.13E-07				
39	SMIM10L2A	2.43	1.09E-04				
40	CYFIP2	2.43	1.08E-12				
41	ZBBX	2.42	1.78E-12				
42	DDB2	2.40	1.13E-11				
43	RPS27L	2.39	6.77E-07				
44	F11R	2.37	3.18E-08				

45	SPATA18	2.37	2.62E-07
46	SNX18P12	2.35	5.93E-11
47	AC107959.1	2.34	2.79E-06
48	EBI3	2.34	1.46E-06
49	BAX	2.34	1.09E-06
50	EXTL1	2.32	6.85E-10

Table 4.3. Top 50 upregulated and 50 downregulated genes in HSJD-DIPG-007 cells following atovaquone+RT treatment.

Upregulated Genes				Downregulated Genes			
	Gene	Log2FC	P-value		Gene	Log2FC	P-value
1	FUT1	6.05	4.65E-10	1	PPDPFL	-8.50	1.97E-07
2	GDF15	5.76	1.42E-19	2	ANGPTL4	-8.49	1.17E-18
3	PRODH	5.55	6.77E-08	3	CA9	-6.90	9.02E-11
4	GLS2	5.26	3.52E-08	4	AL109615.2	-5.94	4.39E-08
5	HHATL	5.22	2.58E-09	5	IGFBP3	-5.38	1.20E-17
6	ABCA12	5.06	5.34E-07	6	AC114803.1	-5.19	5.90E-11
7	LINC00475	5.05	2.97E-08	7	PTGS2	-5.05	3.48E-15
8	WDR63	4.96	3.91E-08	8	MIR210HG	-5.04	2.26E-14
9	TRIM22	4.83	2.79E-14	9	STC1	-5.03	8.76E-15
10	NECTIN4	4.78	1.43E-12	10	ADM	-4.97	1.47E-16
11	IP6K3	4.69	1.37E-13	11	KIF20A	-4.81	7.18E-15
12	TFEC	4.61	4.71E-09	12	DDIT4L	-4.79	3.13E-09
13	ZNF423	4.55	3.48E-12	13	HNF1A	-4.71	1.58E-06
14	PLIN4	4.48	1.05E-13	14	NDRG1	-4.41	1.79E-13
15	MUC19	4.38	1.14E-08	15	LINC02783	-4.28	9.01E-08
16	FXYD2	4.37	1.49E-08	16	APLN	-4.20	1.71E-07
17	CDKN1A	4.33	9.96E-19	17	PLK1	-4.15	6.76E-14
18	CHRNA9	4.27	1.63E-07	18	AP001107.5	-3.98	1.71E-07
19	TMEM229B	4.07	3.24E-08	19	HRH3	-3.88	2.11E-09
20	MIR7-3HG	4.00	5.69E-11	20	SLAMF9	-3.88	2.90E-06
21	INHBE	3.98	2.62E-11	21	CENPA	-3.85	1.26E-12
22	PURPL	3.97	6.91E-11	22	IGFBP5	-3.68	5.96E-14
23	CD70	3.92	7.71E-11	23	CCNB1	-3.62	1.30E-13
24	PINCR	3.91	4.43E-08	24	DLGAP5	-3.60	2.94E-16
25	F11R	3.84	2.34E-08	25	HILPDA	-3.55	6.62E-15
26	AC004264.1	3.81	2.17E-10	26	GPR22	-3.54	1.07E-08
27	AL353138.1	3.76	8.19E-12	27	TMEM45A	-3.52	1.15E-13
28	PHLDA3	3.68	2.72E-17	28	AP002852.1	-3.50	3.53E-11
29	PPP1R14A	3.61	4.04E-06	29	EGLN3	-3.50	4.04E-12
30	IL11	3.57	2.93E-06	30	NEK2	-3.47	1.04E-12
31	PGF	3.56	4.42E-08	31	ASPM	-3.47	3.51E-15
32	AC068057.1	3.54	3.80E-07	32	CENPF	-3.46	5.91E-16
33	LNCTAM34A	3.41	5.75E-12	33	OLFM3	-3.41	6.14E-06
34	EBI3	3.37	1.81E-10	34	CDCA2	-3.40	2.58E-15
35	FLRT1	3.34	7.71E-07	35	HJURP	-3.40	4.24E-14
36	PLA2G4C	3.30	5.56E-12	36	CCNA2	-3.40	1.30E-14
37	EDA2R	3.28	1.87E-16	37	PIF1	-3.38	6.82E-13
38	GAS6-AS1	3.28	3.04E-07	38	MKI67	-3.32	6.32E-16
39	PLK2	3.28	5.95E-16	39	C4orf47	-3.31	1.95E-11
40	MAP1LC3C	3.22	5.54E-10	40	FAM83D	-3.27	6.51E-15
41	FDXR	3.20	1.41E-16	41	TCAF2	-3.25	2.96E-06
42	CYP4F2	3.15	1.15E-06	42	BUB1	-3.22	4.33E-16
43	PTCHD4	3.12	4.01E-17	43	CDC20	-3.20	1.03E-13
44	HAP1	3.11	1.58E-08	44	DOK3	-3.19	2.36E-11

45	OSCAR	3.10	4.21E-07	45	AL109615.3	-3.19	8.98E-09
46	GRIN2C	3.08	5.77E-09	46	AMPD3	-3.18	4.25E-08
47	LINC00346	3.05	1.37E-06	47	CDCA3	-3.18	3.55E-15
48	CSTA	3.04	1.84E-07	48	KIF18B	-3.17	1.94E-14
49	ROCK1P1	3.04	9.35E-09	49	AC097534.2	-3.17	2.01E-11
50	SLC6A9	2.98	6.55E-13	50	GTSE1	-3.17	4.89E-15

4.2.7 The improved blood-brain-barrier penetrant version - ASD atovaquone formulation demonstrates similar efficacy as commercially available atovaquone formulation

Although atovaquone can penetrate the BBB, evidence in literature suggests that its penetrability into the brain is limited. In order to repurpose atovaquone for DIPG treatment, a formulation with higher bioavailability giving higher atovaquone levels in the brain is needed. A recent study formulated atovaquone as ASD showing significantly higher brain and plasma concentration achieved in mice treated with ASD atovaquone formulation (123). Therefore, we compared the mitochondrial and hypoxia inhibition efficacies of the ASD atovaquone formulation with the commercial atovaquone formulation.

Both atovaquone formulations significantly decreased the OCR of HSJD-DIPG-007 cells at a similar rate compared to control (****$P < 0.0001$) and there was no difference in the OCR inhibition from either of the two formulations at all the tested doses (**Figure 4.14A**). Similarly, ECAR profile was also very consistent, with no differences observed from both formulations at all the tested doses (**Figure 4.14B**). Both the formulations also appeared to have similar hypoxia inhibition efficacy as both commercial and ASD atovaquone decreased hypoxia in HSJD-DIPG-007 neurospheres at 10 μM to similar level and completely abolished hypoxia at 30 μM (**Figure 4.14C**).

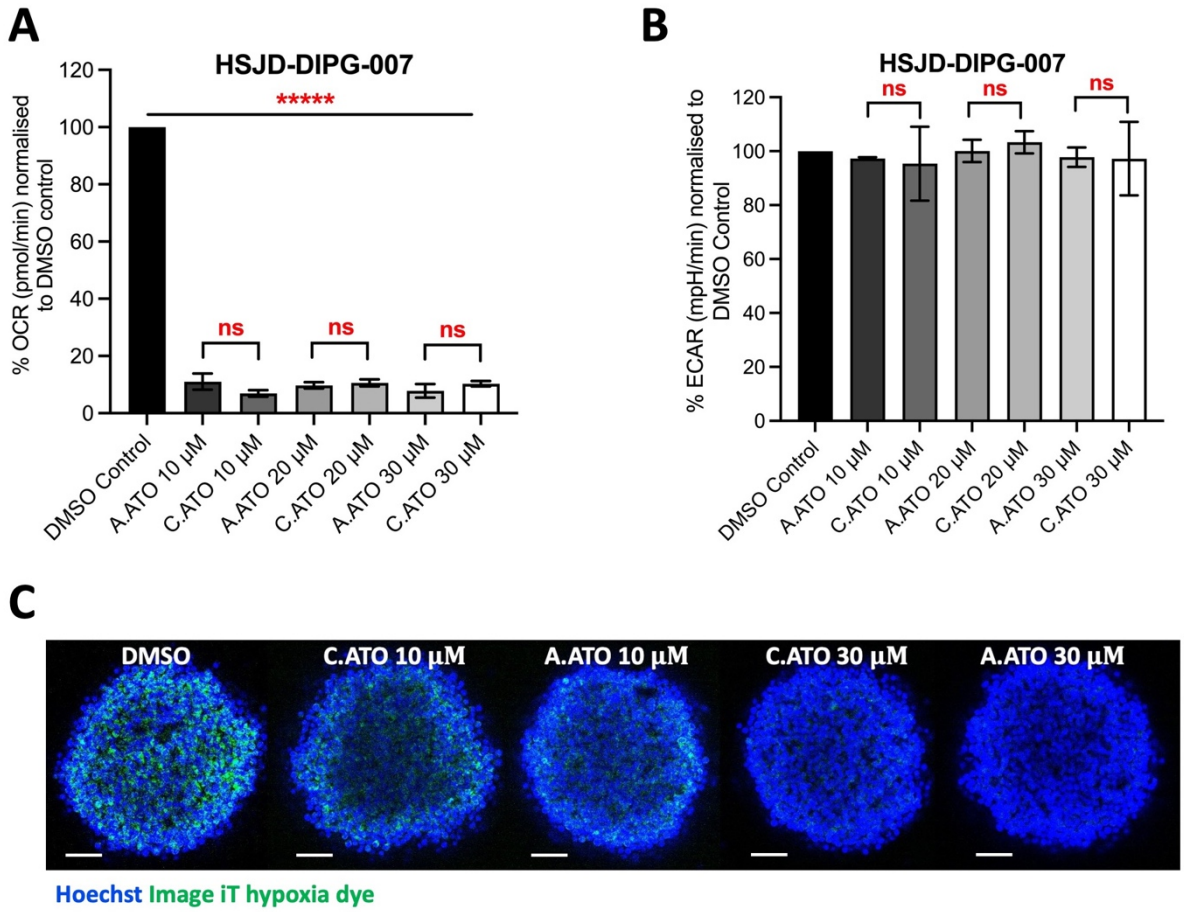

Figure 4.14. Comparing the mitochondrial and hypoxia inhibition efficacies of commercial vs amorphous solid dispersion (ASD) atovaquone formulations.
(A-B) HSJD-DIPG-007 cells treated with commercial or ASD atovaquone formulations (10-30 µM) and OCR and ECAR were measured in real-time using Seahorse XFe24 Analyser over a period of 4 hours. Data is normalised to DMSO control (0 µM Atovaquone). Statistical analysis was performed using one-way ANOVA with Tukey's multiple comparisons test, data is presented relative to control (0 µM Atovaquone) (****P < 0.0001). Data are presented as means ± SD of two independent experiments with three replicates in each. (C) HSJD-DIPG-007 neurospheres were cultured for 3 days to obtain neurospheres ~500 µm in diameter. These were treated with commercial or ASD atovaquone formulations (10-30 µM) for 24 hours. Image iT hypoxia dye (green staining for hypoxia) and Hoechst (blue staining for nuclei) were used to stain the neurospheres. Five replicates per condition were setup and the experiment was performed twice. Scale bar = 100 µm.

4.2.8 Assessing the anti-proliferative efficacy of the combination of atovaquone and proguanil compared to atovaquone alone against DIPG cultures

The widespread evidence of reported synergy between atovaquone/proguanil combination in parasites prompted us to investigate whether the combination is also synergistic in DIPG cultures. Atovaquone/proguanil combination is used for the treatment of uncomplicated malaria and is clinically available at a fixed ratio 2.5:1 as Malarone (250 mg of atovaquone and 100 mg of proguanil for adults, and 62.5 mg of atovaquone and 25 mg of proguanil for children).

First, we investigated whether the combination of atovaquone/proguanil exhibits stronger anti-proliferative efficacy in DIPG cultures compared to atovaquone alone. We decided to test the clinical ratio 2.5:1, testing maximum dose of 30 µM:12 µM using MTS assays. There was no significant difference in the inhibition of cell viability of DIPG cell lines (HSJD-DIPG-007, SU-DIPG-XVII and SU-DIPG-VI) from the combination of atovaquone/proguanil compared to atovaquone alone (**Figure 4.15A-C**).

As there was no synergistic effect of the combination of atovaquone/proguanil at 2.5:1 against DIPG cell lines, we then increased the proguanil doses up to 100 µM and used lower atovaquone doses 5 µM and 10 µM which do not inhibit cell viability. When treated with proguanil alone, the IC_{50} values of HSJD-DIPG-007, SU-DIPG-XVII and SU-DIPG-VI were 43.5 µM, 87 µM and 94 µM respectively (**Figure 4.15D-F)**. Again, there was no significant difference in the inhibition of cell viability of DIPG cell lines from the combination of atovaquone/proguanil compared to proguanil alone (**Figure 4.15D-F**). Overall, in all of the anti-proliferative assays, the effects observed from the combination treatment was similar to single treatments (**Figure 4.15A-F**).

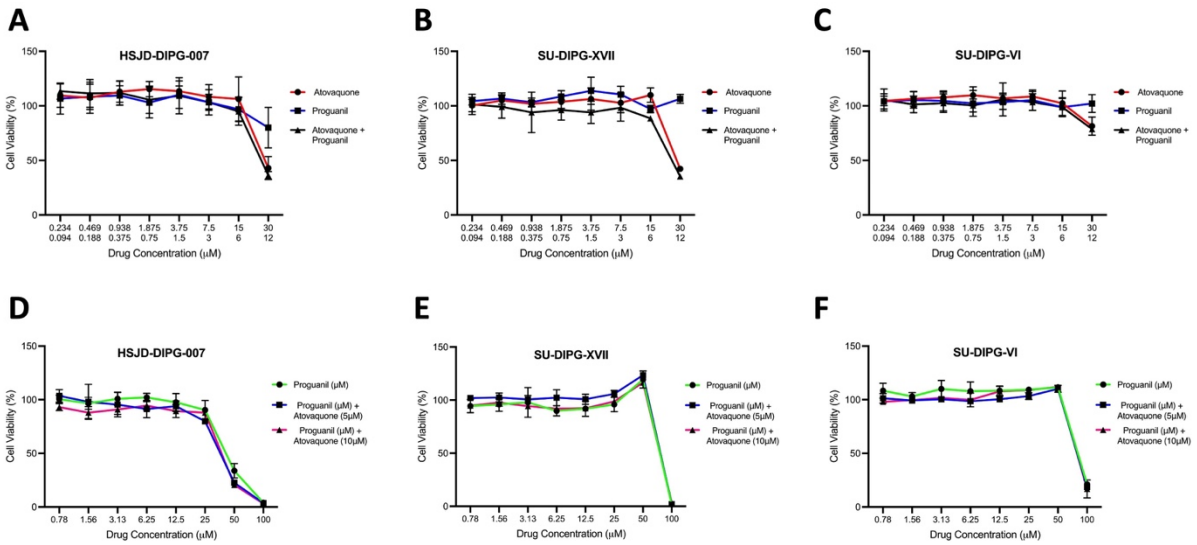

Figure 4.15. Dose-response curves of atovaquone, proguanil and the combination of atovaquone/proguanil against DIPG cell lines.

(A-F) HSJD-DIPG-007, SU-DIPG-XVII and SU-DIPG-VI were treated with atovaquone and proguanil for 72 hours and cell viability was assessed using MTS cell proliferation assay. Data are presented as means of three independent experiments, with error bars indicating SD (n=3).

4.2.9 Assessing the OCR inhibition efficacy of the combination of atovaquone and proguanil compared to atovaquone alone against DIPG cultures

As no synergistic interaction in terms of proliferation inhibition was observed, we further decided to investigate the OCR inhibition efficacy of the combination of atovaquone/proguanil against DIPG cultures. As proguanil is a biguanide and a mitochondrial complex I inhibitor, and atovaquone is a mitochondrial complex III inhibitor, we hypothesised that the combination of atovaquone/proguanil could more strongly impact the mitochondrial activity. This might result a significantly lower OCR from the combination treatment compared to atovaquone alone.

First, we tested the OCR response from the combination at the clinical ratio 2.5:1 (2.5 µM:1 µM), treating SU-DIPG-XVII cells for 4 hours. The combination of atovaquone/proguanil and atovaquone alone resulted in significantly lower OCR compared to control (****P<0.0001), however there was no significant difference in the OCR inhibition from the combination (20.7 pmol/min) compared to atovaquone alone (24.3 pmol/min) (**Figure 4.16A**). Because 2.5 µM atovaquone was very strong on its own in reducing OCR, we then decided to lower the atovaquone dose to 1 µM and increase the proguanil doses to 8, 10 and 12 µM. Atovaquone at 1 µM significantly reduced the OCR of SU-DIPG-XVII cells (***P<0.001) whereas there was no significant reduction in OCR from either of the proguanil doses (**Figure 4.16B**). Interestingly, all of the combinations of atovaquone/proguanil (ATO 1 µM+PRO 8 µM - 271.7 pmol/min, ATO 1 µM+PRO 10 µM – 270.9 pmol/min, ATO 1 µM+PRO 12 µM – 262.7 pmol/min) had a significantly higher OCR than atovaquone alone (ATO 1 µM – 56.2 pmol/min), demonstrating an antagonistic trend (***P<0.001; **Figure 4.16B**).

Similar experiments were repeated using HSJD-DIPG-007 cells, testing 1 µM atovaquone and 8, 10 and 12 µM proguanil. Atovaquone at 1 µM did not reduce the OCR of HSJD-DIPG-007 cells, and the OCR of proguanil alone and the combinations were also similar to the control (**Figure 4.16C**). Hence, we increased the atovaquone dose in subsequent experiment, testing 2.5 µM atovaquone and 8, 10 and 12 µM proguanil. Atovaquone at 2.5 µM significantly reduced the OCR of HSJD-DIPG-007 cells (****P<0.0001) whereas there was no significant reduction in OCR from either of the proguanil doses (**Figure 4.16D**). All of the combinations of atovaquone/proguanil (ATO 1 µM+PRO 8 µM – 43.8 pmol/min, ATO 1 µM+PRO 10 µM – 47.1 pmol/min, ATO 1 µM+PRO 12 µM – 60.3 pmol/min) had a higher OCR than

atovaquone alone (ATO 1 μM – 14.6 pmol/min), demonstrating an antagonistic trend (**Figure 4.16D**).

As there was no inhibitory effect from lower doses of proguanil, we tested whether higher doses of proguanil inhibit the OCR of DIPG cultures, testing a maximum dose of 100 μM. There was a significant reduction in the OCR of SU-DIPG-XVII cells at 4 hours treatment with 50 μM proguanil (134.2 pmol/min) and 100 μM proguanil (70.1 pmol/min) compared to control (255.2 pmol/min) (****P<0.0001; **Figure 4.16E**). As 50 μM and 100 μM proguanil decreased OCR of SU-DIPG-XVII significantly, we combined these doses with 1 μM atovaquone. Similar to the trends observed in previous experiments, both the combinations of atovaquone/proguanil (ATO 1 μM+PRO 50 μM – 105.7 pmol/min, ATO 1 μM+PRO 100 μM – 71.4 pmol/min) had a higher OCR than atovaquone alone (ATO 1 μM – 7.0 pmol/min), demonstrating an antagonistic trend (**Figure 4.16D**).

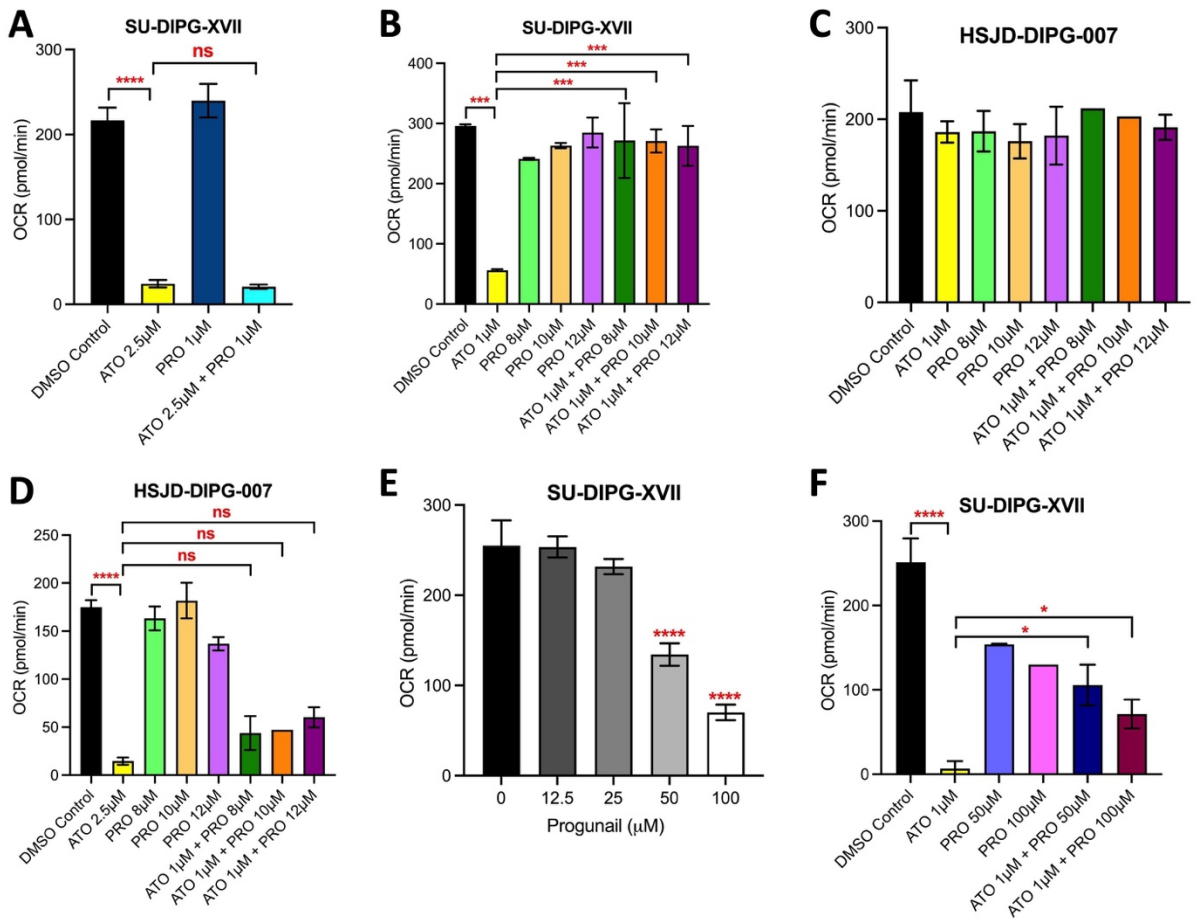

Figure 4.16. Metabolic changes in oxygen consumption rate (OCR) of DIPG cell lines following treatment with atovaquone, proguanil and the combination of atovaquone/proguanil.
SU-DIPG-XVII and HSJD-DIPG-007 were treated with atovaquone, proguanil and the combination at the doses shown and OCR was measured in real-time using Seahorse XFe24 Analyser over a period of 4 hours. Statistical analysis was performed using one-way ANOVA with Tukey's multiple comparisons test (*P < 0.05, ***P < 0.001, ****P < 0.0001). Data are presented as means ± SD of two independent experiments with three replicates in each.

4.2.10 Assessing the anti-proliferative and OCR inhibition efficacy of the combination of atovaquone and other biguanides (phenformin and metformin) compared to atovaquone alone against DIPG cultures

As atovaquone/proguanil combination demonstrated no synergy in terms of both proliferation inhibition and OCR inhibition against DIPG cultures, we were interested in investigating how other biguanides (complex I inhibitors) interact with atovaquone. Here, we assessed phenformin and metformin in combination with atovaquone. Our lab group has previously established dose response curves and assessed the OCR inhibition efficacy of phenformin and metformin alone against DIPG cultures and doses were picked based on our previous results.

Phenformin doses up to 2.5 mM was combined with atovaquone doses 5 µM and 10 µM which do not inhibit cell viability. Similar to proguanil, there was no significant difference in the inhibition of cell viability of DIPG cell lines from the combination of atovaquone/phenformin compared to phenformin alone (**Figure 4.17A-C**). The OCR inhibition efficacy of the combination of atovaquone/phenformin was then compared to atovaquone alone, testing 1 µM atovaquone and 50 µM and 100 µM phenformin. Both of the combinations of atovaquone/phenformin (ATO 1 µM+Phen 50 µM – 108.25 pmol/min, ATO 1 µM+Phen 100 µM – 53.9 pmol/min) had a higher OCR than atovaquone alone (ATO 1 µM – 23.8 pmol/min), demonstrating an antagonistic trend similar to as observed with atovaquone/proguanil combinations (*P<0.05; **Figure 4.17D**).

Next, metformin doses up to 2.5 mM was combined with atovaquone doses 5 µM and 10 µM. Similar to proguanil and phenformin, there was no significant difference in the inhibition of cell viability of DIPG cell lines from the combination of atovaquone/metformin compared to metformin alone (**Figure 4.18A-C**). The OCR inhibition efficacy of the combination of atovaquone/metformin was then compared to atovaquone alone, testing 1 µM atovaquone and 5 mM and 10 mM metformin. Both of the combinations of atovaquone/metformin (ATO 1 µM+Met 5 mM – 119.3 pmol/min, ATO 1 µM+Met 10 mM – 80.8 pmol/min) had a higher OCR than atovaquone alone (ATO 1 µM – 35.4 pmol/min), again demonstrating an antagonistic trend similar to as observed with atovaquone/proguanil and atovaquone/phenformin combinations (*P<0.05; **Figure 4.18D**).

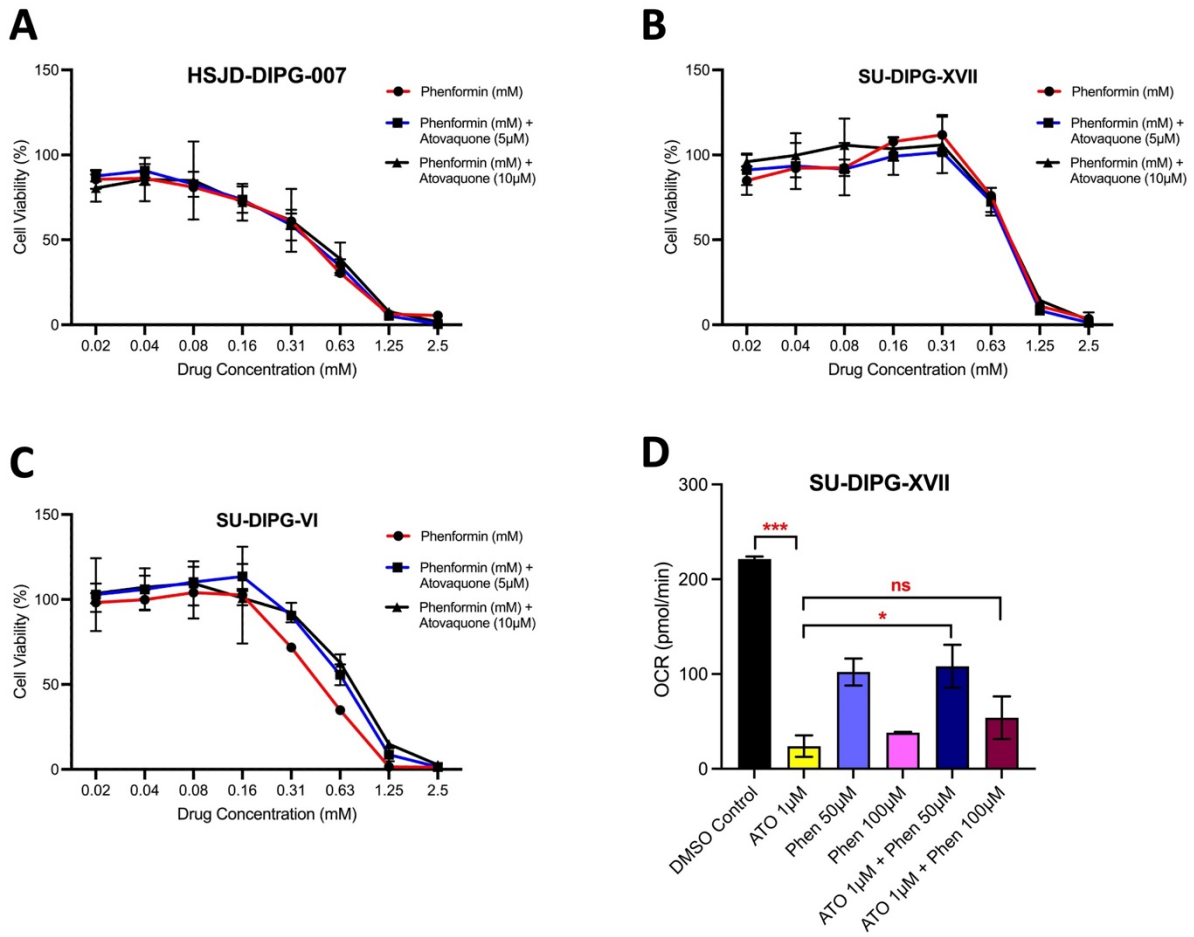

Figure 4.17. Dose-response curves and OCR inhibition efficacy of atovaquone, phenformin and the combination of atovaquone/phenformin against DIPG cell lines.
(A-C) HSJD-DIPG-007, SU-DIPG-XVII and SU-DIPG-VI were treated with atovaquone and phenformin for 72 hours and cell viability was assessed using MTS cell proliferation assay. Data are presented as means of two independent experiments, with error bars indicating SD (n=3). SU-DIPG-XVII were treated with atovaquone, phenformin and the combination at the doses shown and OCR was measured in real-time using Seahorse XFe24 Analyser over a period of 4 hours. Statistical analysis was performed using one-way ANOVA with Tukey's multiple comparisons test (*P < 0.05, ***P < 0.001). Data are presented as means ± SD of two independent experiments with three replicates in each.

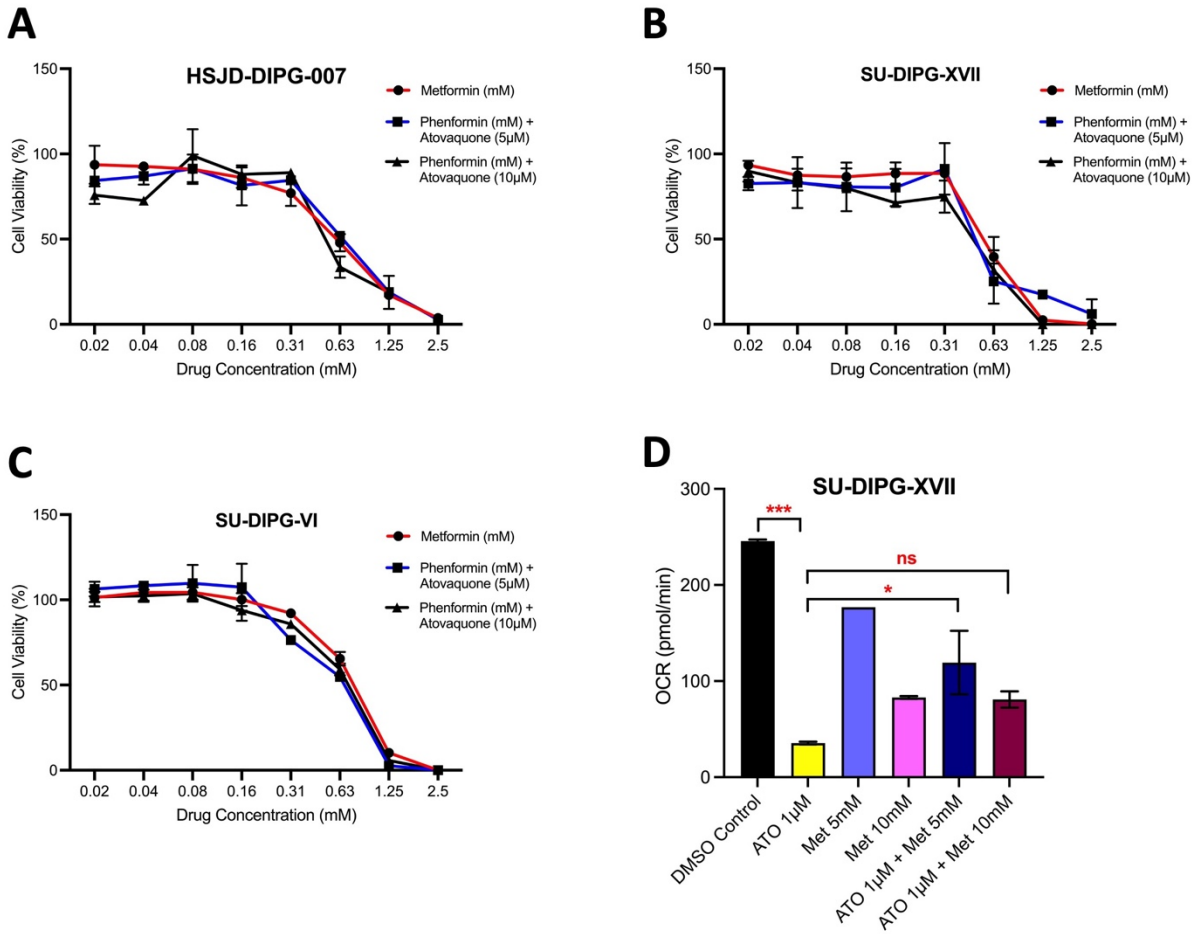

Figure 4.18. Dose-response curves and OCR inhibition efficacy of atovaquone, metformin and the combination of atovaquone/metformin against DIPG cell lines.
(A-C) HSJD-DIPG-007, SU-DIPG-XVII and SU-DIPG-VI were treated with atovaquone and metformin for 72 hours and cell viability was assessed using MTS cell proliferation assay. Data are presented as means of two independent experiments, with error bars indicating SD (n=3). SU-DIPG-XVII were treated with atovaquone, metformin and the combination at the doses shown and OCR was measured in real-time using Seahorse XFe24 Analyser over a period of 4 hours. Statistical analysis was performed using one-way ANOVA with Tukey's multiple comparisons test (*P < 0.05, ***P < 0.001). Data are presented as means ± SD of two independent experiments with three replicates in each.

4.3. Discussion

In chapter 3, we showed increased mitochondrial ETC genes expression in DIPG patient samples compared to non-tumour brain samples, suggesting upregulated OXPHOS expression in DIPGs. Our drug screening identified atovaquone as the most potent OXPHOS inhibitor of all the tested drugs and it was further explored in this chapter 4. Here, we investigated the efficacy of atovaquone alone, compared the efficacy of commercial atovaquone to ASD atovaquone formulation, and assessed the efficacy of the combination of atovaquone/proguanil and other with biguanides compared to atovaquone alone in a range of DIPG cultures.

As expected, atovaquone at 5-30 μM was found to significantly decrease the OCR of a range of DIPG cell lines within 1 hour of treatment (**Figure 4.1A-C**), highlighting its significance as a potent mitochondrial inhibitor in DIPG. This was further validated by Seahorse Mito Stress Test showing atovaquone treatment elicits a very similar inhibitory effect on mitochondrial respiration, ATP production, spare respiratory capacity and proton leak at 10-30 μM on all the tested DIPG cells (**Figure 4.2A-L**). These findings align with previously published work on atovaquone (134, 137-139). The observed decrease in OCR and the overall mitochondrial inhibitory effect from atovaquone could not be due to a decrease in cell number as 24 hour treatment with 30 μM atovaquone had no effect on the viability of DIPG cells (**Figure 4.5A**). This finding is important as it eliminates 'cell number change' as a factor in contributing to any observed changes from atovaquone treatment at 24 hours. Furthermore, no significant changes in ECAR (a surrogate marker for glycolysis) from atovaquone treatment suggests that it does not increase glycolysis as a compensatory mechanism to sustain survival of DIPG cells (**Figure 4.1D-F**). This also indicates that reprogramming of energy metabolism with Warburg's effect likely does not apply to DIPG cells treated with atovaquone and these cells might be utilizing additional metabolic pathways to sustain survival. In support of this, there has been varied responses in cancers treated with atovaquone, with some showing increase in glycolysis level as a compensation to mitochondrial inhibition (136-138) whereas no change in ECAR seen in other cancers (134). In the next steps, it would be interesting to further study this using metabolomics to assess changes in metabolic pathways and specific metabolites following atovaquone treatment.

The anti-mitochondrial activity of atovaquone is not specific to tumour cells only, as it decreased the OCR of hTERT IHA as well (**Figure 4.4A-B**), suggesting that it would also target the mitochondria of normal brain cells in the similar manner. However, the increase in ECAR of hTERT IHA indicates that these cells sustain atovaquone treatment by switching to glycolysis (**Figure 4.4C-D**). In another study, atovaquone treatment also decreased the OCR of normal retinal cells, however there was no change in the ECAR of these cells (134). As the purpose of investigating atovaquone as an OCR inhibitor against DIPG is to decrease hypoxia and hence sensitise these tumours to RT, the observed decrease in OCR of hTERT IHA should likely not be a concern as normal brain tissues are not generally hypoxic. To further support this, the excellent safety profile of atovaquone in both children and adults is well established with minimal reported side effects (109). Additionally, inhibition of mitochondrial biogenesis by anti-cancer therapies have also shown minimal cytotoxic effects on normal cells, with selectivity towards cancer cells (215, 216). Furthermore, prolonged treatment (72 hours) with 30 μM atovaquone did not significantly alter the viability of hTERT IHA compared to most of the DIPG cell lines, signifying some therapeutic window between DIPG tumour cells and normal cells (**Figure 4.5B**). Other studies have reported significant inhibition of cell viability from 10-30 μM atovaquone at 72 hour treatment (134, 135, 137-139, 141). Unlike other DIPG cell lines, the viability of SU-DIPG-VI was not significantly decreased from 30 μM atovaquone suggesting that this cell line is likely resistant at this dose. Nonetheless, the OCR inhibition response in all the DIPG cell lines was very similar.

The hypothesis that mitochondrial dysfunction by atovaquone could lead to an increase in oxygen availability and decrease tumour hypoxia was confirmed by a significant decrease in hypoxia staining in DIPG neurospheres by 2.5-30 μM atovaquone at 24 hour treatment (**Figure 4.7**). Again, as there was no change in cell number by 30 μM atovaquone at 24 hour treatment, so the observed decrease in hypoxia could not be due to a decrease in cell number. Previously, only one other study has assessed hypoxia inhibition in spheroids by atovaquone, showing decrease at 20-30 μM atovaquone in some cancer models (103), whereas our findings show hypoxia decrease in DIPG neurospheres at lower doses as well. Because we are proposing to repurpose atovaquone for hypoxic tumours, we also realised that culture time in experiments play a significant role and longer incubation is essential to obtain a hypoxic model to assess the efficacy of a hypoxia modifying agent. The 3 days (72 hour) culture condition appeared to be ideal for DIPG cells as HIF-1α was stabilised in control in comparison with 24 hour or 48 hour culture time (**Figure 4.8**). This means that similar to tumour growth *in vivo*, the DIPG

neurospheres grow bigger and become hypoxic after longer culturing (72 hours), and thus the efficacy of atovaquone could be well studied. This also highlights the significance of using 3D models to study hypoxia modifiers. 3D models develop hypoxic cores due to rapidly proliferating tumour cells forming an oxygenation gradient, with the central region becoming more hypoxic due to lack to oxygen diffusion compared to peripheral region (217). As opposed to our findings, HIF-1α inhibition was not observed in Aston et al. (2016) study because they assessed it on monolayers (103) whereas we looked at HIF-1α in DIPG neurospheres. We agree with the finding in Aston et al. (2016) study and our preliminary findings have also shown no HIF-1α inhibition in DIPG monolayers. Overall, atovaquone reduced hypoxia expression in 3D DIPG neurospheres which aligned with the decrease in HIF-1α, thus validating that atovaquone could be a potential hypoxia modifier for DIPGs.

In line with the observed decrease in hypoxia and HIF-1α expression in 3D DIPG neurosphere models, atovaquone also strongly improved the efficacy of RT in both of these DIPG models, thus confirming the radiosensitising efficacy of atovaquone. The culture time for DIPG neurospheres was kept consistent across hypoxia and HIF-1α inhibition, and radiosensitisation experiments. Atovaquone as a radiosensitiser as only been assessed by one study where 30 μM atovaquone+10Gy RT significantly decreased hypopharyngeal carcinoma spheroid regrowth. (103). In line with this, combination treatment significantly extended survival in hypopharyngeal carcinoma xenograft model (103). Our findings report radiosensitisation at lower doses 10 μM atovaquone+4Gy in HSJD-DIPG-007 and 20 μM atovaquone+4Gy in SU-DIPG-VI with comparable hypoxia and HIF-1α inhibition at those doses as well. This finding is significant as it highlights that achieving 10-20 μM atovaquone levels in the brain could be sufficient to radiosensitize DIPG tumour *in vivo*.

Additionally, Aston et al (2016) report no radiosensitisation in 2D monolayers up to 20 μM atovaquone+RT (103). This aligns with our results in both SU-DIPG-XVII monolayers and HSJD-DIPG-007 (cultured as monolayers). However, we observed radiosensitisation at 30 μM atovaquone+RT consistently in both DIPG monolayers. We suspect that the observed effect in monolayers is not be due to the reduction in hypoxia because (1) hypoxia cannot be easily modelled in monolayers, and (2) there was a different response in radiosensitisation in HSJD-DIPG-007 as 3D neurospheres compared to HSJD-DIPG-007 as monolayers. As atovaquone induced ROS in a dose dependent manner (**Figure 4.6**), our further investigations showed increased ROS at 30 μM atovaquone+RT in monolayers, suggesting ROS induced oxidative

stress could explain the observed radiosensitisation at higher doses in monolayers. Normal cell functioning requires low levels of ROS which regulates mitosis and apoptosis, however, increased ROS levels induce oxidative stress that could damage key cellular components and molecules such as proteins, lipids and DNA and thus induce cell death (214). The combination of RT and ROS-inducers can lead to intolerable stress, irreparable damage to signalling and DNA, and lead to apoptosis and cell death (214). Similar to our findings, past studies have also shown increased ROS from atovaquone alone treatment (136, 138, 218), however oxidative stress from the combination of atovaquone+RT has not been previously shown. Additionally, cancer cells can use several mechanisms to prevent redox-induced stress such as activation of antioxidant defence systems, including peroxide scavengers that reduce hydrogen peroxide to water (219). Thus, sustained accumulation of ROS would be required to trigger cell death. It is likely that higher doses of atovaquone and RT sustain ROS accumulation and thus also contribute to DIPG radiosensitisation.

Our *in vitro* findings of hypoxia and HIF-1a inhibition by atovaquone (**Figure 4.7-4.8**) were also supported by the KEGG pathway analysis and GVSA identifying significant downregulation of HIF-1a signalling pathway and decrease in the activation of hypoxia pathway (**Figure 4.11-4.13**). GSVA also identified increase in ROS pathway following atovaquone treatment (**Figure 4.13**), thus supporting our *in vitro* results of increased ROS levels (**Figure 4.6**). Interestingly, both KEGG and GVSA identified increase in cholesterol synthesis following atovaquone treatment suggesting that HSJD-DIPG-007 cells are potentially shifting to cholesterol metabolism. This finding provides new direction towards investigating the combination of cholesterol synthesis inhibitors with atovaquone for future DIPG studies. Other interesting findings include atovaquone leading to the activation of immune system pathways (interferon gamma response, interferon alpha response, IL-6/JAK/STAT3 signalling, TNFA signalling via NFKB, and IL2/STAT5 signalling). As hypoxia negatively influences immune responses and creates an immunosuppressive microenvironment (58), decrease in hypoxia by atovaquone might have resulted in the activation of immune system pathways. This also means that investigating the triple combination of atovaquone, immunotherapy, and radiotherapy could be interesting approaches for future studies.

Moreover, we did not find a lot of pathway changes following RT alone treatment likely because the cells were collected within 24 hours post-treatment and significant changes from

RT might require weeks to occur. We followed this treatment setup because we were interested in assessing the transcriptomic changes in HSJD-DIPG-007 cells to support our radiosensitisation results. However, we did find that addition of RT to atovaquone significantly downregulated cell cycle and DNA replication pathways (**Figure 4.11**), decreased the activation of E2F and G2M checkpoint pathways and increased p53 signalling pathway (**Figure 4.13**). All of these suggest that the combination of atovaquone+RT is inducing cell death of HSJD-DIPG-007 cells by affecting the cell cycle pathways.

Following confirmed hypoxia modification and radiosensitising efficacy of atovaquone against DIPG, we addressed its limited BBB penetration issue by investigating ASD atovaquone formulation. ASD formulations are attractive approaches to improve the bioavailability of poorly soluble drugs. Here formulation 1 containing 20% atovaquone, 70% PVP K30, 2.5% Capmul MCM NF, 2.5% Captex 300 NF and 5% Tween80 was used (123). A comparison between commercial atovaquone and ASD atovaquone formulation was essential as the ASD formulation also comprised of additional components unlike pure atovaquone. We showed for the first time that both formulations resulted in similar OCR and hypoxia decrease, adding confidence in investigating the ASD atovaquone for *in vivo* DIPG models. Dosing ASD atovaquone at 100 mg/kg was found to achieve ~37(123) μM brain levels. Our findings have shown that 10 μM atovaquone is sufficient to decrease OCR, inhibit hypoxia and improve the radiosensitivity of DIPG models *in vitro*, thus achieving these levels in the brain will help overcome the major hurdle in treating brain tumours – the BBB. Additionally, as atovaquone is administered orally and not through the invasive approaches such as intrathecally or intravenously, this makes the treatment delivery attractive for paediatric patients.

Assessing the combination of atovaquone/proguanil in DIPG revealed no synergism suggesting that the combination is specific to parasites. The combination targets the parasites mitochondrion, decreasing MMP and inducing parasite cell death. Inhibition of the bc_1 complex by atovaquone inhibits DHODH, inhibiting *de novo* pyrimidine synthesis (109). Proguanil enhances this destabilisation effect of atovaquone (109). Unlike parasites, mammalian cells can also use the salvage pathway to form pyrimidines and survive the combination's effect (128). This could be a possible reason to explain no synergistic proliferation inhibition from the combination against DIPG despite testing a range of doses and combinations.

It is reported in the literature that unlike other biguanides (phenformin and metformin), proguanil has limited mitochondrial penetrability. This is true for lower doses of proguanil as past studies only assessed the OCR inhibition from proguanil at 2 μM and 7 μM (150, 151). Similarly, we found no changes in OCR of DIPG cells treated with proguanil doses up to 25 μM. However, our findings (**Figure 4.16E**) and Gupta et al. (2024) study indicate that proguanil likely penetrates the mitochondria at higher doses evidenced by a significant decrease in OCR of DIPG cells and breast cancer cells (inhibition seen at 50 μM, 100 μM in our study and 40 μM in Gupta et al's study) (156). Hydrophobicity of the biguanides likely influence mitochondrial penetrability and OCR inhibition and there seems to be an inverse relationship between hydrophobicity and biguanide dose inhibiting OCR (150, 151). The order of hydrophobicity is proguanil and phenformin are more hydrophobic than metformin requiring 67 μM, 0.43 mM and 19.4 mM doses to inhibit mitochondrial complex I (151). This supports our findings as we also show proguanil and phenformin inhibit OCR at micromolar levels compared to millimolar levels for metformin.

When combined with proguanil, the OCR inhibition efficacy of atovaquone was worsened i.e., an antagonistic effect was observed. No previous study has assessed the combination's efficacy on cancer cells, however when tested on parasite-infected cells, proguanil concentrations up to 20 μM did not affect mitochondrial respiration and had no effect on the respiration inhibition by atovaquone (148). In another study, the inhibition of OCR of *P. Falciparum* is very similar to atovaquone/proguanil combination and atovaquone alone, 64% and 61% respectively (220). This inhibition of OCR appears to be primarily from atovaquone, with no effect from the addition of proguanil. These findings oppose our findings on cancer cells where the combination appears to impair atovaquone's OCR inhibition efficacy. This observation is likely a biguanide class effect as similar antagonistic OCR response was observed by combining other biguanides phenformin and metformin with atovaquone. A possible explanation for the observed antagonistic trend could be the fact that along with inhibiting mitochondrial complex I, all biguanides also appear to inhibit ATP hydrolysis (151). Inhibition of ATP hydrolysis will prevent the depletion of ATP and try to restore cellular function (221). This could potentially impact the OCR inhibition by the combination of atovaquone/biguanides. Overall, these findings suggest that the combination of atovaquone/proguanil is parasite specific and not ideal for further investigations against DIPG and other cancers.

The results of this chapter highlight the promising hypoxia modification and radiosensitisation efficacy of atovaquone against DIPG. Similar responses from commercial vs the BBB penetrant ASD atovaquone formulation pave a way for assessing the radiosensitising efficacy of this new formulation using orthotopic DIPG models. The combination of ASD atovaquone with RT is examined in “Chapter 6 Animal Studies”.

Chapter 5

Mefloquine – A Potential Radiosensitizer for Diffuse Intrinsic Pontine Glioma

Chapter 5. Mefloquine – A Potential Radiosensitizer for Diffuse Intrinsic Pontine Glioma

5.1. Introduction

The previous chapter demonstrates the promising hypoxia modification and radiosensitising efficacy of atovaquone, the most potent OCR inhibitor identified from our anti-parasitic drug screening against DIPG cultures. The second OCR inhibitor from our screening was ivermectin, however its limited BBB penetrability prevented us from conducting any further investigations on this drug. Mefloquine also significantly reduced the OCR of DIPG cultures and has been widely explored as an anti-cancer agent. This chapter will further investigate on mefloquine as another potential radiosensitiser of DIPG *in vitro*.

Mefloquine belongs to the quinoline class of antimalarials and has been widely used for the chemoprophylaxis and management of malaria for more than three decades (222, 223). It targets *P. falciparum* by binding to the cytoplasmic ribosome (80S subunit), thus inhibiting protein synthesis and killing the malarial parasite (161). Alongside other antimalarials, numerous studies have also reported the pleiotropic effects of mefloquine on cancer cells. Repurposing of mefloquine as an anti-cancer agent is attractive as it has a long-standing clinical record, is inexpensive and also readily available. Although mefloquine continues to be prescribed, its long-term use might result in neuropsychiatric adverse reactions in some patients, hence dose adjustment and monitoring would be required (224).

Mefloquine has been shown to induce cancer cell death via several mechanisms. These include oxidative stress and lysosomal disruption in acute myeloid leukemia (175), chronic lymphocytic leukemia (177), chronic myeloid leukemia (174), and GBM cells (162); inhibiting autophagy in breast cancer cells (176); inhibiting mitochondrial function and mTOR pathway in cervical cancer (173); inhibiting NF-kB signalling and disrupting endolysosomal RAB5/7 in colorectal cancer cells (178, 225); inducing mitochondrial autophagy in esophageal squamous cell carcinoma (ESCC) (179); inhibiting PI3K/AkT/mTOR signalling in gastric cancer (180); suppressing β-catenin pathway in liver cancer (181); and ROS-mediated modulation of Akt, ERK, JNK and AMPK signalling pathways in prostate cancer (182). Additionally, mefloquine has also been reported as an inhibitor of drug efflux pumps including

P-glycoproteins (226), and thus could sensitise resistant cancer cells to standard chemotherapy agents. Currently, an ongoing clinical trial is investigating mefloquine in combination with temozolomide, memantine hydrochloride and metformin in GBM patients after RT (NCT01430351).

Mefloquine appears to be a promising anti-cancer agent with high BBB penetrability, however its efficacy against DIPG has not been explored yet. With a range of known anti-cancer mechanisms of mefloquine, several of these could also augment the effects of radiation, the standard therapy for DIPG. Although identified to induce mitochondrial dysfunction, no previous study has investigated hypoxia modification by mefloquine. Moreover, the radiosensitising efficacy of mefloquine has also not been investigated against any cancer type. As mefloquine exhibits a range of anti-cancer properties in several cancers, it would be interesting to explore its mechanism of action and radiosensitising efficacy against DIPG.

In this chapter, the effect of mefloquine on cell proliferation is assessed by MTS cell proliferation and clonogenic assays. Mitochondrial inhibition and hypoxia inhibition efficacies of mefloquine are assessed by extracellular flux assays, western blots and 3D neurosphere assays for hypoxia. Oxidative stress and radiosensitisation are assessed by flow cytometry and clonogenic assays.

5.2. Results

5.2.1 Mefloquine treatment decreases viability and colony formation capacity of DIPG cells

We first examined the effects of mefloquine on the viability of a panel of DIPG cell lines HSJD-DIPG-007, HSJD-DIPG-012, HSJD-DIPG-013, SU-DIPG-VI, SU-DIPG-XVII using MTS cell proliferation assays. These cell lines were tested in comparison to a normal human astrocyte cell line, hTERT IHA. Treatment with 5 μM mefloquine for 72 hours reduced the viability of HSJD-DIPG-007 (5% remaining viable cells), HSJD-DIPG-012 (13%), HSJD-DIPG-013 (50%), with minimal effect on hTERT IHA (92%), SU-DIPG-VI (98%) and SU-DIPG-XVII (99%) (**Figure 5.1**). Treatment with 10 μM mefloquine for 72 hours reduced the viability of all the DIPG cell lines and also hTERT IHA by > 80% (**Figure 5.1**). The IC_{50} values were calculated for each of the cell lines treated with mefloquine for 72 hours (**Table 5.1**). The IC_{50} values for HSJD-DIPG-007, HSJD-DIPG-012 and HSJD-DIPG-013 are lower than the control cell line hTERT IHA, whereas the IC_{50} values of SU-DIPG-VI and SU-DIPG-XVII are higher than hTERT IHA (**Table 5.1**).

To further assess the anti-proliferative efficacy of mefloquine, we assessed its effect on the colony formation capacity of DIPG cells using soft agar and liquid clonogenic assays. Treatment with mefloquine resulted in a significant dose-dependent decrease in colony numbers in all tested DIPG cell lines HSJD-DIPG-007, SU-DIPG-VI and SU-DIPG-XVII (*P < 0.05, **P < 0.01, ****P < 0.0001, respectively; **Figure 5.2A-C**). Representative survival fraction bar graphs were also plotted showing dose-dependent decrease in surviving fraction (%) of all DIPG cell lines with increasing doses of mefloquine from 0-10 μM (**Figure 5.2D-F**). Thus, mefloquine treatment decreases cell viability and colony formation of all the tested DIPG cell lines.

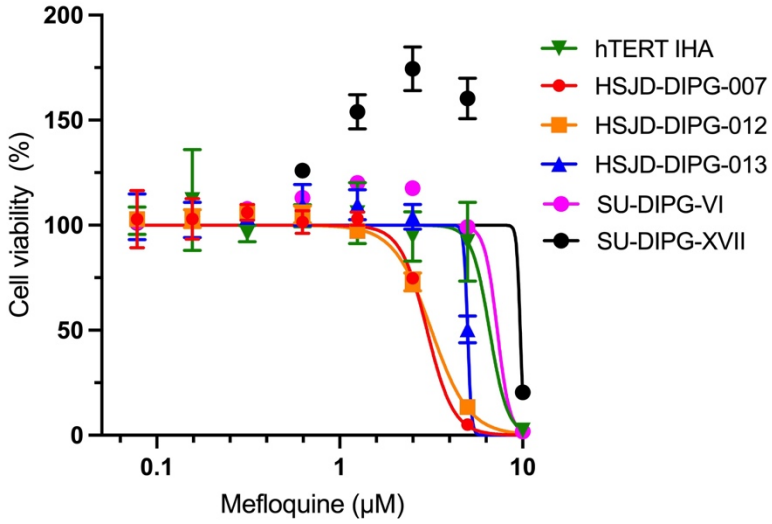

Figure 5.1. *In vitro* effect of mefloquine on the cell viability of DIPG cells and hTERT IHA.
Cells were treated with increasing concentrations of mefloquine for 72 hr and cell viability assessed using MTS cell proliferation assay. Data represents mean cell viability following mefloquine treatment of three independent experiments. Error bars indicate SD; n=3.

Table 5.1. IC_{50} values for mefloquine treatment at 72 hrs on a panel of DIPG cell lines determined by MTS cell viability assays (μM).

Cell Lines	IC_{50} (μM) of Mefloquine
HSJD-DIPG-007	3.00
HSJD-DIPG-012	3.17
HSJD-DIPG-013	5.00
SU-DIPG-VI	7.27
SU-DIPG-XVII	9.70
hTERT IHA	6.75

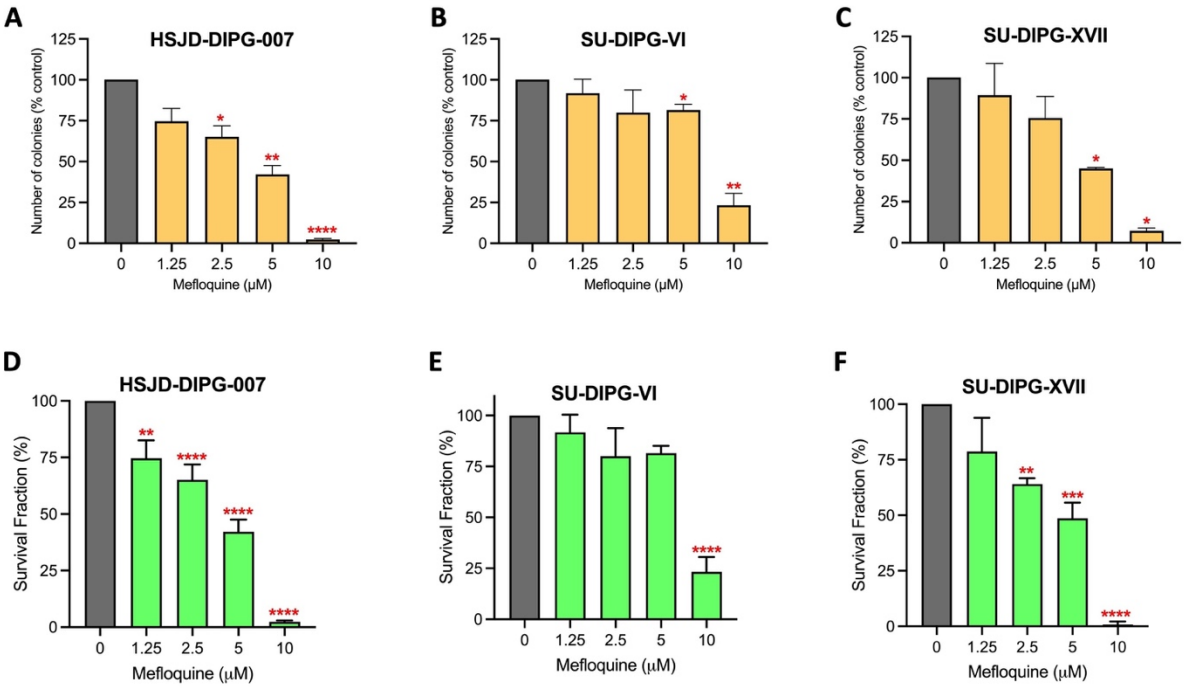

Figure 5.2. Effect of mefloquine on colony formation of DIPG cells.
(A-B) HSJD-DIPG-007 and SU-DIPG-VI neurospheres were cultured overnight and treated with 0-10 μM mefloquine for 24 hours. Drug was removed and cells were seeded on agarose and grown for 14 days. Colonies were stained with MTT. (C) SU-DIPG-XVII cells were cultured overnight and treated 0-10 μM mefloquine for 24 hours. Drug was removed and cells allowed to grow for 14 days. Colonies were stained with crystal violet dye. Colonies were counted manually. Data represents mean colony numbers following mefloquine treatment of two independent experiments. Error bars indicate SD; n=3. Statistical analysis was performed using one-way ANOVA with Tukey's multiple comparisons test, data is presented relative to control (*P < 0.05, **P < 0.01, ****P < 0.0001). (D-F) Bar graph showing dose dependent decrease in survival fraction (%) of DIPG cell lines with increasing doses of mefloquine from 0-10 μM. Statistical analysis was performed using one-way ANOVA with Tukey's multiple comparisons test, data is presented relative to control (**P < 0.01, ***P < 0.001, ****P < 0.0001). Data are presented as means ± SD of two independent experiments with three replicates in each.

5.2.2 Mefloquine increases radiosensitivity of DIPG neurosphere cultures

Following the observed anti-proliferative and colony inhibition capacity of mefloquine, we aimed to assess its radiosensitising efficacy against DIPG cultures. The 3D suspension cultures, HSJD-DIPG-007 and SU-DIPG-VI cells were cultured for 3 days (at 20% O_2) and then treated with mefloquine and 2-4 Gy RT. Mefloquine doses to combine with RT were based on our results in **Figure 5.2** i.e., 2.5 µM and 5 µM for HSJD-DIPG-007 and 5 µM and 10 µM for SU-DIPG-VI. This was because these doses did not completely inhibit colony growth in these cell lines and hence any additive/synergistic effect from RT could be quantified. Mefloquine treatment at 5 µM sensitised HSJD-DIPG-007 neurospheres to radiation with a significant decrease in surviving fraction and colony numbers observed at 5 µM mefloquine+2Gy RT and 5 µM mefloquine+4Gy RT (**Figure 5.3A-B**). Similarly, mefloquine treatment at 10 µM sensitised SU-DIPG-VI neurospheres to radiation with a significant decrease in surviving fraction and colony numbers observed at 10 µM mefloquine+2Gy RT and 10 µM mefloquine+4Gy RT (**Figure 5.3C-D**).

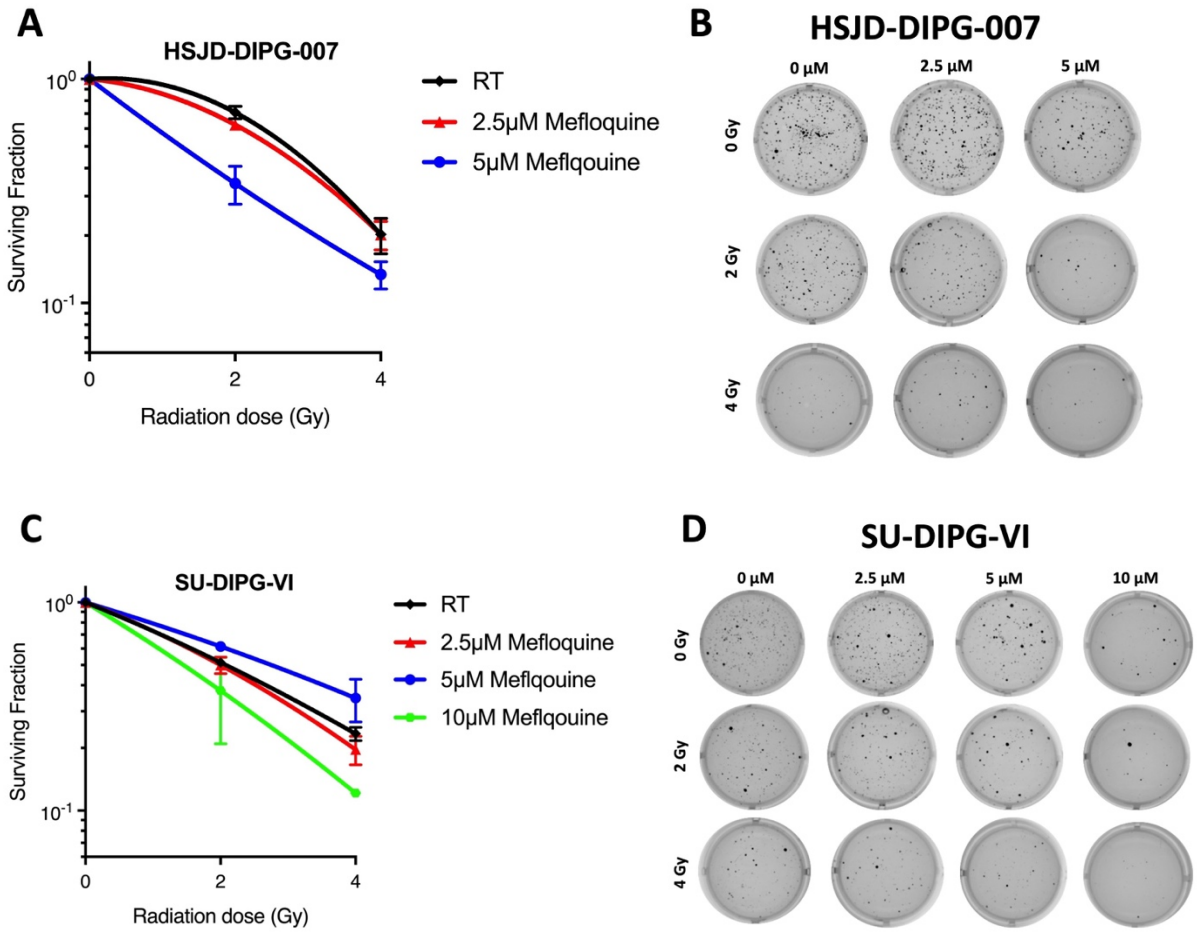

Figure 5.3. Effect of mefloquine on the radiosensitivity of DIPG cultures.
(A-D) HSJD-DIPG-007 and SU-DIPG-VI neurospheres were cultured for 72 hours and treated with 2.5-10 μM mefloquine for 6 hours followed by 2-4 Gy RT. After 24 hour treatment, drug was removed and cells were seeded on agarose and grown for 14 days. Colonies were stained with MTT dye. Data are presented as means ± SD of two independent experiments with three replicates in each.

5.2.3 Mefloquine induces mitochondrial dysfunction in DIPG neurospheres

Once the radiosensitising efficacy of mefloquine was confirmed, we now assessed the possible mechanisms of the observed radiosensitisation of DIPG neurospheres. It is reported in the literature that mitochondrial dysfunction and mitochondrial autophagy as one of the anti-cancer mechanisms of mefloquine (173, 179). Mefloquine also decreased the OCR of SU-DIPG-XVII and HSJD-DIPG-007 at 10 µM (from our anti-parasitic drug screening). We were interested in assessing whether mefloquine induces mitochondrial dysfunction by decreasing OCR in the 3D neurosphere cultures at the doses equivalent to radiosensitisation findings i.e., 5 µM for HSJD-DIPG-007 and 10 µM for SU-DIPG-VI. HSJD-DIPG-007 and SU-DIPG-VI cells were treated with 2.5-10 µM mefloquine for 4 hour and also 24 hour (pre-treatment) and the OCR and ECAR were analysed using XFe24 Seahorse Analyser. Mefloquine significantly inhibited the OCR of HSJD-DIPG-007 at 5 µM reaching 76% at 4 hour treatment and 64% at 24 hour treatment (**P < 0.01, ****P < 0.0001, respectively; **Figure 5.4A-B**). Mefloquine significantly inhibited the OCR of SU-DIPG-VI at 10 µM reaching 57% at 4 hour treatment and 40% at 24 hour treatment (***P < 0.001, ****P < 0.0001, respectively; **Figure 5.4C-D**). Alongside inhibiting the OCR, mefloquine treatment also significantly decreased the ECAR of HSJD-DIPG-007 at 5 µM reaching 78% at 4 hour treatment and 74% at 24 hour treatment (*P < 0.05, ****P < 0.0001, respectively; **Figure 5.4E-F**). Similarly, there was also a significant decrease in the ECAR of SU-DIPG-VI with 10 µM mefloquine treatment, reaching 63% at both 4 hour and 24 hour treatment (*P < 0.05, ****P < 0.0001, respectively; **Figure 5.4G-H**). Overall, mefloquine decreased both the OCR and ECAR of DIPG cultures.

We also examined the effect of mefloquine on the overall mitochondrial profile of HSJD-DIPG-007 cells using a Seahorse Mito Stress Test. Mefloquine treatment induces mitochondrial dysfunction in DIPG cells evidenced by a significant decrease in basal respiration, maximal respiration, ATP production, spare respiratory capacity and proton leak at 5 µM and 10 µM compared to control (**P < 0.01, ****P < 0.0001; **Figure 5.5A-E**).

The specific mitochondrial target of action of mefloquine is not known. A recent study on ESCC cells identified that mefloquine targets the mitochondrial complex II subunit proteins succinate dehydrogenase C (SDHC) and succinate dehydrogenase D (SDHD) suggesting downregulation of complex II (179). Therefore, we assessed whether mefloquine also affects SDHC and SDHD protein levels of DIPG cells. Western blot analysis revealed that mefloquine

treatment at 5 μM caused a significant decrease in only SDHD levels in HSJD-DIPG-007 cells (**Figure 5.6A-B**), indicating complex II dysfunction.

To further understand whether mefloquine only targets mitochondrial complex II in DIPG, we also examined its effects on all the mitochondrial ETC complexes. HSJD-DIPG-007 cells were pre-treated with 5-10 μM mefloquine for 24 hours and permeabilised with 3 nM XF PMP. Mefloquine at 5 μM caused a slight decrease in the OCR of complex I (89%) whereas the complex specific OCR for complex II, III and IV were significantly decreased to 72%, 77% and 76% respectively relative to control (*P < 0.05, **P < 0.01; **Figure 5.6C**). Treatment with mefloquine at 10 μM significantly decreased the complex specific OCR of all the complexes I, II, III and IV to 38%, 14%, 15% and 50% respectively relative to control (***P < 0.001, ****P < 0.0001; **Figure 5.6C**, suggesting that it affects the entire mitochondria at all complex levels.

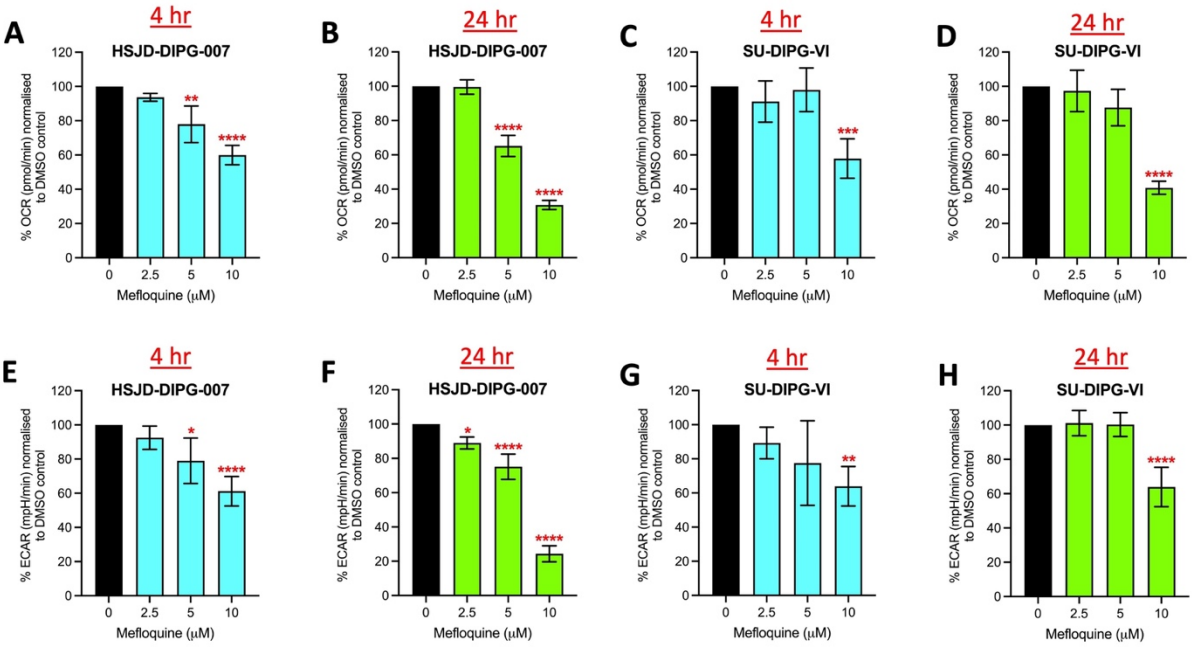

Figure 5.4. Metabolic changes in oxygen consumption rate (OCR) and extracellular acidification rate (ECAR) of DIPG cell lines following treatment with mefloquine.
HSJD-DIPG-007 and SU-DIPG-VI cells were treated with mefloquine (2.5-10 μM) or DMSO control and OCR and ECAR were measured in real-time using Seahorse XFe24 Analyser over a period of 4 hour (real-time) or 24 hour (pretreatment). Data is normalised to DMSO control (0 μM mefloquine). Statistical analysis was performed using one-way ANOVA with Tukey's multiple comparisons test, data is presented relative to control (0 μM mefloquine) (*P < 0.05, **P < 0.01, ***P < 0.001, ****P < 0.0001). Data are presented as means ± SD of two independent experiments with three replicates in each.

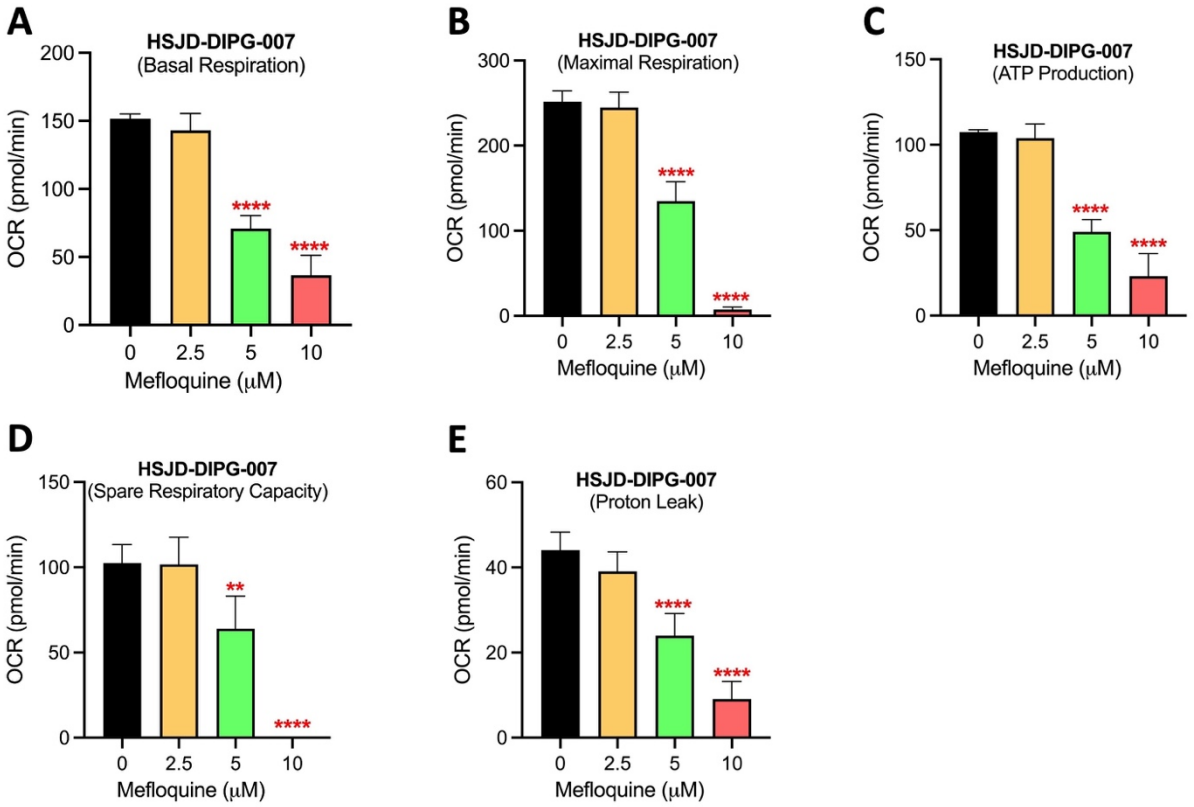

Figure 5.5. Quantification of mitochondrial function following mefloquine treatment.
HSJD-DIPG-007 cells were treated with mefloquine (2.5-10 μM) or DMSO control and several mitochondrial parameters – basal respiration, maximal respiration, ATP production, spare resp. capacity and proton leak were measured using Seahorse XF Cell Mito Stress Test Assay. Statistical analysis was performed using one-way ANOVA with Tukey's multiple comparisons test, data is presented relative to control (0 μM mefloquine) (**P < 0.01, ****P < 0.0001). Data are presented as means ± SD of two independent experiments with three replicates in each.

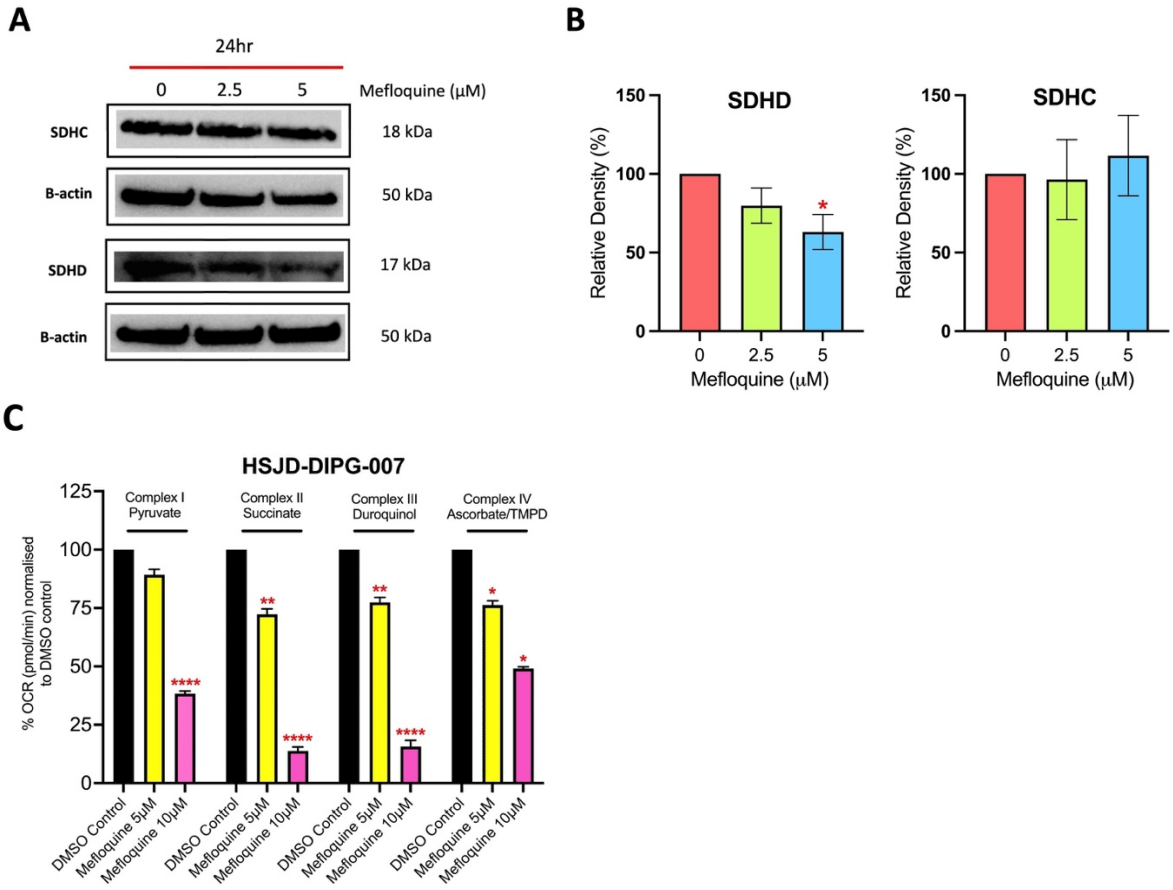

Figure 5.6 Effect of mefloquine on mitochondrial complexes.
(A) Effect of mefloquine on complex II subunits SDHD and SDHC. HSJD-DIPG-007 cells were treated with 2.5-5 μM mefloquine for 24 hours. Staining was performed using primary antibodies rabbit anti-SDHC (1:10,000), rabbit anti-SDHD (1:500), and rabbit anti-β-actin (1:1000). (B) Bar graph of western blot densitometry. Statistical analysis was performed using t-tests, data is presented mean % intensity of SDHD and SDHC normalised to mean % intensity of β-actin (*P<0.05). Each experiment was performed twice. (C) Real-time XF assay measuring mitochondrial complexes specific activity following mefloquine treatment. HSJD-DIPG-007 cells were pretreated with 5 μM and 10 μM mefloquine. Cells were permeabilised with 3 nM XF PMP and OCR was measured using XFe24 analyser. The changes in OCR in response to the different injections was used to determine complex specific activity. Details for calculating complex specific OCR are outlined in the methods chapter. Statistical analysis was performed using one-way ANOVA with Tukey's multiple comparisons test, data is presented relative to control (*P < 0.05, **P<0.01, ***P<0.001, ****P < 0.0001). Data are presented as means ± SD of two independent experiments with three replicates in each.

5.2.4 Mefloquine reduces hypoxia and inhibits HIF-1α expression in DIPG neurospheres

As explained in **chapter 4**, our study hypothesis proposed that inhibition of mitochondrial OXPHOS and OCR of the DIPG cells would spare more available oxygen and thus reduce hypoxia. Since mefloquine decreased the OCR and sensitised HSJD-DIPG-007 cells to RT at 5 μM and SU-DIPG-VI cells at 10 μM, we were interested in assessing whether it decreases hypoxia at similar doses. HSJD-DIPG-007 and SU-DIPG-VI cells were cultured for 3 days to generate neurospheres ~500 μm in diameter. Treatment with 5 μM mefloquine at 24 hours resolved hypoxia evidenced by a complete loss of image iT green hypoxia dye staining in HSJD-DIPG-007 neurospheres, whereas no change was seen at 2.5 μM mefloquine (**Figure 5.7A**). Similarly, treatment with 10 μM mefloquine at 24 hours resolved hypoxia evidenced by a complete loss of image iT green hypoxia dye staining in SU-DIPG-VI neurospheres, whereas no change was seen at 2.5 μM and 5 μM mefloquine (**Figure 5.7B**).

Hypoxia modification by mefloquine was further confirmed by assessing its effect on the expression of the hypoxia regulator HIF-1α. HSJD-DIPG-007 and SU-DIPG-VI cells were cultured for 3 days (at 20% O_2) to form hypoxic neurospheres before treatment with mefloquine. Strong HIF-1α protein expression was observed at 0 μM mefloquine in HSJD-DIPG-007 neurospheres showing HIF-1α is stabilised under hypoxia (**Figure 5.8A**). A decrease in HIF-1α expression was observed in HSJD-DIPG-007 neurospheres treated with 5 μM mefloquine for 24 hours (**Figure 5.8A**). Similarly, there was a decrease in HIF-1α expression in SU-DIPG-VI neurospheres treated with 10 μM mefloquine for 24 hours (**Figure 5.8B**).

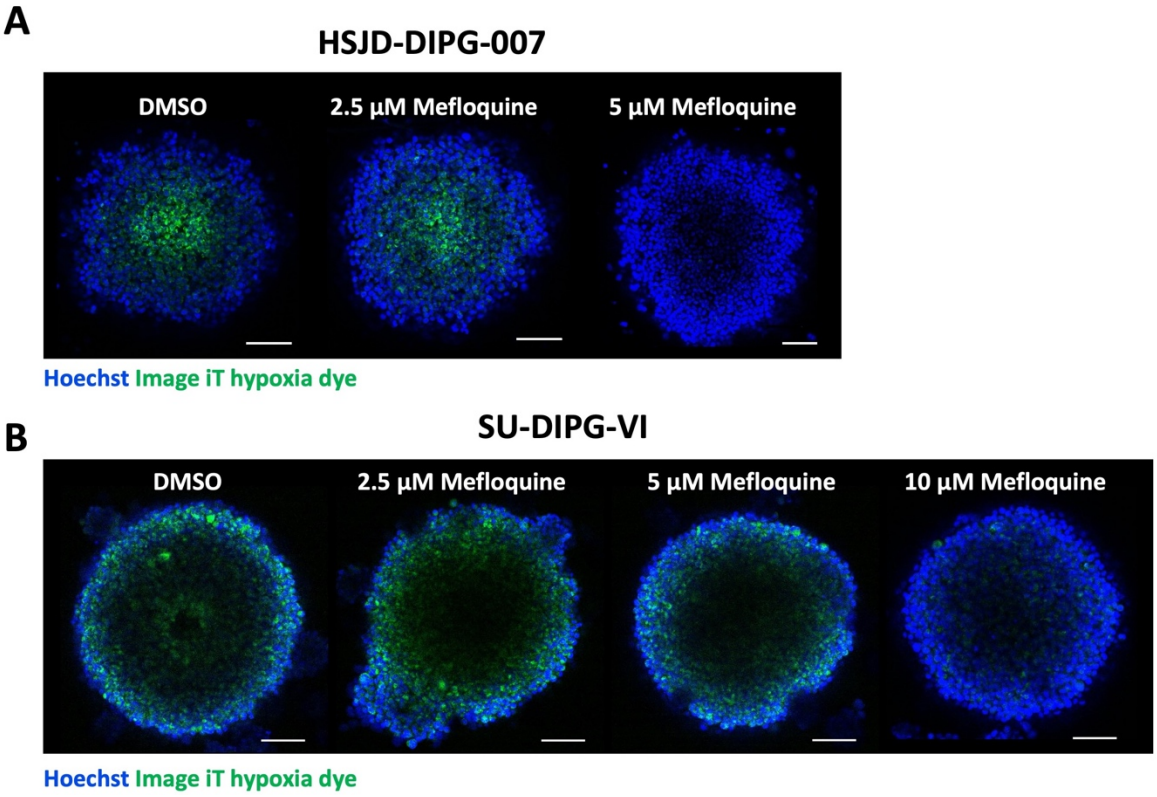

Figure 5.7. Effect of mefloquine treatment on hypoxia within DIPG neurospheres.
(A) HSJD-DIPG-007 and (B) SU-DIPG-VI neurospheres were cultured for 3 days to obtain neurospheres ~500 µm in diameter. These were treated with a range of mefloquine doses 2.5-10 µM for 24 hours. Image iT hypoxia dye (green staining for hypoxia) and Hoechst (blue staining for nuclei) were used to stain the neurospheres. Five replicates per condition were setup and the experiment was performed twice. Scale bar = 100 µm.

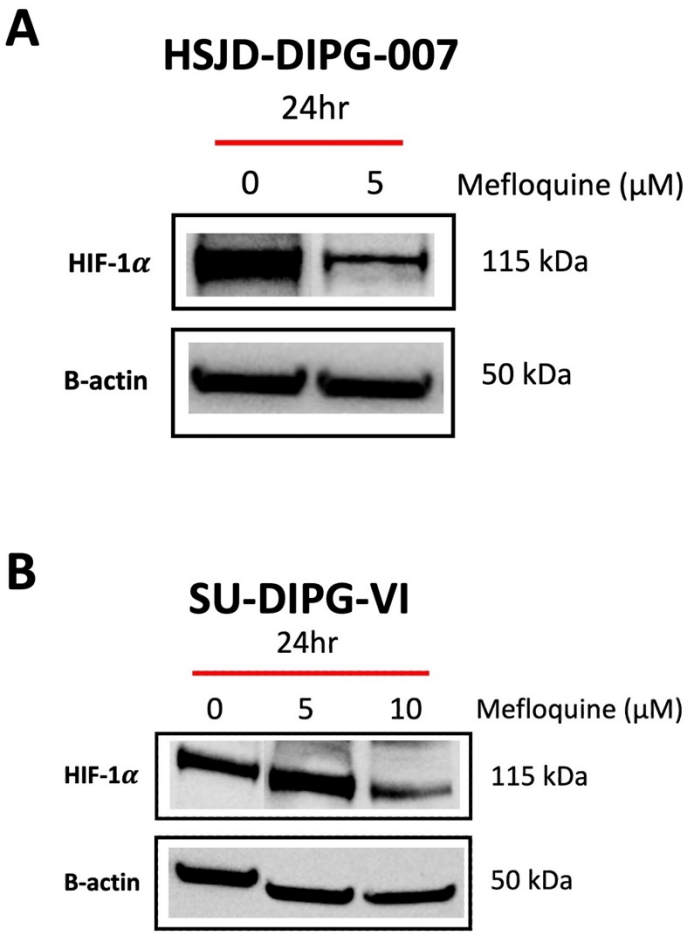

Figure 5.8. Effect of mefloquine treatment on HIF-1α expression in DIPG neurospheres.
(A) HSJD-DIPG-007 and (B) SU-DIPG-VI neurospheres were cultured for 72 hours and treated with mefloquine for 24 hours. Staining was performed using primary antibodies rabbit anti-HIF-1α (1:1000) and rabbit anti-β-actin (1:1000) for HIF-1α and β-actin respectively. Each experiment was performed twice.

5.2.5 Mefloquine treatment increases reactive oxygen species induced oxidative stress in DIPG neurospheres

ROS induced oxidative stress is one of primary sources of dysfunctional mitochondria. As mefloquine appears to decrease mitochondrial functionality, we now assessed its effect on ROS levels at the same dose where it decreased OCR, hypoxia, and sensitised DIPG cells to RT. HSJD-DIPG-007 cells were treated with 5 µM mefloquine and mitochondrial and cellular ROS were measured using MitoSOX Red and DHE dyes. There was a significant increase in MitoSOX Red and DHE fluorescence in HSJD-DIPG-007 cells (**Figure 5.9A-B**). The mean MitoSOX Red fluorescence was 2.08-fold higher and mean DHE fluorescence was 1.30-fold higher compared to control in HSJD-DIPG-007 cells (***P < 0.001, **P<0.01, respectively; **Figure 5.9A-B**).

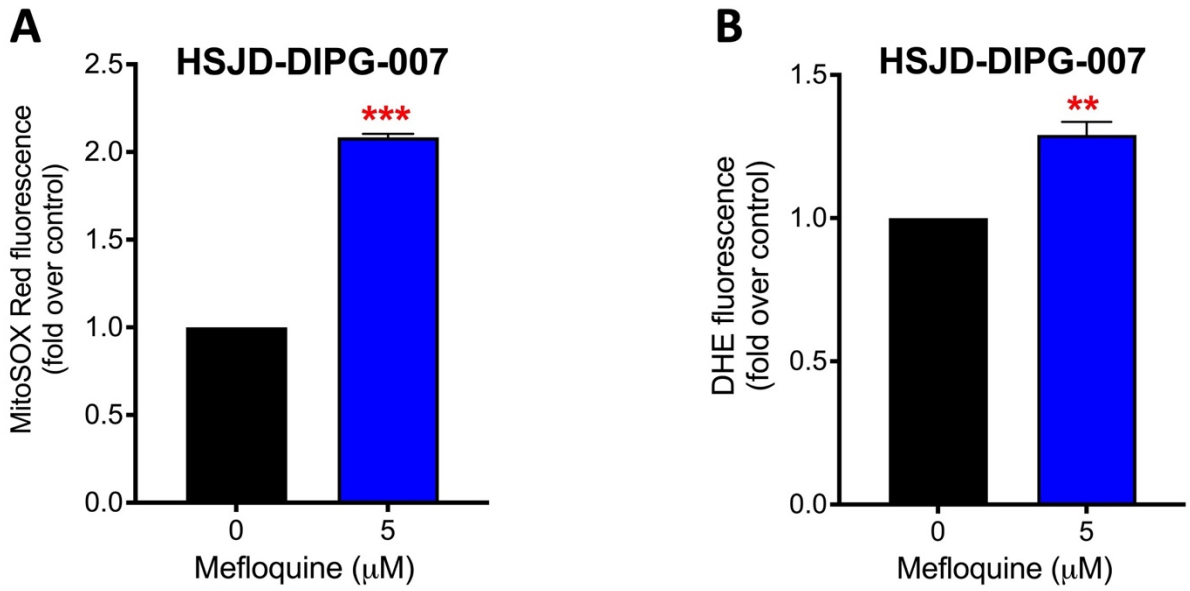

Figure 5.9. Reactive oxygen species production in DIPG cells in response to mefloquine treatment. HSJD-DIPG-007 cells were treated 5 µM mefloquine for 24 hour. Cells were then stained with MitoSOX Red and dihydroethidium (DHE) dyes for 30 mins, washed and analysed with flow cytometry. (A) Mean MitoSOX Red fluorescence. (B) Mean DHE fluorescence. Statistical analysis was performed using t-tests, data is presented as mean fluorescence normalised to DMSO control within each experiment (**P<0.01, ***P<0.001). Data are presented as means ± SD of two independent experiments with three replicates in each.

5.3. Discussion

The results of this chapter highlight the anti-proliferative efficacy, mitochondrial inhibition and promising hypoxia decrease by mefloquine in DIPG cell lines. As DIPGs appear to have upregulated OXPHOS (shown in chapter 3), targeting the mitochondria with mefloquine could resolve hypoxia and also sensitise DIPG to RT. Indeed, the results in this chapter demonstrate that combining mefloquine with RT could radiosensitise DIPG cultures, thus providing evidence of mefloquine as a potential radiosensitiser for DIPG.

Our findings however demonstrate a therapeutic window between some DIPG cell types and normal cells only at lower doses of mefloquine ~5 μM. Despite the potent anti-proliferative efficacy, the drug may only be effective in certain DIPG types that are sensitive to lower mefloquine doses. This is because IC_{50} values of mefloquine for DIPG cells and normal hTERT IHA are in a very similar range pointing towards potential side effects from the drug. This means that repurposing of mefloquine for DIPG treatment would require tight monitoring of patients. Mefloquine is already listed on the WHO list of medicines with well-known side effects. It is reported in the literature that long term use of mefloquine has been associated with neurotoxicity in a minority of patients (227), however its use may be justified in situations where limited treatment options are available i.e., in patients with late-stage cancer. Interestingly, past studies have shown that mefloquine has some therapeutic window between leukemia cells (EC_{50} ~ 8 μM) compared to normal murine bone marrow mononuclear cells (EC_{50} ~ 31.8 μM) (175). Similarly, mefloquine at 10 μM significantly reduced the viability of ESCC cells with no effect on control human embryonic esophageal cells (179). This suggests that normal brain cells could be more sensitive to mefloquine treatment compared to other body cells. However, as mefloquine inhibits the drug efflux pumps P-glycoproteins (226), understanding its anti-cancer mechanism in DIPGs and combining it with other potent drugs could lower mefloquine doses and sensitise the radioresistant DIPG cells to RT.

From the widely reported anti-cancer mechanisms of mefloquine, only two previous studies have explored mitochondrial dysfunction following mefloquine treatment (173, 179). Proteomic and RNA sequencing analysis on ESCC cells suggested that mefloquine treatment mainly affects the mitochondria, inducing significant changes at protein level including in mitochondrial envelope, mitochondrial membrane, succinate dehydrogenase and electron

carrier activity (179). They also reported downregulation of four mitochondrial proteins SDHD, SDHC, NADH: ubiquinone oxidoreductase subunit V3 (NDUFV3) and mitochondrially encoded cytochrome c oxidase III (MTCO3) in response to mefloquine treatment (179). Mitochondrial complex II consists of four subunit proteins SDHA, SDHB, SDHC and SDHD. Our results show that mefloquine decreases the protein expression of SDHD in HSJD-DIPG-007 cells (**Figure 5.6A-B**), suggesting that it induces complex II dysfunction. SDHD anchors the complex II to the inner mitochondrial membrane and serves to transfer electrons to ubiquinone (228). Dysfunction of SDHD could impair complex II dependent mitochondrial respiration, and also impair complex I dependent respiration (228). This aligns with our findings as 5 μM mefloquine significantly decreased the complex II dependent OCR and also slightly decreased the OCR of complex I in HSJD-DIPG-007 cells (**Figure 5.6B**). The 5 μM dose was likely not strong enough, however at higher mefloquine dose of 10 μM, a significant inhibition of both complex I and II were seen (**Figure 5.6B**). However, complex II does not appear to be the specific target of action of mefloquine in DIPG cells as a significant inhibition of complex III and complex IV dependent OCR was also observed in our mitochondrial ETC complexes assay (**Figure 5.6B**). Our findings suggest that mefloquine treatment targets all of the ETC complexes, targeting the mitochondria at several ETC protein levels and inducing an overall mitochondrial disorder in DIPG cells. Similarly, a decrease in protein expression of all of the five mitochondrial complexes was observed following mefloquine treatment in ESCC cells (179). Dysfunction of the mitochondria in DIPG cells is further supported by the significant decrease in key mitochondrial parameters - maximal respiration, ATP production, protein leak and spare respiratory capacity (**Figure 5.5**). Additionally, mutations in SDHD has been shown to impair cell growth, induce apoptosis and necrosis (228). As our findings show that mefloquine decreases SDHD levels, this could be one of the reasons of the observed anti-proliferative effects of mefloquine against DIPGs.

Cancer cells can compensate for the decrease in OCR by increasing ECAR to generate energy i.e., shifting the metabolic profile from OXPHOS to glycolysis. Interestingly, mefloquine also significantly decreased the ECAR of DIPG cells suggesting that it prevents the cells from shifting to glycolysis. The effect of mefloquine on glycolysis in cancers has not been assessed previously. A recent study has shown that mutations in SDHD could impair the glycolytic capacity of cells thus providing an association between loss of SDHD function and glycolysis (228). Our findings show that mefloquine decreases SDHD levels and this might link to the

observed decrease in ECAR in DIPG cells. Furthermore, it is also reported that mefloquine could inhibit enolase and thus interfere with glycolysis in *Schistosoma* spp (229). Enolase is an essential enzyme in glycolysis and it catalyses the conversion of D-2-phosphoglycerate into phosphoenolpyruvate (230). However, whether mefloquine also inhibits enolase in mammalian cells requires further investigation.

Similar to the observations with atovaquone in **chapter 4**, mitochondrial dysfunction with mefloquine treatment could have resulted in the observed hypoxia inhibition and the decrease in HIF-1α expression (**Figure 5.7** and **Figure 5.8**). This is because the effects were seen under similar conditions and at similar mefloquine doses in both HSJD-DIPG-007 and SU-DIPG-VI 3D neurospheres. To our knowledge, the effect of mefloquine on hypoxia and HIF-1α has not been addressed previously. This is a novel finding and now adds an additional mechanism of action to the existing anti-cancer mechanisms of mefloquine.

As hypoxia is one of the major factors responsible for radioresistance in cancers, the observed decrease in hypoxia following mefloquine treatment could have resulted in the improved radiosensitivity of both HSJD-DIPG-007 and SU-DIPG-VI neurospheres. Despite the numerous anti-cancer mechanisms reported, no previous study has assessed the radiosensitising efficacy of mefloquine in cancers. As mefloquine has a range of targets, we believe that the observed radiosensitivity could be due to it targeting DIPGs though numerous ways, with one of them being hypoxia modification.

Future studies could explore additional mechanisms of radiosensitisation by mefloquine in DIPGs. Alterations in TP53 pathway can prevent tumour suppression and drive radioresistance in DIPG (231). As mefloquine has been shown to restore p53 function in cancer cell lines (232), this could be an interesting finding explore further. Past studies suggest the exposure to mefloquine decreases MMP and induces oxidative stress (174, 182). We also show an increase in ROS levels following mefloquine treatment in DIPGs. Further studies could assess the mefloquine induced changes in pathways linked to ROS – Akt, ERK, JNK, and AMPK signalling as these also play roles in carcinogenesis.

Overall, the results of this chapter highlight the promising hypoxia modification and radiosensitisation efficacy of mefloquine against DIPG. Studies have reported that mefloquine

treatment could achieve blood plasma levels of 15.35 μM and peak levels up to 23 μM (233, 234). We have found that mefloquine exhibits radiosensitisation at lower doses than what can be achieved in plasma. Mefloquine is well-absorbed, readily penetrates the BBB, accumulating in the brain and achieving higher concentrations compared to the plasma (234). It is also well-tolerated by children compared to adults and oral delivery makes it an appealing choice of the treatment in children (168). Mefloquine still appears a very potent drug, and as high brain concentrations can be easily achieved, our findings pave way for further investigation of mefloquine as a radiosensitiser using orthotopic DIPG models. As radiation is a standard of care for majority of cancers, combining low doses of mefloquine with RT may improve the efficacy of RT in cancers. We intend to investigate mefloquine's efficacy on its own and in combination with RT using low doses in *in vivo* studies. Adverse effects in *in vivo* studies will be monitored and will provide guidance on the clinical utility of the combination. Based on the results, in future it will be important to investigate synergistic combinations with mefloquine in DIPGs.

Chapter 6

Animal Studies – Generating and Assessing the *in vivo* utility of GFP/Luciferase-expressing HSJD-DIPG-007 DIPG cell line, Hypoxia Staining on DIPG Brain Sections, Drug and RT Studies

Chapter 6. Animal Studies - Generating and Assessing the *in vivo* utility of GFP/Luciferase-expressing HSJD-DIPG-007 DIPG cell line, Hypoxia Staining on DIPG Brain Sections, Drug and RT Studies

6.1. Introduction

Preclinical research on DIPG is important to maximise the chance of benefit to the vulnerable children before exposing them to new treatments. Clinicians require convincing evidence from preclinical research showing that the treatment is both safe and could be effective in children. These evidences include robust efficacy in DIPG relevant models e.g., *in vitro* models - H3K27M-patient derived DIPG cell lines/organoids and *in vivo* models - orthotopic DIPG models. The *in vivo* studies can guide towards confirmation of drug penetration into the brain, pharmacodynamics, pharmacokinetics and drug toxicity, all of which is very useful for the clinicians. Moreover, both *in vitro* and *in vivo* models have their own limitations i.e., *in vitro* models lack complexity of the tumour microenvironment and *in vivo* models differ in immune microenvironment and the developmental contexts also differ from children. For these reasons, clinicals require efficacy in a cascade of experimental models. Together, both *in vitro* and *in vivo* models provide translational evidence to clinicians to help advance treatments to early phase clinical trials.

In the previous chapters, we have demonstrated the promising hypoxia modification and radiosensitising efficacy of atovaquone and mefloquine against DIPG cell lines. Next steps were to investigate the radiosensitising efficacy of these drugs using orthotopic DIPG models by injecting DIPG tumour cells into the pons of the brainstem. Orthotopic models are more clinically relevant models and mimic the aspects of TME as cancer cells are injected into the same organ from which the cancer originated in humans. Prior to performing drug and RT studies, we also tried to generate GFP/luciferase-expressing HJSD-DIPG-007 cells and assessed their utility *in vivo*. We also performed several staining using hypoxia markers on DIPG mouse brain sections. This chapter compiles the results of all the animal studies performed using the three DIPG cell lines SU-DIPG-13P*, parental HSJD-DIPG-007 and GFP/luciferase-expressing HSJD-DIPG-007. There are three separate parts in this chapter with details described below, (1) Using lentiviral transduction to generate GFP/luciferase-expressing HJSD-DIPG-007 cells and assess their utility *in vivo*, (2) immunohistochemistry

(IHC) staining to assess the presence of hypoxia in DIPGs using key hypoxia markers, and (3) drug and RT studies.

Generation of luciferase-expressing tumour cell line by lentiviral transduction holds significance as it allows tracking of tumour progression and also quantification of tumour burden *in vivo* (235). As tumour growth can be monitored longitudinally over a long period of time, this can be extremely useful in optimising treatment starting times. Therefore, we first aimed to perform lentiviral transduction of primary HJSD-DIPG-007 cells to generate stable GFP/luciferase-expressing HJSD-DIPG-007 cells. GFP expression was monitored using fluorescent microscopy and luciferase expression was measured by detecting luminescence using a plate reader and In Vivo Imaging System (IVIS) imaging. The resulting cells were injected into the pons/4th ventricle in the mice and bioluminescence was measured using IVIS imaging.

Next, sections of the orthotopic tumours (HSJD-DIPG-007 and SU-DIPG-13P*) were analysed by Haematoxylin and Eosin (H & E) staining, accompanied by IHC analysis of key hypoxia-related proteins. H3K27M mutation is the main driver in DIPG pathogenesis (236) and an H3K27M antibody that binds the mutant form of the protein was used to identify DIPG tumour cells. Ki67 is a well-known proliferation marker (237) and a Ki67 antibody was used to support H3K2M findings and locate DIPG tumour cells. HIF-1α is a hypoxia regulator and its expression was assessed in DIPG tumour areas to support the presence of hypoxia. Vascular endothelial growth factor A (VEGFA) is regulated by HIF-1α (238). Since hypoxia can induce VEGFA expression, we also examined VEGFA in DIPG models. Carbonic anhydrase IX (CA-IX) is also regulated by HIF-1α mediated transcription and is considered as a hypoxia marker (239). CA-IX expression was therefore also assessed in DIPG models. EF5, a nitroimidazole derivative, binds to cells displaying hypoxia (240) and it was used to further validate the presence of hypoxia in these orthotopic DIPG models. Pimonidazole, another nitroimidazole derivative is a well-known tumour hypoxia marker (241) and was also investigated in these DIPG models. As past evidence in literature suggest that DIPG tumour could be hypoxic (71, 72), and we also found upregulated OXPHOS gene expression in DIPG/DMG patient samples (**Chapter 3**), thus we hypothesis that positive staining with hypoxia markers would be detected in the mice brain sections with DIPG tumour.

Finally, we evaluated the efficacy of drugs and RT. First, we needed to assess the efficacy of RT with dose escalation to establish dose response curves for RT using the SU-DIPG-13P* model. Dose response curves using parental HSJD-DIPG-007 model were already established by our lab group. These experiments were essential to determine optimal RT dose to combine with atovaquone/mefloquine. Athymic nude mice (balb/c nude) were used in these studies to evaluate the efficacy of drugs, RT and their combinations as balb/c nude mice can tolerate whole brain irradiation safely up to 30 Gy in 2 Gy fraction, based on previous studies by our lab group. Optimised RT doses were then combined with ASD atovaquone formulation, survival curves were generated, and brain/plasma concentrations were measured. Due to time constraints, animal studies with mefloquine are yet to be performed. Based on our *in vitro* findings, we hypothesise that the clinically approved anti-parasitic drugs used in this project will reduce tumour hypoxia and improve the efficacy of RT, thereby the combination will eradicate more DIPG cells *in vivo* and enhance the median survival of treated animals.

6.2. Results

6.2.1 Lentiviral transduction of HSJD-DIPG-007 cells

Our collaborators at Kids Research established protocols for lentiviral transduction of SU-DIPG-24, SU-DIPG-XVII and GBM cell lines with a lentiviral vector encoding GFP and luciferase. As there is no evidence suggesting that SU-DIPG-24 and SU-DIPG-XVII cells could form tumours *in vivo*, we opted to use their methodology to generate GFP/luciferase-expressing HSJD-DIPG-007 cells as HSJD-DIPG-007 cells are well reported to form tumours.

Following transductions (approach mentioned in **Chapter 2**), GFP expression was checked at several times (2 days post-transduction, 10 days post-transduction and a few days post-sorting) and a decrease in GFP positive cells was seen, suggesting loss of GFP expression over time (**Figure 6.1A-C**). By comparison, post-sorted GFP/luciferase-expressing cells retained a significantly higher expression (Dr Yuyan Chen, personal communication). We also assessed the luciferase expression in these GFP-luciferase-expressing HSJD-DIPG-007 cells using Bright-glo reagent with luminescence recorded using plate reader. A direct of correlation of cell number with luminescence intensity was observed with 50,000 cells resulting in a luminescence value of 1.8 x 10^4 RLU (**Figure 6.1D**). Our luminescence readings for HSJD-DIPG-007 cells were in 10^4 range whereas our collaborators obtained 10^5 range for the other

DIPG cell line (GFP/luciferase-expressing SU-DIPG-24) at equivalent cell number from their previous experiments (Dr Yuyan Chen, personal communication).

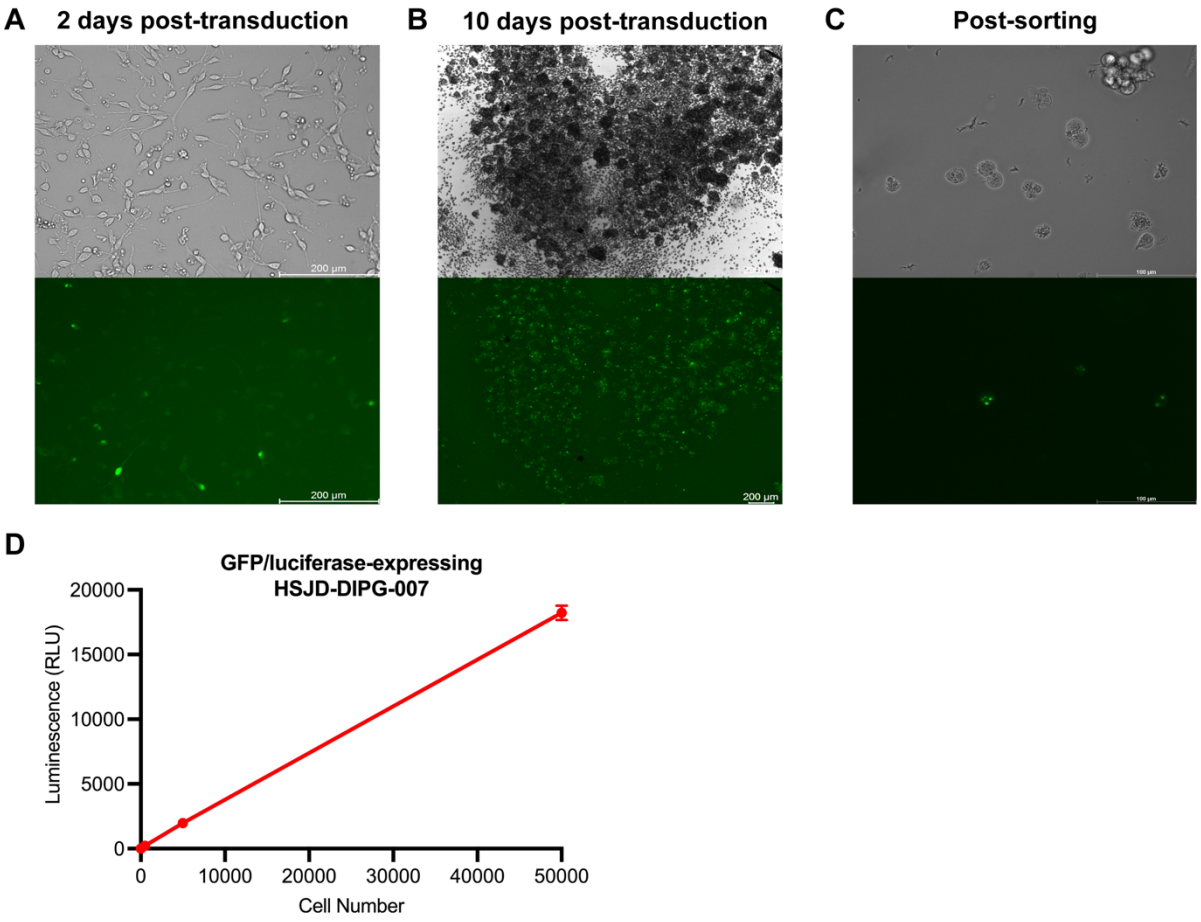

Figure 6.1. Fluorescence microscopy images of GFP/luciferase-expressing HSJD-DIPG-007 cells.
(A) Images taken 2 days after lentiviral transduction (Scale bar = 200 µm). (B) Images taken 10 days after lentiviral transduction (Scale bar = 200 µm). (C) Images taken a few days post sorting (Scale bar = 100 µm). (D) Correlation analysis of cell number with luminescence intensity. GFP/luciferase-expression HSJD-DIPG-007 cells were plated from 0 to 50,000 cells per well and Bright-Glo reagent (Promega) was added (1:1). Luminescence was recorded following 3 mins using plate reader. Data represents mean ± SD of 3 replicates for each cell number. Experiment was performed twice.

6.2.1.1 Comparing the luminescence intensity of GFP/luciferase expressing HSJD-DIPG-007 cells with GFP/luciferase expressing SU-DIPG-24 cells

With the observed loss of GFP expression post-sorting and a lower luminescence intensity, we decided to compare the luciferase expression of GFP/luciferase-expressing HSJD-DIPG-007 cells with the GFP/luciferase-expressing SU-DIPG-24 (prepared by Dr Yuyan Chen's Group), as a positive control. Both cell lines were plated at 0 to 50,000 cells, bright-glo reagent was added and luminescence recorded using plate reader. A direct of correlation of cell number with luminescence intensity was observed in both cell lines with 50,000 cells resulting in a luminescence value of 1.8 x 10^4 RLU in HSJD-DIPG-007 cells and 2.0 x 10^5 in SU-DIPG-24 cells (**Figure 6.2A**). The luminescence of HSJD-DIPG-007 cells measured by plate reader was 11-fold lower than that of SU-DIPG-24 cells (**Figure 6.2A**). Following this, GFP expression was also checked and again only a few GFP positive cells were detected in HSJD-DIPG-007 cells**,** indicating loss of GFP expression (**Figure 6.2B**). GFP expression of SU-DIPG-24 cells was also checked and there were some GFP positive cells (**Figure 6.2C**). As per our collaborators, the GFP expression of SU-DIPG-24 cells in our results seems to be much lower compared to their previous work also suggesting loss of GFP expression over time in these cells. However, the luminescence readings of SU-DIPG-24 cells in our results were consistent with their findings.

Next, we decided to measure luciferase expression of both cell lines using the IVIS system. Previously, our collaborators had successfully measured luminescence of SU-DIPG-24 single neurospheres using IVIS and we used their protocol for our HSJD-DIPG-007 cells. First, both HSJD-DIPG-007 and SU-DIPG-24 cells were cultured on u-bottom plates to form single neurospheres. Despite 5 days of culture with three replicates, the GFP/luciferase-expressing HSJD-DIPG-007 cells did not associate to form single neurospheres unlike the SU-DIPG-24 cells (**Figure 6.2D**). It appeared that unlike parental HSJD-DIPG-007 cells which form a single neurosphere with u-bottom plates, GFP/luciferase-expressing HSJD-DIPG-007 do not. We then plated both GFP/luciferase-expressing HSJD-DIPG-007 and SU-DIPG-24 as single cells at 7.5k, 15k, 30k and 40k, added bright-glo reagent and recorded luminescence using IVIS (**Figure 6.2E**). An increase in luminescence signal intensity was observed with increasing cell number in both the cell lines (**Figure 6.2E**). The average radiance for the 40,000 HSJD-DIPG-007 cells was 1.13 x 10^8 p/sec/cm^2/sr and the average radiance for the 40,000 SU-DIPG-24 cells was 6.97 x 10^8 p/sec/cm^2/sr (**Figure 6.2F**). The luminescence of HSJD-DIPG-007 cells

measured by IVIS was 6-fold lower than that of SU-DIPG-24 cells (**Figure 6.2F**). It appears that the plate reader is more sensitive to luminescence measurements compared to IVIS as a higher 11-fold difference was detected between HSJD-DIPG-007 and SU-DIPG-24 with the plate reader compared to 6-fold difference detected with IVIS system.

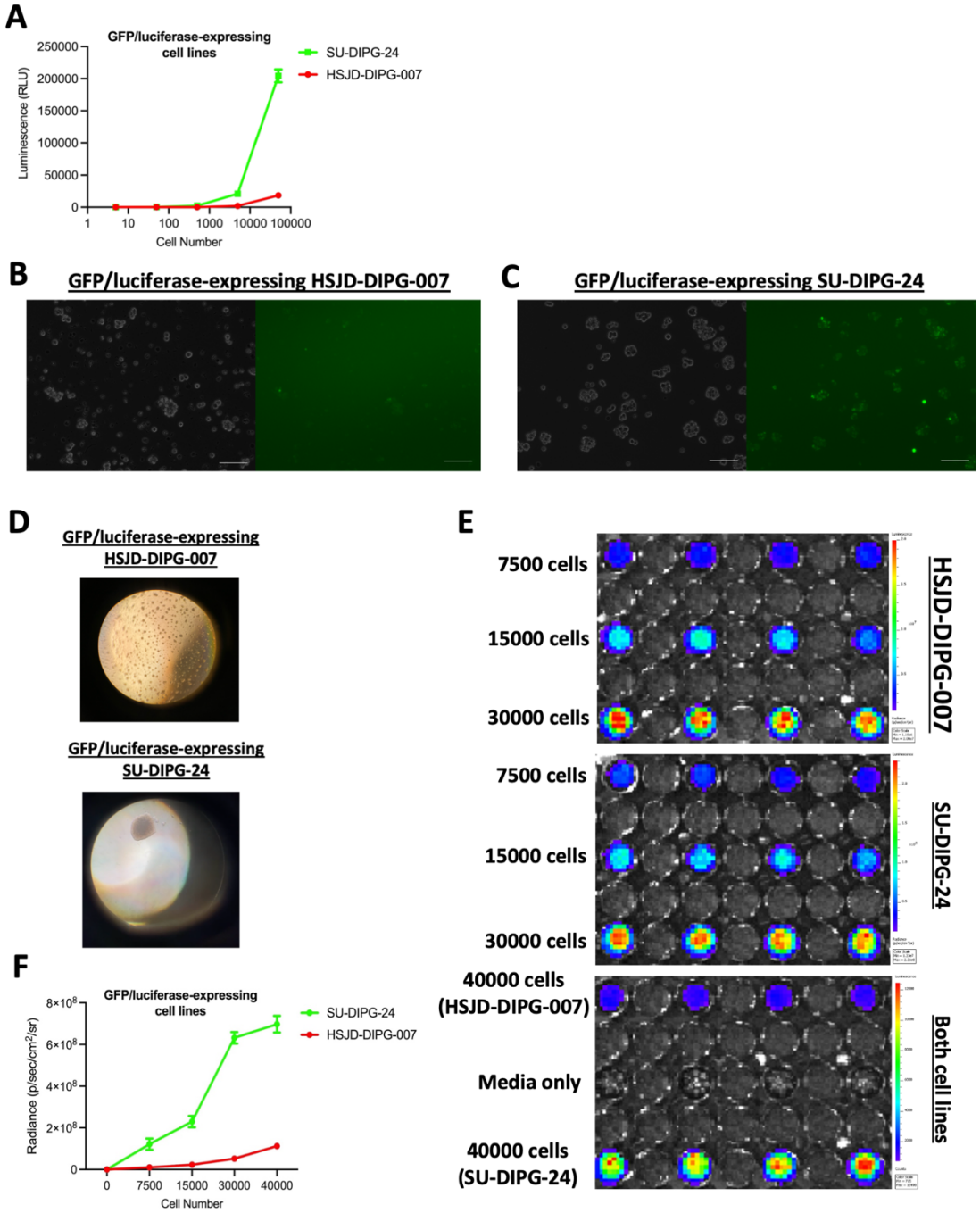

Figure 6.2. Comparing luminescence intensity of GFP/luciferase-expressing HSJD-DIPG-007 and SU-DIPG-24 cells.

(A) Correlation analysis of cell number with luminescence intensity measured with plate reader. GFP/luciferase-expression HSJD-DIPG-007 and SU-DIPG-24 cells were plated from 0 to 50,000 cells per well and Bright-Glo reagent (Promega) was added (1:1). Luminescence was recorded following 3

mins. Data represents mean ± SD of 3 replicates for each cell number. Experiment was performed twice. (B-C) Fluorescence microscopy images of GFP/luciferase-expressing HSJD-DIPG-007 and SU-DIPG-24 cells. Images taken from fresh revived cells (Scale bar = 100 µm). (D) Appearance of GFP/luciferase-expressing HSJD-DIPG-007 and SU-DIPG-24 cells following 5 days of culture. (E-F) Measuring luminescence vs cell number correlation of GFP/luciferase-expressing HSJD-DIPG-007 cells and SU-DIPG-24 cells with IVIS system. (E) Both cell lines were plated from 7.5k to 40k using 96-well plate and Bright-Glo reagent (Promega) was added (1:1). Luminescence was recorded following 3 mins. (F) Graph of average radiance vs cell number. Data represents mean ± SD of 4 replicates for each cell number. Experiment was performed twice.

6.2.1.2 Investigating the utility of GFP/luciferase expressing HSJD-DIPG-007 cells in vivo

Although the luminescence readings in GFP/luciferase-expressing HSJD-DIPG-007 cells were lower than those of the SU-DIPG-24 cells, it still appeared that the luminescence signal dramatically increases with the increase in cell number. We obtained an average radiance of 1.13 x 10^8 p/sec/cm^2/sr with 40,000 seeded cells, and as 200,000 HSJD-DIPG-007 cells are required in the orthotopic xenograft model, we reasoned that there was sufficient luminescence signal to be detected in the mouse experiments. Therefore, we decided to assess their utility *in vivo*. First, the GFP/luciferase-expressing HSJD-DIPG-007 were freshly revived and their luminescence was confirmed with IVIS imaging prior to injecting into the mouse. The cells were plated as single cells at 7.5k, 15k, 30k and 60k, bright-glo reagent was added and luminescence was recorded (**Figure 6.3A**). There was an increase in luminescence signal intensity with increasing cell number. The average radiance for the 40,000 HSJD-DIPG-007 cells was 4.0 x 10^7 p/sec/cm^2/sr and the average radiance 60,000 HSJD-DIPG-007 cells was 5.10 x 10^7 p/sec/cm^2/sr (**Figure 6.3B)**. It appeared that the luminescence of HSJD-DIPG-007 cells seemed to decrease over time as the IVIS reading with 40,000 cells this time was 2.8-fold lower than that measured the first time as in **Figure 6.2F** (1.13 x 10^8 p/sec/cm^2/sr first time compared to 4.0 x 10^7 p/sec/cm^2/sr this time).

Next, parental and GFP/luciferase-expressing HSJD-DIPG-007 cells were intracranially injected (200,000 cells/mouse) into the pons/4th ventricle of balb/c nude mice using stereotactic equipment at specific coordinates. **Figure 6.3C** shows the experimental plan. The purpose of this experiment was to track tumour progression and also quantify tumour burden by IVIS imaging of GFP/luciferase-expressing HSJD-DIPG-007 model and to compare survival difference between both the HSJD-DIPG-007 models. At 37 days post-tumour injection, all the mice with GFP/luciferase-expressing HSJD-DIPG-007 cells were injected with 150 mg/kg of luciferin and imaged every 5 min for 30 mins using IVIS. No signal was detected even after 30

mins (image not shown). Imaging was performed again at 60 days post-tumour injection, however no bioluminescence signal was detected even at last timepoint of 30 mins (**Figure 6.3D**). Consistent with our lab group's previous work, the median survival of parental HSJD-DIPG-007 was 77 days (n=4) whereas the GFP/luciferase-expressing HSJD-DIPG-007 did not reach median survival up until 105 days post-tumour injection (**Figure 6.3E**). One mouse in GFP/luciferase-expressing HSJD-DIPG-007 group was culled at 70 days which appeared to be an outlier as the remaining 4 mice were healthy at 105 days. This mouse was culled due to an eye infection with pus discharge and a mass noticed on the head. **Figure 6.3F** shows IHC performed on this mouse brain and no H3K27M-positive tumour cells were detected (details on IHC optimisations are in **section 6.2.2**). We also used one of the mouse from the parental HSJD-DIPG-007 group as a positive control for H3K27M and lots of H3K27M positive cells were detected (**Figure 6.3G**). Given the lack of luminescence signal, it was not possible to continue with the planned luminescence imaging, and the experiment was terminated following obtaining approval from the animal ethics committee. Instead, in the following sections we used parental HSJD-DIPG-007 model for assessing the radiosensitising efficacy of drugs.

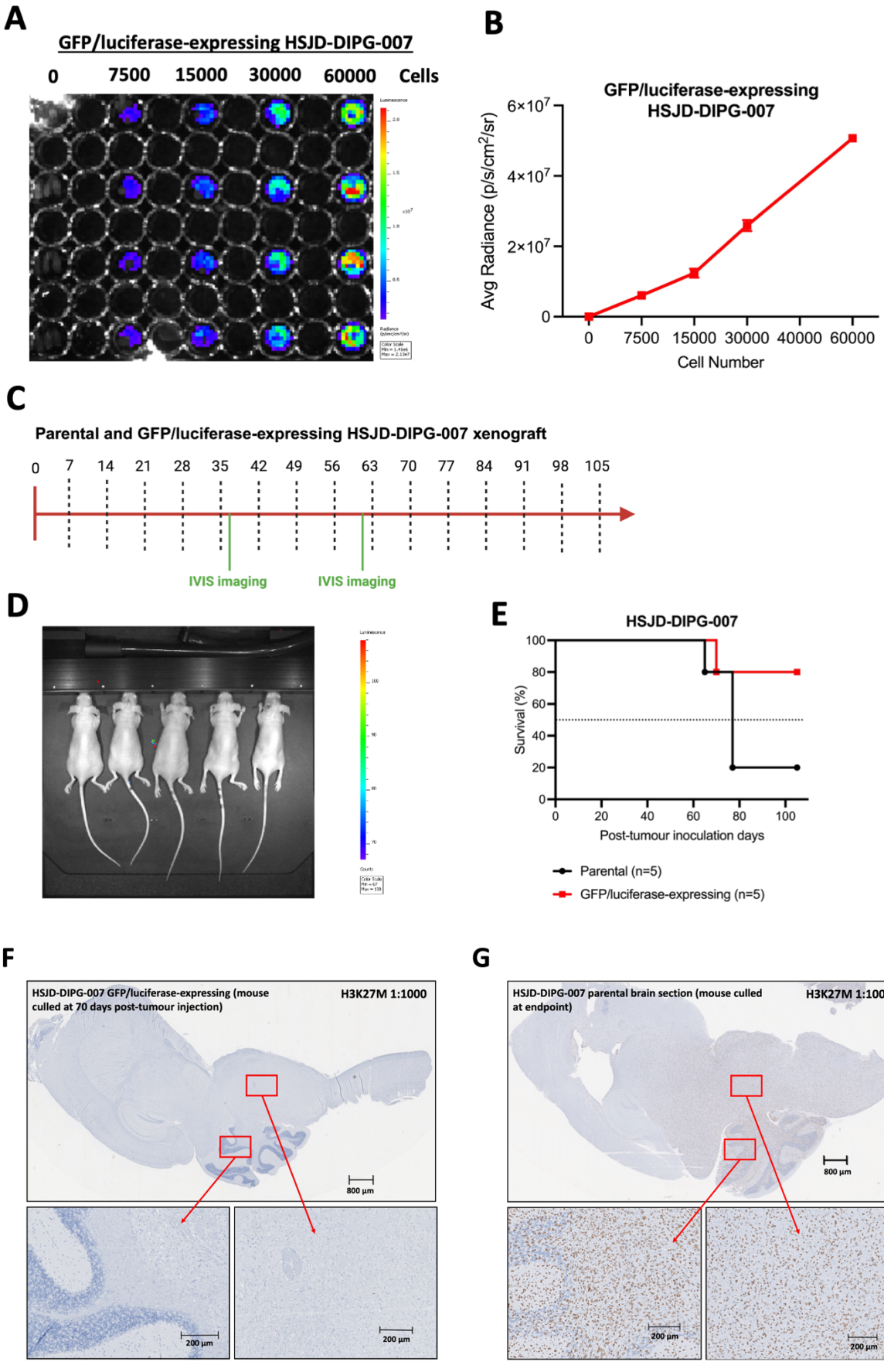
A
GFP/luciferase-expressing HSJD-DIPG-007
0
7500
15000
30000
60000
Cells
B
GFP/luciferase-expressing
HSJD-DIPG-007
Avg Radiance (p/s/cm²/sr)
6×10⁷
4×10⁷
2×10⁷
0
0
7500
15000
30000
40000
60000
Cell Number
C
Parental and GFP/luciferase-expressing HSJD-DIPG-007 xenograft
0
7
14
21
28
35
42
49
56
63
70
77
84
91
98
105
IVIS imaging
IVIS imaging
D
E
HSJD-DIPG-007
Survival (%)
100
80
60
40
20
0
0
20
40
60
80
100
Post-tumour inoculation days
Parental (n=5)
GFP/luciferase-expressing (n=5)
F
HSJD-DIPG-007 GFP/luciferase-expressing (mouse culled at 70 days post-tumour injection)
H3K27M 1:1000
800 µm
200 µm
200 µm
G
HSJD-DIPG-007 parental brain section (mouse culled at endpoint)
H3K27M 1:1000
800 µm
200 µm
200 µm

Figure 6.3. Assessing *in vivo* utility of GFP/luciferase-expressing HSJD-DIPG-007 cells.
(A-B) Correlation between luminescence and cell number. Freshly revived GFP/luciferase-expressing HSJD-DIPG-007 cells were plated from 7.5k to 60k using 96-well plate and Bright-Glo reagent (Promega) was added (1:1). Luminescence was recorded following 3 mins using IVIS Imaging. (B) Graph of average radiance vs cell number. Data represents mean ± SD of 4 replicates for each cell number. (C) Layout of the animal study using parental and GFP/luciferase-expressing HSJD-DIPG-007 xenograft. Green lines represent times of IVIS imaging. (D) Representative image of mice injected with GFP/luciferase-expressing HSJD-DIPG-007 cells. Image taken 60 days post tumour injection. Mice were injected with 150 mg/kg of luciferin and imaged every 5 min for 30 mins. The following image is from the last timepoint. (E) Survival curves of parental and GFP/luciferase-expressing HSJD-DIPG-007 cells. (F-G) H3K27M IHC staining using HSJD-DIPG-007 GFP/luciferase-expressing and HSJD-DIPG-007 parental brain sections. Images are representative of brain samples obtained at endpoint.

6.2.2 Immunohistochemistry analysis of hypoxia markers in orthotopic DIPG models

6.2.2.1 Optimising H3K27M and Ki67 staining to identify DIPG tumour cells

Brain sections from SU-DIPG-13P* and HSJD-DIPG-007 orthotopic xenografts were used to test our hypothesis that DIPGs are potentially hypoxic tumours. First, we performed H&E staining on the brain sections and confirmed the presence of tumour area following discussions with the pathologist A/Prof Winny Varikatt. Next, H3K27M and Ki67 antibodies were optimised using HSJD-DIPG-007 brain sections and 1:1000 and 1:400 were selected as optimal concentrations for H3K27M and Ki67 respectively. These optimal concentrations were used to identify tumour cells in the subsequent staining of brain sections before proceeding with hypoxia staining.

H&E staining of SU-DIPG-13P* brain sections suggest that in this model, the xenografted tumour appears to grow as a solid mass, with tumour cells rapidly infiltrating in the cerebellum and the brainstem regions in some cases (**Figure 6.4A-B)**. Although, the cells were injected at specific coordinates in the brainstem in the pons region, however visualising multiple H&E sections at endpoint revealed some tumour cells in the brainstem but the majority rapidly spreading to the cerebellum (**Figure 6.4A-B)**. Interestingly, H3K27M staining was not detected in SU-DIPG-13P* brain section in regions where there were tumour cells grouped together (**Figure 6.4A-B)**. This was consistently seen with several SU-DIPG-13P* brain sections, with two of the representative brain sections shown in **Figure 6.4A-B**. H3K27M staining was detected in SU-DIPG-13P* brain sections only in the regions with tumour cells spread sparsely (**Figure 6.4A**). Lots of Ki67 positive cells were detected in SU-DIPG-13P* brain region, confirming the presence of tumour cells (**Figure 6.4B**).

Unlike SU-DIPG-13P*, the HSJD-DIPG-007 tumour grows diffusely with tumour cells spreading around the entire brainstem and also other brain regions (**Figure 6.4C)**. As opposed to SU-DIPG-13P*, visualising tumour cells with H&E in this model was more difficult due to the spread of tumour cells. However, H3K27M and Ki67 positive cells confirmed the presence of tumour cells in the brainstem region (**Figure 6.4C)**.

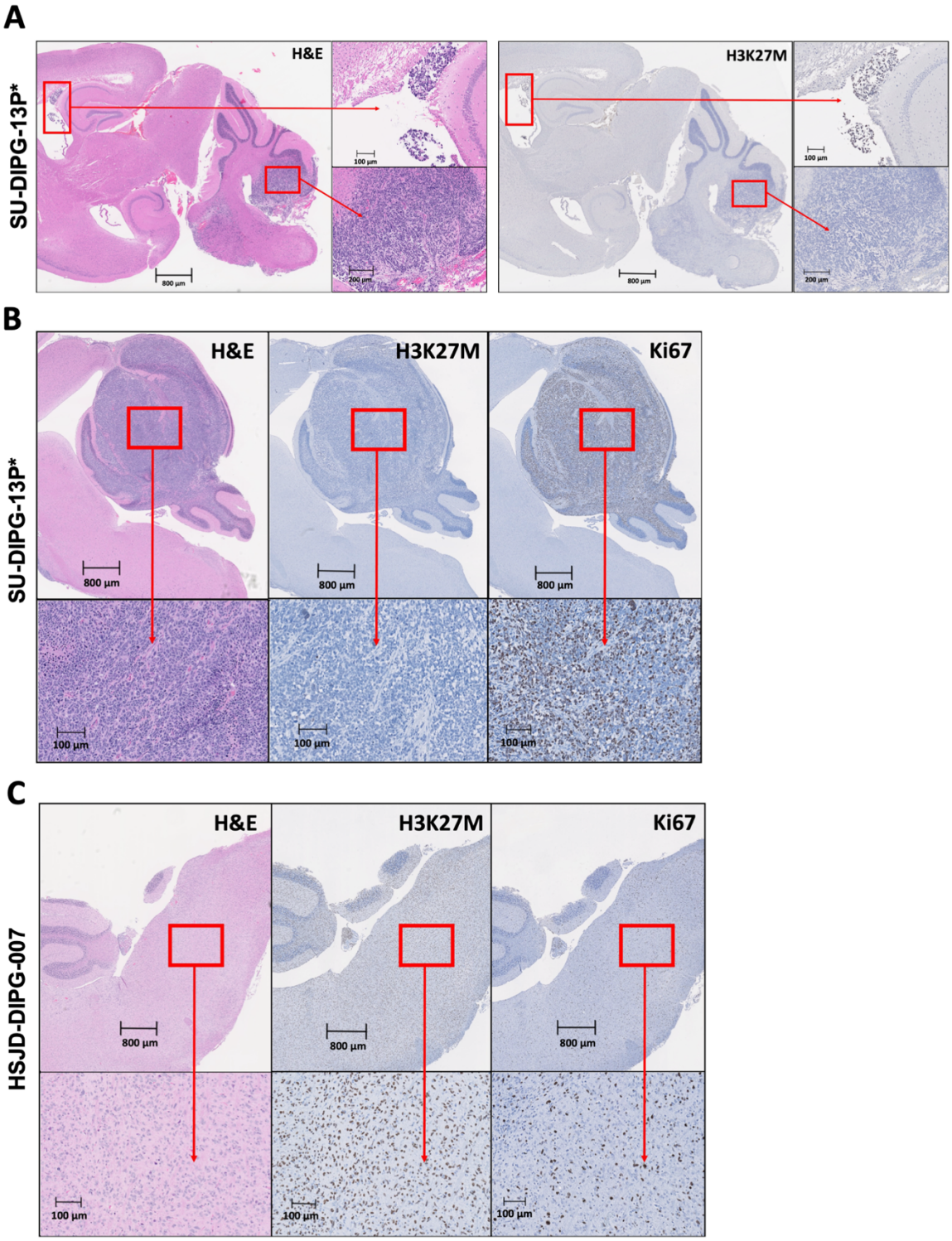

Figure 6.4. H&E and IHC staining using SU-DIPG-13P* and HSJD-DIPG-007 brain sections.
(A) H&E and H3K27M positive cells in the cerebellum, brainstem and other regions of the brain of SU-DIPG-13P* model. Images are representative of brain samples obtained at endpoint. (B) H&E, H3K27M and Ki67 positive cells in the cerebellum of SU-DIPG-13P* model. Images are representative of brain samples obtained at endpoint. (C) H&E, H3K27M and Ki67 positive cells in the brainstem of HSJD-DIPG-007 model. Images are representative of brain samples obtained at endpoint.

6.2.2.2 Identification of HIF-1α as a marker for hypoxia

Once tumour cells were identified and H3K27M and Ki67 were optimised, we were now interested in assessing the presence of hypoxia in DIPG tumours using a range of antibodies. HIF-1α, a well-known transcription factor, is upregulated under hypoxic conditions (213). The human GI tract is highly hypoxic compared to most body tissues (242). Therefore, we used human stomach tissue as a positive control for HIF-1α antibody staining (**Figure 6.5A**). We then investigated the HIF-1α staining in SU-DIPG-13P* brain section. Interestingly, there was strong HIF-1α positive staining at 1:200 dilution was in the similar region as tumour cells as confirmed with H&E (**Figure 6.5B**).

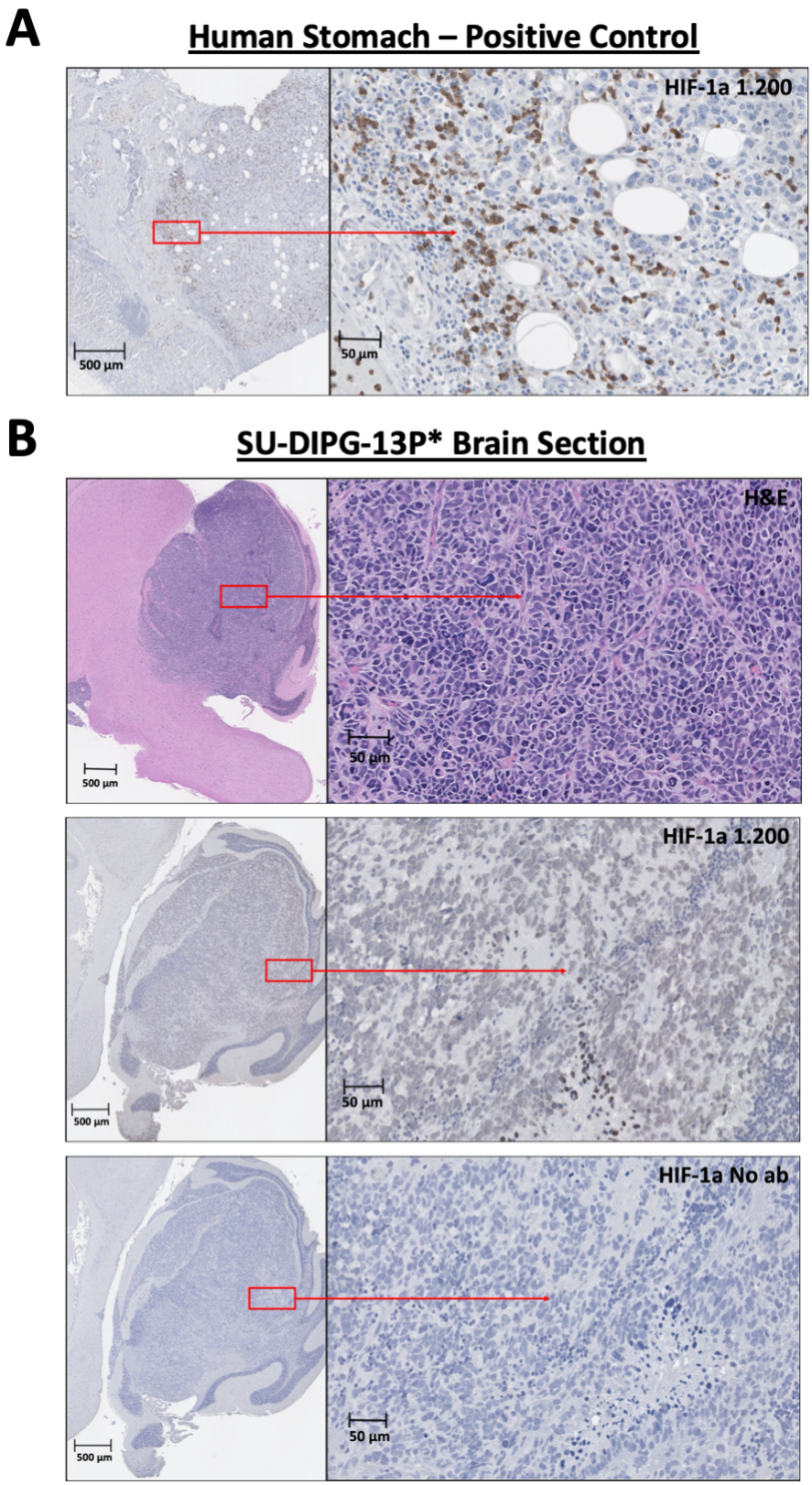

Figure 6.5. H&E and HIF-1*α* IHC staining using human stomach tissue and SU-DIPG-13P* brain sections. (A) HIF-1*α* staining on human stomach tissue section. (B) H&E and HIF-1*α* staining in the cerebellum of SU-DIPG-13P* model. Images are representative of brain samples obtained at endpoint.

6.2.2.3 Identification of VEGFA as a marker for hypoxia

A hypoxic microenvironment is a potent stimulator of VEGFA which is upregulated by HIF-1α (238). Studies have shown that VEGFA colocalised with EF5 staining, another hypoxia marker (243). We therefore investigated the expression of VEGFA in DIPG tumour regions. We first used the human stomach tissue as a positive control for VEGFA antibody staining (**Figure 6.6A**). VEGFA staining was then performed on SU-DIPG-13P* brain section. There was a strong VEGFA positive staining at 1:50 dilution found in the similar region as tumour cells as confirmed with H&E (**Figure 6.6B**).

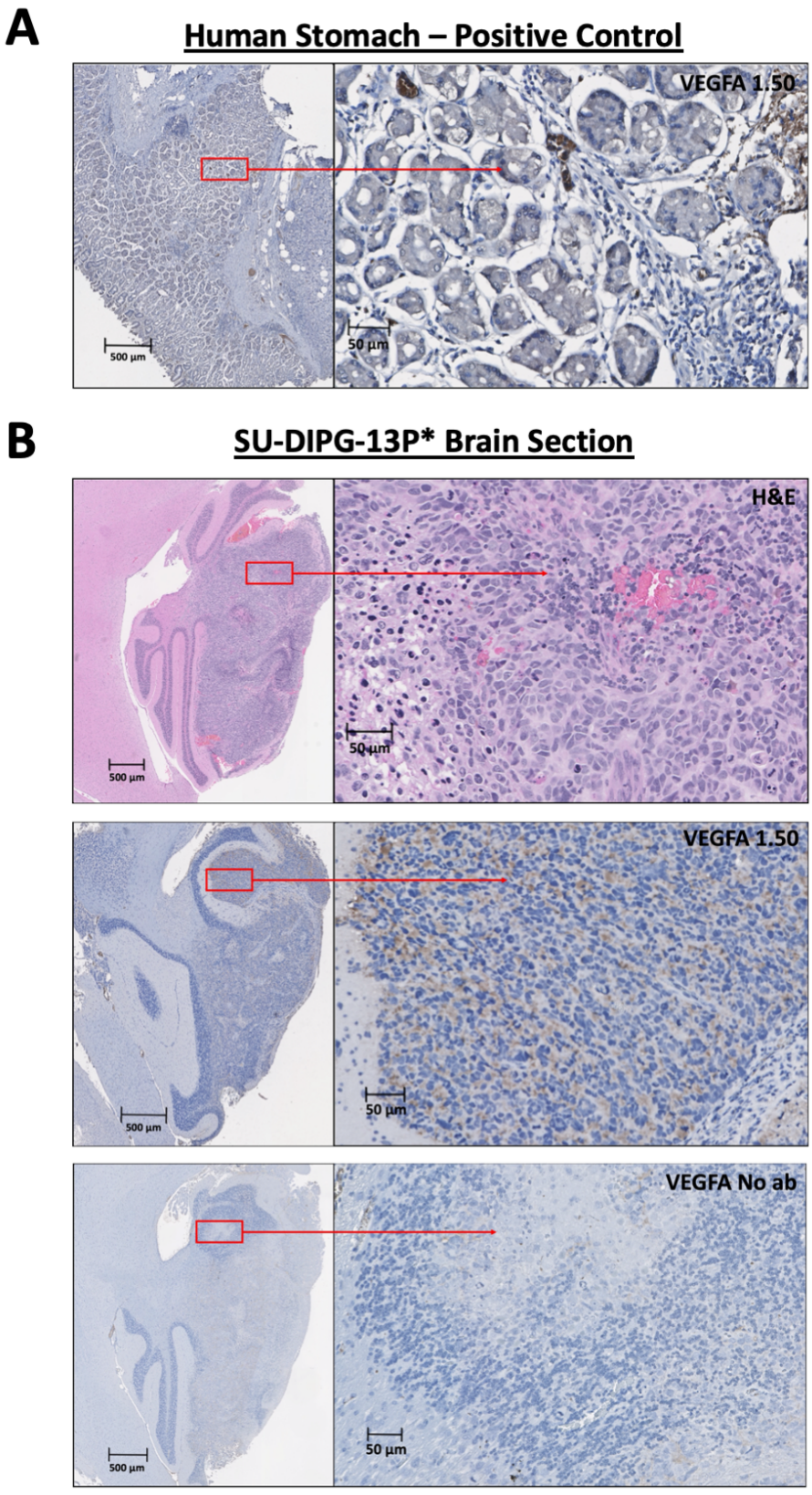

Figure 6.6. H&E and VEGFA IHC staining using human stomach tissue and SU-DIPG-13P* brain sections. (A) VEGFA staining on human stomach tissue section. (B) H&E and VEGFA staining in the cerebellum of SU-DIPG-13P* model. Images are representative of brain samples obtained at endpoint.

6.2.2.4 Identification of CA-IX as a marker for hypoxia

HIF-1α also upregulates the expression of CA-IX, another marker for hypoxia that is preferentially expressed in solid tumours (239). Therefore, we investigated the expression of CA-IX in DIPG tumour regions. Again, human stomach tissue was used as a positive control for CA-IX antibody staining (**Figure 6.7A**). We then performed the CA-IX staining SU-DIPG-13P* brain region. Interestingly, the staining did not colocalise with the tumour region and instead the entire brain section was stained with CA-IX (**Figure 6.7B**). Similarly, when performed on HSJD-DIPG-007 brain region, the staining also did not colocalise with the H3K27M positive region and instead the entire brain section was stained with CA-IX (**Figure 6.7C**).

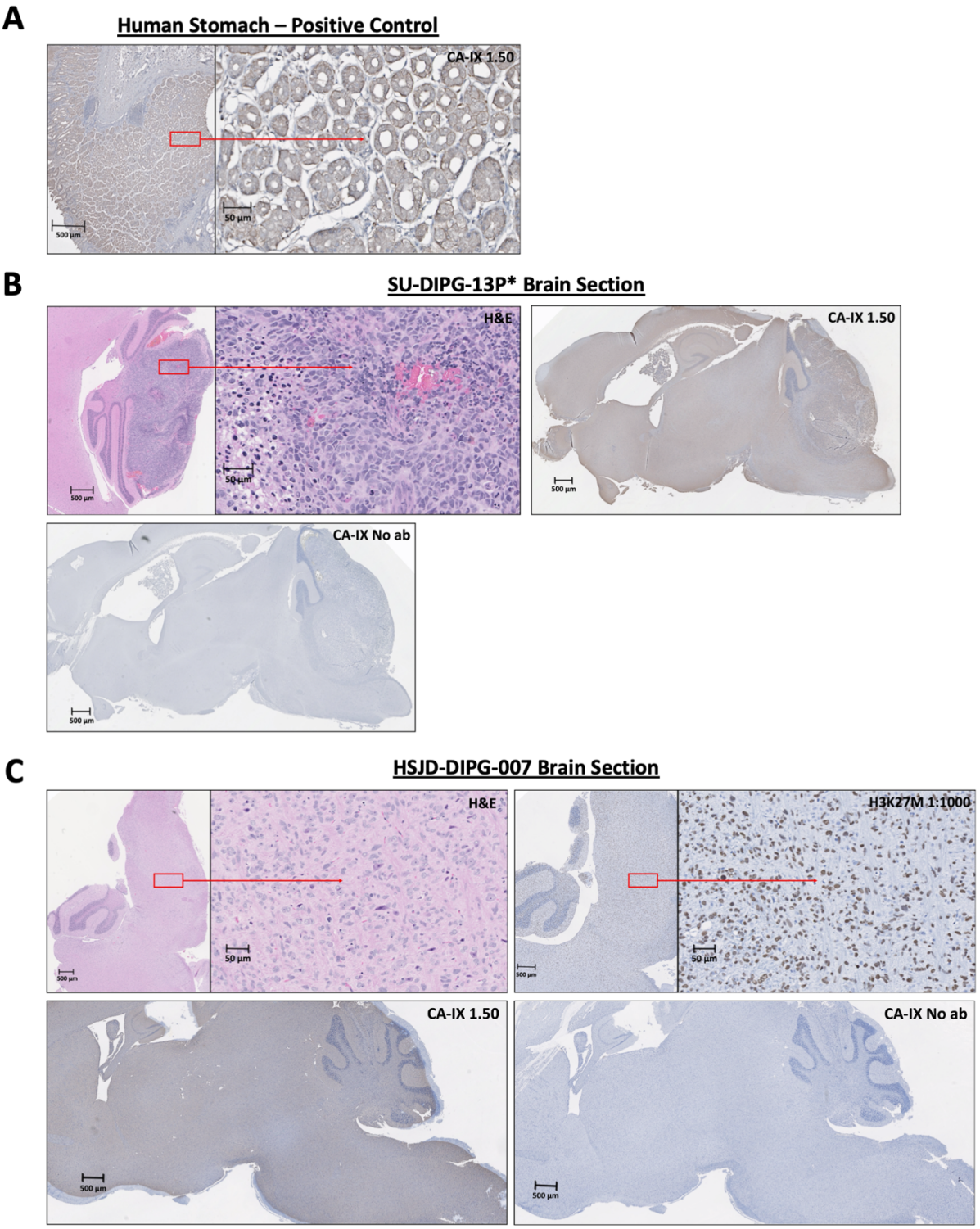

Figure 6.7. H&E and CA-IX IHC staining using human stomach tissue, SU-DIPG-13P* and HSJD-DIPG-007 brain sections.

(A) CA-IX staining on human stomach tissue section. (B) H&E and CA-IX staining in SU-DIPG-13P* model. Images are representative of brain samples obtained at endpoint. (B) H&E, H3K27M and CA-IX staining in HSJD-DIPG-007 model. Images are representative of brain samples obtained at endpoint.

6.2.2.5 Identification of EF5 as a marker for hypoxia

EF5 has been developed as a hypoxia marker and used to study hypoxia in several tumour types (244). Here we stained HSJD-DIPG-007 tumour sections with EF5 to assess hypoxia in this tumour model. Mice bearing HSJD-DIPG-007 tumour were injected with EF5 at 10 mg/kg at endpoint 3 hour before euthanisation. **Figure 6.8** shows H3K27M staining on HSJD-DIPG-007 brain section, with EF5 positive cells colocalising with the tumour cells.

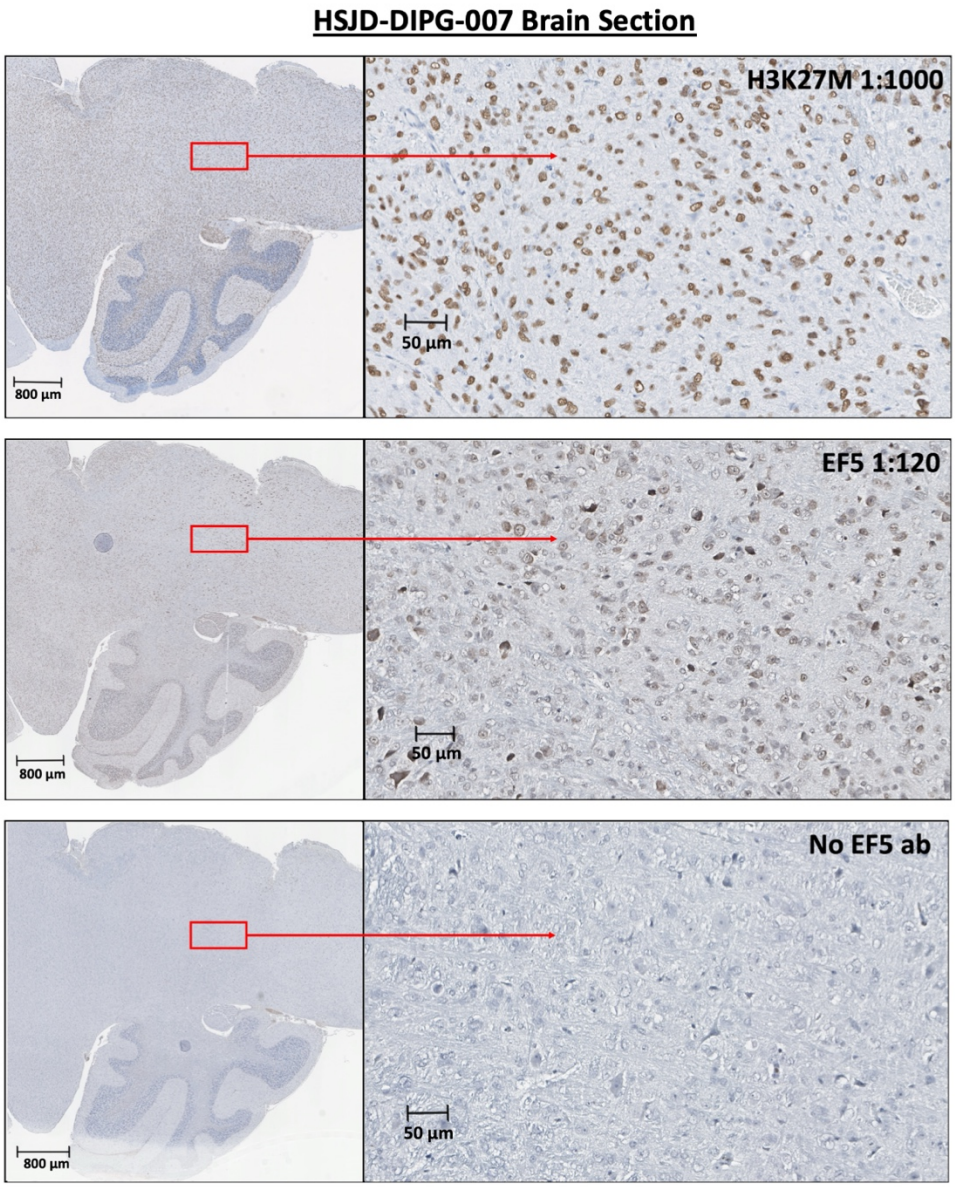

Figure 6.8. H3K27M and EF5 optimisation IHC staining using HSJD-DIPG-007 brain sections.
Images are representative of brain samples obtained at endpoint.

6.2.2.6 Identification of pimonidazole as a marker for hypoxia

We also assessed pimonidazole staining in the DIPG tumour areas using Hypoxyprobe™ (pimonidazole hydrochloride). Pimonidazole is a well-reported hypoxia marker and has been used for the assessment of hypoxia in several tissues with IHC (241). HSJD-DIPG-007 and SU-DIPG-13P* tumour-bearing mice were injected with pimonidazole at 100 mg/kg at endpoint 1 hour before euthanisation. **Figure 6.9A** shows H&E and H3K27M staining on HSJD-DIPG-007 brain section, however pimonidazole staining was not detected despite several optimisations of the protocol and testing various antibody concentrations. We also assessed pimonidazole staining on SU-DIPG-13P* model, however no staining was detected in the brain region (image not shown).

As the GI tract is known to be hypoxic, we dissected the caecum, intestine and stomach of the HSJD-DIPG-007 mouse injected with pimonidazole, and performed pimonidazole and CA-IX staining on these tissue sections. As CA-IX was detected in human stomach tissue (**Figure 6.7A**) and is a well-reported hypoxia marker, we used it as a positive control for hypoxia in the gut regions. Strong CA-IX staining was detected in caecum, stomach and intestines sections of the mice (**Figure 6.9B-D**). However, pimonidazole staining was not detected in any of these regions (**Figure 6.9B-D**).

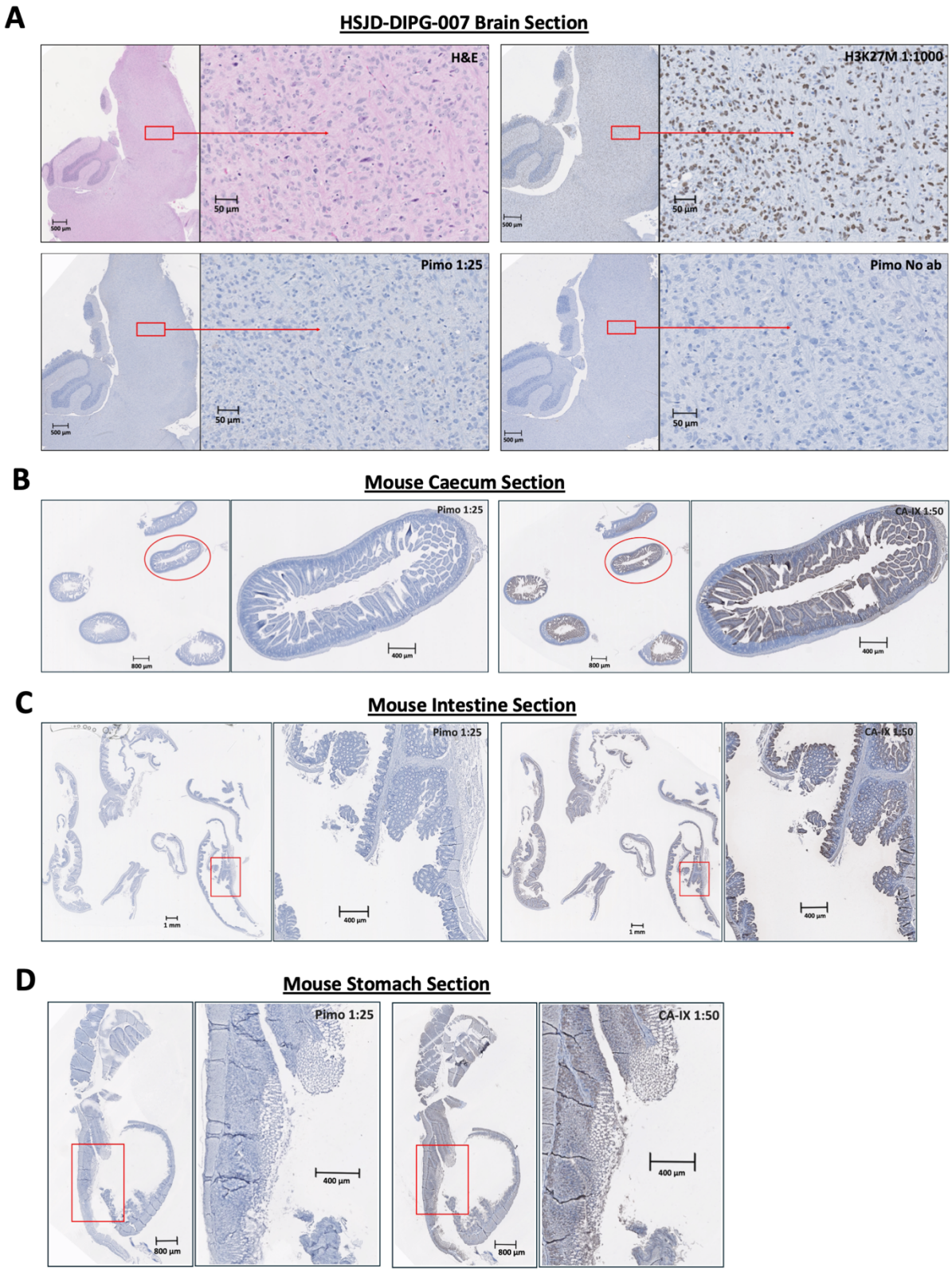

Figure 6.9. H&E, pimonidazole and CA-IX IHC staining using HSJD-DIPG-007 brain, caecum, intestine and stomach sections.

(A) H&E, H3K27M and pimonidazole staining using HSJD-DIPG-007 brain section. Images are representative of brain samples obtained at endpoint. (B) Pimonidazole and CA-IX staining in mouse caecum section. (C) Pimonidazole and CA-IX staining in mouse intestine section. (D) Pimonidazole and CA-IX staining in mouse stomach section.

6.2.3 RT and drug studies

6.2.3.1 RT and drug studies using SU-DIPG-13P model*

In the previous section (**6.2.2**), we found positive HIF-1α, VEGFA and EF5 staining in the brain sections of DIPG-tumour bearing mice, thus supporting the presence of hypoxia in this tumour model. As atovaquone has been shown to decrease hypoxia and improve RT response, *in vitro* (**Chapter 4**), we now aimed to investigate its radiosensitising efficacy using an SU-DIPG-13P* orthotopic model. First, we established dose response curves for RT to determine the optimal RT dose to combine with atovaquone. SU-DIPG-13P* cells were intracranially injected (400,000 cells/mouse) into the pons of balb/c nude mice using stereotactic equipment at specific coordinates. **Figure 6.10A** shows the experimental plan. Mice were treated with whole-brain RT at 10, 20 and 30 Gy was delivered using XRAD320. RT was started 2 weeks post-tumour injection and administered as multiple fractionated doses (2 Gy per fraction per day for five days a week). The median survival of control group was 28.5 days, which was significantly extended by 10 Gy RT group to 49 days (**P<0.01). The 20 Gy and 30 Gy groups had a significant effect on survival and did not reach endpoint (**P<0.01, ***P<0.001) (**Figure 6.10B**). The experiment was terminated following approval from the animal ethics committee and the remaining mice were humanely euthanised. The first mouse in the 30 Gy RT group could be an outlier as it was culled 25 days post tumour injection due to >20% weight loss and haemorrhage was subsequently noted in brain sections (**Figure 6.10C**). Overall, 10 Gy RT seemed to extend survival of SU-DIPG-13P* model and was picked as an optimal dose to combine with atovaquone.

Next, atovaquone and RT combination study was performed. Again, SU-DIPG-13P* cells were intracranially injected (400,000 cells/mouse) into the brainstem of balb/c nude mice. Since both commercial atovaquone and ASD atovaquone formulation resulted in a similar level of OCR and hypoxia decrease *in vitro* (**chapter 4**), and ASD atovaquone is a better BBB penetrant version (123) we used the latter in our *in vivo* studies. **Figure 6.11A** shows the experimental plan for this study. Here, ASD atovaquone was given at 200 mg/kg/day in sterile PBS. This dosage was selected based on previously published work on commercial atovaquone with similar schedule extending survival in hypopharyngeal carcinoma model (103). ASD atovaquone was given over a period of 10 days with treatment started at day 10. RT at 10 Gy with 2 Gy fraction per day was started at day 14. The last 5 days of ASD atovaquone treatment coincided with RT with atovaquone treatment given 1 hour prior to RT. The median survival

of vehicle control was 26 days and was not significantly different to ASD atovaquone only group with a median survival of 27 days (**Figure 6.11B**). The median survival was significantly extended by ASD atovaquone+10 Gy RT to 45 days compared to control (***P<0.001). The median survival was further significantly extended by 10 Gy RT to 51.5 days compared to control (***P<0.0009) (**Figure 6.11B**). All the mice tolerated ASD atovaquone very well and there were no side effects from the treatment. At the endpoint, the control mice were intraperitoneally injected with 100 mg/kg pimonidazole to facilitate detection of hypoxia and euthanised 1 hour post-injection (pimonidazole staining results discussed in **Section 6.2.2**).

Alongside the atovaquone/RT combination study, we also measured the concentration of ASD atovaquone in the plasma and various regions of the brain (cerebellum, brainstem and prefrontal cortex). Brain and plasma concentration analysis was performed by Dr Ryan J. Duchatel at The University of Newcastle. **Figure 6.12A** shows the experimental plan for this study. ASD atovaquone was given at 200 mg/kg/day in sterile PBS, over a period of 6 days. On the 6th day, mice were sacrificed 1 hour post-dosing, bloods were collected via cardiac puncture and brain regions were excised and evaluated for ASD atovaquone concentration. An average plasma concentration of 47900 ng/ml (130.6 μM) was achieved (**Figure 6.12B**). ASD atovaquone concentrations in the cerebellum, brainstem and prefrontal cortex were 3635 ng/g, 3795 ng/g and 1765 ng/g respectively (**Figure 6.12C**). In comparison to the previously developed atovaquone formulations, the nanosuspension and nanoemulsion formulations (131, 132), the ASD atovaquone formulation appeared to result in the highest brain levels (**Figure 6.12D**).

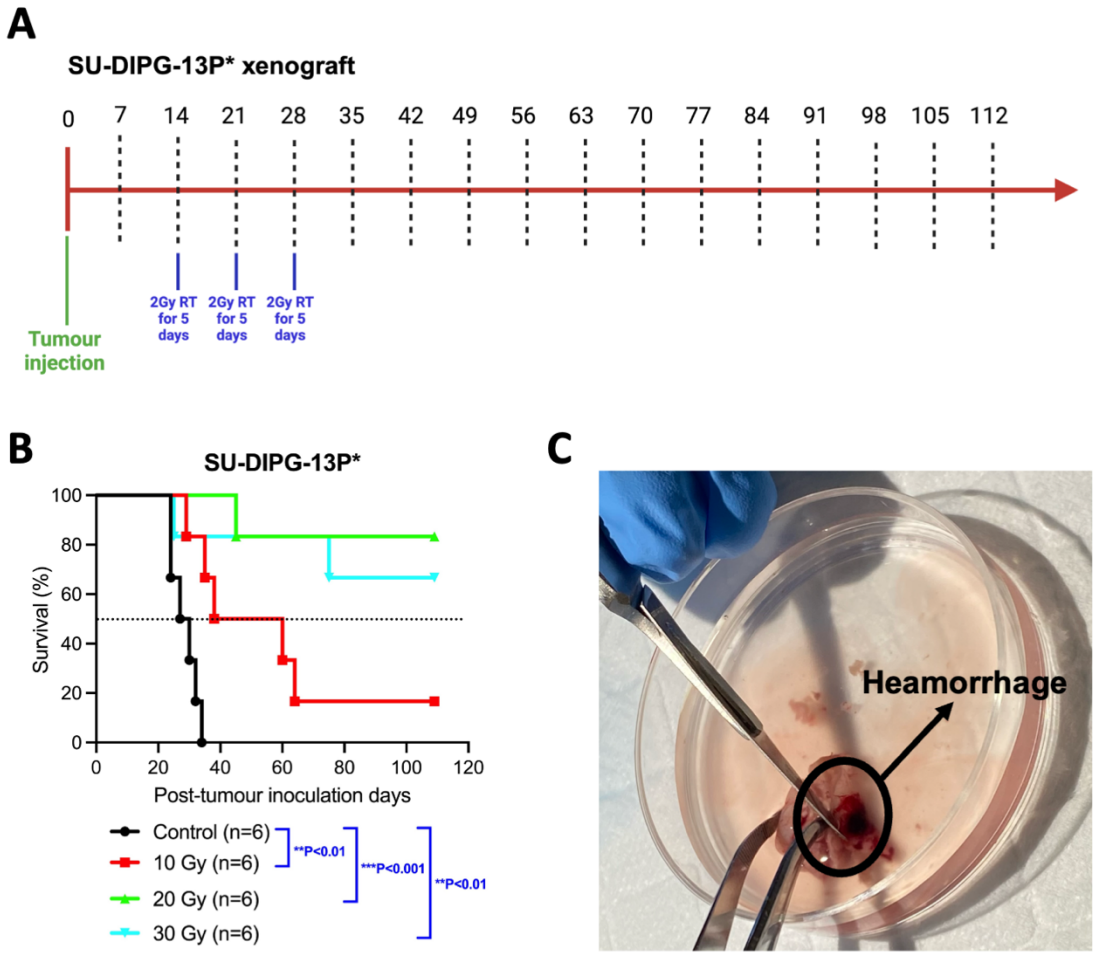

Figure 6.10. Assessing the efficacy of RT using SU-DIPG-13P* model.
(A) Layout of the animal study for RT only using SU-DIPG-13P* xenograft. (B) RT dose response survival curves using SU-DIPG-13P* model. Mice were treated with 10, 20 and 30 Gy RT in 2 Gy fractions over five days a week. Treatment was started two weeks post tumour injection. Significance was calculated using log-rank (Mantel-Cox) test. (C) Heamorrhage noticed on dissected mouse brain from 30 Gy group.

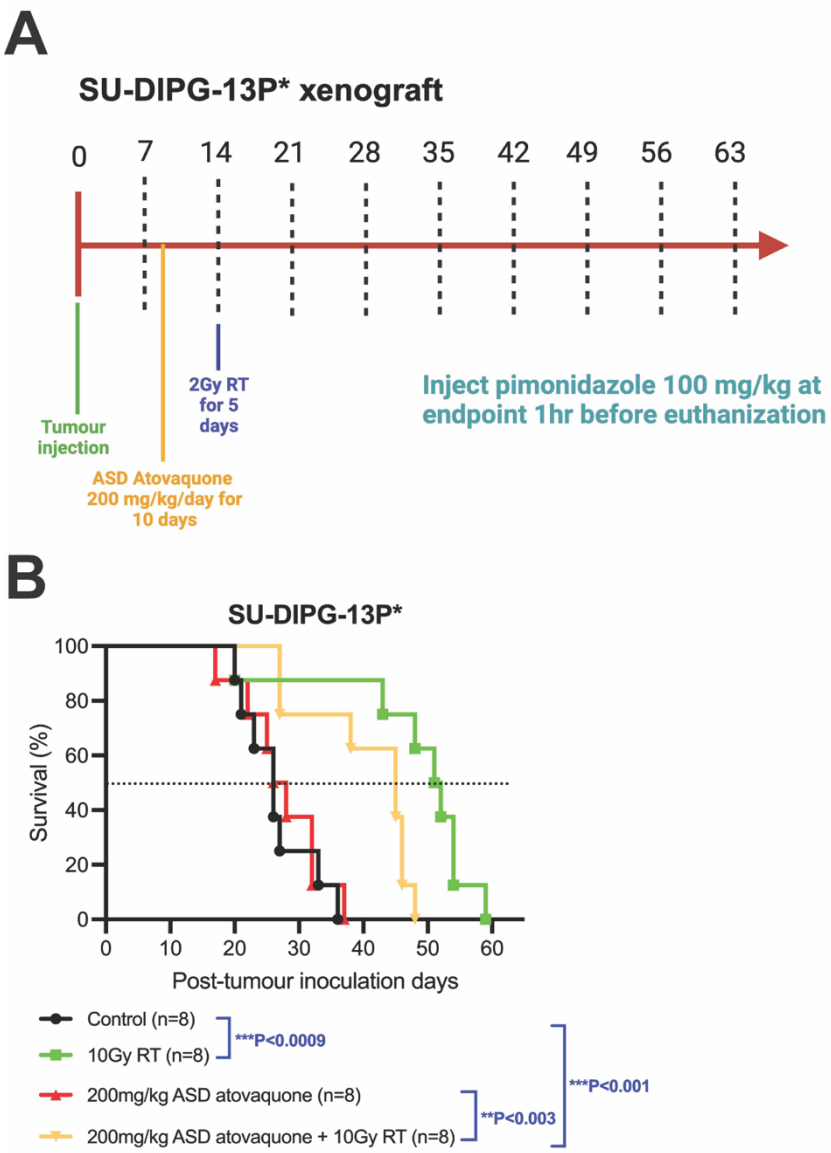

Figure 6.11. Assessing the efficacy of ASD atovaquone and RT using SU-DIPG-13P* model.
(A) Layout of the animal study. Mice were treated with 10 Gy RT in 2 Gy fractions over 5 days a week and with 200mg/kg/day ASD atovaquone for 10 days. ASD atovaquone treatment was started at day 9 and RT was started at day 13. Control mice were injected with pimonidazole at 100 mg/kg at endpoint 1 hour post euthanisation. (B) ASD atovaquone and RT dose response survival curves using SU-DIPG-13P* model. Significance was calculated using log-rank (Mantel-Cox) test.

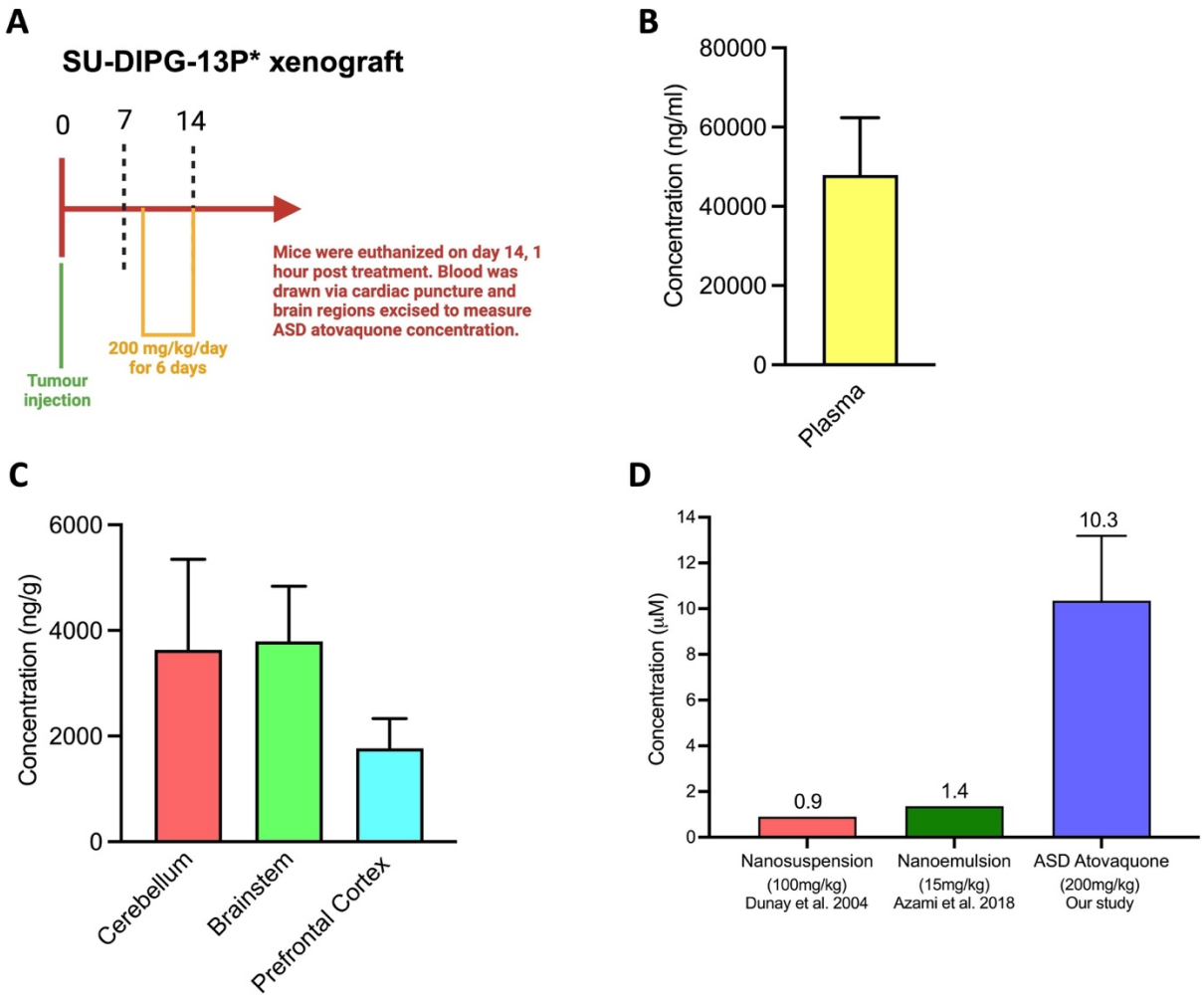

Figure 6.12. Analysis of brain and plasma concentration of ASD atovaquone.
(A) Layout of the animal study for determining ASD atovaquone and concentration using SU-DIPG-13P* xenograft. Mice were treated with 200mg/kg/day ASD atovaquone for 6 days. (B-C) Mass spectrometry analysis of atovaquone concentrations performed on *in vivo* samples of mice injected with DIPG cells. (B) ASD atovaquone concentration in plasma (n=4 mice). (C) ASD atovaquone concentration in cerebellum, brainstem and prefrontal cortex (n=5 mice). (D) Comparison of ASD atovaquone concentrations with previously prepared atovaquone formulations.

6.2.3.2 RT and drug studies using parental HSJD-DIPG-007 model

The radiosensitising efficacy of ASD atovaquone was also investigated using HSJD-DIPG-007 model. As we were not successful in generating stable GFP/luciferase-expressing HSJD-DIPG-007 cells (**section 6.2.1**), we used the parental HSJD-DIPG-007 model for this experiment. Dose response curves for RT for HSJD-DIPG-007 model had already been established by our lab group and 10 Gy was used as the optimal dose to combine with atovaquone. RT treatment schedule was followed based on our lab group's previous work and drug treatment was initiated a week prior to that. HSJD-DIPG-007 cells were intracranially injected (200,000 cells/mouse) into the brainstem of balb/c nude mice. **Figure 6.13A** shows the experimental plan for this study. ASD atovaquone was given at 200 mg/kg/day in sterile PBS, over a period of 12 days with treatment started at day 21. RT at 10 Gy with 2 Gy fraction per day was started at day 28. The last 5 days of ASD atovaquone treatment coincided with RT with atovaquone treatment given 1 hour prior to RT. The median survival of vehicle control was 76 days and was not significantly different to ASD atovaquone only group with a median survival of 70.5 days (**Figure 6.13B**). The median survival was extended to 80 days in 10 Gy RT group, however this was not significantly different compared to vehicle control (**Figure 6.13B**). The median survival was significantly extended by ASD atovaquone+10 Gy RT to 90 days compared to control (**P<0.0052) (**Figure 6.13B**). All the mice tolerated ASD atovaquone very well and there were no side effects from the treatment. At the endpoint, some control mice were injected intraperitoneally with 100 mg/kg pimonidazole and euthanised 1 hour post-injection whereas others were injected intraperitoneally with 10 mg/kg EF5 and euthanised 3 hour post-injection. The brains were excised and IHC was performed (pimonidazole and EF5 staining results discussed in **Section 6.2.2**).

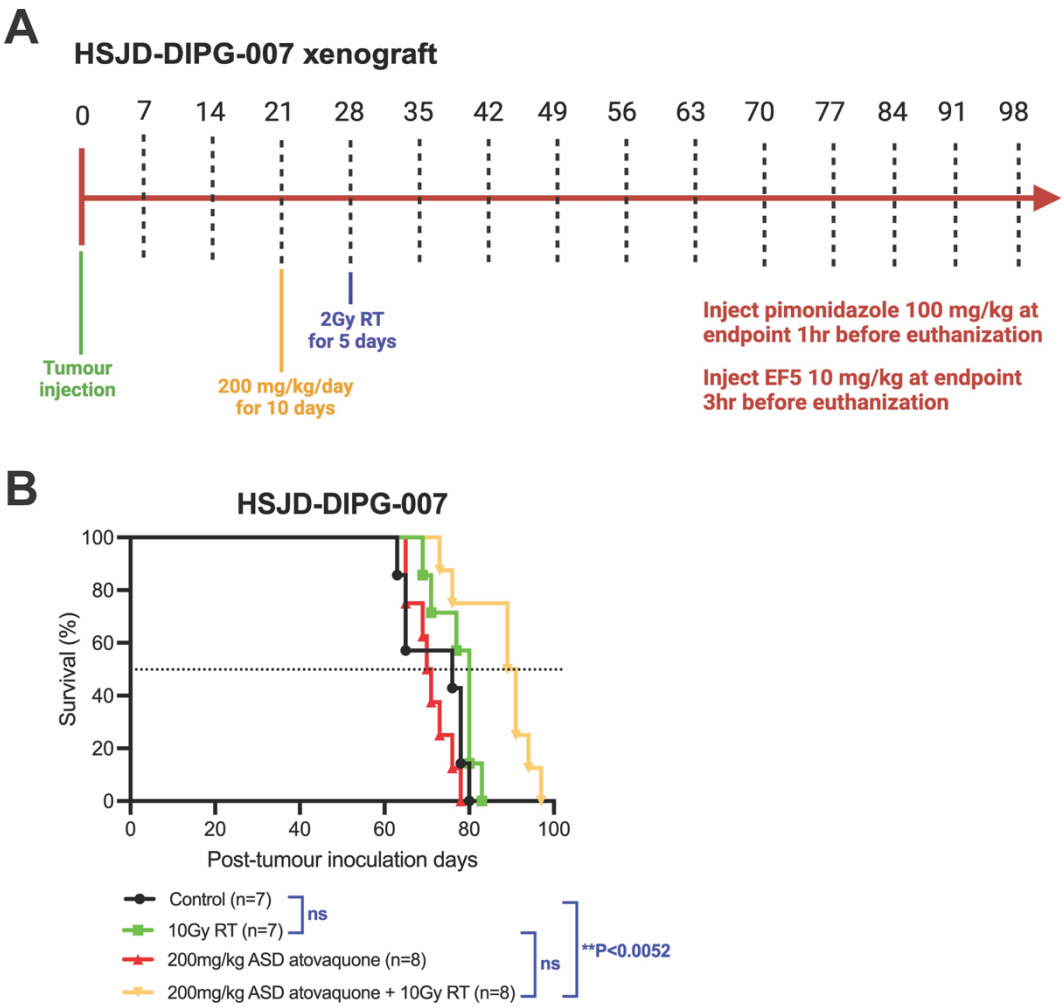

Figure 6.13. Assessing the efficacy of ASD atovaquone and RT using HSJD-DIPG-007 model.
(A) Layout of the animal study. Mice were treated with 10 Gy RT in 2 Gy fractions over 5 days a week and with 200mg/kg/day ASD atovaquone for 12 days. ASD atovaquone treatment was started at day 21 and RT was started at day 28. Some control mice were injected with pimonidazole at 100 mg/kg at endpoint 1 hour post euthanisation and others were injected with EF5 at 10 mg/kg at endpoint 3 hour post euthanisation. (B) ASD atovaquone and RT dose response survival curves using HSJD-DIPG-007 model. Significance was calculated using log-rank (Mantel-Cox) test.

6.3. Discussion

In chapter 6, we performed lentiviral transduction of HSJD-DIPG-007 to create stable GFP/luciferase expressing cells. Our aim was to inject these cells into the mice, monitor tumour growth longitudinally over time and determine optimal treatment starting time. However, we observed loss of GFP and luciferase expression over time in these cells, with reasoning discussed below. Next, we aimed to assess the presence of hypoxia in these DIPG models using a range of hypoxia markers. We detected positive HIF-1α, VEGFA and EF5 staining colocalising in the tumour region, supporting the presence of hypoxia in these tumour models. Finally, we performed animal studies investigating the radiosensitising efficacy of ASD atovaquone using SU-DIPG-13P* and HSJD-DIPG-007 xenografts. Atovaquone and RT combination only significantly extended survival in HSJD-DIPG-007 model compared to vehicle control.

6.3.1 Lentiviral transduction of HSJD-DIPG-007 cells

Our findings suggest that there are real differences in lentiviral transduction of different DIPG cell lines. We performed lentiviral transduction for the first time following the similar protocol from our collaborators who were successful in generating the GFP/luciferase-expressing SU-DIPG-24 and SU-DIPG-XVII using GFP-luciferase fusion protein. All of their transduced cells appeared to stably express luciferase despite several passages. In our work, the GFP/luciferase-expressing HSJD-DIPG-007 appeared to lose the GFP expression initially whilst the luciferase signal, although lower than that of SU-DIPG-24, was still maintained with fewer passages (**Figure 6.1-6.2**). Despite the stable luciferase signal, our collaborators had also seen loss of GFP over time with SU-DIPG-24 and SU-DIPG-XVII following several passages, suggesting that it is likely that the GFP and luciferase signal might not correlate well in these DIPG cell lines. Therefore, we concluded that our GFP/luciferase-expressing HSJD-DIPG-007 could still useable for *in vivo* investigation as the IVIS readings showed an increase luminescence signal with increasing cell number (**Figure 6.2E-F**). Despite imaging twice at 37 and 60 days, no signal was detected *in vivo* which could either be because there is a loss of luciferase expression over time as seen by a 2.8-fold decrease in luminescence signal with IVIS when comparing **Figure 6.2E-F** with **Figure 6.3A-B**. Another reasoning is that lentiviral transduction modified the behaviour of the HSJD-DIPG-007 cells, affecting their engraftment capacity, such that these likely do not form tumours *in vivo*. We say this because the mice injected with

GFP/luciferase-expressing HSJD-DIPG-007 cells did not reach median survival up until 105 days (**Figure 6.3E**). Additionally, no H3K27M staining was detected in the GFP/luciferase-expressing HSJD-DIPG-007 model (**Figure 6.3F**). Their change in behaviour is further supported by the finding that despite 5 days of culture, the GFP/luciferase-expressing HSJD-DIPG-007 cells did not form single neurosphere with u-bottom plates (**Figure 6.2D**) as opposed to parental HSJD-DIPG-007 cells which easily clump into one neurosphere within 48 hours of culture.

There could be several reasons for our observed findings and further optimisation could improve our methodology of generating stable luciferase-expressing HSJD-DIPG-007 cells. Firstly, we did not try a range of MOI (multiplicity of infections) which correspond to the number of lentiviral particles needed per cell to obtain maximum efficiently transduced cells (245). We used MOI of 3.6 based on other DIPG cell lines, however testing several MOIs to determine the optimal MOI might increase transduction efficiency (245). Secondly, exposure to fetal bovine serum (FBS) has been shown to improve transduction efficiency. The HSJD-DIPG-007 cells are normally cultured in serum-free media, however a protocol published by Meel et al. (2018) suggests that short-term FBS exposure could enhance transduction and result in higher expression of GFP fluorescent proteins (246). Our next approach would be to follow their transduction method however as FBS exposure can induce permanent changes in glioma cells by inducing differentiation hence, it is recommended to validate the identity of the cell line, expression of stem cell markers, and engraftment capacity by comparing transduced cells against parental untransduced cells (246). Thirdly, we transduced the cells with GFP-luciferase fusion protein and our approach involved using GFP to sort for and isolate luciferase expressing clones. We performed sorting almost one month post transduction. However, a protocol by Brennan et al. (2018) recommends that the most efficient method is to FACS sort individual GFP expressing cells within a week post transduction (235). Similarly, the protocol by Meel et al. (2018) also sorted the GFP positive cells within two weeks following transduction (246). Because we performed sorting very late, the cells might have already lost GFP signal leading us to obtaining very few GFP-luciferase positive cells. Hence, future approaches should consider this and aim to perform sorting at an earlier stage to obtain higher GFP expressing cells. Fourthly, as we used the fusion GFP-luciferase protein, it would be interesting to modify the plasmid to separate out the GFP and luciferase proteins so these can be expressed separately. This would rule out any issues regarding the correlation of GFP and luciferase signal as with the GFP-luciferase fusion protein. All of the reasonings discussed here might

help in improving the transduction efficiency and generating stable luciferase-expressing HSJD-DIPG-007 cells for *in vivo* usage.

6.3.2 Immunohistochemistry analysis of hypoxia markers in orthotopic DIPG models

The expression of various endogenous proteins can be used to infer tumour hypoxia. The results in this section provide some evidence to validate the presence of hypoxia in DIPGs, thus providing strong support towards our study hypothesis. From our knowledge, no previous study has shown positive IHC staining with hypoxia markers in DIPGs. We found positive HIF-1α staining colocalising in the SU-DIPG-13P* tumour region suggesting activation of hypoxia sensing pathways in DIPG. Previous studies have assessed HIF-1α expression in several tumour types with IHC patterns showing increased HIF-1α expression suggestive of hypoxia in these tumours (247). As HIF-1α activates VEGFA, we also observed VEGFA staining colocalising in the SU-DIPG-13P* tumour area. Positive relationship between HIF-1α and VEGFA has been shown in clinical studies (248). Moreover, we also observed high expression of EF5, a clinically relevant marker for tumour hypoxia, in HSJD-DIPG-007 tumour area colocalising with H3K27M positive tumour cells. The advantage of using EF5 is that it distributes evenly across tissues, including the brain, and it only binds to viable hypoxic cells so no signal will be generated in regions with dead cells (240). A previous study has also shown positive EF5 staining in areas with higher Ki67 cells suggesting increase in hypoxia in areas with rapid tumour proliferation (249).

We also assessed CA-IX staining however the entire brain region in both tumour models was stained. CA-IX appeared to work well in the stomach tissue staining. It could be that there are differences in hypoxia thresholds for different antibodies. Despite testing a range of CA-IX antibodies from several sources, we found the entire brain area to be stained, suggesting that these antibodies might not be specific for brain tissues. Another study has also concluded that there can be unappreciated differences in hypoxia staining markers across similar tissues (249). Additionally, we also found that several studies on brain tumours appear to use the well characterised M75 antibody which is highly specific for CA-IX detection instead of the commercial CA-IX antibodies (250-252). As we have been trying several commercial CA-IX antibodies, this might also be the reason for the non-specific staining seen in our results. Therefore, the next steps would be to assess CA-IX expression using the M75 antibody.

Finally, we looked at the expression of pimonidazole and no staining was detected in both DIPG tumour models despite trying different antigen retrieval buffers and various antibody concentrations. Past studies have injected pimonidazole at 60-120 mg/kg and euthanised mice within 1 hour post injection. Similar to those, we also injected pimonidazole at 100 mg/kg and euthanised mice at 1 hour post injection. However, we realised that there are differences in the tissue processing methods between our study and some past studies involving pimonidazole staining technique. Our methodology for IHC involved using FFPE brain sections. Here, mice brains were fixed in formalin for 24 hours, formalin was replaced with 70% ethanol, and FFPE blocks were prepared. However, some past studies have employed a different protocol for tissue processing such as freezing tissues in -40°C isopentane and storing in -80°C until processing, or excising tumours and freezing on liquid nitrogen before processing (253, 254). It is hard to conclude if tissue processing is a major source of no staining detected in our study. Moreover, our IHC staining protocol for all the hypoxia staining markers was very similar and probably requires modification for detecting pimonidazole staining. This could be true because no pimonidazole staining was detected in the brain and also in the gut tissues, whereas CA-IX was detected in the mouse gut regions. We used HRP-conjugated secondary antibody but alternatives could be investigated as recommended by the hypoxyprobe^{TM} pimonidazole protocol.

Overall, the HIF-1α, VEGFA and EF5 positive staining in SU-DIPG-13P* and HSJD-DIPG-007 brain sections provide some evidence of hypoxia in DIPG tumours. This also provides strong links to our findings showing increased expression of mitochondrial ETC complexes genes in DIPGs (**Chapter 3)**. High dependence on mitochondrial OXPHOS is a hallmark of cancer and targeting this pathway with OXPHOS inhibitors (atovaquone/mefloquine) would reduce hypoxia in DIPGs. These results also support to our strategy of radiosensitising DIPG tumours by alleviating hypoxia. In the next steps, it would be interesting to show that atovaquone/mefloquine decreases the expression of these hypoxia markers post completion of treatment.

6.3.3 RT and drug studies

The results in this section show that 6 consecutive days of ASD atovaquone treatment at 200 mg/kg resulted in mean blood plasma concentration of ~130 μM. These levels are higher compared to Aston et al. (2018) study who achieved mean blood plasma concentration of 68.6 μM following 5 days of consecutive treatment with commercial atovaquone (103). Literature

reports that the oral bioavailability of atovaquone could be enhanced with food especially with high-fat diet (109). Aston et al. (2016) study used high-fat diet for their mice to improve atovaquone concentrations achieved (103). Interestingly, we did not use high fat diet in our study and obtained much higher plasma levels suggesting that ASD atovaquone on its own is less dependent on high-fat diet.

The brain levels achieved in our study were 10x lower at ~10 μM compared plasma levels, however these are significantly higher than previously prepared atovaquone formulations (131, 132). Additionally, our brain levels from ASD atovaquone are also lower than those reported in Takabe et al. (2018) study (123). The brain levels from ASD atovaquone obtained in their study was ~37 μM whereas we obtained ~10 μM. This could be due to differences in tissue processing between the studies. Moreover, unlike their study, our study included an additional wash step where the mice brain were perfused with saline prior to excising the sections, and this could also be a factor contributing to the differences in our findings. Nonetheless, as 10 μM was sufficient to decrease hypoxia and HIF-1α expression (**chapter 4**), achieving this level in the tumour region should be sufficient to improve the efficacy of RT in eradicating more DIPG tumour cells.

Our findings show that the median survival in ASD atovaquone+RT was worse compared to RT alone in SU-DIPG-13P* model suggesting that the combination did not improve survival in this model. The improved survival from the combination was likely from the effect of RT alone and the addition of atovaquone did not improve the efficacy of RT in this model. SU-DIPG-13P* is an aggressive tumour model with tumour cells infiltrating and growing like a solid mass (see H&E staining in **section 6.2.2 – Figure 6.4A-B and 6.5B**). Due to the growth pattern of these cells, we suspect that the drug was likely unable to reach the tumour cells and reduce hypoxia effectively as the treatment was started at day 10 post-tumour injection. We believe that starting treatment earlier and prolonging it for few additional days might vary the results that we achieved. This would be the next step to investigate radiosensitising efficacy of atovaquone using SU-DIPG-13P* by starting treatment earlier.

Furthermore, we found that the combination of ASD atovaquone+RT significantly extended survival in the HSJD-DIPG-007 xenograft model by 14 days. As this tumour model grows diffusely, the drug would have easily accessed the tumour area and eradicated hypoxia, thus improving the efficacy of RT in this model. This is further supported by our *in vitro* findings

showing 10 μM atovaquone reduces hypoxia, HIF-1α expression and improved the radiosensitivity of HSJD-DIPG-007 neurospheres (**Chapter 4**). Additionally, there was no significant difference in median survival between vehicle control and ASD atovaquone alone groups across both the models. The mice also well-tolerated the ASD atovaquone with no reported side-effects with 10 and 12 consecutive days of treatment, thus validating the safety profile of atovaquone. Our findings here provide promising evidence of atovaquone as a radiosensitiser of DIPG *in vivo*, and also support our *in vitro* findings (**Chapter 4**). Next steps would be to validate the radiosensitising efficacy of ASD atovaquone with other DIPG orthotopic models to provide further confidence in our findings.

Chapter 7

Conclusions and Future Directions

Chapter 7. Conclusions and Future Directions

The prognosis of DIPG remains dismal despite decades of ongoing clinical research. Almost all patients with DIPG die within 2 years from diagnosis (3). The sensitive brainstem location poses a challenge to surgical resection and various chemotherapeutics have failed to show any benefit. The current management of DIPG is reliant on RT, however it only offers temporary symptomatic relief, with tumour inevitably recurring within 3-8 months due to radioresistance (4). Therefore, there is an urgent need for more research and to develop novel therapeutics for this devasting disease.

As RT is the mainstay of treatment for DIPG, improving the effectiveness of RT appears to be most promising approach to enhance the survival outcomes of patients suffering with DIPG. Hence, in this study, we aimed to investigate novel treatments to improve the efficacy of RT in DIPG patients. An understanding of the mechanisms of radioresistance suggests that tumour hypoxia is one of the major contributing factors to clinical radioresistance. Hypoxia is a well-reported feature of many solid tumours including adult HGGs (64). Although there is no direct evidence of hypoxia in DIPGs, studies suggest the involvement of HIF-hypoxia signalling in paediatric HGGs, and have also observed low tissue perfusion in DIPG patients, proposing that DIPGs may also have a hypoxic TME (71, 72). The findings of this study also provide further support to the hypothesis that hypoxia could be a significant feature of DIPG TME. In **Chapter 3** of this thesis, we found elevated mRNA expression of a range of mitochondrial ETC genes in DIPG/DMG patient samples suggesting that DIPGs have upregulated OXPHOS. An increase in oxidative metabolism means that there is increased oxygen utilisation which could result in the development of localized hypoxia. Moreover, the presence of hypoxia is also supported in **Chapter 6** where we found increased expression of hypoxia markers HIF-1α, VEGFA and EF5 colocalising with the tumour regions in DIPG tumour-bearing mice brain sections. The hypoxia markers staining is a novel finding and supports our hypothesis, thus also suggesting that alleviating hypoxia could be an attractive strategy to improve the efficacy of RT in DIPG patients.

As DIPGs appear to have upregulated OXPHOS, we aimed to target tumour hypoxia by targeting mitochondrial OXPHOS of DIPG cells. Mitochondria are the powerhouse of the cells and the main source of oxygen utilization. Thus, inhibiting OXPHOS could reduce OCR and

increase oxygen availability in the tumour region. This would lead to a decrease in hypoxia and thus enhance radiosensitisation of the tumour cells. Hence, this study explored the radiosensitising efficacy of OXPHOS inhibitors against DIPG. In **Chapter 3**, we performed an OXPHOS inhibition drug screening and identified atovaquone and mefloquine as potent OCR inhibitors. Both of these drugs have not been previously studied in DIPG. Both compounds penetrate the BBB and were selected for further investigations in next chapters. As ivermectin doesn't penetrate the BBB, quinacrine was the third best compound in terms of OCR inhibition and BBB penetration. In future, studies could also investigate quinacrine's efficacy against DIPG.

In **Chapter 4**, we aimed to assess the hypoxia modification and radiosensitising efficacy of atovaquone. We found that atovaquone significantly decreased the OCR of all the tested DIPG cell lines and targeted the overall mitochondrial profile by decreasing a range of mitochondrial parameters. The anti-mitochondrial effect was achieved by specifically targeting the mitochondrial complex III of DIPG cells. Exposure to atovaquone treatment increased ROS levels suggesting that it also increases oxidative stress. Furthermore, atovaquone as an OXPHOS inhibitor, decreased hypoxia staining in 3D DIPG neurospheres, decreased the expression of HIF-1α in 3D cultures and sensitised these 3D DIPG neurosphere models to RT. Atovaquone also radiosensitised 2D DIPG cultures and our findings demonstrate that this effect is likely due to additional mechanisms including increased ROS-mediated oxidative stress following atovaquone+RT treatment. Overall, these findings supported the study hypothesis and validate atovaquone as a radiosensitiser of DIPG *in vitro*. Our findings are novel as atovaquone's efficacy has not been previously explored in DIPG. In the next steps, we also compared the efficacy of commercial atovaquone with the improved BBB penetrant version, ASD atovaquone formulation. Here, we showed for the first time that ASD atovaquone has similar efficacy to commercial atovaquone. This paved way for assessing ASD atovaquone in *in vivo* studies. In **Chapter 6**, the combination of ASD atovaquone+RT significantly extended survival of HSJD-DIPG-007 orthotopic DIPG model compared to single treatments. This promising finding validates the efficacy of atovaquone as radiosensitiser *in vivo*. However, atovaquone treatment did not demonstrate radiosensitisation in the aggressive DIPG model - SU-DIPG-13P*, likely due to delayed atovaquone treatment schedule. It is important to show efficacy in multiple *in vivo* models to validate the drug efficacy for advancing clinical trials. Hence, the future directions include validating the *in vivo* efficacy of ASD atovaquone using

other DIPG models. The study using SU-DIPG-13P* model should be repeated with a revised atovaquone treatment plan. Additionally, given atovaquone's established safety and tolerability, further optimisation to improve brain penetration could enhance its therapeutic utility. It would also be useful to obtain brain sections post atovaquone treatment and validate the decrease in hypoxia markers following treatment with IHC.

Moreover, the RNA sequencing findings in **Chapter 4** confirm some of our *in vitro* findings including decrease in hypoxia-HIF signalling and increase in ROS pathway following atovaquone treatment. The RNA sequencing results also demonstrate some novel findings including atovaquone treatment resulting in an increase in cholesterol metabolism pathways and steroid biosynthesis, glycine, serine and theorine metabolism and terpenoid backbone biosynthesis. This suggests that the cells may be shifting to cholesterol metabolism following atovaquone treatment. Future studies could perform metabolomic study to further support and understand the metabolic changes in DIPG cells following atovaquone treatment. This will be useful in devising novel combination strategies with an aim to block additional pathways that DIPG cells might be utilising to survive atovaquone treatment effect.

Furthermore, another interesting finding from our RNA sequencing results (**Chapter 4**) is an increase in the activation of several immune system pathways following atovaquone treatment. As hypoxia contributes to immune suppression (58), our findings suggest that modulating hypoxia by atovaquone could enhance immune activation in DIPG. These interesting findings provide a basis for future studies to explore about how atovaquone alters the "cold" TME of DIPG and changes the specific immune cells and immune pathways. As hypoxia is a known barrier to both RT and immunotherapy (58), our findings reveal that decreasing hypoxia by atovaquone increases the efficacy of RT and increases immune activation, the next steps could also consider investigating the combination of OXPHOS inhibitors with RT and immunotherapy against DIPG. This could an intriguing area of research for future studies on DIPG.

In **Chapter 5**, we aimed to assess the hypoxia modification and radiosensitising efficacy of the second best OCR inhibitor mefloquine. Unlike atovaquone, mefloquine decreased both the OCR and ECAR of DIPG cells suggesting that it decreases both mitochondrial and glycolytic metabolism of DIPG cells. Mefloquine appears to target the mitochondria at all complex levels

as we observed a decrease in complex-specific OCR of all complexes. However, similar to a previous study, we also observed a decrease in the protein expression of complex II subunit SDHD. Mutations in SDHD are shown to impair cell proliferation and metabolism (228). A decrease in SDHD by mefloquine could be linked to its anti-proliferative efficacy and the observed decrease in OCR and ECAR. Moreover, mefloquine also decreased hypoxia staining in 3D DIPG neurospheres and decreased the expression of HIF-1α in 3D cultures suggesting that a decrease in OCR by mefloquine could resolve hypoxia. Mefloquine treatment also radiosensitised the DIPG cells to RT, supporting our study hypothesis and validating mefloquine as a radiosensitiser *in vitro*. Our *in vitro* findings provide sufficient evidence to consider and study mefloquine's radiosensitising using orthotopic DIPG models. Mefloquine is also attractive as it readily penetrates the BBB and accumulates in the brain, achieving high concentrations (170, 171). Although there are well-reported side effects from mefloquine, we intend to use low doses of mefloquine for future planned animal studies. Our findings will provide further insight on the feasibility of mefloquine for DIPG.

Additionally, we also performed the lentiviral-transduction to generate stable GFP/luciferase-expressing HSJD-DIPG-007 cells (in **Chapter 6**). The purpose was to track tumour progression and guide with treatment starting times. Unfortunately, these cells appeared to lose their GFP and luciferase expression over time. The lentiviral transduction appeared to modify the behaviour of these cells such that they appeared to lose their engraftment capacity as the mice injected with these cells did not reach endpoint up until 105 days. Also, no bioluminescence signal was detected when these mice were imaged multiple times with IVIS imaging. Future studies could improve on the current lentiviral transduction methodology in several ways including trying a range of MOIs to improve transduction efficiency, incorporating short-term FBS exposure in the protocol to enhance transduction, FACS sorting the individual GFP expressing cells earlier i.e., within a week post transduction and considering modification of the GFP-luciferase protein plasmid to separate out the GFP and luciferase proteins so any correlation issues between GFP and luciferase signal could be ruled out.

This study has several limitations that should be addressed in future work. Firstly, time and resource constraints prevented us from performing additional validations of atovaquone and mefloquine using orthotopic DIPG models. The *in vivo* studies were also carried out on immunodeficient mice, which do not fully recapitulate the tumour microenvironment of

paediatric brain tumours. Future radiosensitisation work should also consider utilizing immunocompetent mice models to better reflect clinical setting. Time-constraints also limited further optimisation of lentiviral transductions for the cell line HSJD-DIPG-007. Moreover, despite repeated attempts, staining for hypoxia markers (CA-IX and pimonidazole) was unsuccessful due to technical challenges. These limitations highlight the need for further investigations to strengthen the translational potential of our findings.

In summary, the results in this study provide strong evidence supporting the strategy of targeting OXPHOS to reduce hypoxia and enhance radiosensitivity of DIPG. As RT is the primary management option for DIPG, and is also widely utilised in other solid tumours, the addition of OXPHOS inhibitors represents an attractive approach to improve therapeutic response. The drugs explored in this study (atovaquone and mefloquine) are repurposed drugs, with established pharmacokinetic safety profiles, including prior use in paediatric patients, which enhances their translational relevance. We demonstrated that atovaquone enhances radiosensitivity of DIPG models *in vitro* and, importantly, the BBB-penetrant formulation ASD atovaquone prolonged survival in orthotopic DIPG model when combined with RT. Mefloquine was also identified as another potential radiosensitiser of DIPG *in vitro*. Beyond DIPG, these findings may have valuable implications on other hypoxic brain tumours such as glioblastoma, ependymoma, and medulloblastoma, as well as extracranial tumours where RT is the main treatment modality. Along with impairing RT response, hypoxia also has negative impact on immune function and these OXPHOS inhibitors could also be combined with immunotherapy and chemotherapy. Clinical feasibility could be supported by the availability of hypoxia biomarkers to enable careful patient selection and also assessing hypoxia status of the patient with imaging tools. Additionally, validating our findings across additional DIPG orthotopic models, including immunocompetent models, will further strengthen the evidence for clinical translation. Overall, the work presented in this thesis highlights a promising therapeutic strategy that leverages repurposed, clinically available drugs to improve radiotherapy outcomes in DIPG.

References

1. Jones C, Baker SJ. Unique genetic and epigenetic mechanisms driving paediatric diffuse high-grade glioma. Nature reviews Cancer. 2014;14(10):651-61.
2. Hargrave D, Bartels U, Bouffet E. Diffuse brainstem glioma in children: critical review of clinical trials. The lancet oncology. 2006;7(3):241-8.
3. Srikanthan D, Taccone MS, Van Ommeren R, Ishida J, Krumholtz SL, Rutka JT. Diffuse intrinsic pontine glioma: current insights and future directions. Chinese neurosurgical journal. 2021;7(1):6-.
4. Warren KE. Diffuse intrinsic pontine glioma: poised for progress. Frontiers in oncology. 2012;2:205-.
5. Larson JD, Kasper LH, Paugh BS, Jin H, Wu G, Kwon C-H, et al. Histone H3.3 K27M Accelerates Spontaneous Brainstem Glioma and Drives Restricted Changes in Bivalent Gene Expression. Cancer cell. 2019;35(1):140-55.e7.
6. Donaldson SS, Laningham F, Fisher PG. Advances Toward an Understanding of Brainstem Gliomas. Journal of clinical oncology. 2006;24(8):1266-72.
7. Bentayebi K, Aked RE, Ezzahidi O, Alami AB, Louati S, Ouadghiri M, et al. Targeting molecular mechanisms underlying treatment efficacy and resistance in DIPG: A review of current and future strategies. Brain disorders. 2024;14:100132.
8. Albright AL, Guthkelch AN, Packer RJ, Price RA, Rourke LB. Prognostic factors in pediatric brain-stem gliomas. Journal of neurosurgery. 1986;65(6):751-5.
9. Fisher PG, Breiter SN, Carson BS, Wharam MD, Williams JA, Weingart JD, et al. A clinicopathologic reappraisal brain stem tumor classification: Identification of pilocytic astrocytoma and fibrillary astrocytoma as distinct entities. Cancer. 2000;89(7):1569-76.
10. Cohen KJ, Jabado N, Grill J. Diffuse intrinsic pontine gliomas - Current management and new biologic insights. Is there a glimmer of hope? Neuro-oncology (Charlottesville, Va). 2017;19(8):1025-34.
11. Barkovich AJ, Krischer J, Kun LA, Packer RJ, Zimmerman RA, Freeman CR, et al. Brain Stem Gliomas: A Classification System Based on Magnetic Resonance Imaging. Pediatric neurosurgery. 1990;16(2):73-83.
12. Ezponda T, Licht JD. Molecular Pathways: Deregulation of Histone 3 Lysine 27 Methylation in Cancer—Different Paths, Same Destination. Clinical cancer research. 2014;20(19):5001-8.
13. Wierzbicki K, Ravi K, Franson A, Bruzek A, Cantor E, Harris M, et al. Targeting and Therapeutic Monitoring of H3K27M-Mutant Glioma. Current oncology reports. 2020;22(2):19-.
14. Liu G, Qiu Y, Zhang P, Chen Z, Chen S, Huang W, et al. Immunogenic Cell Death Enhances Immunotherapy of Diffuse Intrinsic Pontine Glioma: From Preclinical to Clinical Studies. Pharmaceutics. 2022;14(9):1762.
15. Louis DN, Perry A, Reifenberger G, von Deimling A, Figarella-Branger D, Cavenee WK, et al. The 2016 World Health Organization Classification of Tumors of the Central Nervous System: a summary. Acta Neuropathologica. 2016;131(6):803-20.
16. Louis DN, Perry A, Wesseling P, Brat DJ, Cree IA, Figarella-Branger D, et al. The 2021 WHO Classification of Tumors of the Central Nervous System: a summary. Neuro-oncology (Charlottesville, Va). 2021;23(8):1231-51.
17. Argersinger DP, Rivas SR, Shah AH, Jackson S, Heiss JD. New developments in the pathogenesis, therapeutic targeting, and treatment of h3k27m-mutant diffuse midline glioma. Cancers. 2021;13(21):5280.

18. Moini J, Piran P. Chapter 9 - Brainstem. In: Moini J, Piran P, editors. Functional and Clinical Neuroanatomy: Academic Press; 2020. p. 293-317.
19. Weisbrod LJ, Thiraviyam A, Vengoji R, Shonka N, Jain M, Ho W, et al. Diffuse intrinsic pontine glioma (DIPG): A review of current and emerging treatment strategies. Cancer letters. 2024;590:216876.
20. Haas-Kogan DA, Banerjee A, Kocak M, Prados MD, Geyer JR, Fouladi M, et al. Phase i trial of tipifarnib in children with newly diagnosed intrinsic diffuse brainstem glioma. Neuro-oncology (Charlottesville, Va). 2008;10(3):341-7.
21. Hennika T, Becher OJ. Diffuse Intrinsic Pontine Glioma: Time for Cautious Optimism. Journal of child neurology. 2016;31(12):1377-85.
22. Hayashi A, Ito E, Omura M, Aida N, Tanaka M, Tanaka Y, et al. Hypofractionated radiotherapy in children with diffuse intrinsic pontine glioma. Pediatrics international. 2020;62(1):47-51.
23. Stereotactic biopsy split-course radiation therapy for diffuse midline glioma, SPORT-DMG STUDY.
24. Fontanilla HP, Pinnix CC, Ketonen LM, Woo SY, Vats TS, Rytting ME, et al. Palliative reirradiation for progressive diffuse intrinsic pontine glioma. American journal of clinical oncology. 2012;35(1):51-7.
25. Eberle F, Lautenschläger S, Engenhart-Cabillic R, Jensen AD, Carl B, Stein M, et al. Carbon ion beam reirradiation in recurrent high-grade glioma. Cancer management and research. 2020;12:633-9.
26. Saeed AM, Khairnar R, Sharma AM, Larson GL, Tsai HK, Wang CJ, et al. Clinical Outcomes in Patients with Recurrent Glioblastoma Treated with Proton Beam Therapy Reirradiation: Analysis of the Multi-Institutional Proton Collaborative Group Registry. Advances in radiation oncology. 2020;5(5):978-83.
27. Muroi A, Mizumoto M, Ishikawa E, Ihara S, Fukushima H, Tsurubuchi T, et al. Proton therapy for newly diagnosed pediatric diffuse intrinsic pontine glioma. Child's nervous system. 2020;36(3):507-12.
28. Subashi E, Cordero FJ, Halvorson KG, Qi Y, Nouls JC, Becher OJ, et al. Tumor location, but not H3.3K27M, significantly influences the blood–brain-barrier permeability in a genetic mouse model of pediatric high-grade glioma. Journal of neuro-oncology. 2016;126(2):243-51.
29. Kulubya ES, Kercher MJ, Phillips HW, Antony R, Edwards MSB. Advances in the Treatment of Pediatric Brain Tumors. Children (Basel). 2022;10(1):62.
30. Kline C, Felton E, Allen IE, Tahir P, Mueller S. Survival outcomes in pediatric recurrent high-grade glioma: results of a 20-year systematic review and meta-analysis. Journal of neuro-oncology. 2018;137(1):103-10.
31. Kline C, Liu SJ, Duriseti S, Banerjee A, Nicolaides T, Raber S, et al. Reirradiation and PD-1 inhibition with nivolumab for the treatment of recurrent diffuse intrinsic pontine glioma: a single-institution experience. Journal of neuro-oncology. 2018;140(3):629-38.
32. Cacciotti C, Choi J, Alexandrescu S, Zimmerman MA, Cooney TM, Chordas C, et al. Immune checkpoint inhibition for pediatric patients with recurrent/refractory CNS tumors: a single institution experience. Journal of neuro-oncology. 2020;149(1):113-22.
33. Mount CW, Majzner RG, Sundaresh S, Arnold EP, Kadapakkam M, Haile S, et al. Potent antitumor efficacy of anti-GD2 CAR T cells in H3-K27M+ diffuse midline gliomas. Nature medicine. 2018;24(5):572-9.
34. Majzner RG, Ramakrishna S, Yeom KW, Patel S, Chinnasamy H, Schultz LM, et al. GD2-CAR T cell therapy for H3K27M-mutated diffuse midline gliomas. Nature (London). 2022;603(7903):934-41.

35. Ylösmäki E, Cerullo V. Design and application of oncolytic viruses for cancer immunotherapy. Current opinion in biotechnology. 2020;65:25-36.
36. Martinez-Velez N, Marigil M, García-Moure M, Gonzalez-Huarriz M, Aristu JJ, Ramos-García LI, et al. Delta-24-RGD combined with radiotherapy exerts a potent antitumor effect in diffuse intrinsic pontine glioma and pediatric high grade glioma models. Acta neuropathologica communications. 2019;7(1):64-.
37. Martínez-Vélez N, Garcia-Moure M, Marigil M, González-Huarriz M, Puigdelloses M, Gallego Pérez-Larraya J, et al. The oncolytic virus Delta-24-RGD elicits an antitumor effect in pediatric glioma and DIPG mouse models. Nature communications. 2019;10(1):2235-.
38. Cockle JV, Brüning-Richardson A, Scott KJ, Thompson J, Kottke T, Morrison E, et al. Oncolytic Herpes Simplex Virus Inhibits Pediatric Brain Tumor Migration and Invasion. Molecular therapy Oncolytics. 2017;5(C):75-86.
39. Ochs K, Ott M, Bunse T, Sahm F, Bunse L, Deumelandt K, et al. K27M-mutant histone-3 as a novel target for glioma immunotherapy. Oncoimmunology. 2017;6(7):e1328340-e.
40. Mueller S, Taitt JM, Villanueva-Meyer JE, Bonner ER, Nejo T, Lulla RR, et al. Mass cytometry detects H3.3K27M-specific vaccine responses in diffuse midline glioma. The Journal of clinical investigation. 2020;130(12):6325-37.
41. Benitez-Ribas D, Cabezón R, Flórez-Grau G, Molero MC, Puerta P, Guillen A, et al. Immune response generated with the administration of autologous dendritic cells pulsed with an allogenic tumoral cell-lines lysate in patients with newly diagnosed diffuse intrinsic pontine glioma. Frontiers in oncology. 2018;8:127.
42. Zhou T, Zhang LY, He JZ, Miao ZM, Li YY, Zhang YM, et al. Review: Mechanisms and perspective treatment of radioresistance in non-small cell lung cancer. Frontiers in immunology. 2023;14:1133899-.
43. Busato F, Khouzai BE, Mognato M. Biological Mechanisms to Reduce Radioresistance and Increase the Efficacy of Radiotherapy: State of the Art. International journal of molecular sciences. 2022;23(18):10211.
44. McKeown SR. Defining normoxia, physoxia and hypoxia in tumours-implications for treatment response. British journal of radiology. 2014;87(1035):20130676-.
45. Liao C, Liu X, Zhang C, Zhang Q. Tumor hypoxia: From basic knowledge to therapeutic implications. Seminars in cancer biology. 2023;88:172-86.
46. Sørensen BS, Horsman MR. Tumor Hypoxia: Impact on Radiation Therapy and Molecular Pathways. Frontiers in oncology. 2020;10:562-.
47. Emami Nejad A, Najafgholian S, Rostami A, Sistani A, Shojaeifar S, Esparvarinha M, et al. The role of hypoxia in the tumor microenvironment and development of cancer stem cell: a novel approach to developing treatment. Cancer cell international. 2021;21(1):62-.
48. Begg K, Tavassoli M. Inside the hypoxic tumour: reprogramming of the DDR and radioresistance. Cell death discovery. 2020;6(1):77-.
49. Baumann R, Depping R, Delaperriere M, Dunst J. Targeting hypoxia to overcome radiation resistance in head & neck cancers: real challenge or clinical fairytale? Expert review of anticancer therapy. 2016;16(7):751-8.
50. Wicks EE, Semenza GL. Hypoxia-inducible factors: cancer progression and clinical translation. The Journal of clinical investigation. 2022;132(11).
51. Kietzmann T, Mennerich D, Dimova EY. Hypoxia-Inducible Factors (HIFs) and phosphorylation: Impact on stability, localization, and transactivity. Frontiers in cell and developmental biology. 2016;4:11-.
52. Gilkes DM, Semenza GL, Wirtz D. Hypoxia and the extracellular matrix: drivers of tumour metastasis. Nature reviews Cancer. 2014;14(6):430-9.

53. Peng P-H, Hsu K-W, Chieh-Yu Lai J, Wu K-J. The role of hypoxia-induced long noncoding RNAs (lncRNAs) in tumorigenesis and metastasis. Biomedical Journal. 2021;44(5):521-33.
54. Kuo TC, Kung HJ, Shih JW. Signaling in and out: Long-noncoding RNAs in tumor hypoxia. Journal of biomedical science. 2020;27(1):59-.
55. Yang P, Ding J, Bian Y, Ma Z, Wang K, Li J. Long non-coding RNAs and cancer mechanisms: Immune cells and inflammatory cytokines in the tumor microenvironment. Medical oncology (Northwood, London, England). 2022;39(7):108-.
56. Chen D, Lu T, Tan J, Li H, Wang Q, Wei L. Long non-coding RNAs as communicators and mediators between the tumor microenvironment and cancer cells. Frontiers in oncology. 2019;9:739-.
57. Miranda-Galvis M, Teng Y. Targeting hypoxia-driven metabolic reprogramming to constrain tumor progression and metastasis. International journal of molecular sciences. 2020;21(15):1-17.
58. Mudassar F, Shen H, Cook KM, Hau E. Improving the synergistic combination of programmed death-1/programmed death ligand-1 blockade and radiotherapy by targeting the hypoxic tumour microenvironment. Journal of medical imaging and radiation oncology. 2022;66(4):560-74.
59. Crabtree HG, Cramer W. The action of radium on cancer cells. II.—Some factors determining the susceptibility of cancer cells to radium. Proceedings of the Royal Society of London Series B, Containing papers of a biological character. 1933;113(782):238-50.
60. Gray LH, Conger AD, Ebert M, Hornsey S, Scott OC. The concentration of oxygen dissolved in tissues at the time of irradiation as a factor in radiotherapy. British journal of radiology. 1953;26(312):638-48.
61. Thomlinson RH, Gray LH. The Histological Structure of Some Human Lung Cancers and the Possible Implications for Radiotherapy. British journal of cancer. 1955;9(4):539-49.
62. Beckers C, Pruschy M, Vetrugno I. Tumor hypoxia and radiotherapy: A major driver of resistance even for novel radiotherapy modalities. Seminars in cancer biology. 2024;98:19-30.
63. Brown JM, Wilson WR. Exploiting tumour hypoxia in cancer treatment. Nature reviews Cancer. 2004;4(6):437-47.
64. Dhani NMD, Fyles AMD, Hedley DMDP, Milosevic MMD. The Clinical Significance of Hypoxia in Human Cancers. Seminars in nuclear medicine. 2015;45(2):110-21.
65. Park JH, Lee HK. The Role of Hypoxia in Brain Tumor Immune Responses. Brain tumor research and treatment. 2023;11(1):39-46.
66. Erecińska M, Silver IA. Tissue oxygen tension and brain sensitivity to hypoxia. Respiration physiology. 2001;128(3):263-76.
67. Beppu T, Kamada K, Yoshida Y, Arai H, Ogasawara K, Ogawa A. Change of oxygen pressure in glioblastoma tissue under various conditions. Journal of neuro-oncology. 2002;58(1):47-52.
68. Colwell N, Larion M, Giles AJ, Seldomridge AN, Sizdahkhani S, Gilbert MR, et al. Hypoxia in the glioblastoma microenvironment: Shaping the phenotype of cancer stem-like cells. Neuro-oncology (Charlottesville, Va). 2017;19(7):887-96.
69. Marampon F, Gravina GL, Zani BM, Popov VM, Fratticci A, Cerasani M, et al. Hypoxia sustains glioblastoma radioresistance through ERKs/DNA-PKcs/HIF-1α functional interplay. International journal of oncology. 2014;44(6):2121-31.
70. Kessler J, Hahnel A, Wichmann H, Rot S, Kappler M, Bache M, et al. HIF-1α inhibition by siRNA or chetomin in human malignant glioma cells: effects on hypoxic radioresistance and monitoring via CA9 expression. BMC cancer. 2010;10(1):605-.

71. Fuchs Q, Pierrevelcin M, Messe M, Lhermitte B, Blandin AF, Papin C, et al. Hypoxia inducible factors' signaling in pediatric high-grade gliomas: Role, modelization and innovative targeted approaches. Cancers. 2020;12(4):979.
72. Yeom KW, Lober RM, Nelson MD, Panigrahy A, Blüml S. Citrate concentrations increase with hypoperfusion in pediatric diffuse intrinsic pontine glioma. Journal of neuro-oncology. 2015;122(2):383-9.
73. Rafałowska U. Transport of malate and citrate into rat brain mitochondria under hypoxia and anesthesia. Neurochemical research. 1979;4(3):355-64.
74. Overgaard J, Sand Hansen H, Overgaard M, Bastholt L, Berthelsen A, Specht L, et al. A randomized double-blind phase III study of nimorazole as a hypoxic radiosensitizer of primary radiotherapy in supraglottic larynx and pharynx carcinoma. Results of the Danish Head and Neck Cancer Study (DAHANCA) Protocol 5-85. Radiotherapy and oncology. 1998;46(2):135-46.
75. Grogan M, Thomas GM, Melamed I, Wong FLW, Pearcey RG, Joseph PK, et al. The importance of hemoglobin levels during radiotherapy for carcinoma of the cervix. Cancer. 1999;86(8):1528-36.
76. Tharmalingham H, Hoskin P. Clinical trials targeting hypoxia. British journal of radiology. 2019;92(1093):20170966-.
77. Dusault LA. The effect of oxygen on the response of spontaneous tumours in mice to radiotherapy. British journal of radiology. 1963;36(430):749-54.
78. Aquino-Parsons C, Hukin J, Green A. Concurrent carbogen and radiation therapy in children with high-risk brainstem gliomas. Pediatric Blood & Cancer. 2008;50(2):397-9.
79. Hoskin PJ, Rojas AM, Bentzen SM, Saunders MI. Radiotherapy With Concurrent Carbogen and Nicotinamide in Bladder Carcinoma. Journal of clinical oncology. 2010;28(33):4912-8.
80. Janssens GO, Rademakers SE, Terhaard CH, Doornaert PA, Bijl HP, Van Ende PD, et al. Accelerated Radiotherapy With Carbogen and Nicotinamide for Laryngeal Cancer: Results of a Phase III Randomized Trial. Journal of clinical oncology. 2012;30(15):1777-83.
81. Bussink J, Kaanders JHAM, Strik AM, van der Kogel AJ. Effects of nicotinamide and carbogen on oxygenation in human tumor xenografts measured with luminescense based fiber-optic probes. Radiotherapy and oncology. 2000;57(1):21-30.
82. Hunter FW, Wouters BG, Wilson WR. Hypoxia-activated prodrugs: paths forward in the era of personalised medicine. British journal of cancer. 2016;114(10):1071-7.
83. Peeters SGJA, Zegers CML, Biemans R, Lieuwes NG, Van Stiphout RGPM, Yaromina A, et al. TH-302 in combination with radiotherapy enhances the therapeutic outcome and is associated with pretreatment [F]HX4 hypoxia PET imaging. Clinical cancer research. 2015;21(13):2984-92.
84. Hajj C, Russell J, Hart CP, Goodman KA, Lowery MA, Haimovitz-Friedman A, et al. A Combination of Radiation and the Hypoxia-Activated Prodrug Evofosfamide (TH-302) is Efficacious against a Human Orthotopic Pancreatic Tumor Model. Translational oncology. 2017;10(5):760-5.
85. Takakusagi Y, Kishimoto S, Naz S, Matsumoto S, Saito K, Hart CP, et al. Radiotherapy Synergizes with the Hypoxia-Activated Prodrug Evofosfamide: In Vitro and in Vivo Studies. Antioxidants & redox signaling. 2018;28(2):131-40.
86. Li Y, Zhao L, Li XF. The Hypoxia-Activated Prodrug TH-302: Exploiting Hypoxia in Cancer Therapy. Frontiers in pharmacology. 2021;12:636892-.
87. Qannita RA, Alalami AI, Harb AA, Aleidi SM, Taneera J, Abu-Gharbieh E, et al. Targeting Hypoxia-Inducible Factor-1 (HIF-1) in Cancer: Emerging Therapeutic Strategies and Pathway Regulation. Pharmaceuticals (Basel, Switzerland). 2024;17(2):195.

88. Courtney KD, Infante JR, Lam ET, Figlin RA, Rini BI, Brugarolas J, et al. Phase I Dose-Escalation Trial of PT2385, a First-in-Class Hypoxia-Inducible Factor-2 alpha Antagonist in Patients With Previously Treated Advanced Clear Cell Renal Cell Carcinoma. Journal of clinical oncology. 2018;36(9):867-74.
89. Choueiri TK, Bauer TM, Papadopoulos KP, Plimack ER, Merchan JR, McDermott DF, et al. Inhibition of hypoxia-inducible factor-2α in renal cell carcinoma with belzutifan: a phase 1 trial and biomarker analysis. Nature medicine. 2021;27(5):802-5.
90. Liao C, Zhang Q. Understanding the Oxygen-Sensing Pathway and Its Therapeutic Implications in Diseases. The American journal of pathology. 2020;190(8):1584-95.
91. Ashton TM, McKenna WG, Kunz-Schughart LA, Higgins GS. Oxidative Phosphorylation as an Emerging Target in Cancer Therapy. Clinical cancer research. 2018;24(11):2482-90.
92. Rose S, Bennuri SC. Mitochondrial Metabolism. In: Frye RE, Berk M, editors. The Therapeutic Use of N-Acetylcysteine (NAC) in Medicine. Singapore: Springer Singapore; 2019. p. 73-103.
93. Kuehlbrandt W. Structure and function of mitochondrial membrane protein complexes. BMC biology. 2015;13(1):89-.
94. Nolfi-Donegan D, Braganza A, Shiva S. Mitochondrial electron transport chain: Oxidative phosphorylation, oxidant production, and methods of measurement. Redox biology. 2020;37:101674-.
95. Secomb TW, Hsu R, Ong ET, Gross JF, Dewhirst MW. Analysis of the Effects of Oxygen Supply and Demand on Hypoxic Fraction in Tumors. Acta oncologica. 1995;34(3):313-6.
96. Gopal YNV, Gammon S, Prasad R, Knighton B, Pisaneschi F, Roszik J, et al. A novel mitochondrial inhibitor blocks MAPK pathway and overcomes MAPK inhibitor resistance in melanoma. Clinical cancer research. 2019;25(21):6429-42.
97. Birkenmeier K, Dröse S, Wittig I, Winkelmann R, Käfer V, Döring C, et al. Hodgkin and Reed–Sternberg cells of classical Hodgkin lymphoma are highly dependent on oxidative phosphorylation. International journal of cancer. 2016;138(9):2231-46.
98. Whitaker-Menezes D, Martinez-Outschoorn UE, Flomenberg N, Birbe R, Witkiewicz AK, Howell A, et al. Hyperactivation of oxidative mitochondrial metabolism in epithelial cancer cells in situ: Visualizing the therapeutic effects of metformin in tumor tissue. Cell cycle (Georgetown, Tex). 2011;10(23):4047-64.
99. Viale A, Pettazzoni P, Lyssiotis CA, Ying H, Sánchez N, Marchesini M, et al. Oncogene ablation-resistant pancreatic cancer cells depend on mitochondrial function. Nature (London). 2014;514(7524):628-32.
100. Zannella VE, Pra AD, Muaddi H, McKee TD, Stapleton S, Sykes J, et al. Reprogramming metabolism with metformin improves tumor oxygenation and radiotherapy response. Clinical cancer research. 2013;19(24):6741-50.
101. Shen H, Yu M, Tsoli M, Chang C, Joshi S, Liu J, et al. Targeting reduced mitochondrial DNA quantity as a therapeutic approach in pediatric high-grade gliomas. Neuro-oncology (Charlottesville, Va). 2020;22(1):139-51.
102. Chevalier B, Pasquier D, Lartigau EF, Chargari C, Schernberg A, Jannin A, et al. Metformin: (future) best friend of the radiation oncologist? Radiotherapy and oncology. 2020;151:95-105.
103. Ashton TM, Fokas E, Kunz-Schughart LA, Folkes LK, Anbalagan S, Huether M, et al. The anti-malarial atovaquone increases radiosensitivity by alleviating tumour hypoxia. Nature communications. 2016;7(1):12308-.

104. Benej M, Hong X, Vibhute S, Scott S, Wu J, Graves E, et al. Papaverine and its derivatives radiosensitize solid tumors by inhibiting mitochondrial metabolism. Proceedings of the National Academy of Sciences - PNAS. 2018;115(42):10756-61.
105. Mudassar F, Shen H, O'Neill G, Hau E. Targeting tumor hypoxia and mitochondrial metabolism with anti-parasitic drugs to improve radiation response in high-grade gliomas. Journal of experimental & clinical cancer research. 2020;39(1):1-208.
106. Baggish AL, Hill DR. Antiparasitic agent atovaquone. Antimicrobial agents and chemotherapy. 2002;46(5):1163-73.
107. Osei-Akoto A, Orton LC, Owusu-Ofori S, Osei-Akoto A. Atovaquone-proguanil for treating uncomplicated malaria. Cochrane database of systematic reviews. 2005;2019(5):CD004529.
108. Lalloo DG, Hill DR. Preventing malaria in travellers. BMJ. 2008;336(7657):1362-6.
109. Nixon GL, Moss DM, Shone AE, Lalloo DG, Fisher N, O'Neill PM, et al. Antimalarial pharmacology and therapeutics of atovaquone. Journal of antimicrobial chemotherapy. 2013;68(5):977-85.
110. Fieser LF, Heymann H, Seligman AM. Naphthoquinone antimalarials; metabolic degradation. The Journal of pharmacology and experimental therapeutics. 1948;94(2):112-24.
111. Fieser LF, Chang FC. Naphthoquinone antimalarials; metabolic oxidation products. The Journal of pharmacology and experimental therapeutics. 1948;94(2):85-96.
112. Fawaz G, Haddad FS. The Effect of Lapinone (M-2350) on P. Vivax Infection in Man. American journal of tropical medicine. 1951;s1-31(5):569-71.
113. Hudson AT, Dickins M, Ginger CD, Gutteridge WE, Holdich T, Hutchinson DBA, et al. 566C80: A potent broad spectrum anti-infective agent with activity against malaria and opportunistic infections in AIDS patients. Drugs under experimental and clinical research. 1991;17(9):427-35.
114. Patent WO9320044. 1,4 Naphthoquinone derivatives with antiprotozoal and anti-parasitic activity. http://www.freepatentsonline.com/EP0634996.html. (29 October 2024, date last accessed).
115. Rolan PE, Mercer AJ, Weatherley BC, Holdich T, Meire H, Peck RW, et al. Examination of some factors responsible for a food-induced increase in absorption of atovaquone. British journal of clinical pharmacology. 1994;37(1):13-20.
116. Fry M, Pudney M. Site of action of the antimalarial hydroxynaphthoquinone, 2-[trans-4-(4'-chlorophenyl) cyclohexyl]-3- hydroxy-1,4-naphthoquinone (566C80). Biochemical pharmacology. 1992;43(7):1545-53.
117. Biagini GA, Viriyavejakul P, O'Neill PM, Bray PG, Ward SA. Functional Characterization and Target Validation of Alternative Complex I of Plasmodium falciparum Mitochondria. Antimicrobial Agents and Chemotherapy. 2006;50(5):1841-51.
118. Srivastava IK, Rottenberg H, Vaidya AB. Atovaquone, a Broad Spectrum Antiparasitic Drug, Collapses Mitochondrial Membrane Potential in a Malarial Parasite. The Journal of biological chemistry. 1997;272(7):3961-6.
119. Seymour KK, Yeo AET, Rieckmann KH, Christopherson RI. dCTP levels are maintained in Plasmodium falciparum subjected to pyrimidine deficiency or excess. Annals of tropical medicine and parasitology. 1997;91(6):603-9.
120. Hammond DJ, Burchell JR, Pudney M. Inhibition of pyrimidine biosynthesis de novo in Plasmodium falciparum by 2-(4- t-butylcyclohexyl)-3-hydroxy-1,4-naphthoquinone in vitro. Molecular and biochemical parasitology. 1985;14(1):97-109.
121. Morrisey JM, Mather MW, Vaidya AB, Painter HJ. Specific role of mitochondrial electron transport in blood-stage Plasmodium falciparum. Nature. 2007;446(7131):88-91.

122. Bulusu V, Jayaraman V, Balaram H. Metabolic Fate of Fumarate, a Side Product of the Purine Salvage Pathway in the Intraerythrocytic Stages of Plasmodium falciparum. The Journal of biological chemistry. 2011;286(11):9236-45.
123. Takabe H, Warnken ZN, Zhang Y, Davis DA, Smyth HDC, Kuhn JG, et al. A repurposed drug for brain cancer: Enhanced atovaquone amorphous solid dispersion by combining a spontaneously emulsifying component with a polymer carrier. Pharmaceutics. 2018;10(2):60.
124. Beerahee M. Clinical pharmacology of atovaquone and proguanil hydrochloride. Journal of travel medicine. 1999;6(1):S13-S7.
125. Dixon R, Pozniak AL, Watt HM, Rolan P, Posner J. Single-dose and steady-state pharmacokinetics of a novel microfluidized suspension of atovaquone in human immunodeficiency virus-seropositive patients. Antimicrobial Agents and Chemotherapy. 1996;40(3):556-60.
126. Falloon J, Sargent S, Piscitelli SC, Bechtel C, LaFon SW, Sadler B, et al. Atovaquone Suspension in HIV-Infected Volunteers: Pharmacokinetics, Pharmacodynamics, and TMP-SMX Interaction Study. Pharmacotherapy. 1999;19(9):1050-6.
127. Hughes WT, Kennedy W, Shenep JL, Flynn PM, Hetherington SV, Fullen G, et al. Safety and Pharmacokinetics of 566C80, a Hydroxynaphthoquinone with Anti-Pneumocystis carinii Activity: A Phase I Study in Human Immunodeficiency Virus (HIV)-Infected Men. The Journal of infectious diseases. 1991;163(4):843-8.
128. Looareesuwan S, Chulay JD, Canfield CJ, Hutchinson DBA, De Alencar F, Anabwani G, et al. Malarone(TM) (atovaquone and proguanil hydrochloride): A review of its clinical development for treatment of malaria. The American journal of tropical medicine and hygiene. 1999;60(4):533-41.
129. Cheung TW. Overdose of atovaquone in a patient with AIDS [6]. AIDS (London). 1999;13(14):1984-5.
130. Ferguson DJP, Huskinson-Mark J, Araujo FG, Remington JS. An ultrastructural study of the effect of treatment with atovaquone in brains of mice chronically infected with the ME49 strain of Toxoplasma gondii. International journal of experimental pathology. 1994;75(2):111-6.
131. Dunay IR, Heimesaat MM, Bushrab FN, Müller RH, Stocker H, Arasteh K, et al. Atovaquone Maintenance Therapy Prevents Reactivation of Toxoplasmic Encephalitis in a Murine Model of Reactivated Toxoplasmosis. Antimicrobial Agents and Chemotherapy. 2004;48(12):4848-54.
132. Azami SJ, Amani A, Keshavarz H, Najafi-Taher R, Mohebali M, Faramarzi MA, et al. Nanoemulsion of atovaquone as a promising approach for treatment of acute and chronic toxoplasmosis. European journal of pharmaceutical sciences. 2018;117:138-46.
133. Jermain SV, Brough C, Williams RO. Amorphous solid dispersions and nanocrystal technologies for poorly water-soluble drug delivery – An update. International journal of pharmaceutics. 2018;535(1-2):379-92.
134. Ke F, Yu J, Chen W, Si X, Li X, Yang F, et al. The anti-malarial atovaquone selectively increases chemosensitivity in retinoblastoma via mitochondrial dysfunction-dependent oxidative damage and Akt/AMPK/mTOR inhibition. Biochemical and biophysical research communications. 2018;504(2):374-9.
135. Kapur A, Mehta P, Simmons AD, Ericksen SS, Mehta G, Palecek SP, et al. Atovaquone: An Inhibitor of Oxidative Phosphorylation as Studied in Gynecologic Cancers. Cancers. 2022;14(9):2297.
136. Fiorillo M, Lamb R, Tanowitz HB, Mutti L, Krstic-Demonacos M, Cappello AR, et al. Repurposing atovaquone: Targeting mitochondrial complex III and OXPHOS to eradicate cancer stem cells. Oncotarget. 2016;7(23):34084-99.

137. Tian S, Chen H, Tan W. Targeting mitochondrial respiration as a therapeutic strategy for cervical cancer. Biochemical and biophysical research communications. 2018;499(4):1019-24.
138. Chen D, Sun X, Zhang X, Cao J. Targeting mitochondria by anthelmintic drug atovaquone sensitizes renal cell carcinoma to chemotherapy and immunotherapy. Journal of biochemical and molecular toxicology. 2018;32(9):e22195-n/a.
139. Sbirkov Y, Ivanova T, Burnusuzov H, Gercheva K, Petrie K, Schenk T, et al. The Protozoan Inhibitor Atovaquone Affects Mitochondrial Respiration and Shows In Vitro Efficacy Against Glucocorticoid-Resistant Cells in Childhood B-Cell Acute Lymphoblastic Leukaemia. Frontiers in oncology. 2021;11:632181-.
140. Xie F, Gong J, Tan H, Zhang H, Ma J. Preclinical evidence of synergism between atovaquone and chemotherapy by AMPK-dependent mitochondrial dysfunction. European journal of pharmacology. 2021;907:174256.
141. Lv Z, Yan X, Lu L, Su C, He Y. Atovaquone enhances doxorubicin's efficacy via inhibiting mitochondrial respiration and STAT3 in aggressive thyroid cancer. Journal of bioenergetics and biomembranes. 2018;50(4):263-70.
142. Xiang M, Kim H, Ho VT, Walker SR, Bar-Natan M, Anahtar M, et al. Gene expression–based discovery of atovaquone as a STAT3 inhibitor and anticancer agent. Blood. 2016;128(14):1845-53.
143. Wood SJ, Frank D, Haas EB, Wang W, Meisel JL, Khanna N. Repurposing atovaquone as a STAT3 inhibitor for the treatment of platinum resistant ovarian cancer. Journal of clinical oncology. 2024;42(16_suppl):TPS5631-TPS.
144. Ward SA, Helsby NA, Skjelbo E, Brosen K, Gram LF, Breckenridge AM. The activation of the biguanide antimalarial proguanil co-segregates with the mephenytoin oxidation polymorphism-a panel study. British journal of clinical pharmacology. 1991;31(6):689-92.
145. Radloff PD, Philips J, Nkeyi M, Kremsner PG, Radloff PD, Hutchinson D, et al. Atovaquone and proguanil for Plasmodium falciparum malaria. The Lancet (British edition). 1996;347(9014):1511-4.
146. Pudney M, Gutteridge W, Zeman A, Dickins M, Woolley JL. Atovaquone and proguanil hydrochloride: A review of nonclinical studies. Journal of travel medicine. 1999;6(1):S8-S12.
147. Peters W. Chemotherapy and drug resistance in malaria. 2nd ed. ed. London: Academic Press; 1987.
148. Srivastava IK, Vaidya AB. A Mechanism for the Synergistic Antimalarial Action of Atovaquone and Proguanil. Antimicrobial Agents and Chemotherapy. 1999;43(6):1334-9.
149. Fidock DA, Wellems TE. Transformation with Human Dihydrofolate Reductase Renders Malaria Parasites Insensitive to WR99210 but does not Affect the Intrinsic Activity of Proguanil. Proceedings of the National Academy of Sciences - PNAS. 1997;94(20):10931-6.
150. Bridges HR, Sirviö VA, Agip ANA, Hirst J. Molecular features of biguanides required for targeting of mitochondrial respiratory complex I and activation of AMP-kinase. BMC biology. 2016;14(1):65-.
151. Bridges HR, Jones AJY, Pollak MN, Hirst J. Effects of metformin and other biguanides on oxidative phosphorylation in mitochondria. Biochemical journal. 2014;462(3):475-87.
152. Skinner-Adams TS, Fisher GM, Riches AG, Hutt OE, Jarvis KE, Wilson T, et al. Cyclization-blocked proguanil as a strategy to improve the antimalarial activity of atovaquone. Communications biology. 2019;2(1):166.

153. Zhang N, Sundquist J, Sundquist K, Ji J. Proguanil and atovaquone use is associated with lower colorectal cancer risk: a nationwide cohort study. BMC medicine. 2022;20(1):1-439.
154. Nyunt M, Plowe CV. CHAPTER 82 - MALARIA. Elsevier Inc; 2009. p. 1141-70.
155. Knox C, Wilson M, Klinger CM, et al. DrugBank 6.0: the DrugBank Knowledgebase for 2024. Nucleic Acids Res. 2024 Jan 5;52(D1):D1265-D1275. doi: 10.1093/nar/gkad976. PMID: 37953279; PMCID: PMC10767804.
156. Gupta N, Curcic M, Srivastava SK. Proguanil Suppresses Breast Tumor Growth In Vitro and In Vivo by Inducing Apoptosis via Mitochondrial Dysfunction. Cancers. 2024;16(5):872.
157. Xiao D, Hu X, Peng M, Deng J, Zhou S, Xu S, et al. Inhibitory role of proguanil on the growth of bladder cancer via enhancing EGFR degradation and inhibiting its downstream signaling pathway to induce autophagy. Cell death & disease. 2022;13(5):499-14.
158. Wu Y, Wu T, Hu X, Xu S, Xiao D, Wu J, et al. Proguanil synergistically sensitizes ovarian cancer cells to olaparib by increasing DNA damage and inducing apoptosis. International journal of medical sciences. 2022;19(2):233-41.
159. National Academies of Sciences E, Medicine, Division H, Medicine, Practice BoPH, Public H, et al. Assessment of Long-Term Health Effects of Antimalarial Drugs When Used for Prophylaxis. Washington, D.C: National Academies Press; 2020.
160. Adshead S. The adverse effects of mefloquine in deployed military personnel. Journal of the Royal Naval Medical Service. 2014;100(3):232-7.
161. Wong W, Bai X-C, Sleebs BE, Triglia T, Brown A, Thompson JK, et al. Mefloquine targets the Plasmodium falciparum 80S ribosome to inhibit protein synthesis. Nature microbiology. 2017;2(6):17031.
162. Geng Y, Kohli L, Klocke BJ, Roth KA. Chloroquine-induced autophagic vacuole accumulation and cell death in glioma cells is p53 independent. Neuro-oncology (Charlottesville, Va). 2010;12(5):473-81.
163. Derek GW, Anthony PS. 51 - Chemotherapy of infections. Fifth Edition ed: Elsevier Ltd; 2018. p. 581-629.
164. Kollaritsch H, Karbwang J, Wiedermann G, Mikolasek A, Na-Bangchang K, Wernsdorfer WH. Mefloquine concentration profiles during prophylactic dose regimens. Wiener Klinische Wochenschrift. 2000;112(10):441-7.
165. Simpson JA, Price R, Kuile F, Teja-Isavatharm P, Nosten F, Chongsuphajaisiddhi T, et al. Population pharmacokinetics of mefloquine in patients with acute falciparum malaria. Clinical pharmacology and therapeutics. 1999;66(5):472-84.
166. Van Riemsdijk MM, Sturkenboom MCJM, Ditters JM, Tulen JHM, Ligthelm RJ, Overbosch D, et al. Low body mass index is associated with an increased risk of neuropsychiatric adverse events and concentration impairment in women on mefloquine. British journal of clinical pharmacology. 2004;57(4):506-12.
167. Lobel HO, Campbell CC, Hightower AH, Eng T, Miani M, Eng T, et al. Long-term malaria prophylaxis with weekly mefloquine. The Lancet (British edition). 1993;341(8849):848-51.
168. ter Kuile FO, Nosten F, Thieren M, Luxemburger C, Edstein MD, Chongsuphajaisiddhi T, et al. High-Dose Mefloquine in the Treatment of Multidrug-Resistant Falciparum Malaria. The Journal of infectious diseases. 1992;166(6):1393-400.
169. FDA Approved Products: Lariam (mefloquine hydrochloride) oral tablets (https://accessdata.fda.gov/drugsatfda_docs/label/2009/019591s026s028lbl.pdf) Accessed on 30 October 2024.
170. Jones R, Kunsman G, Levine B, Smith M, Stahl C. Mefloquine distribution in postmortem cases. Forensic science international. 1994;68(1):29-32.

171. Pham YT, Nosten F, Farinotti R, White NJ, Gimenez F. Cerebral uptake of mefloquine enantiomers in fatal cerebral malaria. International journal of clinical pharmacology and therapeutics. 1999;37(1):58-61.
172. Baudry S, Pham YT, Baune B, Vidrequin S, Crevoisier CH, Gimenez F, et al. Stereoselective Passage of Mefloquine Through the Blood-Brain Barrier in the Rat. Journal of pharmacy and pharmacology. 1997;49(11):1086-90.
173. Li H, Jiao S, Li X, Banu H, Hamal S, Wang X. Therapeutic effects of antibiotic drug mefloquine against cervical cancer through impairing mitochondrial function and inhibiting mTOR pathway. Canadian journal of physiology and pharmacology. 2017;95(1):43-50.
174. Xiang W, Lam YH, Sng C, Cheong MA, Than H, Hwang WYK, et al. Mefloquine Effectively Targets Blast Phase Chronic Myeloid Leukemia through Inducing Oxidative Stress and Lysosomal Disruption. Blood. 2016;128(22):5426-.
175. Sukhai MA, Prabha S, Hurren R, Rutledge AC, Lee AY, Sriskanthadevan S, et al. Lysosomal disruption preferentially targets acute myeloid leukemia cells and progenitors. The Journal of clinical investigation. 2013;123(1):315-28.
176. Sharma N, Thomas S, Golden EB, Hofman FM, Chen TC, Petasis NA, et al. Inhibition of autophagy and induction of breast cancer cell death by mefloquine, an antimalarial agent. Cancer letters. 2012;326(2):143-54.
177. Das S, Dielschneider R, Chanas-LaRue A, Johnston JB, Gibson SB. Antimalarial drugs trigger lysosome-mediated cell death in chronic lymphocytic leukemia (CLL) cells. Leukemia research. 2018;70:79-86.
178. Xu X, Wang J, Han K, Li S, Xu F, Yang Y. Antimalarial drug mefloquine inhibits nuclear factor kappa B signaling and induces apoptosis in colorectal cancer cells. Cancer science. 2018;109(4):1220-9.
179. Xie Y, Zhang J, Lu B, Bao Z, Zhao J, Lu X, et al. Mefloquine Inhibits Esophageal Squamous Cell Carcinoma Tumor Growth by Inducing Mitochondrial Autophagy. Frontiers in oncology. 2020;10:1217-.
180. Liu Y, Chen S, Xue R, Zhao J, Di M. Mefloquine effectively targets gastric cancer cells through phosphatase-dependent inhibition of PI3K/Akt/mTOR signaling pathway. Biochemical and biophysical research communications. 2016;470(2):350-5.
181. Li Y-H, Yang S-L, Zhang G-F, Wu J-C, Gong L-L, Ming Z, et al. Mefloquine targets β-catenin pathway and thus can play a role in the treatment of liver cancer. Microbial pathogenesis. 2018;118:357-60.
182. Yan K-H, Yao C-J, Hsiao C-H, Lin K-H, Lin Y-W, Wen Y-C, et al. Mefloquine exerts anticancer activity in prostate cancer cells via ROS-mediated modulation of Akt, ERK, JNK and AMPK signaling. Oncology letters. 2013;5(5):1541-5.
183. Yan K-H, Lin Y-W, Hsiao C-H, Wen Y-C, Lin K-H, Liu C-C, et al. Mefloquine induces cell death in prostate cancer cells and provides a potential novel treatment strategy in vivo. Oncology letters. 2013;5(5):1567-71.
184. Cerami E, Gao J, Dogrusoz U, Gross BE, Sumer SO, Aksoy BA, et al. The cBio Cancer Genomics Portal: An open platform for exploring multidimensional cancer genomics data. Cancer discovery. 2012;2(5):401-4.
185. Gao J, Aksoy BA, Dogrusoz U, Dresdner G, Gross B, Sumer SO, et al. Integrative analysis of complex cancer genomics and clinical profiles using the cBioPortal. Science signaling. 2013;6(269):pl1-pl.
186. Hanahan D, Weinberg Robert A. Hallmarks of Cancer: The Next Generation. Cell. 2011;144(5):646-74.
187. Sriskanthadevan S, Jeyaraju DV, Chung TE, Prabha S, Xu W, Skrtic M, et al. AML cells have low spare reserve capacity in their respiratory chain that renders them susceptible to oxidative metabolic stress. Blood. 2015;125(13):2120-30.

188. Hu J, Locasale JW, Bielas JH, O'Sullivan J, Sheahan K, Cantley LC, et al. Heterogeneity of tumor-induced gene expression changes in the human metabolic network. Nature biotechnology. 2013;31(6):522-9.
189. Roesch A, Vultur A, Bogeski I, Wang H, Zimmermann KM, Speicher D, et al. Overcoming intrinsic multidrug resistance in melanoma by blocking the mitochondrial respiratory chain of slow-cycling JARID1B cells. Cancer cell. 2013;23(6):811-25.
190. Beerkens APM, Boreel DF, Nathan JA, Neuzil J, Cheng G, Kalyanaraman B, et al. Characterizing OXPHOS inhibitor-mediated alleviation of hypoxia using high-throughput live cell-imaging. Cancer & metabolism. 2024;12(1):13-.
191. Najjar YG, Menk AV, Sander C, Rao U, Karunamurthy A, Bhatia R, et al. Tumor cell oxidative metabolism as a barrier to PD-1 blockade immunotherapy in melanoma. JCI insight. 2019;4(5).
192. Boreel DF, Span PN, Heskamp S, Adema GJ, Bussink J. Targeting oxidative phosphorylation to increase the efficacy of radio- And immune-combination therapy. Clinical cancer research. 2021;27(11):2970-8.
193. Rademakers SE, Span PN, Kaanders JHAM, Sweep FCGJ, van der Kogel AJ, Bussink J. Molecular aspects of tumour hypoxia. Molecular oncology. 2008;2(1):41-53.
194. Wilson WR, Hay MP. Targeting hypoxia in cancer therapy. Nature reviews Cancer. 2011;11(6):393-410.
195. Collingridge DR, Piepmeier JM, Rockwell S, Knisely JPS. Polarographic measurements of oxygen tension in human glioma and surrounding peritumoural brain tissue. Radiotherapy and oncology. 1999;53(2):127-31.
196. Rampling R, Cruickshank G, Lewis AD, Fitzsimmons SA, Workman P. Direct measurement of pO2 distribution and bioreductive enzymes in human malignant brain tumors. International journal of radiation oncology, biology, physics. 1994;29(3):427-31.
197. Michealraj KA, Kumar SA, Kim LJY, Cavalli FMG, Przelicki D, Wojcik JB, et al. Metabolic Regulation of the Epigenome Drives Lethal Infantile Ependymoma. Cell. 2020;181(6):1329-45.e24.
198. Sharma LK, Lu J, Bai Y. Mitochondrial Respiratory Complex I: Structure, Function and Implication in Human Diseases. Current medicinal chemistry. 2009;16(10):1266-77.
199. Fullerton M, McFarland R, Taylor RW, Alston CL. The genetic basis of isolated mitochondrial complex II deficiency. Molecular genetics and metabolism. 2020;131(1-2):53-65.
200. Chandel NS. Mitochondrial complex III: An essential component of universal oxygen sensing machinery? Respiratory physiology & neurobiology. 2010;174(3):175-81.
201. Zong S, Wu M, Gu J, Liu T, Guo R, Yang M. Structure of the intact 14-subunit human cytochrome c oxidase. Cell research. 2018;28(10):1026-34.
202. Jonckheere AI, Smeitink JAM, Rodenburg RJT. Mitochondrial ATP synthase: architecture, function and pathology. Journal of inherited metabolic disease. 2012;35(2):211-25.
203. Reinecke F, Smeitink JAM, van der Westhuizen FH. OXPHOS gene expression and control in mitochondrial disorders. Biochimica et biophysica acta. 2009;1792(12):1113-21.
204. Heddi A, Stepien G, Benke PJ, Wallace DC. Coordinate Induction of Energy Gene Expression in Tissues of Mitochondrial Disease Patients. The Journal of biological chemistry. 1999;274(33):22968-76.
205. Pagniez-Mammeri H, Loublier S, Legrand A, Bénit P, Rustin P, Slama A. Mitochondrial complex I deficiency of nuclear origin. I. Structural genes. Molecular genetics and metabolism. 2012;105(2):163-72.
206. Goetzman E, Gong Z, Zhang B, Muzumdar R. Complex II Biology in Aging, Health, and Disease. Antioxidants. 2023;12(7):1477.

207. Borisov VB. Defects in mitochondrial respiratory complexes III and IV, and human pathologies. Molecular aspects of medicine. 2002;23(5):385-412.
208. Xu Y, Xue D, Bankhead A, Neamati N. Why All the Fuss about Oxidative Phosphorylation (OXPHOS)? Journal of medicinal chemistry. 2020;63(23):14276-307.
209. Looareesuwan S, Viravan C, Webster HK, Kyle DE, Hutchinson DB, Canfield CJ. Clinical Studies of Atovaquone, Alone or in Combination with other Antimalarial Drugs, for Treatment of Acute Uncomplicated Malaria in Thailand. The American journal of tropical medicine and hygiene. 1996;54(1):62-6.
210. Turrens JF. Mitochondrial formation of reactive oxygen species. The Journal of physiology. 2003;552(2):335-44.
211. Lee D-W, Selamoglu N, Lanciano P, Cooley JW, Forquer I, Kramer DM, et al. Loss of a Conserved Tyrosine Residue of Cytochrome b Induces Reactive Oxygen Species Production by Cytochrome bc1. The Journal of biological chemistry. 2011;286(20):18139-48.
212. Close DA, Johnston PA. Detection and impact of hypoxic regions in multicellular tumor spheroid cultures formed by head and neck squamous cell carcinoma cells lines. SLAS discovery. 2022;27(1):39-54.
213. Ziello JE, Jovin IS, Huang Y. Hypoxia-Inducible Factor (HIF)-1 regulatory pathway and its potential for therapeutic intervention in malignancy and ischemia. The Yale journal of biology & medicine. 2007;80(2):51-60.
214. Dayal R, Singh A, Pandey A, Mishra K. Reactive oxygen species as mediator of tumor radiosensitivity. Journal of cancer research and therapeutics. 2014;10(4):811-8.
215. Lamb R, Ozsvari B, Lisanti CL, Tanowitz HB, Howell A, Martinez-Outschoorn UE, et al. Antibiotics that target mitochondria effectively eradicate cancer stem cells, across multiple tumor types: Treating cancer like an infectious disease. Oncotarget. 2015;6(7):4569-84.
216. Škrtić M, Sriskanthadevan S, Jhas B, Gebbia M, Wang X, Wang Z, et al. Inhibition of Mitochondrial Translation as a Therapeutic Strategy for Human Acute Myeloid Leukemia. Cancer cell. 2011;20(5):674-88.
217. Muz B, De La Puente P, Azab F, Luderer M, Azab AK. The role of hypoxia and exploitation of the hypoxic environment in hematologic malignancies. Molecular cancer research. 2014;12(10):1347-54.
218. Coates JTT, Rodriguez-Berriguete G, Puliyadi R, Ashton T, Prevo R, Wing A, et al. The anti-malarial drug atovaquone potentiates platinum-mediated cancer cell death by increasing oxidative stress. Cell death discovery. 2020;6(1):110-.
219. Nizami ZN, Aburawi HE, Semlali A, Muhammad K, Iratni R. Oxidative Stress Inducers in Cancer Therapy: Preclinical and Clinical Evidence. Antioxidants. 2023;12(6):1159.
220. Murphy AD, Lang-Unnasch N. Alternative Oxidase Inhibitors Potentiate the Activity of Atovaquone against Plasmodium falciparum. Antimicrobial Agents and Chemotherapy. 1999;43(3):651-4.
221. Acin-Perez R, Benincá C, Fernandez del Rio L, Shu C, Baghdasarian S, Zanette V, et al. Inhibition of ATP synthase reverse activity restores energy homeostasis in mitochondrial pathologies. The EMBO journal. 2023;42(10):e111699-n/a.
222. Foley M, Tilley L. Quinoline antimalarials: Mechanisms of action and resistance. International journal for parasitology. 1997;27(2):231-40.
223. Schlagenhauf P, Adamcova M, Regep L, Schaerer MT, Rhein H-G. The position of mefloquine as a 21st century malaria chemoprophylaxis. Malaria journal. 2010;9(1):357-.
224. Health, Medicine D, Board on Population H, Public Health P, National Academies of Sciences E, Medicine. MEFLOQUINE. United States: National Academies Press; 2020.
225. Takeda M, Koseki J, Takahashi H, Miyoshi N, Nishida N, Nishimura J, et al. Disruption of endolysosomal Rab5/7 efficiently eliminates colorectal cancer stem cells. Cancer research (Chicago, Ill). 2019;79(7):1426-37.

226. Riffkin CD, Chung R, Wall DM, Zalcberg JR, Cowman AF, Foley M, et al. Modulation of the function of human MDR1 P-glycoprotein by the antimalarial drug mefloquine. Biochemical pharmacology. 1996;52(10):1545-52.
227. Toovey S. Mefloquine neurotoxicity: A literature review. Travel medicine and infectious disease. 2009;7(1):2-6.
228. Bandara AB, Drake JC, Brown DA. Complex II subunit SDHD is critical for cell growth and metabolism, which can be partially restored with a synthetic ubiquinone analog. BMC cell biology. 2021;22(1):35-.
229. Manneck T, Keiser J, MÜLler J. Mefloquine interferes with glycolysis in schistosomula of Schistosoma mansoni via inhibition of enolase. Parasitology. 2012;139(4):497-505.
230. Avilán L, Gualdrón-López M, Quiñones W, González-González L, Hannaert V, Michels PAM, et al. Enolase: A Key Player in the Metabolism and a Probable Virulence Factor of Trypanosomatid Parasites-Perspectives for Its Use as a Therapeutic Target. Enzyme Research. 2011;2011(2011):983-96.
231. Werbrouck C, Evangelista CCS, Lobón-Iglesias MJ, Barret E, Le Teuff G, Merlevede J, et al. TP53 pathway alterations drive radioresistance in diffuse intrinsic pontine gliomas (DIPG). Clinical cancer research. 2019;25(22):6788-800.
232. Ferguson MW, Gerak CAN, Chow CCT, Rastelli EJ, Elmore KE, Stahl F, et al. The antimalarial drug mefloquine enhances TP53 premature termination codon readthrough by aminoglycoside G418. PloS one. 2019;14(5):e0216423-e.
233. Krudsood S, Looareesuwan S, Wilairatama P, Leowattana W, Tangpukdee N, Chalermrut K, et al. Effect of artesunate and mefloquine in combination on the Fridericia corrected QT intervals in Plasmodium falciparum infected adults from Thailand. Tropical medicine & international health. 2011;16(4):458-65.
234. Dow GS, Koenig ML, Wolf L, Gerena L, Lopez-Sanchez M, Hudson TH, et al. The Antimalarial Potential of 4-Quinolinecarbinolamines May Be Limited due to Neurotoxicity and Cross-Resistance in Mefloquine-Resistant Plasmodium falciparum Strains. Antimicrobial Agents and Chemotherapy. 2004;48(7):2624-32.
235. Brennan TV, Lin L, Huang X, Yang Y. Generation of Luciferase-expressing Tumor Cell Lines. Bio-protocol. 2018;8(8).
236. Pun M, Pratt D, Nano PR, Joshi PK, Jiang L, Englinger B, et al. Common molecular features of H3K27M DMGs and PFA ependymomas map to hindbrain developmental pathways. Acta neuropathologica communications. 2023;11(1):25-19.
237. Li LT, Jiang G, Chen Q, Zheng JN. Ki67 is a promising molecular target in the diagnosis of cancer (Review). Molecular medicine reports. 2015;11(3):1566-72.
238. Tang N, Wang L, Esko J, Giordano FJ, Huang Y, Gerber H-P, et al. Loss of HIF-1α in endothelial cells disrupts a hypoxia-driven VEGF autocrine loop necessary for tumorigenesis. Cancer cell. 2004;6(5):485-95.
239. Ambrosio MR, Di Serio C, Danza G, Rocca BJ, Ginori A, Prudovsky I, et al. Carbonic anhydrase IX is a marker of hypoxia and correlates with higher Gleason scores and ISUP grading in prostate cancer. Diagnostic pathology. 2016;11(1):45-.
240. Evans SM, Hahn S, Pook DR, Jenkins WT, Chalian AA, Zhang P, et al. Detection of hypoxia in human squamous cell carcinoma by EF5 binding. Cancer research (Chicago, Ill). 2000;60(7):2018-24.
241. Evans SM, Koch CJ. Prognostic significance of tumor oxygenation in humans. Cancer letters. 2003;195(1):1-16.
242. Singhal R, Shah YM. Oxygen battle in the gut: Hypoxia and hypoxia-inducible factors in metabolic and inflammatory responses in the intestine. The Journal of biological chemistry. 2020;295(30):10493-505.

243. Ziemer LS, Koch CJ, Maity A, Magarelli DP, Horan AM, Evans SM. Hypoxia and VEGF mRNA Expression in Human Tumors. Neoplasia (New York, NY). 2001;3(6):500-8.
244. Evans SM, Hahn SM, Magarelli DP, Koch CJ. Hypoxic heterogeneity in human tumors: EF5 binding, vasculature, necrosis, and proliferation. American journal of clinical oncology. 2001;24(5):467-72.
245. Zhang B, Metharom P, Jullie H, Ellem KAO, Cleghorn G, West MJ, et al. The significance of controlled conditions in lentiviral vector titration and in the use of multiplicity of infection (MOI) for predicting gene transfer events. Genetic vaccines and therapy. 2004;2(1):6-.
246. Meel MH, Metselaar DS, Waranecki P, Kaspers GJL, Hulleman E. An efficient method for the transduction of primary pediatric glioma neurospheres. MethodsX. 2018;5:173-83.
247. Zhong H, De Marzo AM, Laughner E, Lim M, Hilton DA, Zagzag D, et al. Overexpression of hypoxia-inducible factor 1α in common human cancers and their metastases. Cancer research (Chicago, Ill). 1999;59(22):5830-5.
248. Farooq M, Bhat GR, Besina S, Thakur N, Zahoor S, Rather RA, et al. Expression of HIF-1α and markers of angiogenesis and metabolic adaptation in molecular subtypes of breast cancer. Translational medicine communications. 2023;8(1):1-13.
249. Chaudary N, Pintilie M, Schwock J, Dhani N, Clarke B, Milosevic M, et al. Characterization of the tumor-microenvironment in patient-derived cervix xenografts (OCICx). Cancers. 2012;4(3):821-45.
250. Haapasalo JA, Nordfors KM, Hilvo M, Rantala IJ, Soini Y, Parkkila AK, et al. Expression of Carbonic Anhydrase IX in Astrocytic Tumors Predicts Poor Prognosis. Clinical cancer research. 2006;12(2):473-7.
251. Korkolopoulou PMD, Perdiki MMD, Thymara IMD, Boviatsis EMD, Agrogiannis GMD, Kotsiakis XMD, et al. Expression of hypoxia-related tissue factors in astrocytic gliomas. A multivariate survival study with emphasis upon carbonic anhydrase IX. Human pathology. 2007;38(4):629-38.
252. Proescholdt MA, Mayer C, Kubitza M, Schubert T, Liao SY, Stanbridge EJ, et al. Expression of hypoxia-inducible carbonic anhydrases in brain tumors. Neuro-oncology (Charlottesville, Va). 2005;7(4):465-75.
253. Lemasson B, Christen T, Serduc R, Maisin C, Bouchet A, Le Duc G, et al. Evaluation of the relationship between MR estimates of blood oxygen saturation and hypoxia: Effect of an antiangiogenic treatment on a gliosarcoma model. Radiology. 2012;265(3):743-52.
254. Burrell JS, Walker-Samuel S, Baker LCJ, Boult JKR, Jamin Y, Ryan AJ, et al. Evaluation of novel combined carbogen USPIO (CUSPIO) imaging biomarkers in assessing the antiangiogenic effects of cediranib (AZD2171) in rat C6 gliomas. International journal of cancer. 2012;131(8):1854-62.